Diss. 2006 - 02
March

Systematic investigation of the isotopic distributions measured in the fragmentation of ^{124}Xe and ^{136}Xe projectiles

D. Henzlová

(Dissertation Technical University Prague)

Gesellschaft für Schwerionenforschung mbH
Planckstraße 1 · D-64291 Darmstadt · Germany
Postfach 11 05 52 · D-64220 Darmstadt · Germany

CZECH TECHNICAL UNIVERSITY IN PRAGUE

Faculty of Nuclear Sciences and Physical Engineering

DOCTORAL THESIS

Systematic investigation of the isotopic distributions measured in the fragmentation of ^{124}Xe and ^{136}Xe projectiles

Prague 2005 Daniela Henzlová

The doctoral thesis was produced at GSI Darmstadt in Germany
and in collaboration with the Nuclear Physics Institute of
Academy of Sciences of Czech Republic in Řež

Supervisors:

RNDr. Vladimír Wagner, CSc., NPI ASCR, 250 68 Řež, Czech Republic
Dr. Karl-Heinz Schmidt, GSI, Planckstr. 1, 642 91 Darmstadt, Germany

October 2005 Darmstadt

To my beloved mum and family

CONTENTS

7. Symmetry energy of hot fragments 101

Appendices:

Introduction

The isotopic composition of the final residues formed in the high-energy reactions of exotic beams serves as an important source of information on the properties of the nuclear systems under extreme conditions. It is especially the extension of the present knowledge towards the limits of the existing nuclei, which motivates the experimental activities in the regions of very exotic nuclei (with extreme neutron or proton contents), and it is one of the main interests of nowadays nuclear physics to gain a deeper insight into their properties in order to pin down the nuclear equation of state and to track its isospin dependence, which may allow to obtain information relevant for better understanding of some specific astrophysics scenarios such as supernovae explosions and properties of neutron stars. To perform such investigations, the RIB (rare ion beam) facilities are considered and built around the world in order to provide the high-energy beams of exotic nuclei [EURISOL, RIA, FAIR (SUPER-FRS), RIBF]. To obtain information about the production of the exotic isotopes and possible intensities provided by the RIB devices, theoretical models predicting the production cross sections need to be tested for the validity of their predictions, especially in the range of the less experimentally explored exotic isotopes.

The experimental data on the isotopic distributions of the final residues produced in the reactions of two projectiles with extremely different neutron contents thus naturally serve not only to learn more details about the properties of nuclei under the extreme conditions, but provide a unique database for comparison with the present tools used to predict the production cross sections at the same time.

Within this work, the projectile-like residues produced in the peripheral to mid-peripheral reactions of ^{136}Xe(N/Z=1.52)+Pb and ^{124}Xe(N/Z=1.30)+Pb at 1 A GeV are investigated. In particular, the isotopic composition of the final residues measured in a broad range of nuclear charge is studied, profiting from the very good isotopic resolution of the high-resolution magnetic spectrometer Fragment Separator (FRS) at GSI, Darmstadt. This information provides an extensive database to explore the influence of the N/Z of the initial system on the isotopic composition of the final residues and is used for the comparison with presently the most extensively used empirical parameterization of the production cross sections, EPAX [Süm90, Süm00] (chapter 5) and with the ABRABLA code [Gaim91], which is based on the abrasion-ablation model of the heavy-ion collision (chapter 6).

As found in (e.g. [Sri02,Mor93]), upon introducing high excitation energy into the nuclear system formed in the collision a process of break-up (or multifragmentation) was observed experimentally, where the highly excited nuclear system disintegrates into smaller fragments of various sizes. This process was observed for excitation energies introduced in the collision exceeding app. 3 MeV per nucleon [Xi97,Bad93]. The investigation of this process gains a considerable experimental as well as theoretical interest due to its similarity to the process of liquid-gas phase transition known from the macroscopic thermodynamics. Indeed, during the process of the nuclear break-up new phenomena, not present in case of an evaporation process, occur, and the properties of the produced fragments may be considerably different from the typical evaporation residues. It is one of the greatest challenges of present nuclear physics to investigate this process experimentally in order to extract information on its characteristics, which may help to identify the signatures of the liquid-gas phase transition in finite nuclear systems and to constrain the nuclear equation of state.

Experimentally the characteristics of the nuclear system formed in break-up may be extracted from the properties of species emitted by this system. In the recent past, the investigations of the isotopic composition of the fragments produced in the nuclear break-up evolved to a very important tool to gain a deeper insight into the specific properties of the breaking-up nuclear system. The experimental investigations concentrated predominantly on the properties of light and intermediate-mass fragments (IMF, $3 \leq Z \leq 20$) especially in the nuclear charge range app. $Z \leq 10$ (e.g. [Ma04,Pag04,Xu00,Poch97,Tsa97b]), which is in part motivated by the observation that due to the large energetic separation between the ground and lowest-lying excited states, the light fragments are not so strongly influenced by the evaporation process. Therefore, they may be used, within reasonable assumptions, to access the properties of the initial excited system. Another reason for focusing on lighter products is the limitation in the mass resolution of the majority of the presently used experimental devices, which allows for an isotopic identification in the mass range generally not exceeding $A \sim 20$. Moreover, the major part of the experimental investigations of the process of nuclear break-up was performed in the heavy-ion collisions in the Fermi energy regime (~ 20 - 50 *A* MeV). In this energy range the exchange of nucleons between the interacting projectile and target, the process of isospin diffusion, affects the isotopic composition of the primary excited fragments entering the break-up stage and thus also the isotopic properties of the final residues, which as a consequence are not uniquely defined by the characteristics of the break-up process. Also a significant compression and angular momentum are involved in these reactions affecting the final observables. From this point of view it may be especially interesting to move the investigations of the break-up process towards relativistic beam energies, where this initial uncertainty on the N/Z of the primary fragments is removed, since due to the high velocities of the interacting nuclei, the primary fragments keep on average the N/Z of the projectile. At the same time, in the reactions in the relativistic energy regime the influence of the dynamical effects is minimized.

Indeed, according to [Hub91,Schm93], in the relativistic energy regime, the excitation energies sufficient for occurrence of the nuclear break-up (exceeding app. 3 MeV per nucleon) are acquired already in rather peripheral collisions corresponding to a rather low mass loss, and thus the contribution of this process to the production of final residues measured in this work may be expected. Profiting especially from the isotopic identification available in the broad nuclear-charge range, the investigations of the highly excited system undergoing the nuclear break-up may be extended towards the heavier residues formed in the reaction. It is one of the aims of this work to search for the signatures of the break-up process in the isotopic distributions of the final residues explored over a broad range of the nuclear charge and eventually to extract information on some properties of the nuclear system formed in this process. Within the framework of a statistical multifragmentation model (SMM) [Bon95], the shape of the *initial* isotopic distributions of the hot fragments formed in the nuclear break-up (i.e. before the evaporation) is determined directly by the physical conditions of the reaction process. According to this description, the *initial* isotopic distributions are approximately Gaussian with the mean values and widths defined mainly by the isotopic composition of the reaction system, its temperature and magnitude of the symmetry energy (symmetry-energy coefficient) [Bot02], where the symmetry energy may be parameterized as:

$$E_{sym} = \gamma(\rho,T) \cdot \frac{(A-2Z)^2}{A}, \qquad (1)$$

with $\gamma(\rho,T)$ representing the symmetry-energy coefficient.

As predicted in [Bot02], the first moments (mean values) of the isotopic distributions are affected predominantly by the isotopic composition of the initial reaction system, while the second moments (widths) are in particular influenced by the magnitude of the symmetry energy and the temperature, where high values of temperature and/or low values of the symmetry-energy coefficient cause broadening of the *initial* isotopic distributions, since the production of isotopes more far apart from the maximum of the isotopic distribution is allowed.

However, experimentally only the *final* isotopic distributions of the cold residues at the end of the evaporation process are accessible. The evaporation process strongly affects both the first as well as the second moments of the isotopic distributions so that the information available in the *initial* distributions may be masked or even completely removed in the course of the deexcitation. Thus many of the experimental investigations are based on the isotopic yield ratios, where the distortions due to the secondary deexcitation process should be largely minimized: in [Alb85] the double-isotopic-ratio method was developed to determine the nuclear temperature, and with its use the nuclear caloric curve was deduced (e.g. [Poch95, Ma97, Hau00]); in [Tsa01a] the exponential dependence on the neutron and proton number of the yield ratios of the same isotopes produced in the reactions with very different initial neutron content, termed isoscaling, was observed. Based on this observation, a method introduced in [Bot02] to extract the coefficient of the symmetry-energy term of the nuclear equation of state was proposed.

Nevertheless, also the bulk characteristics of the full isotopic distributions may be investigated to infer some properties of the highly excited nuclear system. A recent experimental observation [Schm02] has shown that the mean N-over-Z ($<N>/Z$) ratio of the largest fragments surviving the reaction process preserves a sensitivity to the N/Z of the initial system even at the end of the evaporation cascade. The closer analysis of this observation suggested that the mean isotopic composition of the final residues reveals sensitivity to the length of the evaporation process, with this length being determined solely by the thermal conditions at the beginning of the process. The observation that the isotopic composition of the final residues is sensitive to the excitation energy was made already in [Morr80,Sté91,Schm93], however, here only residues close to the projectile were investigated.

It is one of the main interests of this work to explore the final isotopic distributions in the broad nuclear-charge range, in order to study the extent to which the properties of the hot nuclear system formed in the heavy-ion collision might have survived the evaporation process. In particular, the sensitivity of the final isotopic composition to the length of the evaporation process is investigated, with the special emphasis on the influence of the emission of larger clusters ($Z>2$), which was not considered in [Schm02]. As well the isoscaling phenomenon over the broad range of the nuclear charge is explored and the symmetry-energy coefficient is extracted. For the former analysis, the nuclear reaction code ABRABLA is used, which allows to test the validity of its predictions at the same time. The isotopic distributions obtained in the two experiments are as well compared with the empirical parameterization EPAX.

The text of the thesis is organized as follows: In chapter 1 an overview on the experimental investigations of the process of nuclear break-up based on the isotopic observables is presented, focusing in particular on the nuclear thermometry and the isoscaling phenomenon and related analysis of the symmetry-energy coefficient. Chapters 2 and 3 describe the experimental technique used to measure the final isotopic distributions in the broad range of nuclear charge and the corresponding data analysis. In chapter 4 the experimental results in terms of velocity, isotopic, mass and charge distributions as well as the mean N-over-Z are presented and in chapter 5 the comparison of the experimental data with the EPAX parameterization is performed. Chapter 6 introduces the ABRABLA code and investigates the sensitivity of the isotopic composition of the experimental data to the excitation energy at the beginning of the evaporation process. The information extracted in this investigation is used to explore the thermal conditions at this stage. Finally, in chapter 7 the yield ratio of the isotopes produced in the two reactions measured within this work (^{136}Xe+Pb and ^{124}Xe+Pb) is investigated for the manifestation of the isoscaling phenomenon, and the method proposed in [Bot02] to extract the symmetry-energy coefficient of hot fragments is applied to these data. The main achievements of the investigations performed in this text are summarized in the Conclusions. Appendices following the main text provide the figure gallery of the isotopic distributions compared with EPAX and different options of the ABRABLA code as well as the full listing of the isotopic cross sections measured within this work.

Chapter 1

Experimental investigations of properties of the highly excited nuclear systems

Heavy-ion collision is a process, where many of the peculiar properties of the nuclear systems under the extreme conditions of excitation energies and densities may be studied. The heavy-ion collision in the relativistic energy regime may be viewed as an abrasion process, where depending on the impact parameter few to majority of the nucleons from the interacting projectile and target nuclei are stripped off. This process leads to the formation of target- and projectile-like primary fragments (spectators), which may be considerably excited and of the so called participant zone composed of the removed nucleons (participants). Different aspects of the reaction process and nuclear properties may be studied by investigating remnants of the reaction process. While the properties of a highly compressed and excited nuclear system may be accessed by studying the participant zone, the highly excited, normal to low density regimes may be accessed in the projectile- (target-) like spectators depending on the violence of the collision. It is the latter case, which is investigated in our experiments.

Indeed, the properties of the highly excited nuclear systems formed in such collisions may considerably differ from the properties of cold nuclei observed in the nature and especially quite new phenomena may occur if the nucleus gets substantially excited. It is a tempting task to access these phenomena and to learn more about their characteristics with the experimental and theoretical tools presently available. In the following section the process of nuclear break-up occurring at the high excitation energies will be described and its ‘relation’ to the liquid-gas phase transition in nuclear matter will be discussed. As mentioned in the introduction, the final isotopic distributions are in the main focus of this work and are investigated to search for the signatures of the process of nuclear break-up. In this chapter an overview on some of the methods investigating the properties of highly excited nuclear system undergoing the break-up process based on the investigation of the isotopic composition of the final fragments is presented. The main focus is concentrated on two specific features that will be studied also in this work, the determination of the nuclear temperature and the extraction of the coefficient of the symmetry-energy in the binding-energy formula.

1.1. Break-up of the highly excited nucleus and the process of the liquid-gas phase transition

In the heavy-ion collisions a substantial amount of excitation energy may be introduced in the interacting nuclei. It was observed in many experiments that upon exciting the nucleus in the collision above the energies of the order of 3 MeV per nucleon, the increased production of many smaller fragments was detected, suggesting the multifragment break-up of the highly excited nuclear source (e.g. [Poch95,Schü96,Bor01,Ves04]). This new phenomenon in the high excitation energies is called multifragmentation (multifragment break-up) and is presently under extensive experimental investigation as a possible manifestation of the liquid-gas phase transition in nuclear matter.

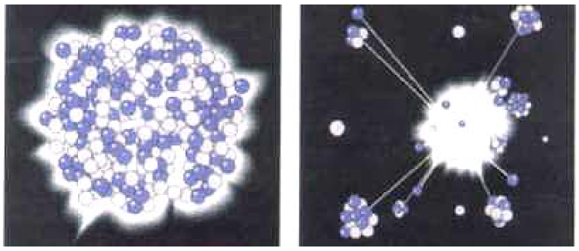

Fig. 1.1: Schematic view of the nuclear break-up: (left) expanding excited nucleus; (right) multifragment break-up.

The occurrence of the liquid-gas phase transition in nuclear matter is connected with the nature of the nucleon-nucleon interaction and is predicted by many theoretical investigations [Nör00, Müll95, Bon95, Poch97]. In fact the shape of the nuclear interaction potential is very similar to the Lenard-Jones molecular potential, with short-range repulsive core followed by a long-range attractive interaction part (Fig. 1.2).

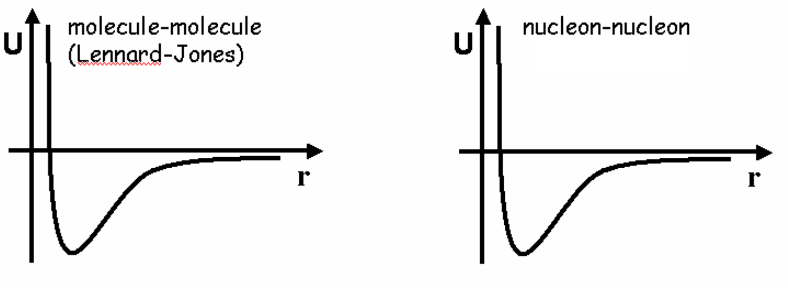

Fig. 1.2: A schematic representation of the similarity between the molecular and nuclear potentials (arbitrary units).

Considering the Lenard-Jones form of potential, the van der Waals equation of state may be derived. In Fig. 1.3 some isotherms obtained from the van der Waals equation are shown. They reveal an S-like shape in a region, where the increase of pressure results in an increase of volume. In this region it is energetically favorable for the system to split into two distinct phases. The phase transition occurs, which in the real gases proceeds along the line of constant pressure indicated by a horizontal line (Maxwell construction). Since the nature of the nuclear potential is very similar to the form of the Lenard-Jones potential, a liquid-gas phase transition is expected in infinite nuclear matter.

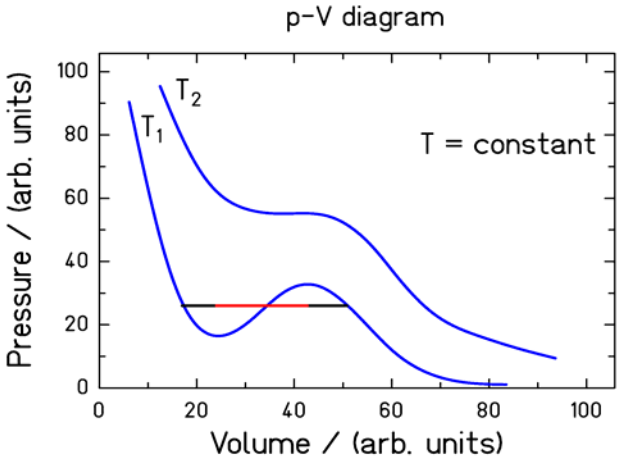

Fig. 1.3: Isotherms for two different temperatures, obtained from the van der Waals equation.

However, the thermodynamical description of the process of a phase transition in the nuclear system, which is a *finite* and *two-component* (consisting of protons and neutrons), is considerably different than as known from the macroscopic thermodynamics of single component systems. Several theoretical attempts were made to describe the liquid-gas phase transition in finite systems [Nör00, Lar99, Col02]. Some works investigated also the influence of the isospin-asymmetry of the system on the phase transition [Müll95, Bar98, Lar99, Bar02, Marg03], however mostly for infinite nuclear matter. Generally in case of finite two-component systems the discontinuities in the phase diagram are no longer predicted. The phase transition should manifest itself through different observations, such as a bimodal distribution of specific order parameter [Chom01], abnormal kinetic energy fluctuations due to divergent and negative branches in the heat capacity [Chom99], or through critical behaviors manifested by different types of specific scalings [Fish67, Bote00]. Also the observation of the apparent flattening of the nuclear caloric curve attained a considerable interest [Rich01, Ma97, DasGu00], which is known as a manifestation of the first-order liquid-gas phase transition in the macroscopic systems. The phase transition in the two-component system is expected to lead to the process of isospin fractionation [Müll95, Bar98, Bar02, Marg03,Chom04], where the liquid phase (fragments) formed in the phase transition is more symmetric in *N*/*Z* than the gas of nucleons and light clusters.

Apart from the processes related to the phase transition, the process of nuclear break-up may reveal additional interesting features. As proposed by [Frie88, Nör00], before the break-up, the highly excited system expands to larger volume under the influence of the thermal pressure. Under such conditions new phenomena may occur, affecting the formation of the fragments. According to [LeFev05, She05], the formation of fragments in the multifragment break-up of the highly excited nuclear system may lead to the lowering of the coefficient of symmetry energy below the value known to be valid for cold nuclei. Indeed, the nuclear break-up is a process where many new features may be expected and the investigations of this process may help to extend our understanding of the properties of nuclei formed at high excitation energies and low densities.

As mentioned in the introduction the main ‘limitation’ of the experimentalists is caused by the fact that only cold residues are experimentally detected and thus often elaborate theoretical tools are needed in order to extract the information on the hot system properties from the experimental data. In the following sections some of such tools developed in particularly for investigations of the nuclear temperature and the symmetry-energy coefficient will be introduced, which are based on the isotopically identified final residues.

1.2. Nuclear temperature and nuclear caloric curve

The isotopically resolved residues may be used to extract the temperature of the excited nuclear system formed in the collision, which allows to reconstruct the nuclear caloric curve, providing thus an additional insight into the thermodynamical properties of the nuclear system undergoing the break-up process. However, the experimental determination of the nuclear temperature is a difficult task, since we study dynamically evolving nuclear systems, which cool down by evaporation before reaching the detector set-up. The influence of evaporation and the dynamical evolution of the nuclear system complicate the determination of the nuclear temperature from the properties of the measured final residues.

The temperature of a macroscopic body is usually determined by contact of the system of interest with some object which properties (e.g. volume, pressure…) are temperature dependent. Having calibrated these properties, the temperature of the system of interest may be measured. In the temperature measurement of nuclei one has to face a different situation – nucleus is a small (microscopic) system and it is not possible to find an object small enough not to disturb the conditions of the measurement. The determination of the temperature of the nuclear system is thus usually based on the detection and properties of individual fragments emitted by this system. The idea is based on the assumption that these fragments have been produced in the thermal equilibrium with the whole system and share therefore a common temperature, i.e. the nuclear system is assumed to act as a heat bath [Morr94]. For the purpose of the nuclear temperature investigations several methods were established (slope thermometer [Morr94,Ode00], thermal bremsstrahlung [d’Ent02,Ort04], population of the excited levels [Poch87,Morr94]) and each of them has its limitations as well as advantages. In the following, one of the most widely used methods of nuclear temperature determination, based on the isotopic yields, i.e. the double-ratio method, is described in more detail and a recently established method based on simple HHe yields ratio is introduced. Finally the experimentally extracted nuclear caloric curve is discussed and the possible contribution of this work to the broad topic of the nuclear thermometry is mentioned.

1.2.1. Double-isotope ratio

The double-isotope ratio of suitably selected isotopes was proposed in [Alb85] as a tool to determine the temperature of the excited nucleus. Here, using the grand-canonical approximation (system of certain volume in heat and particle bath, which determines its temperature T and chemical potential μ), the yield of a given isotope may be determined as follows [Alb85]:

$$Y(N,Z) = A^{3/2} \frac{V}{\lambda_T^3} Z^{\text{int}} \exp(\mu(N,Z)/T) \tag{1.1}$$

where A is the mass of the isotope, V is the volume of the disassembling system, λ_T is the thermal nucleon wave-length, $\mu(N,Z)$ stands for the chemical potential of a given isotope and Z^{int} is the internal partition function expressed as:

$$Z^{\text{int}} = \sum_i (2J_i + 1) \cdot \exp(-E_i / T) \tag{1.2}$$

where the sum runs over the energy levels of the isotope, J_i is the spin and E_i is the energy of the given state.

If apart from the thermal equilibrium also the chemical equilibrium is assumed, then the chemical potential of the isotope N, Z may be directly related to the chemical potentials of the free nucleons μ_p and μ_n:

$$\mu(N,Z) = Z\mu_\text{p} + N\mu_\text{n} + B(N,Z) \tag{1.3}$$

where $B(N,Z)$ is the binding energy of isotope N, Z.
So that finally:

$$Y(N,Z) \sim Z^{\text{int}} \rho_p^Z \rho_n^N \exp(B(N,Z)/T) \tag{1.4}$$

where $\rho_p = \exp(\mu_p / T)$ and $\rho_n = \exp(\mu_n / T)$ are the free proton and neutron densities, respectively. From equation (1.4) it is obvious that the ratio of the yields of two different isotopes is proportional to $\rho_p^{Z_1-Z_2} = \exp((Z_1 - Z_2) \cdot \mu_p / T)$ and $\rho_n^{N_1-N_2} = \exp((N_1 - N_2) \cdot \mu_n / T)$, and to the difference of the binding energies of these isotopes:

$$\frac{Y(N_1,Z_1)}{Y(N_2,Z_2)} \sim \frac{Z_1^{\text{int}}}{Z_2^{\text{int}}} \rho_p^{Z_1-Z_2} \rho_n^{N_1-N_2} \exp(B(N_1,Z_1) - B(N_2,Z_2)/T) \tag{1.5}$$

Based on this expression, a double ratio may be calculated. If always two adjacent isotopes are used in each single ratio (i.e. $Z_2=Z_1$, $N_2=N_1+1$) then the dependence on the $\rho_p^{Z_1-Z_2}$ and $\rho_n^{N_1-N_2}$ cancels in the double ratio. The double ratio obtained in this way depends solely on the difference of the binding energies, which are generally known especially for the light isotopes most often used:

$$\frac{Y(N_1,Z_1)/Y(N_1+1,Z_1)}{Y(N_2,Z_2)/Y(N_2+1,Z_2)} = \frac{1}{a}\exp(\Delta B/T) \tag{1.6}$$

where $\Delta\text{B} = (B(N_1,Z_1) - B(N_1{+}1,Z_1) - B(N_2,Z_2) + B(N_2{+}1,Z_2))$ and a is a term containing the internal partition function and mass. A similar expression was derived in [Kol97] without the assumption of chemical equilibrium.

An approximation is usually made to use ground states only in evaluation of term a and to treat modifications of yields due to decay of higher-lying states as a perturbation [Poch01]. However, under this assumption the expression (1.6) leads to the temperature determination based on the ground-state yields. In reality the experimentally determined yields may be affected by the sequential feeding due to the decay of higher lying excited states of the same isotope and from particle decays of heavier excited fragments. The influence of these effects on the extracted temperature should be carefully investigated and eventually corrected for. Correction factors to the secondary feeding for 18 double ratios were deduced in [Tsa97a]. These corrections were applied to the experimental data, resulting in improved agreement between the temperature values extracted from double ratios using different isotopes [Tsa97a,Mil98].

Expression (1.6) is the basis for the temperature determination from the experimentally measured yields of suitably chosen isotopes. Presently there are various combinations of light isotopes used in this expression ranging from deuteron up to oxygen. The uncertainty of the temperature determination using this method is proportional to $T/\Delta B$ [Alb85], therefore the stability of this method against uncertainties in the experimentally determined double ratio may be improved by using the isotopes largely separated in the binding energy (i.e. $\Delta B >> T$). From this point of view the $^3He/^4He$ ratio is favored and often used as a part of the double ratio, since the binding energy difference of these two helium isotopes is 20.6 MeV.

1.2.2. Simple HHe ratio

A special version of this approach is the temperature determination using the single ratio of ^3H and ^3He isotopes and knowing the N/Z of the multifragmenting source (quasiprojectile) [Ves01], according to relation:

$$\frac{Y(^3H)}{Y(^3He)} \sim \exp\left(\frac{\mu_n - \mu_p}{T}\right) \cdot \exp\left(\frac{F_{He} - F_H}{T}\right) \tag{1.7}$$

where $\rho_n = \exp(\mu_n/T)$ and $\rho_p = \exp(\mu_p/T)$ represent the neutron and proton free densities, and F_{He} , F_H are the internal free energies of ^3He and ^3H fragments respectively.

According to the Fermi gas model at zero temperature, the separation energies S_n, S_p can be identified with the chemical potentials μ_n, μ_p. This approximation may be extended to nonzero temperatures, since only a moderate change of the chemical potential with temperature is predicted in the Fermi gas model [Ves01]. Using this approximation the difference of chemical potentials may be expressed as follows [Ves01]:

$$\mu_n - \mu_p \approx S_p - S_n = (-43.44 \pm 0.97) + (38.57 \pm 0.94)\frac{N}{Z} \ \text{[MeV]} \tag{1.8}$$

where the separation energy difference has been expressed using the N/Z ratio of the multifragmenting source [Ves01]. The second term on the right hand side in equation (1.7) depends only very weakly on the N/Z of the source and thus it may be assumed to be constant and independent on the source N/Z [Ves01]. Then the ratio of ^3H and ^3He yields may be directly expressed as a function of the N/Z and temperature of the multifragmenting source:

$$\ln\frac{Y(^3H)}{Y(^3He)} = \ln K(T) + \frac{\mu_n - \mu_p}{T} \sim K'(T) + (38.57/T)\frac{N}{Z} \tag{1.9}$$

where $K(T)$ stands for the difference of free energies from the right hand side of equation (1.7) and factor $K'(T)$ includes all the terms independent on the *N/Z* of the multifragmenting source and arising after substituting the expression (1.8). Knowing the dependence of the ^{3}H, ^{3}He ratio on the *N/Z* of the source, the temperature may be determined from the slope of the linear fit. As may be expected from the origin of this method, it provides temperatures very close to the values extracted using the double-isotope ratios.

1.2.3. Caloric curve

Using the double-isotope ratio method one of the first caloric curves of nuclei was obtained, which was deduced using the double ratio of ^{3,4}He-^{6,7}Li isotopes [Poch95] (Fig. 1.4). It was observed that the nuclear temperature plotted versus excitation energy exhibits a plateau-like region over a broad range of excitation energies. Saturation in the caloric curve is one of the prominent observations related to the first-order phase transition in macroscopic systems. Since, as is the case of for example water at constant pressure, with increasing excitation energy per molecule (i.e. heating up the system), the temperature increases until it reaches the point where any further increase of energy is consumed for the destruction of the molecular bounds in order to transform the liquid into the gaseous phase. In this region the value of temperature remains unchanged over a rather broad range of energies.

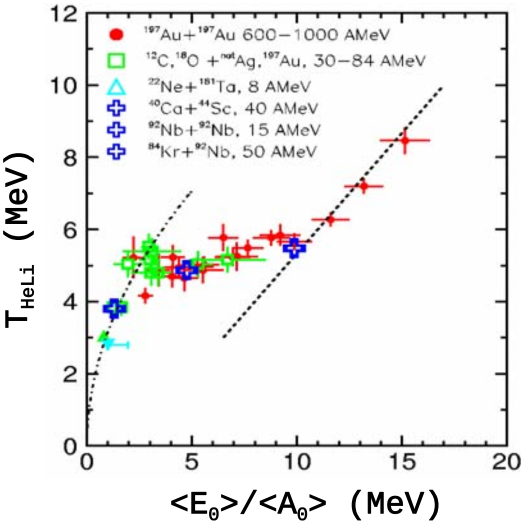

Fig. 1.4: Nuclear caloric curve from the double ratio of ^{3,4}He-^{6,7}Li isotopes in different reactions and beam energy regimes [Poch95].

This alluring similarity between the nuclear and macroscopic caloric curves triggered other experimental activities, and many further nuclear caloric curves have been accumulated up to now, exhibiting a more or less consistent behavior [Rich01]. The possible interpretation of the flattening observed in the nuclear caloric curve as a signature of the liquid-gas phase transition was, however, subject to an extensive debate over the last years [Rich01,Ma97,DasGu00]. From the thermodynamic point of view not only the energy supplied to the system (excitation energy) serves as the order parameter of the liquid-gas phase transition, but also the density (or volume) does. Then the nuclear caloric curve is a two-dimensional surface depending both on the excitation energy and on the volume of the system [Chom04]. Therefore, to interpret the observed temperature dependence on the excitation energy, the relationship between the excitation energy and volume of the system should be taken into account as well. However, on the contrary to the macroscopic systems, in case of nuclear reactions the volume is determined by the dynamics of the reaction process and cannot be directly controlled. Nevertheless, it may be possibly measured and taken into account in the subsequent analysis [Chom04]. In the recent past many efforts has been made in order to understand and eventually correct for the differences exhibited among some experimental nuclear caloric curves, and up to now more and more coherent picture is being obtained [Rad00,Nat02,Chom04]. Indeed, the nuclear caloric curve remains one of the most prominent experimental results addressing the thermodynamical properties of the highly excited nuclear systems formed in the nuclear reactions.

In this work the isotopically resolved residues are available in the broad range of the nuclear charge. Both methods discussed in the preceding sections, which are based on the isotopically resolved final residues, provide the temperature information from a very limited range of the isotopes and it would be desirable to obtain the complementary information also from the investigation of the heavier isotopes. Nevertheless, it is mainly the disturbing influence of the evaporation process, which is the leading limitation in the correct determination of the nuclear temperature, especially concerning the possible extensions towards the heavier residues, which are even more influenced by this process. Indeed, as discussed in [Char98, Duf82], the isotopic composition of the final residues after the long evaporation process is expected to gradually approach the region of equilibrium neutron and proton emission probabilities, known as the evaporation-attractor line (EAL) or the residue corridor. The isotopic composition of the final residues not too close to the projectile should thus no longer depend on the initial conditions of the reaction process. The extent to which the corridor appears to be ‘attractive’ to the final residues, however, depends on the neutron or proton excess of the initial system. In case of very n- (or p-) rich initial systems the contribution of emission of more complex clusters during the evaporation may even prevent the final residues from reaching the residue corridor at all [Char98].

As mentioned in the introduction, it was observed in [Schm02] that the mean N-over-Z ($\langle N\rangle/Z$) ratio of the largest residues surviving the reaction process preserves a sensitivity to the N/Z of the initial system even at the end of the evaporation cascade. The closer analysis of this observation suggested that the mean isotopic composition of the final residues depends on the excitation energy (and thus to the thermal conditions) at the beginning of the evaporation process. It is one of the interests of this work to investigate this sensitivity with the new set of experimental data, which also allow to compare the influence of the different N/Z of the projectile. Since the contribution of emission of more complex clusters ($Z>2$) in the evaporation may considerably influence the course of the deexcitation process, the special emphasis is put on the investigation of the influence of the emission of these clusters during evaporation, which was not considered in the investigation of [Schm02].

1.3. Symmetry energy

The balance between the Coulomb and symmetry energy is responsible for the bending of the stability valley for heavy nuclei, since while the symmetry energy favors nuclei with $N=Z$ the repulsive Coulomb interaction among protons shifts the most stable configuration towards the more n-rich region. While the symmetry energy in the nuclear binding for cold nuclei at normal density is quite well known, its dependence on density and temperature is still only poorly explored. However, it is the symmetry energy at extreme temperatures and densities, which is of particular interest for many astrophysical considerations. The magnitude of the symmetry energy determines the properties of neutron stars [Latt04,Dan02] and conditions of supernovae explosions, which are responsible for the release of heavy elements observable in the nature [Don94]. In particular, the one-dimensional calculations of core-collapse supernovae utilizing the advanced nuclear equations of state (energy of the nucleus as a function of density and temperature) usually fail to explode [Jan00,Mezz01]. These observations motivate an interest in investigation of the symmetry energy under extreme conditions, which in the terrestrial environment are achievable only in nuclear reactions.

According to [Frie88, Nör00] thermal pressure develops in the highly excited nucleus formed in the heavy-ion collision, which results in an expansion in larger volume and lower densities. The occurrence of the nuclear break-up at densities below the normal nuclear density may be found in various theoretical descriptions of this process (e.g. [Bon95,Nör00]). Nuclei produced in the multifragment break-up are thus expected to be formed in hot and dilute environment and the study of their properties provides a unique opportunity to access the symmetry energy of the nuclear system at subnuclear densities and high temperatures. In [Tsa01a] it was observed that the yield ratio of a given isotope produced in two reactions with different isospin asymmetries exhibits an exponential dependence on proton and neutron number, an observation known as isoscaling. It was shown in [Bot02] that within the statistical interpretation the isoscaling may be used to extract the symmetry-energy coefficient of hot fragments formed in the multifragment break-up.

1.3.1. Isoscaling and extraction of the symmetry energy coefficient

The isoscaling concerns an observation that the yield ratios of the same fragments produced in reactions with different isospin asymmetry exhibit an exponential dependence on N and Z, which was found in many reaction mechanisms and predicted based on statistical as well as dynamical descriptions [Tsa01c,Bar05,Ono03]. This trend may be understood within the grand-canonical approximation, where the yield of a given isotope may be described according to relation [Tsa01b,Ran81]:

$$Y_i(N,Z) = F_i(N,Z,T_i)\exp(B(N,Z)/T_i)\exp(N\mu_{n,i}/T_i + Z\mu_{p,i}/T_i) \qquad (1.10)$$

where factor $F_i(N,Z,T_i)$ contains information about the secondary decay from particle stable and unstable states to final ground state yield of isotope N, Z, $B(N,Z)$ is the binding energy of this isotope, T_i is the temperature of the source system, and μ_n and μ_p are the neutron and proton chemical potentials, respectively. If the two reactions are characterized by similar temperatures T, the binding energy terms cancel in the ratio. Moreover, if it is possible to assume that the influence of the secondary deexcitation is similar for the two reactions, the ratio of yields of a given isotope depends solely on the differences between the proton and neutron chemical potentials:

$$R_{21}(N,Z) = Y_2(N,Z)/Y_1(N,Z) = C\exp(\alpha N + \beta Z) \tag{1.11}$$

with three parameters *C*, *α* and *β*, where $\alpha = \Delta\mu_n / T$ and $\beta = \Delta\mu_p / T$. Here the notation is adopted that $Y_2(N,Z)$ and $Y_1(N,Z)$ stand for the yield of isotope (*N,Z*) in the more neutron-rich and more neutron-deficient reaction system respectively.

Alternatively, the isoscaling may be displayed in terms of the scaled isotope or isotone ratios $S(N)$ or $S(Z)$, where the expression (1.11) is multiplied by the inverse of the exponential of *Z* or *N*, respectively. Then are all the isotopes or isotones, respectively expressed as a function of only one variable (*N* or *Z*):

$$S(N) = R_{21}(N,Z)\exp(-\beta Z) \tag{1.12}$$

$$S(Z) = R_{21}(N,Z)\exp(-\alpha N) \tag{1.13}$$

Plotting the experimentally determined ratio $R_{21}(N,Z)$ ($S(Z)$ or $S(N)$) as a function of *N* (or *Z*) the corresponding isoscaling parameter *α* (or *β*) may be extracted from the fit. It was shown that both parameters assume very close values differing only in sign (parameter *β* is negative) [Tsa01a]. Nevertheless, systematically slightly larger values of the parameter *β* were observed for the reaction systems investigated [Bot02]. As well the exponential dependence on the proton number is slightly worse respected, which may be a consequence of the Coulomb interaction among protons [Tsa01c]. Therefore, the dependence on the neutron number (in equations (1.11) and/or (1.13)) is most often used to investigate the isoscaling phenomenon.

Within the framework of the SMM code (Statistical Multifragmentation Model) [Bon95] it was shown that a relationship between the isoscaling parameter *α* and the symmetry-energy coefficient may be extracted. As may be seen below equation (1.11), the isoscaling parameter *α* is expressed through the difference in the neutron chemical potentials. According to [Bot02], in the low temperature limit (*T*→0) within the grand-canonical approximation the chemical potential may be related to the symmetry energy and the following formula for the difference of the neutron chemical potentials is extracted:

$$\Delta\mu_n = \mu_1 - \mu_2 \approx -4\gamma\left(\frac{Z_1^2}{A_1^2} - \frac{Z_2^2}{A_2^2}\right) \tag{1.14}$$

where γ stands for the symmetry-term coefficient and Z_1,A_1 and Z_2,A_2 are the charges and masses of the two source systems. The difference of chemical potentials then depends essentially only on the symmetry-energy coefficient and on the isotopic compositions of the two sources. It was shown in [Bot02] that the difference of the neutron chemical potentials is rather insensitive to temperature, which allows to extend the above relation to nonzero temperature values. Then the *α*-parameter may be expressed as follows:

$$\alpha = \frac{\Delta\mu_n}{T} = -\frac{4\gamma}{T}\left(\frac{Z_1^2}{A_1^2} - \frac{Z_2^2}{A_2^2}\right) \tag{1.15}$$

Provided that the temperature and the isotopic composition of the two source systems are known, the above relation may be used to extract the coefficient of the symmetry energy term from the isoscaling parameter α. However, the equation (1.15) refers to hot system formed at temperature T and thus it is the apparent symmetry coefficient (γ_{app}), which is determined by applying this formula to the experimental data. The influence of the evaporation process on the isoscaling parameters was investigated in [Bot02], where a significant lowering of both parameters was observed on the contrary to [Tsa01b], where it was found that while the β parameter slightly changes due to the evaporation process, which is probably related to the influence of the Coulomb interaction, the parameter α remains rather unaffected. According to [Bot02], the influence of the evaporation process depends on the excitation energy and is generally small for the lower values of parameters α and β. Therefore, the influence of the evaporation process should be investigated for each experiment individually.

Fig. 1.5 below shows an example of the recent experimental investigation of the symmetry energy coefficient based on the above analysis, performed in reactions ^{12}C + $^{112,124}Sn$ at E/A = 300 MeV and 600 MeV in [LeFev05]. In Fig. 1.5 only the apparent symmetry energy coefficient is shown. The investigation of the influence of the evaporation process, performed in the paper ([LeFev05]), suggests that the decrease of the 'real' symmetry energy coefficient with the centrality should be even stronger than suggested by the dependence of γ_{app}.

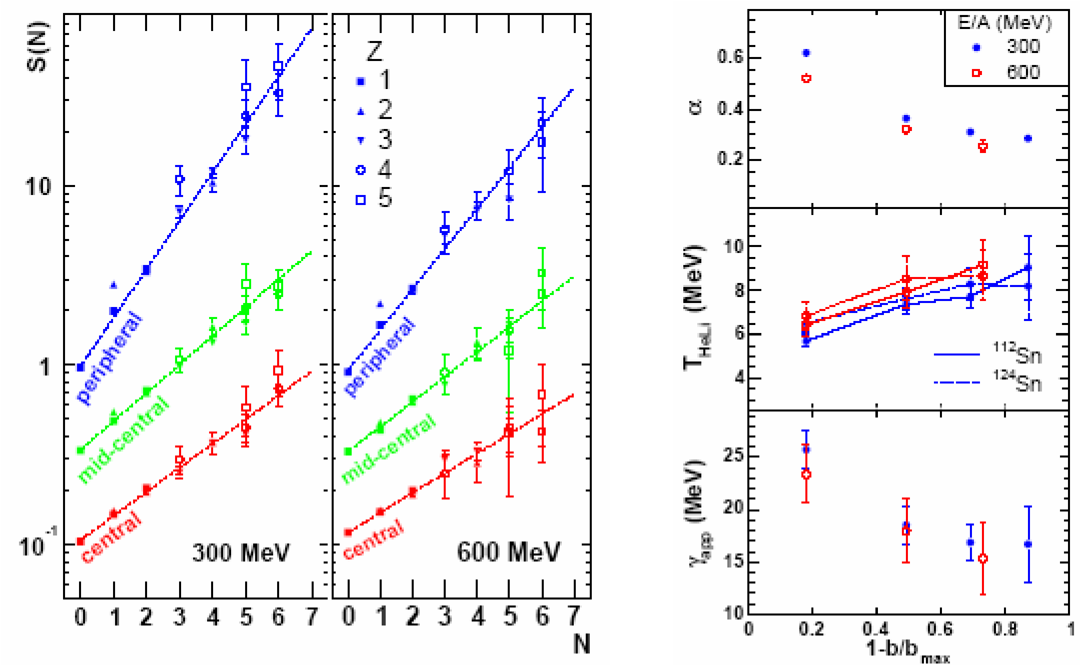

Fig. 1.5: (left) Scaled isotopic ratios S(N) for ^{12}C + $^{112,124}Sn$ at E/A = 300 MeV (left panel) and 600 MeV (right panel) for the different centralities of the collisions (see [LeFev05]). The dashed lines are the results of exponential fits. Only statistical errors are displayed. (right) Isoscaling coefficient α (top), double-isotope temperatures T_{HeLi} (middle) and resulting γ_{app} (bottom) for E/A = 300 MeV (full symbols) and 600 MeV (open symbols), as a function of the centrality parameter $1-b/b_{max}$. The temperatures for the ^{112}Sn and ^{124}Sn targets are distinguished by full and dashed lines, respectively.

The investigations of the isoscaling and the related attempts to extract the symmetry energy coefficient predominantly concentrated on the lighter residues in the nuclear-charge range Z~1-8 [LeFev05,She05]. The investigation of the isoscaling phenomenon in heavy-ion collisions in the Fermi-energy regime were performed also in a broader range of the nuclear charge [Sou03,Sou04] for the purpose of investigation of the isospin-equilibration.

The isotopic distributions measured in the frame of this work for a broad range of elements allow to explore to what extent is the isoscaling phenomenon respected in almost full range of the nuclear charge up to the projectile in the relativistic heavy-ion collisions. It is one of the interests of this work to explore the isoscaling behavior in the broad nuclear-charge range measured at the Fragment Separator and to extract the corresponding symmetry-energy coefficient from these data. The application of the above ideas to the experimental data measured within this work may be found in chapter 7.

Chapter 2

Experimental approach

The properties of the hot nuclei were investigated predominantly from the isotopically resolved light and intermediate mass fragments in the nuclear charge range typically $Z \leq 10$ (e.g. [Ma04,Pag04,Xu00,Poch97,Tsa97b]). One of the reasons was the limited mass resolution achievable with the large acceptance experimental devices. The isotopic identification of these devices is usually based either on the ΔE-$B\rho$ measurement or on the $\Delta E/E$ method, in combination with the time-of-flight measurement (e.g.[ALADIN,LASSA,CHIMERA]). Due to the technical limitations the mass resolution of these devices is limited to the mass range usually not exceeding $A = 20$. To extend the investigations of the isotopic properties of the final residues over the broader range of the nuclear charge, a high-resolution magnetic spectrometer the Fragment Separator (FRS) at GSI, Darmstadt was used in the present work.

In the following the experimental complex of GSI with the main focus on the beam delivery system and the Fragment Separator will be introduced. The principles of the isotopic identification at the Fragment Separator and its detector system will be described.

2.1. The experimental complex at GSI

The present experimental facility of GSI-Darmstadt is shown in Fig. 2.1. It consists of several experimental areas, which utilize the beam delivered by the accelerator system. The GSI accelerator system consists of the ~ 100 meters long linear accelerator UNILAC coupled to the heavy-ion synchrotron SIS having a perimeter of 216 meters. It can deliver any stable-ion beam ranging from hydrogen to uranium. The ions of interest are pre-accelerated in the UNILAC up to the energy of 12 A MeV. After the injection to the SIS, the ions are further accelerated up to the energy, which is defined by the maximum magnetic bending power of 18 Tm. This corresponds to energies of 1 to 4.5 A GeV depending on the ion specie.

The ions generated in the ion source carry still most of the electrons, the actual ionic charge state depends on the ion source. On the way through the linear accelerator, the ions are partially stripped to allow reaching the desired energy at the end of the UNILAC. The beam energy obtainable by the SIS, defined by the maximum bending power, may be slightly increased by increasing the ionic charge state of the ions of interest through their interaction with the thin carbon foil located at the entrance of the SIS.

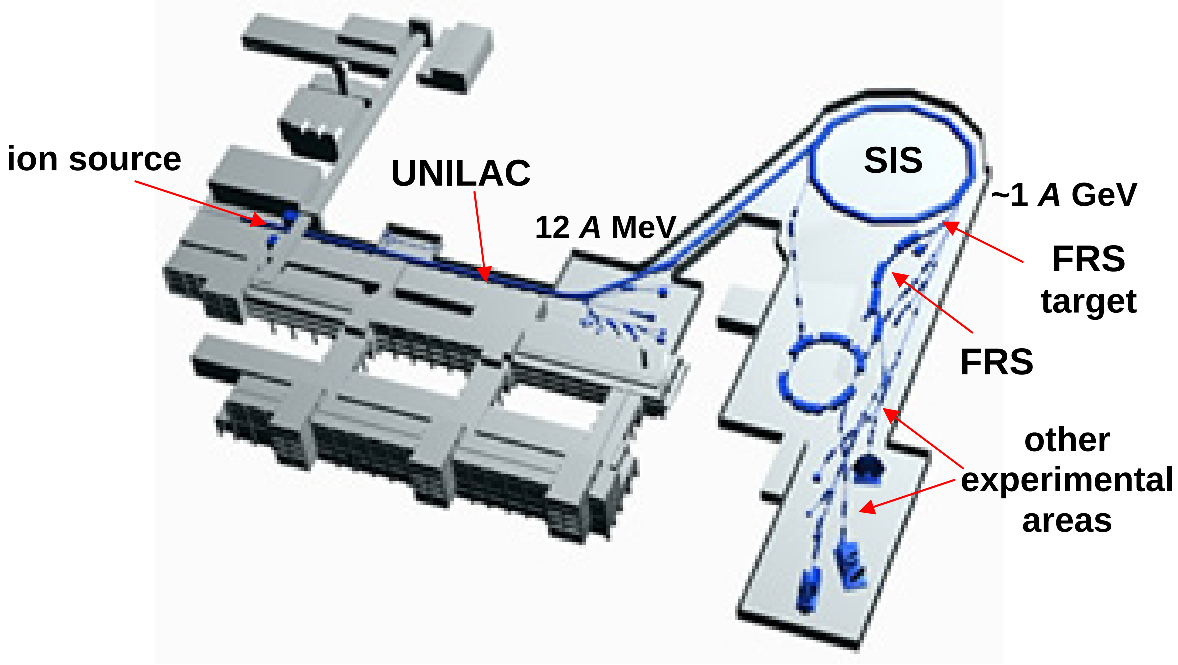

Fig. 2.1. The experimental complex at GSI Darmstadt

The intensities of the beam range presently from 10^{10} particles per second for neon, to a maximum of 10^9 particles per second for gold or uranium. The maximum intensity is limited by the space charge limit of the SIS, beyond which the magnetic field on the SIS quadrupoles is not sufficient to balance the Coulomb repulsion between the accelerating ions. The final beam quality is very high, with excellent energy resolution (the momentum spread, $\delta p=\Delta p/p$, is always below 10^{-3}) and small emittance (around 2.5 mm·mrad) [Ste92].

In the frame of this work two experiments were carried out with two xenon beams, each of 1 *A* GeV energy – ^{124}Xe and ^{136}Xe. The ions were extracted from the ECR ion source and entered the SIS with the charge states 47+ and 48+ (47 resp. 48 electrons stripped off) for ^{124}Xe and ^{136}Xe, respectively, where they were accelerated to the desirable energy of 1 *A* GeV. After the extraction from SIS, the remaining electrons were stripped off due to the passage of the beam through the SIS vacuum window, the beam monitor and the FRS target. During both experiments the slow extraction mode was used to extract the beam from the SIS, which produces spills of length in the order of a few seconds. In both experiments, the spill length was varied between 1 and 10 sec. in order to keep the maximum counting rate allowed by the detector limits and the data acquisition system. The maximum beam intensity during the experiments was $\sim 3\cdot 10^8$ particles per spill for ^{124}Xe and $\sim 4\cdot 10^7$ particles per spill for ^{136}Xe.

2.2. The monitoring of the beam

The aim of both experiments was to determine the isotopic distributions of the final residues. In order to measure the production cross sections, a continuous monitoring of the number of ions impinging on the target had to be performed. For this purpose a beam monitor, called SEETRAM (SEcondary Electron TRAnsmission Monitor) [Zie92], was used. Its schematic view is shown in Fig.2.2. The SEETRAM consists of three thin foils of 11.5 cm in diameter, which are mounted perpendicular to the beam axis. The outer foils are made of 14 μm thin aluminium layers and are connected to a voltage of +80 V. The middle foil, made of 10 µm thin titanium, is connected to the ground and insulated against the rest of the detector. The foils are curved in order to reduce the sensitivity of the detector to mechanical vibration of the beam line.

A heavy ion passing through the SEETRAM induces the emission of electrons from the middle foil, which drift towards the outer foils connected to +80 V. The current induced in the middle foil is measured by a current digitizer. By adjusting a resistance of the I/U converter in the current digitizer in the range of 10^{-4} to 10^{-10} Ω, the sensitivity of the SEETRAM may be changed from 10^{-4} to 10^{-10} Ampere of the input current, which are transformed to 1 V signal at the output. Seven levels of sensitivity adjustments are possible in total. In order to distinguish the negative part of bipolar noise signals, which may be induced for example due to switching on and off of the extraction septum, the current digitizer produces an adjustable constant offset current.

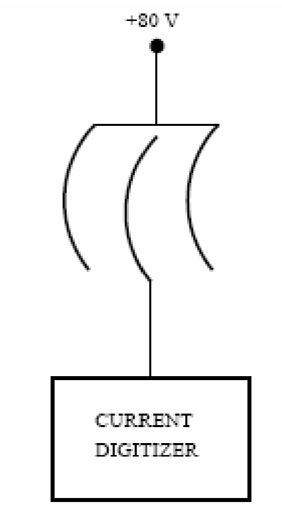

Fig. 2.2. The schematic view of the beam monitor SEETRAM

The advantage of the use of the SEETRAM for monitoring the beam is the fact that due to its design (thin foils), it almost does not affect the beam quality and does not disturb the cross-section measurements. The nuclear-reaction rate in the SEETRAM corresponds to 0.08%, which is well below the reaction rate in most of the targets used at the FRS.

Due to the large drift velocity of the electrons in vacuum, almost no space charge effects limit the operation of the SEETRAM, which is thus able to sustain high beam intensities. The linear dependence of the secondary-electron current on the number of beam particles was measured to preserve over the whole range of beam intensities provided by the SIS [Jur02]. The lower limit of the SEETRAM application is given by the condition that the produced current must be higher than 10^{-12} Ampere in order to distinguish the measured signals from the noise. The corresponding beam intensity depends on the charge and velocity of the projectile (Fig. 2.3 black line).

The SEETRAM provides information about the *current* induced by the traversing beam particles. In order to obtain the corresponding *number* of beam particles, this current must be calibrated. The calibration may be performed using either the self-calibrating ionisation chamber (IC) or the scintillation detector, or both to count the traversing ions. The choice of the calibration detector depends on the charge and velocity of the beam, and is defined by the different limits of application of these detectors. The upper limit of the linear operation of the particle counting in the ionisation chamber is 10^4 particles per second due to pile-up in the main amplifier; and the upper limit of the current signal from the IC corresponds to 10^{-7} Ampere, since above this value the recombination losses become higher than 10 %. The applicability of the scintillator is limited by the ‘dead time’ of electronics and corresponds to counting rates of the order of $\sim 10^5$ particles per second, where saturation effects start to be higher than 1 %. Fig. 2.3 shows the operational limits (coloured lines) of all the detectors for several elements and energy of 1000 A MeV. It may be seen that the use of the ionisation chamber (red and green lines) is well suited for the lighter elements (below Zr), where a sufficient overlap with the SEETRAM operation is observed. On the contrary the applicability of the scintillation detector (blue line) overlaps with the operational limits of SEETRAM (black line) only in the region of heavy ions (above Zr) and thus is better suited for the SEETRAM calibrations in case of heavy beams. In both experiments with the xenon beams the scintillator was used for the SEETRAM calibration. From the correlation between the SEETRAM counts and the number of beam particles measured with the scintillator the corresponding calibration factor was extracted (see chapter 3.1).

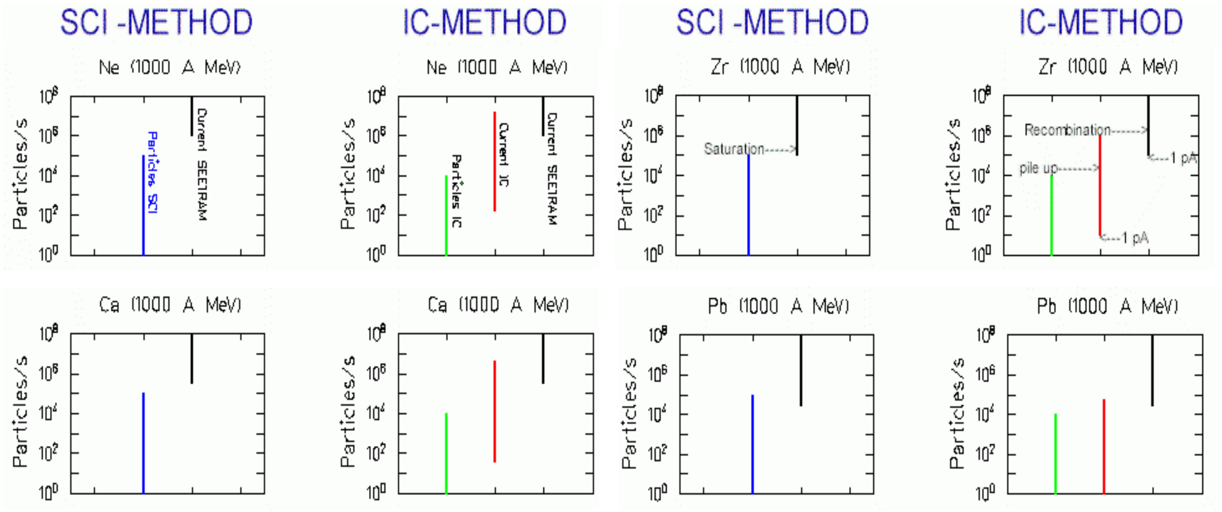

Fig. 2.3: Operational limits of the scintillator (SCI) and the ionization chamber (IC) calibration methods. Different lines represent the regions of applicability of different methods: black line - SEETRAM current, blue line - particle counting by SCI, green line - particle counting by IC, red line - current measured by IC.

2.3. The Fragment Separator

The Fragment Separator is a high-resolution magnetic spectrometer, which allows to separate the final residues from the lightest ones up to the heavy projectile in their mass and nuclear charge. It utilizes the inverse kinematics, which means that the projectile-like fragments exiting the target are detected in flight. A schematic view of the device is shown in Fig. 2.4.

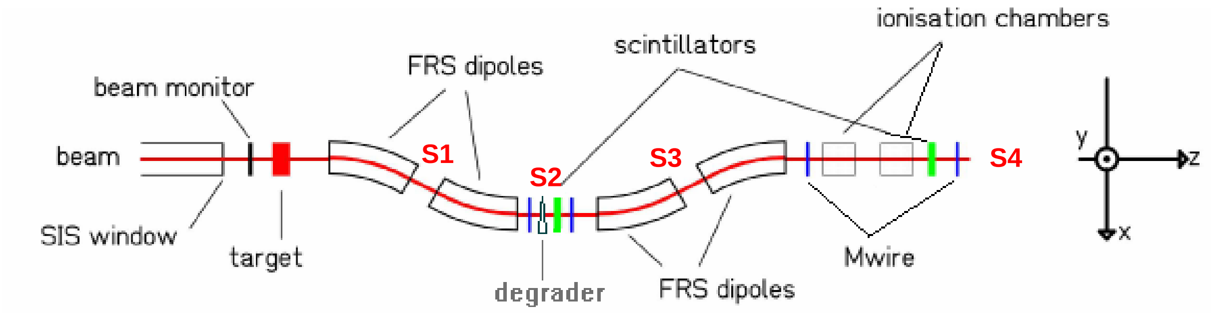

Fig. 2.4. The schematic, top view of the Fragment Separator (FRS)

The FRS is a two-stage magnetic spectrometer consisting of four dipole magnets with a maximum bending power of 18 Tm. The first and the second magnetic stages are separated by the intermediate dispersive image plane (S2). In front of the device is located the beam monitor SEETRAM and its calibration detector system (IC and scintillator). The target ladder is located just in front of the first dipole. It carries several (~75) different target foils, which may be selected by appropriate positioning of the ladder. In both experiments analyzed in this work a natural lead foil of 635 mg/cm^2 thickness was used. The standard FRS detector equipment consists of two plastic scintillation detectors, two ionization chambers and of the system of multiwire-proportional counters (MWPC) located as shown in Fig. 2.4. The description of the working principles of these detectors is given in section 2.4.

The motion of the ions in the magnetic field is ruled by the Lorentz force. The magnetic fields inside the dipoles are uniform and perpendicular to the velocity of the fragment so that the trajectory of a fragment with given A, Z and velocity v in the FRS is defined as:

$$B\rho = \frac{p}{q} = \frac{m_0 \gamma \beta c}{q} \approx \frac{uA}{q} \beta \gamma c \tag{2.1}$$

where B is the magnetic field in the dipole, ρ is the radius of the trajectory, p is the momentum of the fragment, m_0 is its rest mass, u represents the atomic mass unit ($m_0 \approx Au$), q is the ionic charge state of the fragment ($q = Ze$ with e being the electron charge) and $\gamma = \sqrt{(1-\beta^2)^{-1}}$ is the relativistic factor with $\beta = v/c$ (c is the speed of light). From the above equation it may be seen that the bare ions (without any electron, $q=Z$) and those not fully stripped ($q \neq Z$) will follow different trajectories in the FRS. Indeed the fragments produced in the target may capture (or again lose) an electron on their passage through the target material or through other materials in the FRS beam line. The contribution of these not fully stripped ions spoils the isotopic identification and thus it must be kept as low as possible. In case it is needed, an additional layer of suitable (Ti, Nb…) thin material may be used to strip the electrons more efficiently than is the case in the target material or the scintillation detector. In case of the ^{124}Xe and ^{136}Xe beams the contamination of charge states was below 1% so that no additional layer was needed. The method to disentangle the charge states in the data analysis is introduced in chapter 3, section 3.2.3.

The projectile-like fragments produced in the target, which have suitable magnetic rigidities ($B\rho$) enter the Fragment Separator. In the first magnetic stage the fragments are separated according to their magnetic rigidities, so that the fragments having higher velocities ($\beta\gamma c$) and/or larger *A/Z* ratio (resp. *A/q* in case they are not fully stripped) follow the trajectory with larger radius, i.e. are less bent in a given magnetic field *B*. Slower fragments and/or fragments having lower *A/Z* (*A/q*) are on the contrary bent more. As a consequence these fragments will land in different horizontal (x) positions in the intermediate image plane. The position and the magnetic rigidity are related through the dispersion relation:

$$D = \frac{dx}{d(B\rho)/(B\rho)} \ [\text{cm/\%}] \tag{2.2}$$

The dispersion *D* defines the change of the horizontal position if the magnetic rigidity ($B\rho$) changes by 1%. In the achromatic system the total dispersion of the two stages is equal to zero. This assures a point-to-point imaging, and all the fragments produced in the target will land in the same position in the final focal plane. The second magnetic stage thus acts in an opposite way to the first stage and collects again all fragments with different magnetic rigidities.

To separate the fragments in the final focal plane, a layer of material must be inserted in the intermediate image plane. The degrader at S2 may be used for this purpose (Fig. 2.4). The degrader is a suitably shaped layer of material, which is used to reduce the energy of fragments passing through so that behind the degrader they appear with different velocity and thus different $B\rho$. The shape of the degrader is chosen in such a way that the ratio of the magnetic rigidity behind and in front of the degrader is the same for one selected nuclide. Due to the dominating influence of the nuclear charge on the energy loss, the magnetic rigidities of the isotopes of one element behind the degrader are scaled by the same factor. Since this factor is different for different elements, they will land in different horizontal positions in the final focal plane. Therefore, by adding the degrader in the intermediate image plane, the fragments will be separated in the second stage of the FRS according to their charge. In case the fragments are not fully stripped (i.e. on their passage through layers of matter in the beam line catch or loose electrons) the situation is slightly more complicated as discussed in section 3.2.3 of the following chapter.

A similar effect as with use of the degrader is obtained if the scintillator is used instead. In this case, due to the parallel orientation of the surfaces, the energy loss will be approximately the same regardless of the horizontal position along the scintillator. Therefore, the relative change $d(B\rho)/(B\rho)$ of the magnetic rigidity for isotopes of one element will not be the same anymore, rather it will slightly depend on the horizontal position at S2 (i.e. $B\rho$). Nevertheless, due to a low thickness of the scintillator, a separation of different elements in the final focal plane will be to a good extent preserved.

The selection of fragments passing the FRS for a given value of the magnetic fields may thus be viewed on the chart of nuclides as shown in Fig. 2.5. Assuming a certain velocity of the fragments, the selection in the first magnetic stage corresponds to the window limited by constant values of *A/Z*, indicated by the red lines. This rather narrow window in *A/Z* is defined by the acceptance of the FRS (see section 2.3.1). In case of different velocities of fragments these limits are slightly extended especially for light residues. The selection in the second FRS stage, in case of high fragment energies, corresponds to a window in the nuclear charge as displayed by the blue lines.

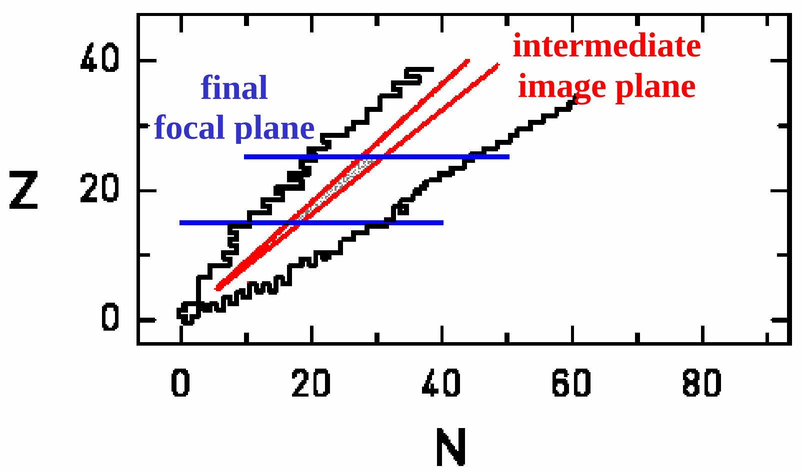

Fig. 2.4: Selection of fragments passing the FRS in one setting of the magnetic fields.

The measurements performed in the present experiments were split into two scans, where for a given projectile the final fragments with low and high nuclear charge, respectively, are selected by the second stage of the FRS. In case of both Xe beams the fragments with charge ~$Z \leq 30$ were measured in the first scan (light fragment settings) and fragments with charge ~$Z \geq 25$ in the second scan (heavy fragment settings). In order to obtain isotopes with different magnetic rigidities (i.e. A/Z and/or velocity) several measurements (around 50) with different values of the magnetic fields had to be performed in each scan. The magnetic fields of the first two dipoles were changed by steps of 1.5%, and the fields of the last two dipoles were correspondingly adjusted to keep a selected nuclear charge on the central trajectory. A step of 1.5% was chosen, since it corresponds to one half of the FRS momentum acceptance (see section 2.3.1). In case of light-fragment settings a degrader in the intermediate image plane was used to assure larger energy losses of heavier fragments to assure that only the fragments up to Z~30 pass through the FRS. During the heavy-fragment settings only the scintillator was sufficient to separate the produced elements in the final focal plane.

It is obvious that fragments exit the target under different angles. To assure that the fragments positions in the intermediate and final image planes do not depend on these angles, a set of quadrupoles is combined with each dipole. The pair or triplet of quadrupoles with drift sections in between act as a lens, thus in combination with the dipole any dependence on the angles is removed, and the focusing effect is achieved. The positions of the fragments in the intermediate and final image planes then depend solely on the magnetic rigidities and charges of the fragments, respectively and may be used for the identification. According to equation (2.1), the isotopic identification using the FRS is based on the measurement of magnetic rigidities ($B\rho$), velocities ($\beta\gamma c$) and ionic charges of the produced fragments. The magnetic rigidity may be determined from the positions of the fragments measured in the intermediate and final image planes according to the following relations:

$$B\rho_2 = B\rho_{central}(1+\frac{x_2}{D_2}) \tag{2.3}$$

where x_2 is the horizontal position measured by the scintillator at S2 and D_2 is the corresponding dispersion. A similar relation holds for the magnetic rigidity in the second FRS stage:

$$B\rho_4 = B\rho_{central}(1+\frac{x_4 - M \cdot x_2}{D_4}) \tag{2.4}$$

where x_4 is the horizontal position measured by the scintillator at S4, D_4 is the dispersion in the second FRS stage and $M = D_4 / D_2$ is the magnification between the first and the second FRS stages. The velocity of each fragment is determined from the measurement of time-of-flight between the two scintillation detectors, and the charge is deduced from the energy loss measured by two ionization chambers located in the final focal plane.

The final mass resolution is very high, and the corresponding resolving power amounts to $A/\Delta A \approx 400$ even for the heaviest residues. This allows to isotopically identify all the reaction products ranging from the lightest ones up to the heavy projectile. The high mass resolution is defined by the resolution of the measurements of $B\rho$ and ToF. The resolution in magnetic rigidity is given by the construction of the FRS and by the position measurement with the scintillation detectors, and is as high as $5 \cdot 10^{-4}$ (FWHM). The resolution of the ToF determination is given by the scintillation detectors, and is as good as 100ps over 36.8 meters. This allows to determine the velocity parameter $\beta\gamma$ with a relative uncertainty of $2.5 \cdot 10^{-3}$. The unique mass resolution of the Fragment Separator is achieved at the expense of a limited angular and momentum acceptance of this device. The consequences of the limited acceptance on the measured results are discussed below.

2.3.1. FRS acceptance

The angular and momentum acceptance of the Fragment Separator correspond to 15 mrad around the beam axis and 3%, respectively. As a consequence only one residue produced per collision in the target is detected, since the magnetic rigidities (*A/Z* and/or velocities) of other products of this collision mostly do not match the same magnetic-field setting of the FRS. As was mentioned in the previous chapter, several measurements with different settings of the magnetic fields are performed to detect residues with different *A/Z* and/or velocities. Because of the possibility to combine several magnetic field settings, the limited acceptance in momentum does not affect the measured results, since the momentum (velocity) distributions of every residue are fully measured by successive scanning of their different parts (see Fig. 2.6). Moreover, the selected step of 1.5% in magnetic rigidity assures sufficient overlap of the velocity distributions measured in the neighboring settings so that the velocity distributions may be reconstructed with a high quality.

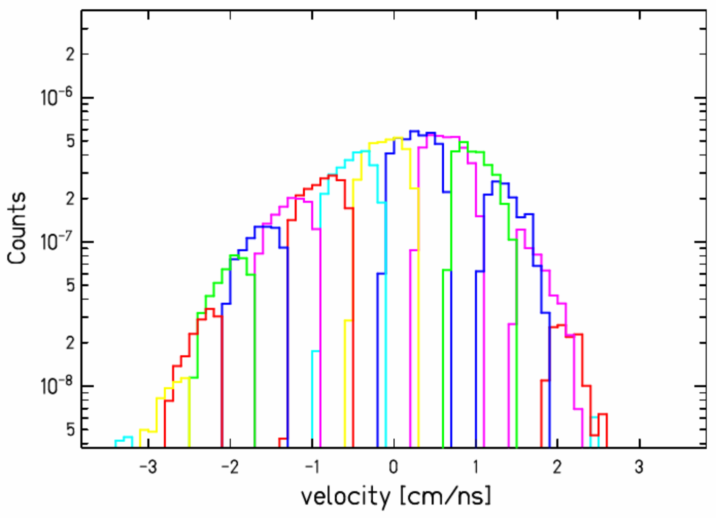

Fig. 2.6: The velocity distribution of the isotope ^{21}Ne produced in the fragmentation of ^{136}Xe projectile. Different colors represent the distributions measured with different settings of magnetic fields.

On the contrary, the limited angular acceptance results in reduced transmission of residues having broad angular distributions and thus in reduction of the measured yields. While the heavy residues are produced with rather narrow angular distributions and they are almost fully transmitted by the FRS, the angular distributions of light residues are rather broad and their transmission may be as low as 10% for the lightest residues. The rather low transmission of the light residues may nevertheless be corrected with the use of a dedicated code [Benll02], which simulates the transmission of every ion through the magnetic fields of the FRS and provides the corresponding correction factor. More details about this correction are given in section 3.3.

The limited angular acceptance of the FRS may be used to separate different reaction mechanisms such as the fragmentation and processes like fission or break-up with one surviving large residue. In case of fragmentation reactions, the final residues occupy a sphere in the three-dimensional velocity space. On the other hand, in case of any binary process the two produced fragments repel each other by the Coulomb repulsion, which strength is proportional to the product of the two charges. This results in a velocity distribution corresponding to the shell of a sphere in the three-dimensional velocity space. The angular acceptance of the FRS may be depicted as a narrow cone as schematically shown in Fig. 2.7, which means that only the parts of the velocity distribution within this cone are accepted by the FRS. Due to the quadrupoles in the FRS beam line, which act as lenses focusing fragments entering under different angles, only the longitudinal component of the fragment velocity is measured with the FRS. As a consequence, any binary process is revealed in the velocity distribution as a double-Gaussian structure (Fig. 2.7 lower part). It may be seen that the binary contribution may be clearly recognized in the two peaks on the side of the distribution. The relative importance of the central fragmentation peak and the two binary side-peaks depends on the relative magnitude of the two processes.

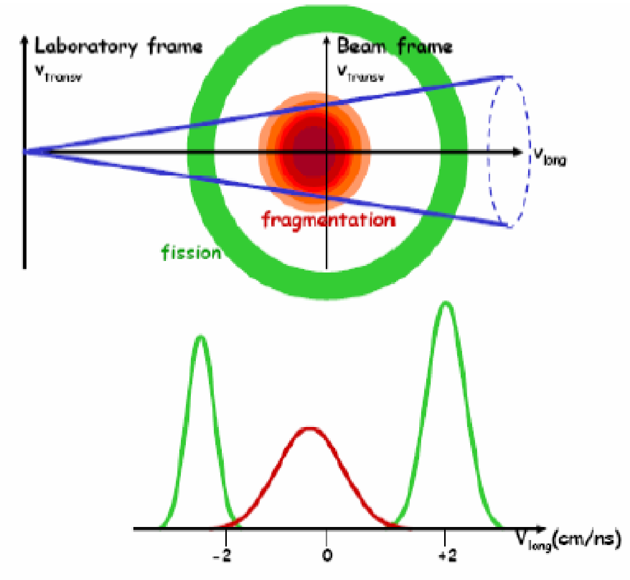

Fig. 2.7: The schematic representation of the velocity distributions of fragmentation and binary processes in the two-dimensional velocity space. The FRS acceptance is shown by the blue cone. In the lower part of the figure: projection of these velocity distributions on the longitudinal velocity axis.

2.4. FRS detection system

In order to assure the high isotopic resolution from the lowest *Z* up to the heavy beam, detectors which provide sufficient resolution over a broad dynamic range are necessary. In the following, the working principles of the standard FRS detectors are described in more detail and their resolution is discussed.

2.4.1. Multiwire proportional counters

MultiWire Proportional Counters (MWPC) are located in each image plane of the Fragment Separator (S1-S4). In total there are 6 MWPCs mounted in the FRS beam line. Only 4 of them were used in the experiments analyzed in this work and they are positioned as shown in Fig. 2.4. The remaining two MWPCs are localized between the first two (S1) and the last two dipoles (S3). Five of the MWPCs are positioned in the vacuum and may be moved in and out of the beam line. The sixth MWPC is localized behind the second scintillator (Fig. 2.4**)** in a fixed position and works in air.

The schematic view of the MWPC is shown in Fig. 2.8. It consists of five parallel wire planes connected to different potentials. For experiments with heavy ions only the anode voltage is applied to accumulate the electrons created in the gas. To detect lighter ions ($Z<6$) a pregap (U_T and U_G voltages) must be used in order to amplify the number of electrons in the avalanche. Nevertheless, the efficiency of MWPC in detecting fragments over a broad dynamical range is rather low, since different voltage settings correspond to the highest efficiencies for detection of different elements. The cathode wires are 50 μm thick, made of tungsten and separated by 1 mm. They are positioned both in x and y directions to allow measurements of horizontal and vertical positions, respectively. The anode consists of 20 μm thick tungsten wires separated by

2 mm, which are positioned under 45° with respect to the cathode wires. The detector is filled with CO_2/argon mixture and separated from the vacuum by 100 μm titanium windows. The gas volume of the last MWPC, located in the final image plane, is separated from the air by 25 μm thick windows made of kapton $(C_{22}\text{-}H_{10}\text{-}O_5\text{-}N_2)_n$. The active area of the detector corresponds to 20x20 cm.

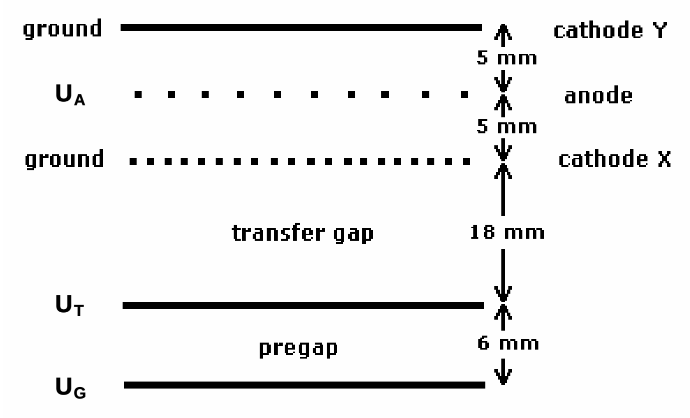

Fig. 2.8: The schematic cross sectional view of the Multiwire-Proportional Counter.

The fragments passing through the MWPC ionize its gas producing a track of positively charged ions and electrons. The produced electrons drift towards the anode and create an avalanche in the cylindrical electric field around the anode wire. The negative anode signal induces a positive signal in the closest cathode wires in both x and y directions. This signal travels towards both ends of the cathode wire, where it passes through a delay line and enters the TDC (time-to-digital converter) to provide a stop signal. The start of the TDC is generated by the anode signal, and the time difference between the start and stop signals from each side of t_x (t_y) cathode wire provides information on the x-left and x-right (y-up and y-down) positions. The exact position in millimeters is determined from the difference of the signals on both ends of the wire:

$$x = \alpha_x (t_{xL} - t_{xR}) + \beta_x , \quad y = \alpha_y (t_{yU} - t_{yD}) + \beta_y \tag{2.5}$$

where $\alpha_{x,y}$ and $\beta_{x,y}$ are the calibration factor and offset, respectively. They are needed to convert the signals from the TDC to millimeters. The offset value accounts for the possible shift of the center of the MWPC with respect to the central trajectory of the FRS. The value of the calibration factor is determined in an independent calibration measurement performed with a movable radioactive source. The value of the calibration factor depends only on the wire spacing and on the delay of the delay lines on both ends of the wires, and may thus be used in all experiments. The value of the offset is usually determined from the position of the beam spot in the MWPC after passing through a narrow opening in the symmetrically positioned slits. The position resolution of the MWPC is around 1 mm.

The avalanche of electrons created by fragment passing through the MWPC is accompanied by a δ-electron cloud produced by interactions of the fragment with other materials in the beam line. These electrons may produce multihit-signals in the cathode wires, which may mask the signal coming from the fragment. To get rid of these multihit-signals, the sum of the signals coming from both ends of the cathode wire is calculated. This sum must be equal to the x (y) dimension of the MWPC (i.e. 20 cm) if the cathode wire was hit only once. If this is not the case and the sum is lower than 20 cm, two or more hits in different positions in the detector occurred and such events must be excluded. With this method, only the true fragment signals are selected and allowed to enter the subsequent analysis.

To assure that the contamination of signals from the electron cloud is as low as possible and at the same time that the multiplication of the electrons produced by the fragment is sufficiently high, an optimization of the anode voltage must be performed. The voltage applied on the anode is usually around 2000V, but the actual value used in the experiment must be optimized for each MWPC and beam separately in order to assure the best conditions for the fragment detection.

The wire structure of the MWPC introduces inhomogenities in the projectile or fragment beam, which may spoil the achromaticity of the Fragment Separator. Therefore, during both Xe beam experiments the MWPCs were used for the calibration measurements only and they were out of the beam line while the measurements of the reaction products were performed. The MWPCs were used to make an initial adjustment of the beam to follow the central trajectory through the Fragment Separator and, due to their high position resolution, they were used to calibrate the positions measured by the scintillation detectors.

2.4.2. Plastic scintillation detectors

Due to their rather low efficiency in detecting lighter residues and the wire structure, the MWPCs were not used to measure the positions of fragments. For this purpose the scintillation detectors are used instead, which measure the time-of-flight of the produced fragments as well. There are two scintillation detectors used at the FRS. One of them is positioned in the intermediate image plane (SCI2) and works in vacuum, while the second one is in the final focal plane (SCI4) and works in air (Fig. 2.4). The scintillator in the intermediate image plane is mounted on a movable ladder. This ladder carries several scintillation plates with different thicknesses. The desired thickness is chosen by proper positioning of the ladder. In the experiments with both Xe beams, a 5 mm thick scintillator at S2 was used, since it is characterized by the best time resolution. The second scintillator was positioned behind both ionization chambers and was as well 5 mm thick.

The schematic view of both scintillation detectors with their electronic equipment is shown in Fig. 2.9 below. The horizontal dimensions of the scintillators cover the whole image plane and correspond to 21 cm in case of SCI2 and 20 cm (^{136}Xe experiment), resp. 21 cm (^{124}Xe experiment) in case of SCI4. The fragment traversing the scintillation detector excites the atoms (or molecules) of the scintillation material, which subsequently deexcite by the emission of photons. These photons move with the in-medium speed of light in the scintillation material towards the photomultipliers (PM) mounted on both sides of the detector. In the PM the photons interact with the photocathode and are converted to electrons by the photoelectric effect. The produced electrons are additionally multiplied in the photomultiplier by the secondary emission from the sequence of dynodes. The signal from the scintillator is used to determine the position, the time-of-flight and charge of the fragments passing through.

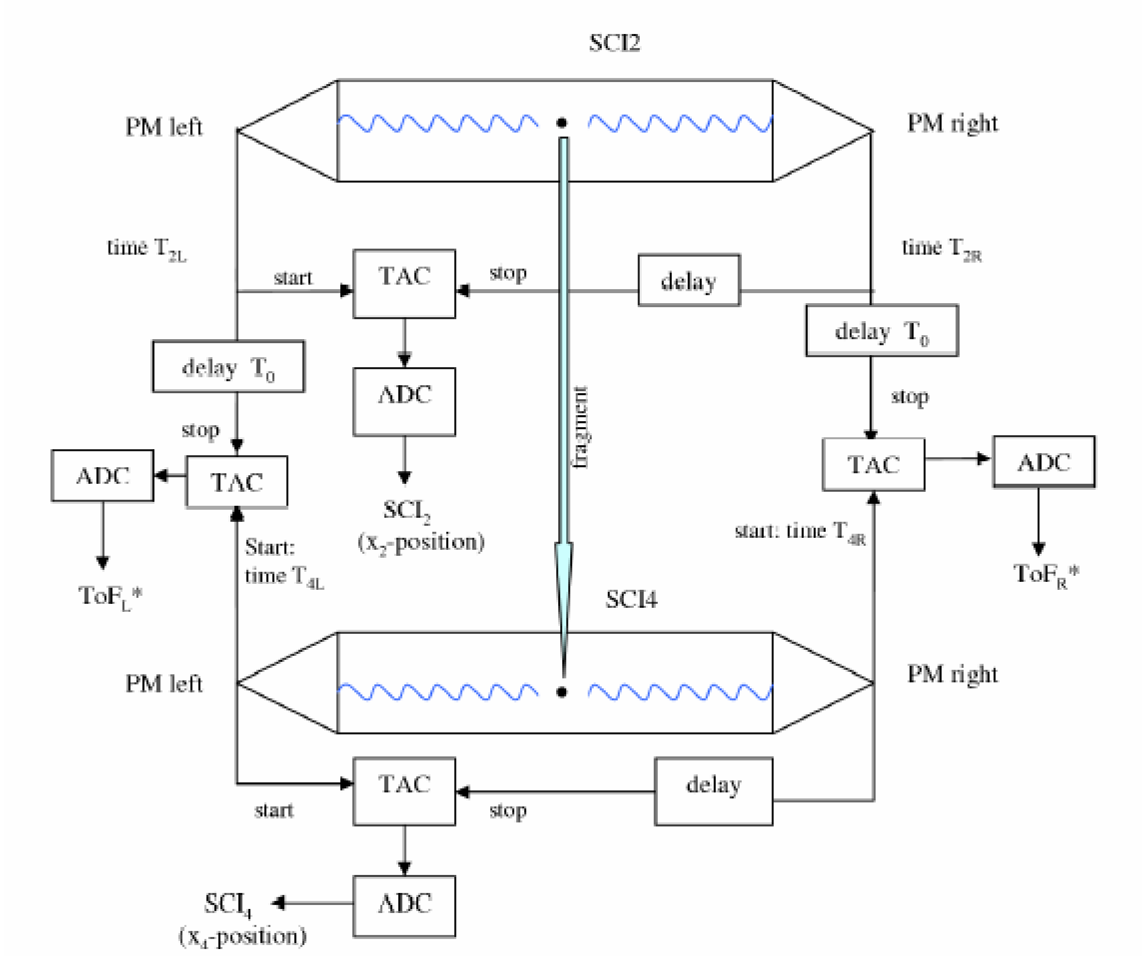

Fig. 2.9: The schematic view of the two scintillation detectors and the corresponding electronics as used at the Fragment Separator.

The signal from the PM enters the constant-fraction discriminator (CFD), where a digital signal corresponding to the time of its arrival is generated. The position of the fragment passing through the scintillator is determined from the difference of the signals from both ends of the detector. These signals enter the time-to-amplitude converter (TAC), where the signal from one end provides the start and the delayed signal from the other end provides the stop. An analog signal corresponding to the time difference between these two signals is generated, which determines the position of the fragment. This analog signal from the TAC is digitized by the amplitude-to-digital converter (ADC) and processed by the data acquisition. To transform the measured position to millimeters, a calibration with the use of the MWPC must be performed (see section 3.2.1). This calibration is performed several times during the experiment to account for a possible radiation damage of the scintillation detector, which may influence its response. The position resolution of the scintillation detectors in both Xe experiments was around ±2 mm, which assures the high resolution in the magnetic rigidity and corresponding high mass resolution of the FRS.

The time-of-flight of the fragments is determined separately from both ends of the scintillation detectors. An average of these two values eliminates the dependence on the time needed to propagate the light inside the volume of the scintillator. To determine the time-of-flight, the signal from the left (right) hand side of the SCI4 is used as a start of the TAC and a delayed signal from left (right) hand side of the SCI2 as a stop. The delay T_0 must be chosen in such a way that $T_2+\mathrm{T}_0 > T_4$. The corresponding analog signals from TAC are again digitized in the ADC. The time-of-flight of every fragment is then determined according to the following equation:

$$ToF^* = \frac{\alpha_L \cdot ToF_L^* + \alpha_R \cdot ToF_R^*}{2} = T_2 + \mathrm{T}_0 - T_4 \tag{2.6}$$

where ToF_L^*, ToF_R^* are the times-of-flight measured by the left- and right-hand side of the two scintillators, respectively, and α_L, α_R are the calibration factors determined in an independent measurement with a pulse generator. The delay T_0 is determined by the measurement of the ToF of the primary beam with exactly known energy. To deduce the real time-of-flight, the delay time T_0 must be subtracted, so that:

$$ToF = \mathrm{T}_0 - ToF^* = T_4 - T_2 \tag{2.7}$$

The fragments produced in the heavy-ion collision may acquire a broad range of velocities, and the range of the ToF measurement must be sufficient to cover all of them. Therefore, the delay T_0 and the range of the TAC (time how long is the module ‘open’ to accept signals) must be properly adjusted before every experiment.

The amplitude of the scintillator signal is proportional to the number of initially created photons, which depends on the energy loss of the fragment. Since the square root of the energy loss is proportional to the nuclear charge, the scintillators may also be used to measure the charge of the fragments. For this purpose, the signals from the PM directly enter a charge-to-digital converter (QDC), where the charge contained in the signal is digitized. The resolution of the charge determination with the scintillation detectors is generally not as good as with the ionization chambers (see next section), but it may serve as a useful tool to identify secondary reactions from correlation of the energy losses measured in SCI2 and in the MUSICs.

To preserve the detection qualities of the scintillation detectors, the counting rate should not exceed 10^5 particles per second. In case of higher counting rates, the detector response starts to saturate, and the time resolution deteriorates. Moreover, under the high radiation exposure the scintillation material may get damaged, which causes deterioration of the scintillation properties of the material and of the transport of light. The position and consequently mass resolution may then be significantly distorted. Therefore, it is always necessary to keep the counting rate on the detector below the safe limits. The scintillator SCI2 is usually exposed to much higher counting rate than the scintillator SCI4 in the final focal plane, since not all the fragments which enter the intermediate focal plane are selected by the second stage of the separator. Therefore, the counting rate on the SCI2 must be carefully monitored during the experiment and, if needed, the beam intensity must be changed.

2.4.3. Multiple-Sampling Ionisation Chambers

At the exit of the Fragment Separator two MUltiple-Sampling Ionisation Chambers (MUSIC) are installed. They are used to measure the charge and the trajectory of the fragments passing through. A schematic view of the MUSIC chamber is shown in Fig. 2.10. The MUSIC is a 60 cm long chamber of 27 x 15 cm in x- and y-direction. The entrance and exit windows, which separate the detector gas from air, are made of thin kapton $(C_{22}\text{-}H_{10}\text{-}O_5\text{-}N_2)_n$ foils to minimize the secondary interactions of the traversing fragments. The chamber is filled with P10 gas (90% Ar, 10% CH4) under atmospheric pressure at room temperature. The gas is continuously flowing through the chamber in order to preserve the detection qualities.

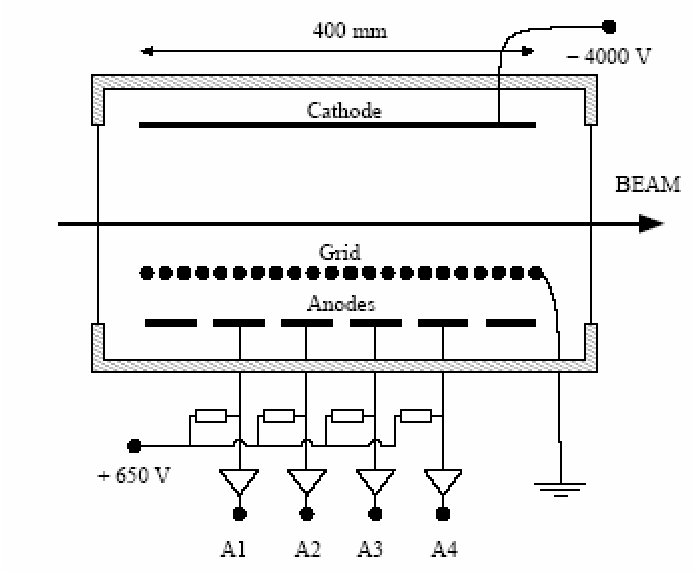

Fig. 2.10: The schematic cross sectional view of the MUSIC chamber with the preamplifiers mounted directly on the chamber.

Inside the chamber there are six anodes. Only four of them are used for the measurements, while the outermost two are used to assure the homogeneity of the electric field. Each of the four anodes is 100 mm long. In order to assure the independence of the signal induced by the electrons on the presence of the positive ions and on the distance of the fragment trajectory from the anodes, a metallic grid (Frisch grid) is placed 23 mm in front of the anodes. This assures that the signal is induced in the anodes only after the electrons have passed the grid. The distance between the anodes and the cathode corresponds to 299 mm, which defines the active volume of the detector.

Fragments passing through the chamber ionize its gas. The created electrons and positively charged ions drift towards the anodes and the cathode with the velocities of 5cm/µs and 5cm/ms, respectively. Once the electrons pass the Frisch grid, the signal is induced in the anodes. The charge-sensitive preamplifiers are mounted on the chamber to transform the current signal to a voltage, which may be transported over longer distances without significant losses. The amplitude of the output voltage signal is proportional to the number of electrons created, which is directly proportional to the fragment energy loss. The output voltage may thus be used to measure the atomic number of the fragment. The charge resolution of the MUSIC chamber is around $\Delta Z(\text{FWHM})=0.4$ and may be additionally improved by summing up the signals from all eight anodes of the two ionization chambers. The resolution may be affected by impurities of the gas and/or changes of the atmospheric pressure or temperature. The influence of the gas impurities as well as of the pressure and temperature conditions in the chamber on the measured energy loss may be correspondingly corrected (see section 3.2.2).

Fragments passing the ionization chamber in different horizontal positions will induce signals on the anodes at different times. The determination of this time may be used as a measure of the distance of the fragment from the corresponding anode in x direction and thus the track and the angle of the fragments may be determined using at least two anodes. To determine the horizontal position, the voltage from the preamplifier is fed into a fast amplifier followed by the CFD, where the digital signal corresponding to the time of the arrival of the analog signal is produced. The response of the CFD may be deteriorated if the range of signal amplitudes is too broad (walk). Different thresholds were thus set on the CFDs connected to each of the four anodes, so that every anode was ‘sensitive’ to a different range of amplitudes (fragment charges). As a consequence a high position resolution was obtained in the whole charge range. To transform the measured position to millimeters, an independent calibration must be performed. Similarly as in case of the scintillation detector, the MWPC is used for this purpose. The position resolution of the MUSIC is a few hundred μm, and the reconstructed track of each fragment allows to determine its angle in the final focal plane, which may be used to improve the mass resolution.

Chapter 3

Data analysis

As discussed in the previous chapter, the main advantage of the Fragment Separator and its detection system is the high mass resolution, which allows to perform an isotopic identification of all residues from the lightest ones up to the heavy projectile. The isotopic distributions in the broad range of nuclear charge thus become available.

To obtain the final isotopic distributions, each detected residue must be identified in its nuclear charge and mass, and the corresponding production cross sections must be evaluated. In this chapter the main steps of the data analysis leading to the determination of the final isotopic distributions in both experiments analyzed within this work (^{136}Xe+Pb and ^{124}Xe+Pb) will be introduced, and specific details related to each of the two analyzed experiments will be mentioned. At first, the calibration of the beam monitor SEETRAM will be described, which is necessary to obtain the normalization of the measured yields in order to determine the production cross sections. In section 3.2 the main principles of mass and nuclear charge identification will be introduced and section 3.3 will describe the determination of the production cross sections by integrating the velocity distributions measured for every residue, with discussion of all the necessary corrections that must be applied

3.1. Calibration of the beam monitor SEETRAM

As mentioned in section 2.2, the beam monitor SEETRAM provides information about the current induced by the traversing beam particles. In order to obtain a correct normalization for the determination of the production cross sections, the signal from the SEETRAM must be calibrated to transform the measured electron current in the number of incident beam particles. This calibration must be performed for each experiment separately, since the response of the beam monitor may change due to the long-term irradiation. The SEETRAM calibrations were performed twice in both Xe experiments, each time at the beginning and at the end of the beam time so that the possible changes of the calibration factor may be accounted for.

As discussed in section 2.2 there are two ways to calibrate the SEETRAM depending on the charge of the incident beam using either the ionisation chamber or the plastic scintillation detector to directly count the traversing ions. In case of both Xe experiments the scintillation detector was used. During the calibration the intensity of the beam was measured by the SEETRAM and scintillation detector simultaneously. The use of the scintillation detector is limited to app. 10^5 particles per second, since above this limit the counting of the scintillator starts to saturate. To perform the calibration, the beam intensity was reduced below the detection limit of the SEETRAM (i.e. below ~ 10^{-12} A of electron current) and subsequently increased in small steps up to the limit of the linear operation of the scintillation detector to obtain a sufficient number of calibration points. Fig. 3.1 below shows an example of the SEETRAM and corresponding scintillator spectra as measured in the ^{136}Xe experiment. Each peak corresponds to one spill (~ 3 sec.) of the ^{136}Xe ions extracted from the SIS. The peaks in the SEETRAM spectra add up to the constant background coming from the positive offset current produced by the current digitizer, which is used to disentangle and correctly subtract the noise signals.

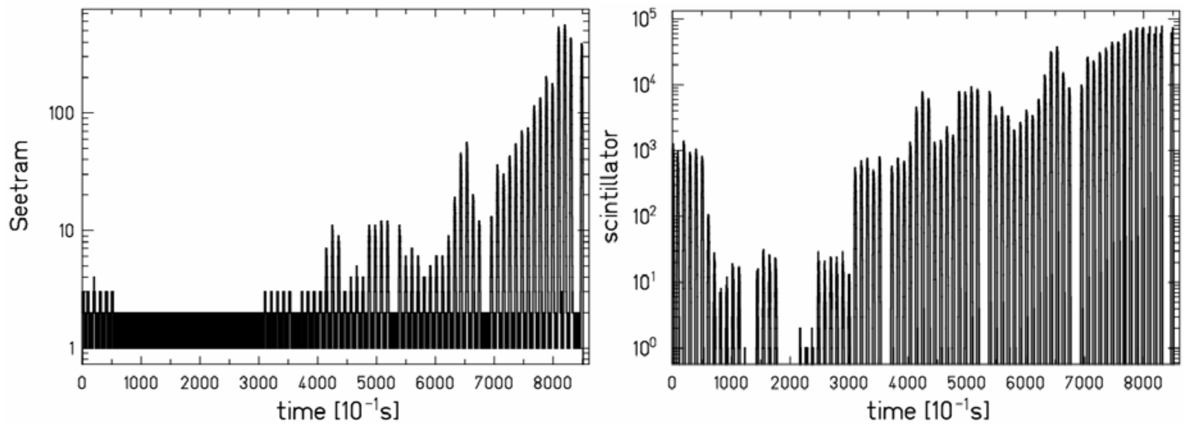

Fig. 3.1: (left) number of counts in each spill as recorded by the SEETRAM; (right) corresponding number of beam particles as recorded by the scintillator.

For the correct calibration it is necessary to properly determine the value of the SEETRAM offset and to check whether it is stable over the whole range of the measurement. The offset value may be determined from the part of the SEETRAM spectra, where the beam intensity is below its detection limit, as is the case in the left part of Fig. 3.1 (left). This value is then subtracted from the SEETRAM spectrum. In the experiments with both Xe beams, the offset current was stable during the calibration measurements, and its value was 2.82±0.22 counts per 10^{-1} s and 1.75±0.27 counts per 10^{-1} s in case of ^{124}Xe and ^{136}Xe beam, respectively. After subtraction of the offset value, the correlation of the SEETRAM counts with the number of beam particles measured by the scintillation detector may be used to determine the SEETRAM calibration factor.

Fig. 3.2 shows the number of ^{136}Xe ions measured by the plastic scintillator versus the corresponding SEETRAM counts. The change of slope in the region between $1.5\cdot10^6$- $2\cdot10^6$ particles per spill (spill length corresponds to ~ 3 sec.) indicates the saturation of the scintillation detector counting.

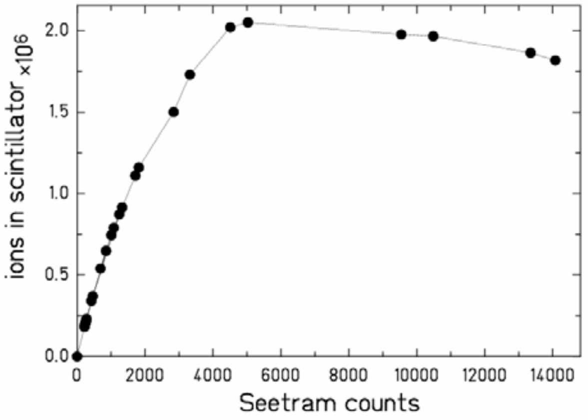

Fig. 3.2: Number of ^{136}Xe ions measured in the scintillator versus the number of SEETRAM counts. Each point represents the result obtained for one spill.

The SEETRAM calibration factor is given directly by the slope of the above displayed dependence in the low-intensity region. To determine the best fit function it should be considered that on the contrary to the SEETRAM counts, the scintillator counts suffer from pile up of subsequent signals. If the time distance between two ions traversing the detector is too short, they are not distinguished but rather counted as a single particle. Depending on the tuning of the electronics, this time resolution is in the order of 1 μs. Due to the exponential nature of time intervals following the Poisson statistics and an eventual time structure in the beam current, the pile up is present already for rather low counting rate (intensities of the beam). Neglecting the time structure of the beam intensity, the relative importance of pile-up may be determined from the ratio of the number of events registered by the scintillator N_{reg} versus the total number of events N_{all}, which may be expressed as:

$$\frac{N_{reg}}{N_{all}} = \frac{\int_{\Delta t_{pu}}^{\infty} \exp(-I \cdot \Delta t) dt}{\int_{0}^{\infty} \exp(-I \cdot \Delta t) dt} = \exp(-I \cdot \Delta t_{\lim}) \tag{3.1}$$

where I represents the intensity of the beam and $\Delta t_{\lim}$ denotes the time resolution of 1 μs. In the first-order approximation, using $N_{all} \equiv I \cdot t$, the number of events registered by the scintillator may be expressed as:

$$N_{reg} \approx (1 - \Delta t_{\lim} I) \cdot It = (I - \Delta t_{\lim} I^2) \cdot t \tag{3.2}$$

The number of counts in the scintillator thus depends quadratically on the beam intensity and therefore the use of a quadratic function to fit the scintillator versus the SEETRAM dependence is more appropriate. The constant of the linear term of this fit then represents the calibration factor.

To obtain a calibration factor using the quadratic fit, it is important to determine correctly the upper limit of the number of SEETRAM counts included in the fit. If this upper limit is too low, the uncertainty of the linear calibration constant is quite high; while if this upper limit is too high, the assumption of a quadratic dependence is not true anymore, since the quadratic fit describes the observed trend only in the first-order approximation. In the latter case, the constant of the linear term deviates in a systematic way from the correct calibration factor. The best way to determine the value of this upper limit is to repeat the quadratic fit to the number of scintillator counts as a function of the SEETRAM counts, assuming different values of the upper limit of the SEETRAM counts in each single fit.

The value of the linear term extracted from the quadratic fit as a function of the upper limit of the SEETRAM counts for the ^{136}Xe beam is sown in Fig. 3.3. In the region of low upper limit values, strong fluctuations of the linear term coefficient may be observed, while for large values of the upper limit a systematic decrease of the linear term coefficient is seen. Between these two regions there is a range of intermediate values of the upper limit of SEETRAM counts, where the linear term coefficient is rather independent of the value of the upper limit. This is the most reliable region from which the correct calibration factor may be determined (blue line).

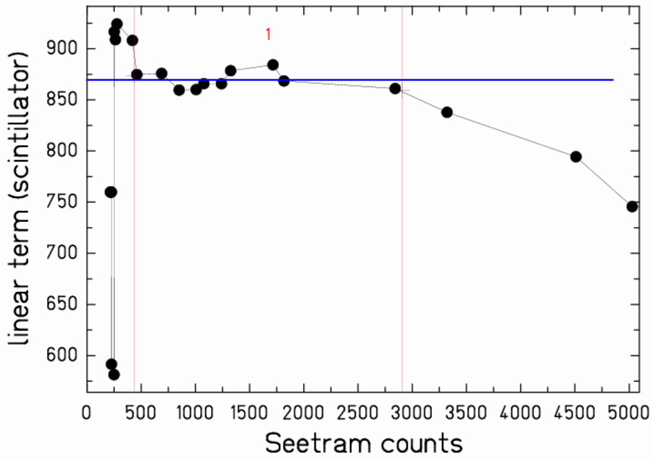

Fig. 3.3: The linear term constant of the quadratic fit of the scintillator versus SEETRAM counts as determined for the ^{136}Xe beam, displayed as a function of the upper limit of the SEETRAM counts included in the fit.

The same fitting procedure was applied to calibrate the SEETRAM counts in case of the ^{124}Xe experiment. The extracted SEETRAM calibration factors for both, ^{124}Xe and ^{136}Xe, beams are summarized in table 3.1 with the corresponding statistical errors (including the uncertainty of the fitting procedure and the offset determination). Different values of the calibration factors may be observed in case of both experiments from the measurements at the beginning and at the end of the beam time. The explanation for this difference could be a possible small change of position of the beam impinging on the SEETRAM between the two measurements. Indeed, it was observed [SEE] that the response of SEETRAM is slightly position dependent. This observation may introduce a systematic uncertainty of the order of 7%, which is the main source of uncertainty of the SEETRAM calibration and has to be considered in the overall systematic error of the production cross sections determined from these experiments. The SEETRAM calibration factor for each beam is finally determined as the average value of the factors extracted from both calibration measurements. As discussed in section 2.2, the value of the calibration factor should depend solely on the nuclear charge and velocity of the beam particle and thus the same calibration factors for the two Xe beams may be expected. The slightly lower value for ^{124}Xe projectile may again be understood as a consequence of the position-sensitive response of the SEETRAM monitor.

Table 3.1: SEETRAM calibration factors for ^{124}Xe and ^{136}Xe beams with corresponding statistical errors

calibration factors ^{124}Xe	final	calibration factors ^{136}Xe	final
816±8	**810**±7	827±4	**833**±4
796±13		870±10	

3.2. Identification of the residues

3.2.1. The basic principles

The identification of the residues is the key part of the data analysis. Several steps must be performed in order to obtain the final identification plot in terms of *Z* versus *A/Z*, namely the position calibration of both scintillation detectors located in the intermediate image and final focal planes, correction and charge calibration of signals from the MUSIC chambers, calibration of the measured time-of-flight and calibration of the FRS dispersions.

In section 2.3 the principles of the isotopic identification with the use of the Fragment Separator were explained. To determine the mass of the final residue, its charge, velocity and magnetic rigidity must be known. The mass identification is then performed according to equation (2.1), which reads, under the assumption that the final residue was fully stripped during its passage through the FRS, i.e. $q=Z$:

$$\frac{A}{Z} = \frac{\mathrm{e}}{\mathrm{u}} \frac{B\rho}{\beta\gamma c} \tag{3.3}$$

here e is the magnitude of the electron charge, u is the atomic mass unit and γ represents the relativistic factor $\gamma = \sqrt{\left(1-\beta^2\right)^{-1}}$ with $\beta = v/c$ and c the speed of light. The method to disregard ionic charge states and to keep only fully stripped residues is addressed in section 3.2.3.

The velocity of every residue is determined from the measurement of its time-of-flight using the relation $v = s/ToF$, where s is the length of the flight path of the residue through the Fragment Separator. To determine the fragment velocity, its time-of-flight is measured between the scintillation detectors located in the intermediate image and final focal planes as described in section 2.4.2 of the previous chapter. In order to obtain the real time-of-flight of the fragments, the value of the delay time T_0, as introduced in section 2.4.2, must be determined in a separate calibration measurement. For this purpose the primary beam passing through layers of matter of various known thicknesses is used. In such a way the ToF of the beam with known velocity is obtained and the value of delay time T_0 may be determined from the linear fit to the time-of-flight versus $1/v_{\mathrm{beam}}$ according to equation:

$$ToF = \mathrm{T}_0 - ToF^* = \mathrm{T}_0 - \frac{s_0}{v_{beam}} \tag{3.4}$$

where ToF^* represents the measured time-of-flight and s_0 is the length of flight part of the beam corresponding to the central trajectory, which may as well be determined from the fit. The values of the delay times as well as the lengths of the central trajectory flight paths determined in both experiments are shown in table 3.2.

Table 3.2. The values of the delay time and the length of the central trajectory flight path determined from the calibration measurements performed in each experiment.

^{124}Xe		^{136}Xe	
T_0 [ns]	s_0 [cm]	T_0 [ns]	s_0 [cm]
180.6±0.3	3745.9±0.8	168.4±0.4	3677.8±1.0

However, fragments with different masses and/or velocities will follow different trajectories in the magnetic field, and the length of their flight paths will be slightly different. Similarly, the length of flight path differs if fragments enter and exit the FRS under different angles. To account for these differences, the following correction of the length of flight path *s* is applied:

$$s = s_0(1+\alpha) + \Delta s \tag{3.5}$$

where s_0 is the length of flight path along the central FRS trajectory. The term in the brackets accounts for the fact that fragments may exit the FRS under different angles α, and the second term corrects for the difference of the length of the actual flight path from the length of flight path corresponding to the central trajectory s_0. The angle α of a fragment exiting the FRS is determined using the pairs of anodes of the two MUSIC detectors in the final focal plane. The factor Δs is determined as follows:

$$\Delta s = a x_2^2 + b x_2 \tag{3.6}$$

The correction Δs depends quadratically on the position of the fragment in the intermediate image plane (x_2) [Ric05a]. The quadratic dependence reflects the quadratically increasing length of the flight path for trajectories with increasing $\Delta B\rho$ (i.e. $B\rho - B\rho_{central}$), due to their different deflections in the magnets. The expression for Δs must vanish if x_2= 0 to assure that $s = s_0$ along the central FRS trajectory. The parameters *a* and *b* are determined from the data in order to achieve the best mass resolution according to method introduced in [Ric05a]. Knowing the time-of-flight and the length of flight path of every residue, its velocity may be calculated.

Since the time-of-flight measurement is performed over the second stage of the Fragment Separator, the magnetic rigidity $B\rho_4$ of every residue in the last two dipoles of the FRS must be determined. The determination of the magnetic rigidity consists of the measurement of the radius of the fragment trajectory in the second FRS stage in the given magnetic field. The value of the magnetic field is measured by the Hall probes, which measure the potential difference (Hall voltage) between the two ends of a conductor, through which an electric current is flowing, created by electrons deflected in the applied magnetic field *B* (Hall effect). The radius of the trajectory of every residue is determined as a correction to the radius of the central FRS trajectory by measuring the fragment positions in the final focal (x_4) and intermediate image (x_2) planes. The magnetic rigidity in the second FRS stage ($B\rho_4$) is then determined from the equation:

$$B\rho_4 = B\rho_{4central}(1 + \frac{x_4 - M \cdot x_2}{D_4}) \tag{3.7}$$

where $B\rho_{4central}$ is the magnetic rigidity of the fragment on the central trajectory with the radius $\rho_{4central}$ corresponding to the radius of the last two dipoles ($\rho_{4central}$ ~11.3 m) and M is the magnification between the intermediate image (S2) and final focal (S4) planes. Since the system is achromatic, the magnification is related to the dispersions of the two stages:

$$M = \frac{D_4}{D_2} \tag{3.8}$$

where D_4 and D_2 are the dispersions in the first and second FRS stage, respectively:

$$D_4 = \frac{dx_4}{d(B\rho_4)/(B\rho_{4central})} \tag{3.9}$$

$$D_2 = \frac{dx_2}{d(B\rho_2)/(B\rho_{2central})} \tag{3.10}$$

The values of dispersions are determined in cm/% and correspond to the change of horizontal position of the fragment in the intermediate image (S2) (or final focal (S4)) plane if the magnetic rigidity of the fragment differs by 1% from the magnetic rigidity corresponding to the central trajectory. The value of the S2 (S4) dispersion is determined experimentally with beam, by changing the value of the magnetic field in the first (second) stage of the FRS in small steps, usually by 1% or 0.5% and by measuring the corresponding x_2 (x_4) positions of the beam. The values of the dispersions measured in both Xe experiments are summarized in table 3.3 below. The slight difference between the dispersion values obtained for the two Xe beams is a consequence of the slightly different ion optics used in the two experiments.

Table 3.3: Dispersions in the first and second stages of the FRS measured in the ^{124}Xe and ^{136}Xe experiments.

^{124}Xe		^{136}Xe	
D_2 [cm/%]	D_4 [cm/%]	D_2 [cm/%]	D_4 [cm/%]
6.41±0.06	8.16±0.09	6.72±0.03	8.79±0.06

The measurement of the horizontal positions of the fragments in the intermediate image (x_2) and final focal (x_4) planes is performed using the plastic scintillator detectors as described in section 2.4.2. The position signal delivered by the scintillators is calibrated with the use of the

MWPC, where the position in millimeters is defined directly by the spacing of the wires and the corresponding delay lines, and may thus be used in all experiments. The calibration is performed by the best fit to the correlation between the position in millimeters measured by the MWPC and the position in channels measured by the plastic scintillator. An example of a calibration plot from the ^{136}Xe+Pb experiment is shown in Fig. 3.4. During the experiment, the scintillation detectors are exposed to high radiation, which may influence their detection qualities. As a consequence, nonlinear tendencies may be observed in the correlation with the MWPC (see Fig. 3.4), which, however, may be corrected by applying the proper position calibration.

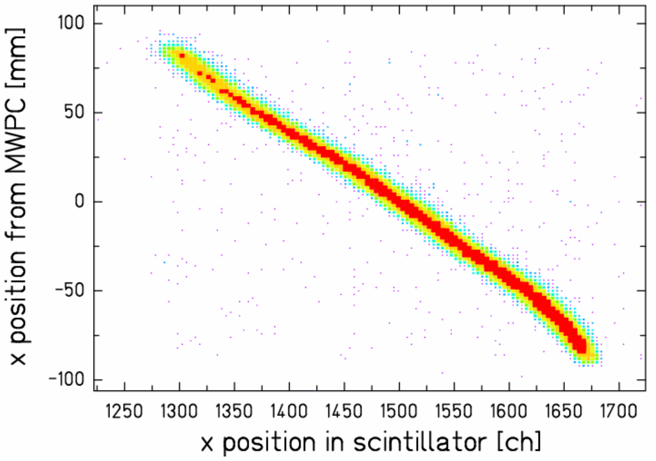

Fig. 3.4: Calibration of the position response of the scintillator in the intermediate image plane (S2) performed in the ^{136}Xe+Pb experiment.

Once the positions x_2 and x_4 are correctly calibrated and the values of the dispersions are known, the magnetic rigidity of every residue in the second stage of the FRS may be determined by means of relation (3.7).

In case there is no layer of material in the intermediate image plane, the magnetic rigidities of the first and the second FRS stages coincide, and the expression (3.7) for the magnetic rigidity in the second FRS stage may be replaced by the corresponding expression for the magnetic rigidity in the first FRS stage:

$$B\rho_2 = B\rho_{2central}(1+\frac{x_2}{D_2}) \tag{3.11}$$

where $B\rho_{2central}$ is the magnetic rigidity of the fragment on the central trajectory with the radius $\rho_{2central}$ corresponding to the radius of the first two dipoles. On the contrary, if some layer of material is placed in the intermediate image plane, the magnetic rigidity in the second stage of the FRS differs from the magnetic rigidity in the first stage, since fragments passing through this layer lose some energy ($dE \sim Z^2$) and consequently their velocity changes. Thus the magnetic rigidity behind the layer of material ($B\rho_4$) differs from the magnetic rigidity in front of the material $B\rho_2$ by $\Delta(B\rho)_{24} = B\rho_2 - B\rho_4$. The magnetic rigidity in the second FRS stage may therefore be alternatively expressed as follows:

$$B\rho_4 = B\rho_{2central} \cdot \left(1 + \frac{x_2}{D_2}\right) - \Delta(B\rho)_{24} \tag{3.12}$$

which is just a different way of formulating relation (3.7).

In order to obtain the information about the horizontal position of the residues in the intermediate image plane, the plastic scintillator at S2 must be present all the time during the experiment. The thickness of the plastic scintillator used in both Xe experiments was 5 mm, and the corresponding change of magnetic rigidity $\Delta(B\rho)_{24}$ due to the energy loss of the fragments in the scintillator material remains below a few per mill of the total $B\rho_4$ value. The term $\Delta(B\rho)_{24}$ may thus be neglected so that the relation (3.12) coincides with the relation (3.11). In case the 5 mm thick scintillator is the only layer of material in the intermediate image plane, the relation (3.11) may be used to determine the magnetic rigidity of the fragments in the second stage of the FRS instead of expression (3.7). To assure a good separation of the fragments in the final focal plane, a thick degrader in the intermediate image plane may be used. In such a case, the difference of the magnetic rigidities $\Delta(B\rho)_{24}$ cannot be neglected anymore, and the original expression (3.7) to calculate the magnetic rigidity in the second FRS stage must be used.

As mentioned in section 2.3, in case of light-fragment settings a degrader in the intermediate image plane was used in both experiments to assure a better separation of light fragments in the final focal plane. In case of heavy-fragment settings no degrader was used in the two experiments. Based on the above considerations, in case of light-fragment settings the relation (3.7) was used to determine the magnetic rigidity $B\rho_4$, while the relation (3.11) was utilized in case of settings with heavy fragments.

From the description in this section it may be seen that there are several parameters and calibration factors entering the quantities in equation (3.3). Their careful evaluation is indispensable in order to achieve a high mass resolution, which is necessary to identify heavy isotopes close to the beam. The mass resolution may be increased by applying a dedicated procedure, described in detail in [Ric05a], for the precise determination of the calibration parameters. This method was used in case of both experiments measured within this work and thus the influence of the uncertainty of the calibration parameters on the mass identification was to a large extent reduced. Apart of velocity (time-of-flight) and magnetic rigidity determination, also the nuclear charge of every residue must be known to perform the mass identification according to equation (3.3). In the following section, additional corrections necessary to obtain a high resolution in the nuclear charge will be introduced, before the isotopic identification of the final residues will be described.

3.2.2. Corrections of the energy-loss signals

To measure the charge of the produced fragments, the two Multiple-Sampling Ionization Chambers located in the final focal plane were used as described in section 2.4.3. The energy loss of a charged particle traversing some material is described by the well known Bethe-Bloch formula (which was extended towards relativistic energies in [Ahl80]):

$$-\frac{dE}{dx}=\frac{4\pi}{m_e c^2}\cdot\frac{nz^2}{\beta^2}\cdot\left(\frac{e^2}{4\pi\varepsilon_0}\right)^2\cdot\left[\ln\left(\frac{2m_e c^2\beta^2}{I(1-\beta^2)}\right)-\beta^2\right] \tag{3.13}$$

where $\beta = v/c$ and v is the velocity of the charged particle, ze is its charge in elementary charge units, m_e is the electron mass, n is the density of electrons in the material and I is the mean ionization potential of the atoms of the material. In order to obtain the charge of the residue with a high resolution, several corrections must be applied to the measured energy loss, which will be detailed below.

From the formula (3.13) it may be seen that the energy loss of the residue is velocity dependent. The energy losses of fragments having the same charge but different velocities will thus be different, causing a broadening of the peaks in the energy-loss spectra. The dependence of the energy loss on the velocity must thus be corrected to improve the charge resolution. This correction was performed with the use of the AMADEUS program [AMA], where the energy loss of a given residue is calculated based on a fast algorithm introduced in [Benll01]. The energy loss of a given fragment (A,Z) for several different velocities may be determined and a corresponding dependence $f(v)=\Delta E(v_{ref})/\Delta E(v)$ extracted, where $\Delta E(v_{ref})$ represents an energy loss corresponding to a reference velocity v_{ref}, which is introduced to remove the dependence of the function $f(v)$ on the charge of the fragment. The reference velocity was chosen as the velocity corresponding to the energy of 1000 A MeV (i.e. v_{ref} = 26.263 cm/ns). The corrected energy loss signal then reads:

$$\Delta E_{corr}=\Delta E_{meas}\cdot f(v) \tag{3.14}$$

Another correction arises from the fact that electrons produced along the track of the charged fragment may undergo subsequent recombination on their drift towards the anodes. According to their magnetic rigidities, the final fragments may enter the ionization chamber in different distances from the anodes, i.e. having different horizontal positions in the final focal plane (x_4). The energy-loss signal from a fragment of a given charge may thus be slightly different depending on its distance from the anode, i.e. on the amount of the recombination of the produced electrons. The process of electron recombination follows an absorption law, which means that the number of electrons traversing a certain distance dx is reduced each time by the same factor. The dependence of the energy-loss signal on the fragment position in the MUSIC may thus be described by an exponential function:

$$\Delta E(x_4)=\Delta E_{40}\cdot\exp(-\lambda x_4) \tag{3.15}$$

where ΔE_{40} is the energy loss in position $x_4 = 0$ and λ is an absorption coefficient. The value of the absorption coefficient may be determined from the fit of the measured energy loss as a function of the horizontal position in the MUSIC chamber (x_4). The position-corrected energy-loss signal then is:

$$\Delta E_{corr}=\Delta E_{meas}\cdot f_1(v)\cdot f_2(x_4) \tag{3.16}$$

where
$$f_2(x_4) = \frac{\Delta E_{40}}{\Delta E(x_4)} = \frac{1}{\exp(-\lambda x_4)} \qquad (3.17)$$

In case of both Xe experiments, a slight dependence of the absorption coefficient on the magnitude of the energy loss was observed. The value of λ was thus determined for each value of energy loss (charge) separately and ranged from $3 \cdot 10^{-4}$ to $7 \cdot 10^{-4}$ mm^{-1}.

Finally, the dependence of the energy-loss signal from the MUSIC on the changes of temperature and pressure conditions inside the chamber must be taken into account. By change of the room temperature or the atmospheric pressure the temperature and pressure, the conditions of the MUSIC gas change as well. As a consequence, the number of electrons created by the ionization of the gas may vary, which affects the measured energy-loss signals. To account for this effect, the positions of the peaks in the energy-loss spectra measured at different times (i.e. at different p, T conditions) must be recorded and any shift with respect to some reference spectrum must be corrected for. In case of both Xe experiments, the energy-loss spectrum measured in the first magnetic field setting of the FRS was chosen as a reference. The positions of the peaks in the energy-loss spectra measured with other magnetic-field settings were corrected to correspond to the reference spectrum, so that peaks in all the energy-loss spectra uniquely overlap.

After performing all the described corrections, the final, corrected energy loss reads:

$$\Delta E_{corr} = \Delta E_{meas} \cdot f_1(v) \cdot f_2(x_4) \cdot f_3(T,p) \qquad (3.18)$$

where $f_3(T,p)$ is a correction applied to the positions of the peaks in the energy-loss spectra measured in different magnetic-field settings. Fig. 3.5 below shows an example of an uncorrected (left) and corrected (right) energy-loss spectrum from the ^{136}Xe+Pb experiment. The calibration of the corrected energy losses is performed based on the identification plot of Z versus A/Z and will be discussed in section 3.2.4.

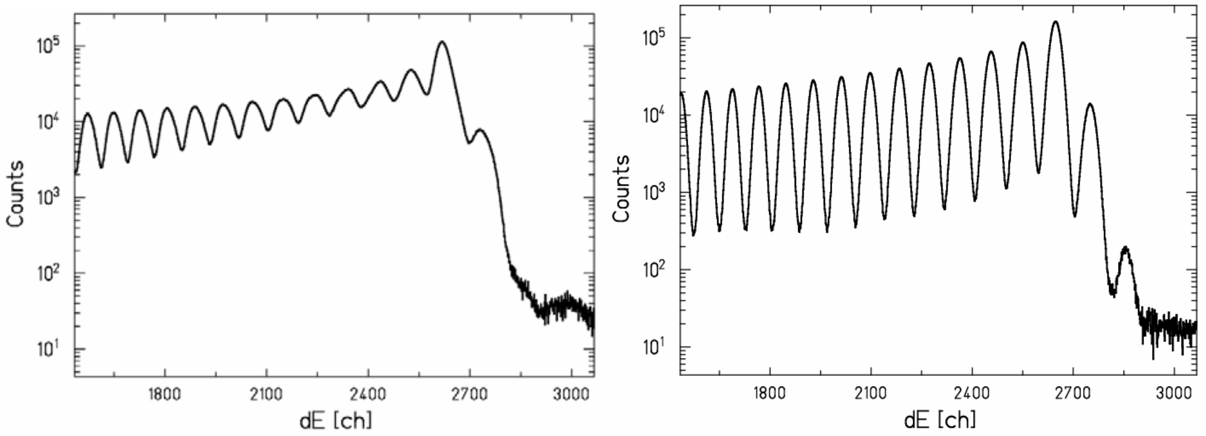

Fig. 3.5: Comparison of the energy loss spectra measured in the first MUSIC chamber in the ^{136}Xe+Pb experiment; (left) uncorrected spectrum; (right) final spectrum after applying all the corrections described in the text. The highest peak corresponds to Z=54.

3.2.3. Identification of charge states

On the passage through various layers of matter in the beam line, the produced fragments may catch or loose electrons. This process basically depends on the velocity of the fragment and the velocity of the electrons on its orbits, and follows the Bohr criterion, which says that the orbital electrons are stripped off if their orbital velocity is less than the velocity of the fragment, and attached in the opposite case. Moreover, there is a slight dependence of the process on the material. These not fully stripped ions complicate the identification, since having different A/q than bare ions they follow different trajectories in the FRS.

The layers of matter in the FRS beam line used during both Xe experiments were the target, the scintillator and in case of light-fragment settings also the degrader, the latter two located in the intermediate image plane. Capture or removal of electrons in the layers of matter in the final focal plane does not affect the measurement, since there is no magnetic field applied and thus the trajectories of fragments do not change.

The change of trajectory of the ion in the magnetic field after the capture or loss of an electron may be used to identify the charge states of the final residues and remove them from the analysis. Let us assume a fragment of mass A and charge $Z = 30$ was produced in the target. Already in the target this fragment may capture an electron from an atom of the target material so that its mass-to-charge ratio $A/q = A/29$. On the passage through the material in the intermediate image plane this electron may be removed or kept so that the mass-to-charge ratio behind the layer of material becomes $A/q = A/30$ or $A/q = A/29$, respectively. The change of the magnetic rigidity will thus be different in the two cases, i.e. $\Delta B\rho \sim (A/29\text{-}A/30)$ and $(A/29\text{-}A/29)$, respectively. According to equation (3.10) this will result in different positions in the final focal plane for the two cases. A similar situation arises if the bare fragment with the mass-to-charge ratio $A/q = A/30$ leaves the target and captures an electron on its passage through the material at S2. In such a case, the change of its magnetic rigidity will correspond to $\Delta B\rho \sim (A/30\text{-}A/29)$, and the corresponding relative change of the magnetic rigidity, i.e. the dispersion, will have the opposite value than in the previous case if the electron was removed. The energy losses in the layer of material were for simplicity neglected. From the above example it is obvious that the final fragments which passed the FRS having one electron in at least one FRS stage land in different positions in the final focal plane. As a consequence, the information on the horizontal position of the final fragments in the final focal plane may be used to disentangle different ionic charge states. In Fig. 3.6 an example of the correlation of the energy loss signal from the MUSIC versus the horizontal S4 position is shown as measured in the ^{136}Xe experiment. The signals in the upper left corner of Fig. 3.6 left correspond to fragments, which passed the second stage of the FRS having one electron (0e,1e).

According to the above example, fragments passing the FRS having one electron in the first FRS stage (1e,0e) would land in the positive positions located symmetrically to the right from the positions of the bare ions. These fragments are however cut out by the limited dimensions of the FRS. In case of fragments passing the FRS with one electron in both stages, the horizontal position in the final focal plane coincides with the position of the bare fragments. In this case the (0e,0e) and (1e,1e) states of the fragments cannot be separated using the measured signals and it is necessary to keep the contribution of this (1e,1e) charge state to the final fragment yield as low as possible. In case of both Xe experiments this contribution was well below 1%.

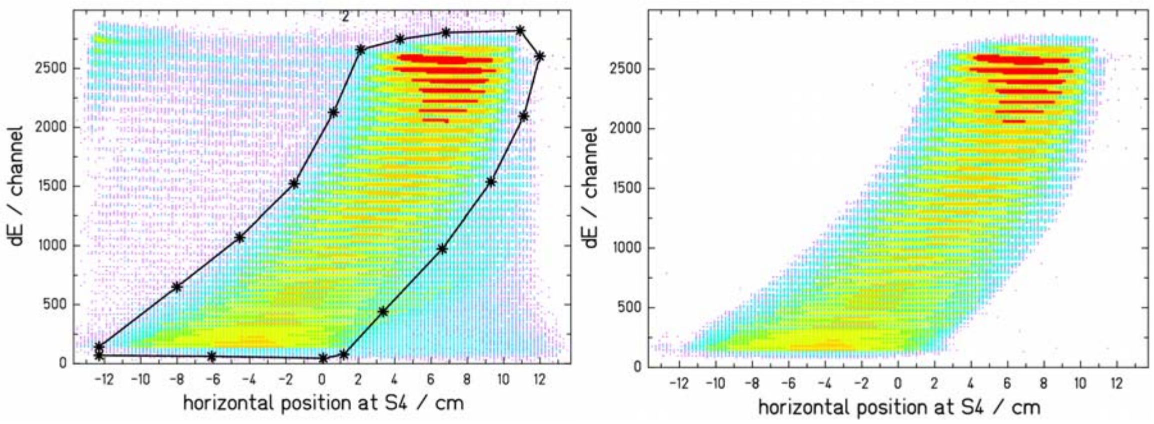

Fig. 3.6: Energy-loss signal from MUSIC1 versus the horizontal position in the final focal plane. (left) original spectrum with charge states in the upper left corner and indication of a cut on the signals from bare fragments; (right) the same spectrum as on the left hand side displayed after the cut.

3.2.4. Mass and nuclear-charge identification

Once only the fully stripped ions are selected by means of the condition shown in Fig. 3.6 left, the mass and nuclear charge may be identified. The easiest way to obtain the identification is to display the energy-loss signals measured by the MUSIC versus the *A/Z* ratio calculated using equation (3.3). In Fig. 3.7, the identification plots from ^{136}Xe+Pb experiment as measured in the light- and heavy-fragment settings are shown. To account for the quadratic dependence of the energy loss on the fragment charge, the square root of the energy loss is displayed on the vertical axis.

Each single spot in the figure corresponds to an individual fragment of given mass *A* and charge *Z*. The high mass resolution achieved in this experiment may be seen in the clear separation of spots corresponding to different isotopes. A regular pattern may be observed in 'positions' of the single isotopes. The vertical 'line' of nuclei in case of the light-fragment settings at $A/Z = 2$ corresponds to the fragments with equal neutron and proton numbers $N=Z$. The fragments on the 'lines' to the right from the $A/Z=2$ 'line' correspond successively to isotopes with $N = Z+1$, $Z+2$ etc., while fragments to the left correspond to $N = Z-1$, $Z-2$ etc. This pattern continues in the heavy-fragment settings.

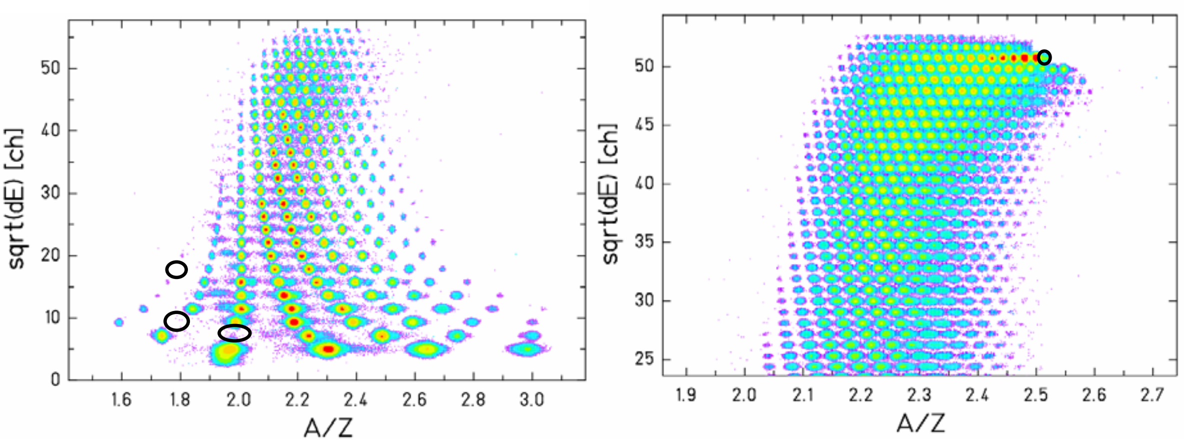

Fig. 3.7: Identification plots from ^{136}Xe+Pb experiment: (left) light-fragment settings; (right) heavy-fragment settings. The black circles mark the locations corresponding to ^{8}Be, ^{9}B and ^{16}F isotopes in the left figure and of the primary beam in the right figure.

The mass and charge identification may now be easily performed. In case of the light-fragment settings several holes may be observed in the spectra, indicated in Fig. 3.7 left by black circles. These correspond to isotopes, which practically immediately decay, i.e. ^{8}Be, ^{9}B and ^{16}F. With the use of these holes, and the regular pattern of $N=Z+k$ (k = -2,-1…) the unique identification both in nuclear charge and mass may be performed. It may be seen that the isotopes of Z=3 were the lightest residues detected and identified in this experiment.

In case of the heavy-fragment settings there is no such unique pattern as in the case of the light-fragment settings. Nevertheless, in this case the beam may be identified so that knowing its location in the identification plot all the remaining fragments may be uniquely identified using the regular pattern similar as in case of the light-fragment settings, and noting that beam is located in the $N=Z+82$ 'line'. The validity of the identification of single isotopes may be controlled by a correct 'overlap' of the isotopes identified in the light and heavy data sets.

In Fig. 3.7, the most intense row of isotopes corresponds to Z=54, since isotopes of xenon are produced by neutron removal reactions, which generally have the highest cross sections. It may be observed that also fragments produced by charge pickup (Z=55, 56) were detected. To identify the beam among the Z=54 isotopes some additional considerations are needed. In case of the measurements with settings of the magnetic fields, when the magnetic rigidity of the beam matches the FRS acceptance, the beam passes through the Fragment Separator. In this case attention must be paid to provide a sufficient shielding by positioning movable slits located at S1 to avoid the damage of the detectors by the high beam intensity. As a consequence, the location of the beam in Fig. 3.7 does not correspond to the most intense spot in row of Z=54 isotopes, but rather to the least intense one as marked by the black circle. The most intense spot corresponds to ^{135}Xe produced in the one-neutron removal reaction, which has the highest cross section. Fig. 3.8 shows an example of the mass resolution of isotopes identified close to the beam in the ^{136}Xe+Pb experiment.

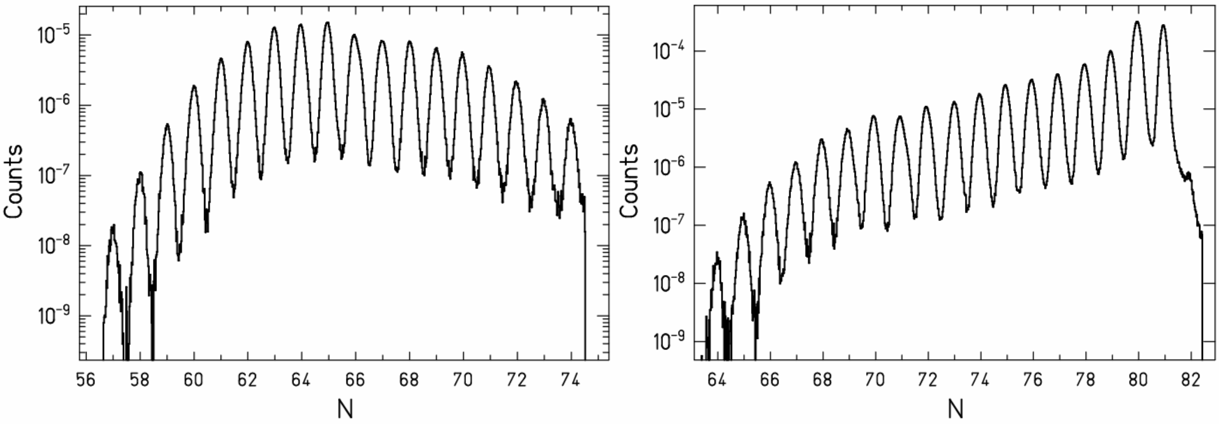

Fig. 3.8: Example of the identification and mass resolution close to the beam as measured in the ^{136}Xe+Pb experiment, Z=50 (left), Z=54 (right). The vertical axes show the number of counts per beam particle measured during the whole experiment.

Similar considerations were applied for the identification of residues from the ^{124}Xe+Pb experiment, and the corresponding identification plots, with identified nuclear charge displayed on the vertical axes, are shown in Fig. 3.9. As may be seen from Fig. 3.9 left, in this experiment light fragments only down to Z=5 were measured due to the different thresholds of the experimental electronics. Several counts corresponding to isotopes of beryllium Z=4 were also registered in this experiment, their measurements were, however, too strongly affected by the experimental thresholds and were excluded from the data analysis. Also in case of this experiment a high mass resolution was achieved as may be seen in the clear separation of spots corresponding to different isotopes.

From Fig. 3.9 left a very poor mass resolution may be observed in the nuclear charge range *Z*=18-22. This observation is most probably a consequence of the wrong function of the constant fraction discriminator used to obtain the position information from the arrival time of signal from the left hand side of the scintillation detector located in the intermediate image plane. This effect has a direct consequence on the determination of the position (x_2) used in the evaluation of the magnetic rigidity (equations (3.7 and 3.11)) and thus on the identification of single isotopes using equation (3.3). Therefore, it deteriorates considerably the mass resolution. As a consequence, in the specified nuclear-charge range, the identification plot of Fig. 3.9 left cannot be used to identify the isotopes of the affected elements. Nevertheless, it was possible to reconstruct the identification of the single isotopes by means of the time-of-flight measurement. For this purpose only the right hand sides of the two scintillation detectors were used, which are unaffected by the distorted function of the single CFD unit. The ToF spectrum for each element separately preserves to a large extent the isotopic resolution and may be used to identify the single isotopes. In Fig. 3.10 an example of such spectrum, recalculated to velocity, for *Z*=21 measured in a single magnetic-field setting is shown. Integrating these spectra the yield of each isotope measured in every magnetic-field setting could have been reconstructed. Nevertheless, the measurement in the charge range of potassium (*Z*=19) was affected so strongly that only two isotopes of this element could have been uniquely identified.

Due to the setting of the FRS in the heavy-fragment scan, the elements *Z*=18-22 were measured also in the heavy-fragment settings, where their distortion due to the broken CFD unit was less severe. However, since these lighter fragments passed the FRS rather close to its borders, their yields are significantly cut. Nevertheless, an attempt was made to reconstruct the isotopes of these elements also from the heavy-fragment settings especially in order to reconstruct the 'missing' isotopes of *Z*=19. To correct for the cut of these isotopes a correction factor was applied, which was determined as a ratio of yield of uncut isotopes reconstructed from the light-fragment settings to the yield determined from the heavy-fragment settings. The cross sections determined by both methods are shown and discussed in section 4.2 of the next chapter.

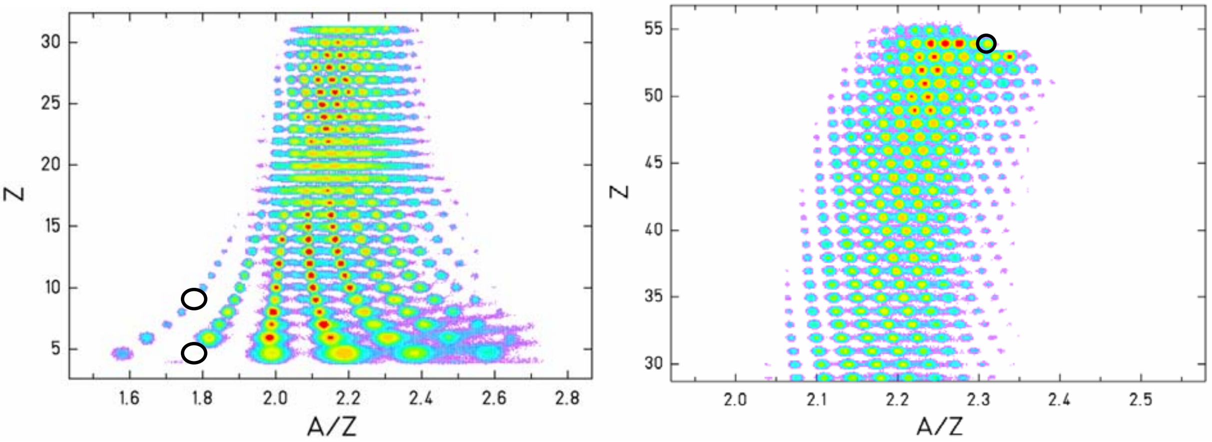

Fig. 3.9: Identification plots from the ^{124}Xe+Pb experiment: (left) light-fragment settings; (right) heavy-fragment settings. The black circles mark the locations corresponding to ^{9}B and ^{16}F isotopes in the left figure and of the primary beam in the right figure.

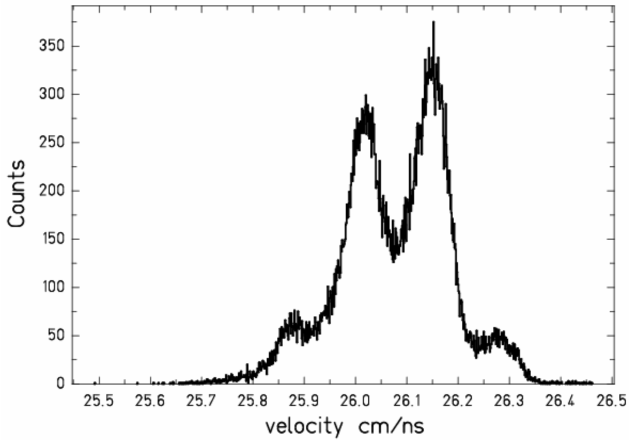

Fig. 3.10: Velocity spectrum for element Z=21 obtained from the right hand side of the scintillator ToF measurement in a single setting of the FRS magnets.

Having identified all the residues measured in both Xe experiments, the production cross sections may be determined. In the next section the final steps of the data analysis, necessary to determine the production cross sections will be introduced.

3.3. Determination of the reaction cross sections

3.3.1. Basic considerations

To determine the production cross sections from the measured yields of single isotopes, the following relation is used:

$$\sigma(N,Z) = \frac{Y_{meas}(N,Z)}{\mathrm{N}_{\mathrm{Pb}} \cdot T(N,Z)} \cdot \alpha(A) \qquad (3.19)$$

Here N_{Pb} is the number of lead-target nuclei per unit area, $Y_{meas}(N,Z)$ stands for the measured production rate per incident projectile, $T(N,Z)$ represents the correction factor for the transmission losses due to the limited angular acceptance of the FRS and $\alpha(A)$ is the correction factor for the losses of the fragments due to their secondary interactions with the material in the beam line. The description of these two corrections, which are necessary to determine the correct production cross sections, will be given at the end of this chapter.

To determine correctly the yield of a given residue it is necessary to know that each count contained in the spot corresponding to given N and Z in the identification plot indeed represents this isotope and does not come from background caused predominantly by the interactions with the material of slits. Moreover, any double counting due to the overlap of the neighboring magnetic-field settings must be avoided. The best way to determine the yield $Y_{meas}(N,Z)$ is therefore a direct integration of the velocity distribution of a given isotope. The velocity distribution of every fragment was fully measured by changing the magnetic fields on the FRS dipoles as mentioned in section 2.3.1. In the following section, the reconstruction of the complete velocity distribution for every detected residue will be described.

3.3.2. Velocity distributions

It is known from the Goldhaber description of the fragmentation process [Gold74] that the velocity distributions of the produced residues have a Gaussian shape due to a random removal of nucleons with various Fermi momenta in the reaction. This shape may be distorted by the location straggling due to the energy losses in the target, which results in a rectangular velocity distribution. The velocity distributions of fragments would then correspond to the convolution of Gaussian and rectangular shapes. In both Xe experiments, the thickness of the lead target (635 mg/cm^2) was selected in such a way to compromise the need of a high production rate and low location straggling to preserve the Gaussian shape of the velocity distributions of the final residues.

Apart of the high mass and charge resolutions also the high-precision measurement of the fragment velocities is one of the great advantages of the Fragment Separator. The velocity determination based on the time-of-flight measurement suffers from an uncertainty given by the time resolution of the scintillators, which does not allow resolution better than 100ps over the ~37m of the flight path. Such a velocity resolution is sufficient for the high resolution in mass, but may still be improved once the A and Z of the fragments are known.

For this purpose the equation (3.3) is used again, this time to extract the velocity of a given residue. Indeed, once the identification of the final residues as described in the previous chapter was performed, the A and Z values in equation (3.3) are integer numbers not suffering from any uncertainty. The equation (3.3) may then be solved to determine the velocity of fragment with given A and Z with the resolution defined solely by the resolution in the magnetic rigidity. This resolution is given by the construction of the Fragment Separator and corresponds to ~$5 \cdot 10^{-4}$ (FWHM), which allows the determination of velocity parameter $\beta\gamma$ with the resolving power of the order of 2000:

$$\beta\gamma c = \frac{e}{u}\frac{A}{Z} B\rho \qquad (3.20)$$

where the magnetic rigidity is determined using equation (3.11). Based on this equation, the velocity of every residue may be determined. The value extracted from this equation corresponds to the velocity of the fragment in the first FRS stage and is determined in the laboratory frame. In order to obtain the velocity of the fragment as produced in the nuclear reaction, the correction to the energy loss of the fragment in the target must be considered. To apply this correction, the assumption is made that the fragment is on average produced in the middle of the target and its velocity is then correspondingly increased by the energy loss calculated in one half of the target material. The assumption is justified by the fact that the reaction cross section does not vary strongly with the small variation of energy that the beam can experience. As well the small effect of the attenuation of the beam in the target may be neglected. Upon applying this correction, the velocity is transformed using the Lorentz transformation into the frame of the projectile.

As mentioned earlier, to fully measure the velocity distributions in case of fragments having distributions broader than the FRS momentum acceptance (i.e. 3%), the magnetic fields on the first two FRS dipoles were changed by steps of 1.5% to assure a sufficient overlap of the velocity distributions measured in the neighboring settings. This at the same time allowed for an increase of statistics, since each setting was as a consequence measured twice. Using equation (3.11) the velocity of every residue in each magnetic field setting was determined. In order to obtain the correct shape of the velocity distribution, the number of counts measured in each setting was normalized to the number of beam ions impinging on the target in this setting. Finally, the velocity distributions from single settings could have been combined and the full velocity distribution as illustrated in Fig. 3.11 was obtained.

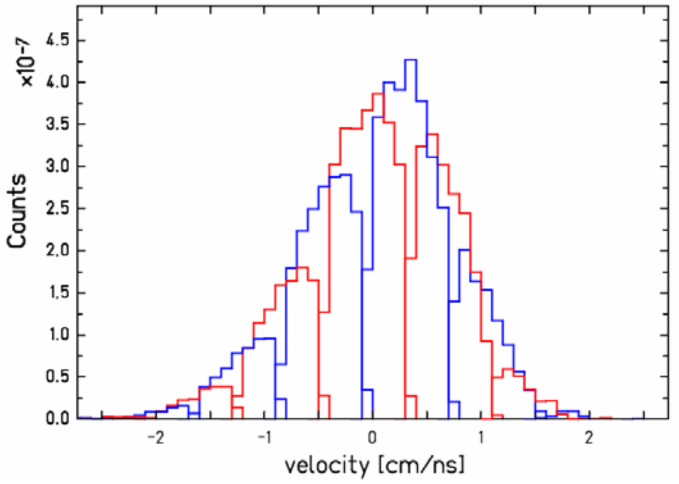

Fig. 3.11: Velocity distribution of the isotope *Z*=15, *N*=16 measured in the ^{136}Xe+Pb experiment. Neighboring settings of the magnetic fields are marked by red and blue colors.

The method to extract the velocity distributions described above could not have been used in case of isotopes of *Z*=18-22 elements identified in the experiment ^{124}Xe+Pb, since in this case the information on the magnetic rigidity in equation (3.11) was not available due to the distorted function of one CFD unit. As a consequence, another method was applied to obtain the total yield of these isotopes. The yield of each isotope of affected elements measured in each magnetic field setting was reconstructed by integration of the time-of-flight spectra as described in section 3.2.4. In order to obtain the total measured yield in all the magnetic field settings, the yield obtained for every single setting was scaled by a factor close to 2 to account for the overlap of the neighboring settings and summed up. With this method the measured total yields of the isotopes of the affected elements could have been reconstructed.

Moreover, it was observed that the distorted function of the CFD unit in case of the light-fragment settings influences the shape and thus the integral of the measured velocity distributions. As discussed above, the velocity distribution is determined based on equation (3.3) using the magnetic rigidity in the first FRS stage, which is determined from the horizontal position in the intermediate focal plane according to expression (3.11). It is at this place, where the position in the intermediate image plane enters and deteriorates the shape of the velocity distribution. An illustration of this effect is shown in Fig. 3.12 left. Similar velocity distributions were observed also for other residues measured in the light-fragment setting. It may be seen that the velocity distributions measured in single magnetic-field setting has a sharp peak on one side. This signals a strongly nonlinear response of the scintillation detector (caused by the CFD unit), accumulating the majority of counts in a limited range of positions and thus velocities. Please, note that this accumulation of events does not significantly disturb the identification pattern in case of these isotopes! To correct for this distortion of the shape of the velocity distributions a similar approach to reconstruct the velocity distribution was used as in case of the *Z*=18-22 elements. This time the number of counts in each setting was determined directly from the single velocity spectrum and after scaling by a factor close to two to account for the overlap of the neighboring settings, the velocity distribution was reconstructed as may be seen in Fig. 3.12 right. From these reconstructed velocity distributions the yield of every residue could have been determined.

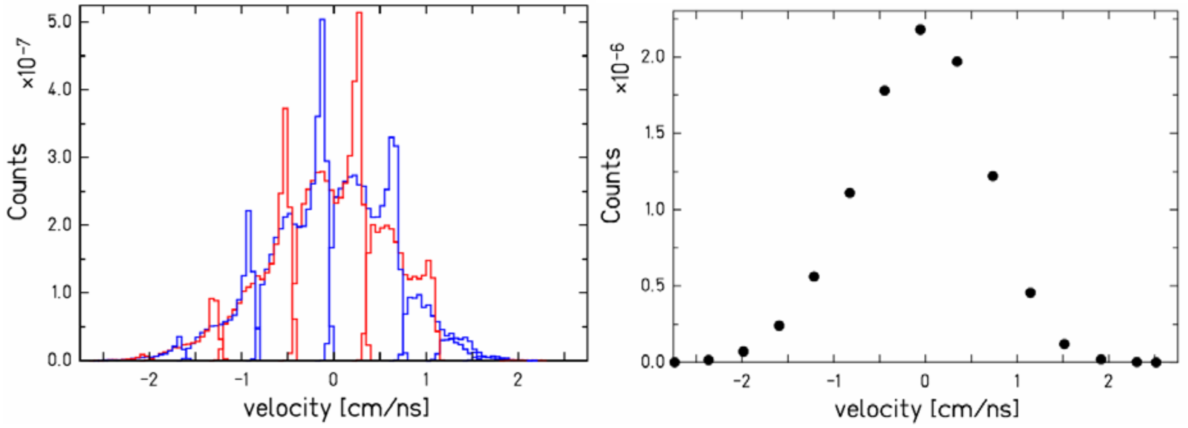

Fig. 3.12: Example of the influence of the distorted function of the CFD unit on the velocity distribution of isotope Z=15, N=16 measured in the ^{124}Xe+Pb experiment.

Event-by-event correction of the reduced FRS transmission

From Fig. 3.11 a rather curved shape of the velocity distributions measured in single magnetic-field settings in the ^{136}Xe+Pb experiment may be seen. This is a consequence of the reduced transmission of the fragments passing close to the spatial borders of the Fragment Separator with respect to the transmission of fragments passing in the vicinity of the central trajectory. It causes a decrease in the number of counts on both sides of the velocity distribution measured in a single setting and produces the observed curved shape. This feature is a consequence of the ion optical properties of the FRS and must be corrected for before the velocity distribution may be integrated to obtain the final fragment yield. This correction could be applied only in case of the ^{136}Xe+Pb data and undisturbed velocity distributions measured in heavy-fragment settings of the ^{124}Xe+Pb experiment.

To correct for the reduced transmission of the fragments passing close to the borders of the FRS, the transmission of the FRS as a function of position of the fragment in the intermediate image and final focal planes must be determined. The transmission of a residue having an angular distribution of width σ_θ in the laboratory frame may be calculated as follows [Benll02]:

$$T(x_2,x_4) = 1 - \exp\left(-\frac{\alpha_{eff}^2(x_2,x_4)}{2\sigma_\theta^2}\right) \tag{3.21}$$

where $\alpha_{eff}(x_2,x_4)$ denotes the effective angular acceptance of the FRS in millirads. The use of the effective angular acceptance accounts for a nonspherical cross section of the FRS tube, which is defined by the shape of the quadrupoles. The value α_{eff} represents the radius of a circular aperture of the same area as the cross section of the FRS tube. The width of the angular distribution σ_θ may be obtained from the width of the measured velocity distribution in the projectile frame $\sigma_{v_{frag}}$ according to relation:

$$\sigma_\theta = \frac{\sigma_{v_{frag}}}{v_{beam}} \cdot \sqrt{1-\beta_{beam}^2} \tag{3.22}$$

where v_{beam} denotes the velocity of the beam in the laboratory frame and $\beta_{beam} = v_{beam}/c$.

For the purpose of determination of the FRS transmission a code developed in [Benll02] was used. With this code, the so called transmission matrix corresponding to the ion-optical setting of the FRS used in the two Xe experiments was calculated. This transmission matrix determines the FRS angular acceptance $\alpha_{eff}(x_2, x_4)$ as 'seen' by the fragment passing through a given horizontal position in the intermediate image (x_2) and final focal (x_4) planes (Fig. 3.13).

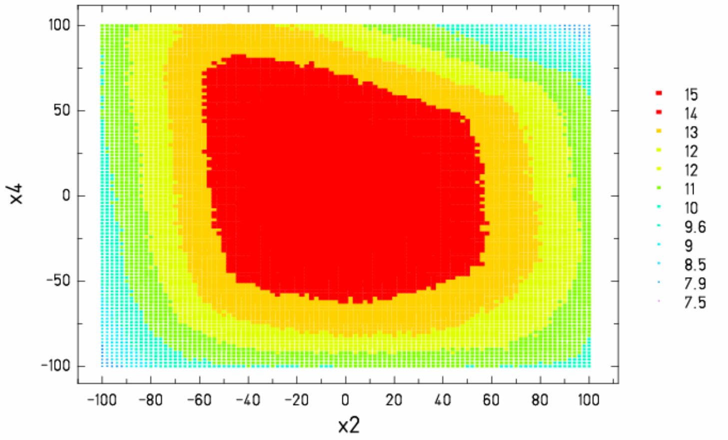

Fig. 3.13: Transmission matrix calculated for the ^{136}Xe+Pb experiment. The color coding corresponds to different values of the angular acceptance of the FRS 'seen' by the fragments passing at different x_2 and x_4 positions.

The angular acceptance of fragments moving on the central trajectory (x_{20}, x_{40}) corresponds to the full FRS acceptance, i.e. 15 mrad. On the contrary, the angular acceptance for fragments passing close to the limits of the FRS geometrical dimensions (±10 cm at S2 and/or S4) is considerably decreased (down to ~ 9 mrad). To correct for this reduction of the angular acceptance close to the borders of the Fragment Separator, the transmission coefficient $T(x_2, x_4)$ according to equation (3.21) was calculated for every fragment, i.e. for every x_2 and x_4 position. The weighting factor $W(x_2, x_4)$ was then calculated as the ratio of transmission coefficients corresponding to the full versus the actual acceptance:

$$W(x_2, x_4) = \frac{T(x_{20}, x_{40})}{T(x_2, x_4)} \tag{3.23}$$

This weighting factor was subsequently used as a weight of each count in the velocity distribution. Fig. 3.14 shows the velocity distribution from Fig. 3.11 after correction for the reduced FRS transmission.

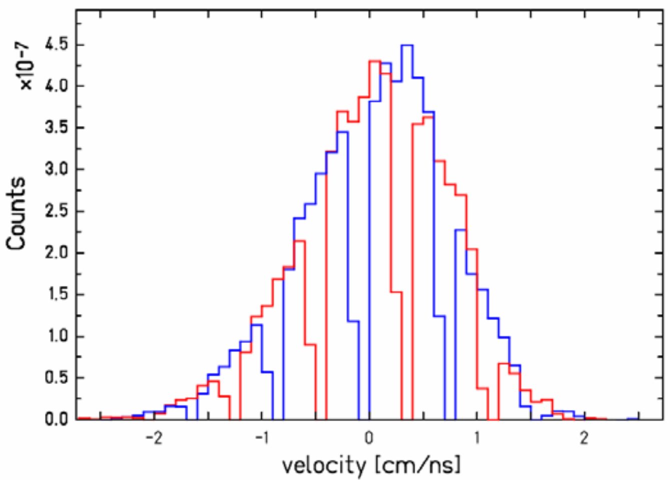

Fig. 3.14: Velocity distribution of the isotope Z=15, N=16 from the ^{136}Xe+Pb experiment corrected for the reduction of the FRS transmission. Neighboring settings of the magnetic fields are marked by red and blue colors.

It may be seen that after introducing this weight the correct shape of the velocity distribution in every single setting was reconstructed, and the velocity distributions from the neighbouring settings smoothly overlap. Velocity distributions of all other isotopes were corrected in the same way (apart of light-fragment settings of ^{124}Xe+Pb experiment). These corrected velocity distributions may now be integrated to determine the normalized yields of all measured residues $Y_{meas}(N,Z)$.

In order to obtain correct yields and thus reliable production cross sections, the transmission matrix must correctly reproduce the features of the FRS acceptance 'seen' by the particles. It was observed during the data analysis that a slight readjustment of the transition matrix was necessary in order to obtain a smooth shape of the velocity distribution shown in Fig. 3.14. The readjustment of the transmission matrix in the 'horizontal direction' changes the angular acceptance 'seen' by particles traversing at given x_2 position and thus modifies the shape of the velocity distribution measured in a single magnetic-field setting. This readjustment causes no uncertainty at all, since the Gaussian shape of the velocity distributions may be used as a guide to determine which adjustment of the transmission matrix is the correct one. With this 'horizontal' readjustment the correct shape of the velocity distribution could have been reconstructed. On the contrary, the change of the transmission matrix in the 'vertical direction' changes the angular acceptance 'seen' by particles traversing at given x_4 position and introduces a change of the integral of the velocity distribution in each single magnetic-field setting. Any readjustment of the transmission matrix in the vertical direction would cause changes in the integral of the full velocity distribution and thus in the determined yields $Y_{meas}(N,Z)$. No readjustment of the transmission matrix in the 'vertical direction' was therefore performed. Nevertheless, any possible uncertainty of the transmission matrix in reproducing the angular acceptance as a function of x_4 position introduces a systematic error affecting especially the isotopes passing in x_4 positions, where the variation of the values of $\alpha_{eff}(x_2, x_4)$ in the transmission matrix is the largest. By assuming the uncertainty of the transmission matrix in the ‘vertical direction’ not exceeding ±1-2cm, which was the case observed for the ‘horizontal direction’, the introduced systematic error may be evaluated to correspond roughly to ~ 10% for isotopes passing close to the borders of S4.

3.3.3. Applied corrections

Having obtained the measured yield of every detected residue, the production cross sections may be determined by means of equation (3.19). In this section, the corrections accounting for the limited angular acceptance of the FRS and for the secondary reactions, which are necessary to determine the correct production cross sections, will be introduced.

Transmission correction

The event-by-event correction discussed in the previous section was introduced to account for the *relative* reduction of the transmission of the fragments passing close to the borders of the FRS versus those moving on the central trajectory. As a consequence, a smooth Gaussian shape of the velocity distributions was reconstructed. Nevertheless, the yields obtained by the integration of these velocity distributions still do not correspond to the real production yields. Indeed, due to the broad angular distributions of especially light residues some part of them never enters the Fragment Separator, since they leave the target under too large angles. Therefore, the measured yield $Y_{meas}(N,Z)$ must be appropriately corrected to account for these ‘lost’ fragments.

For this purpose, similar considerations as in the previous section are used. Again, equation (3.21) is used to determine the transmission coefficient $T(N,Z)$, except now T and α_{eff} are independent of the position and α_{eff} denotes the full FRS acceptance, i.e. 15 mrad. While in the previous section only the *relative* difference between the acceptance in the middle and close to the borders of the FRS was corrected, now we attempt to correct the *absolute* yield for the fact that fragments outside the 15mrad acceptance of FRS are never detected. It is the value of this transmission coefficient $T(N,Z)$, determined for each isotope, which finally enters equation (3.19).

The importance of this correction decreases with increasing charge of the residue, since heavier residues are produced with narrower angular distributions and the angular acceptance of the FRS is adapted to the emittance of heavy fragmentation products. In case of both Xe experiments, the transmission $T(N,Z)$ varied between 25% for Z~10 and reached 100% for Z~40. The uncertainty of this correction is given mainly by the determination of the width of the velocity distribution, used to determine σ_θ. The uncertainty of the widths of the velocity distributions was determined to correspond to 5%, which results in the systematic error of the absolute transmission correction, which decreases with increasing charge and ranges from 9% for Z=10 to values below 1% for Z>33.

In case of light-fragment settings from the ^{124}Xe+Pb experiment a slightly different approach had to be used, since in this case the even-by-event correction of the velocity distributions was not possible, and thus the correction for the angular acceptance for different elements passing in different x_4 position must be still considered. Therefore, the different values of α_{eff} have to be considered in equation (3.21) depending on the position of fragment in the final focal plane (i.e. T and α_{eff} in (3.21) are only x_4 dependent). In section 2.3 it was discussed that the second stage of the FRS selects the fragments according to their charge and thus the position of fragments in the final focal plane is related to Z. By displaying the dependence of Z on the position at S4 (analog of Fig. 3.6 for light-fragment settings considered here), the range of x_4 positions corresponding to one element may be selected and from the transmission matrix (Fig. 3.13), the corresponding *mean* angular acceptance $< \alpha_{eff} >$ may be extracted. The value $< \alpha_{eff} >$ is determined for the case of x_2=0, since for the considered settings only one point per setting is available in the velocity distributions. This mean value is subsequently used in equation (3.21) to determine the corresponding transmission coefficient, which finally enters relation (3.19). This approach basically substitutes both above introduced methods (event-by-event as well as the absolute transmission corrections). The uncertainty of this method includes both aspects discussed in the previous two (uncertainty of widths of velocity distributions and of transmission matrix). Moreover, additional uncertainty is introduced by this method, which is related to the fact that a mean value of the angular acceptance $< \alpha_{eff} >$ is used in equation (3.21). The influence of this uncertainty depends on the span of positions, which correspond to a given element. In case of light-fragment settings of the ^{124}Xe+Pb experiment this influence is rather low, since the position of various elements span typically ~2-3 centimeters and the corresponding error of the transmission coefficient mostly does not exceed 1%. The systematic error of this approach is thus determined mainly by the two earlier mentioned contributions and it was estimated to correspond to ~7% for isotopes passing close to the center of the FRS and ~17% for isotopes passing close to borders.

Correction for secondary reactions

Apart of the transmission correction, the measured yield $Y_{meas}(N,Z)$ must be corrected for the secondary reactions in the target and materials in the FRS beam line. In case of both Xe experiments a rather thin (635 mg/cm^2) lead target was used, which assures that contributions from the secondary reactions in the target material do not exceed 1% for all the fragments. Nevertheless, the produced fragment may still undergo a nuclear reaction in the scintillator or in case of the light-fragment settings in the degrader in the intermediate image plane and may thus transform to some lighter product. To account for these losses due to the secondary nuclear reactions, the measured yields must be appropriately corrected. Only losses of the fragments due to the secondary reactions must be corrected, since the magnetic rigidities of products of the secondary reactions in the intermediate image plane are, in the majority of cases, outside the acceptance of the second stage of the FRS so that these products will not be transmitted by the last two dipoles. Similarly the secondary nuclear reactions of fragments in the final focal plane do not affect the measured yields in case they do not lead to change of the nuclear charge, which is determined using the MUSIC chamber. The contribution of the charge-changing reactions in the MUSIC chamber, however, remains well below 0.5% and may thus be neglected.

Tables 3.4a,b summarize the percentage of the nuclear reactions of fragments with different mass numbers in materials present in the FRS beam line during the light and heavy-fragment settings. The lowest rows list the values of the corresponding correction factor α calculated to account for losses of the residue of given mass. The correction factor $\alpha(A)$ used in equation (3.19) was determined for every residue from the fit of the values listed in tables 3.4a,b. The percentage of nuclear reactions as a function of mass was determined using the program AMADEUS [AMA] by means of the Glauber calculation of the total nuclear reaction cross section developed in [Bene98]. The uncertainty of this calculation corresponds to ~10%, which determines the systematic error, caused by this correction that ranges from 0.3% for *A*=5 to 1% for *A*=60 in case of light-fragment settings and from 0.6% for *A*=50 1% for *A*=136 in case of heavy-fragment settings.

Table 3.4a: The percentage of nuclear reactions for different masses calculated in the layers of materials present in the intermediate image plane during the light-fragment settings. In the last row, the correction factor applied in equation (3.19) is listed.

	A						
	60	**50**	**40**	**30**	**20**	**10**	**5**
nucl. reac. in scintillator [%]	6.57	5.96	5.28	4.52	3.64	2.52	1.74
nucl. reac. in degrader [%]	4.22	3.91	3.57	3.19	2.73	2.11	1.65
nucl. reac. tot [%]	10.79	9.87	8.85	7.71	6.37	4.63	3.39
α	**1.1079**	**1.0987**	**1.0885**	**1.0771**	**1.0637**	**1.0463**	**1.0339**

Table 3.4b: The same as in table 3.4a for the case of the heavy-fragment settings.

	A								
	136	**120**	**110**	**100**	**90**	**80**	**70**	**60**	**50**
nucl. reac. in scintillator [%]	10.31	9.62	9.18	8.70	8.21	7.70	7.16	6.57	5.96
α	**1.1031**	**1.0962**	**1.0918**	**1.0870**	**1.0821**	**1.0770**	**1.0716**	**1.0657**	**1.0596**

3.4. Uncertainty of the measured production cross sections

As discussed in the previous sections, there are several factors entering the determination of the production cross sections, which contribute to the systematic uncertainty of the measured results. There are several sources of uncertainties, which may be listed as follows:

(i) calibration of the SEETRAM counts
(ii) transmission correction
(iii) correction for secondary reactions
(iv) other contributions

In the following a brief summary of the single contribution is presented.

(i) As discussed in section 3.1, the main source of the uncertainty of the SEETRAM calibration concerns the observation that its response is slightly position dependent. As a consequence, the uncertainty of the calibration was deduced to be 7%.

(ii) Due to the specific problems related to some parts of the experimental data, different procedures had to be applied in order to correct for the limited angular acceptance of the Fragment Separator. The uncertainty of the transmission correction introduced by these procedures was discussed below each method separately and may be summarized as follows:

> Event-by-event correction plus absolute transmission correction
>
> > The systematic error introduced by this method generally decreases with increasing nuclear charge and ranges from 9% for Z=10 to below 1% for Z=33. Moreover, due to the possible uncertainty of the transmission matrix an additional systematic error of 10% have to be considered in case of fragments passing close to the borders of the FRS. The systematic errors introduced by this method apply to isotopes from all but light-fragment settings from ^{124}Xe+Pb experiment.
>
> S4 dependent absolute transmission correction
>
> > The systematic error introduced by this method corresponds to ~7% for isotopes passing close to the center of the FRS and to ~ 17% for isotopes passing near the borders, which in addition suffer from the possible uncertainty of the transmission matrix. The systematic errors introduced by this method apply to isotopes from light-fragment settings from ^{124}Xe+Pb experiment.

(iii) As introduced in the previous section, the yield losses due to the interaction of fragments in the different layers in the beam line had to be corrected by applying mass dependent correction factor. The systematic error caused by this correction correspond to 0.3-1% for $5 \leq A \leq 60$ in case of light-fragment settings and to 0.6-1% for $50 \leq A \leq 136$.

(iv) As discussed in section 3.2.4, as a consequence of the improper function of the CFD unit in the ^{124}Xe+Pb experiment, isotopes of elements Z=18-22 had to be reconstructed from the ToF spectra measured by the right hand side of the scintillation detector. The resolution of the ToF for some isotopes was rather poor, which is reflected in larger error bars of the single points in the reconstructed velocity distributions of these isotopes. As a consequence also the error bars of the corresponding production cross sections are slightly higher than in case of isotopes of other elements.

Chapter 4

Experimental results

In this chapter, the main features of the measured velocity distributions are discussed and the isotopic distributions of all the final residues measured in both Xe experiments are introduced. The experimental production cross sections were determined from the measured velocity distributions, as described in section 3.3 of the previous chapter, and the corresponding velocity distributions are discussed in section 4.1 below. In section 4.2, the angular-acceptance integrated production cross sections, corrected only for the secondary reactions, are introduced. The main trends of the corresponding isotopic distributions measured in the ^{124}Xe and ^{136}Xe experiments are compared. The transmission and secondary-reaction corrected isotopic distributions are presented in section 4.3. In section 4.4, the charge and mass distributions measured in both experiments are compared. Finally, in section 4.5 the first moments of the final isotopic distributions in terms of the mean N-over-Z ($\langle N\rangle/Z$) ratio are introduced in more detail.

4.1. Velocity distributions

Before the isotopic distributions from both experiments will be introduced, the measured velocity distributions should be discussed in more detail. In section 3.3.2 of the previous chapter the approach used to determine and correct the full velocity distributions was described. This method was applied for both experiments, and examples of some velocity distributions are shown in Fig. 4.1 and Fig.4.2 for ^{136}Xe+Pb and ^{124}Xe+Pb, respectively.

Let us discuss the velocity distributions measured in ^{136}Xe+Pb first. From Fig. 4.1 it may be seen that in case of the lightest isotopes, in particularly ^{6}Li and ^{10}B, the shape of the velocity distribution is not a single Gaussian peak, rather it seems to be composed of two slightly shifted Gaussian components. As discussed in section 2.3.1, due to the limited FRS angular acceptance double-humped shape of the velocity distribution may be observed in case the processes such as fission or break-up with surviving large residue are present, where only the outer shell of sphere in the three-dimensional velocity space is populated due to the Coulomb repulsion. The velocity distribution then consists of two outer peaks corresponding to the above mentioned processes and eventually of the central peak, which corresponds to fragmentation. In case of the lightest residues, the outer Gaussian peaks may be partially or even fully masked by the broad velocity distribution of the fragmentation residue. This is probably the case for the ^{6}Li and ^{10}B isotopes shown in Fig. 4.1, where only the left outer peak may be partially observed and thus apparently only two instead of three Gaussian components are identified in the velocity distributions. The individual components of the velocity distributions of the lightest residues were extensively analyzed in [Nap04a], where it was found that the outer Gaussian peaks correspond to the break-up of the highly excited nucleus into a surviving large residue accompanied by the smaller fragment(s) rather than to asymmetric fission events. The overview in Fig. 4.1 shows that the shape of the velocity distribution evolves with increasing charge of the residue and the apparent second component disappears around *Z*~10 (^{20}Ne). A clearly Gaussian shape of the velocity distributions may be observed up to the residues in the vicinity of the projectile.

Fig. 4.1: Velocity distributions of several isotopes measured in the ^{136}Xe+Pb experiment (y-axis shows normalized counts).

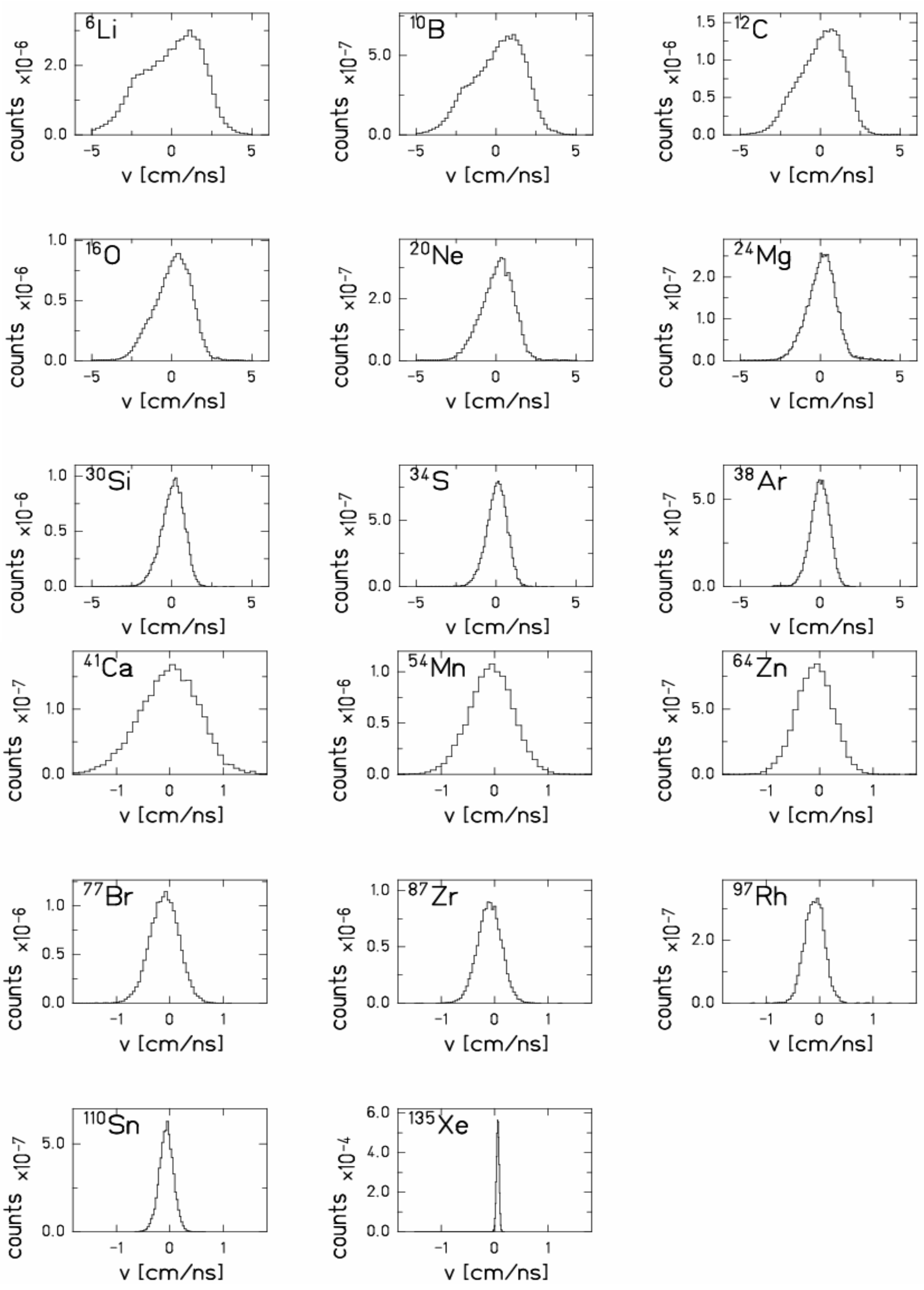

Fig 4.2 shows the velocity distributions measured in the ^{124}Xe+Pb experiment, where the isotopes of *Z*=5 element were the lightest fragments fully measured. As discussed in section 3.3.2 of the previous chapter, the velocity distributions measured in the light-fragment settings had to be reconstructed from the total number of counts measured in each single magnetic-field setting and therefore only one point corresponds to each setting in the velocity distributions of fragments up to ^{54}Mn. Nevertheless, as may be seen from the figures, the reconstructed velocity distributions closely resemble the features observed in the velocity distributions analyzed in the ^{136}Xe+Pb experiment. The velocity distributions above ^{64}Zn were extracted from the heavy-fragment settings, where they could be fully measured.

Fig. 4.2: Velocity distributions of several isotopes measured in the ^{124}Xe+Pb experiment (y-axis shows normalized counts).

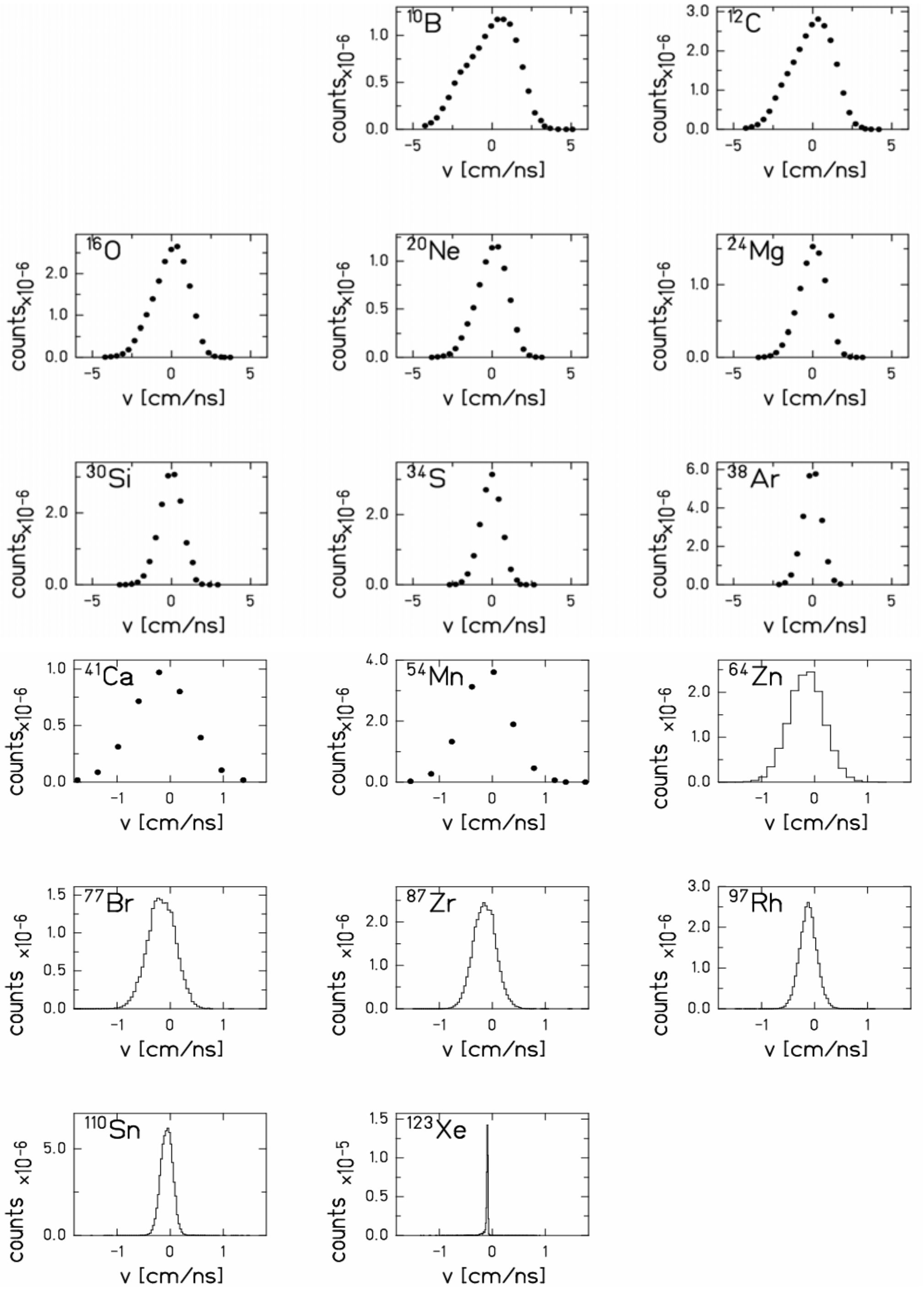

In case of both experiments a decrease of the width of the velocity distributions with increasing nuclear charge may be observed (please, note the change of x-axis scale between ^{38}Ar and ^{41}Ca) as the collision evolves from the more violent one (low impact parameters) towards the very peripheral collisions in the vicinity of projectile. A dominating reason for this broadening is the Fermi-momentum of individual nucleons, which are removed in the collision process [Gold74].

4.2. Angular-acceptance integrated isotopic distributions

In the following, the angular-acceptance integrated isotopic distributions measured in the ^{124}Xe+Pb and ^{136}Xe+Pb experiments are compared and discussed. The angular-acceptance integrated production cross sections of single isotopes were determined by a direct summation of the number of counts in the measured velocity distributions, and only the correction for the secondary reactions was applied. The influence of the correction for the limited FRS acceptance is discussed in the next section. Since the velocity distributions of fragments from both reactions are similar, the angular-acceptance integrated isotopic distributions are well suited for the relative comparison of the products of the two reactions. The interest in the angular-acceptance integrated cross sections lies in the observation that they provide directly measured quantities independent of the assumptions on the three-dimensional velocity distributions needed to model the transmission of fragments through the FRS in order to reconstruct the ‘full’ production cross sections introduced in the next section. The angular-acceptance integrated cross section σ_{acc} may be expressed as:

$$\sigma_{acc} = \int_{0}^{\alpha_{FRS}} \frac{d\sigma}{d\alpha} d\alpha \tag{4.1}$$

where α_{FRS} denotes the FRS acceptance of 15 mrad around the beam axis.

To determine the correction for the secondary reactions, the considerations introduced in subsection of section 3.3.3 were used. The percentage of secondary reactions of produced fragments, which occur directly in the lead target (635 mg/cm^2 thick) remains close to 1% for all the isotopes. This universal correction factor may thus be applied for all the residues. The correction for losses due to the fragment interactions in the materials inside the beam line was determined using the parameterized Glauber calculation [Bene98] of the reaction cross section implemented in the AMADEUS code [AMA] and is detailed in tables 3.4a,b.

The isotopic distributions from both Xe experiments measured in the nuclear-charge range Z=5-55 (^{124}Xe+Pb) and Z=3-56 (^{136}Xe+Pb) are compared in Fig. 4.3. Due to the thresholds of the electronics, some losses may be expected in case of Z=3 isotopes measured in the ^{136}Xe+Pb experiment, and the corresponding production cross sections introduced in Fig. 4.3 should be considered as lower limits only. Please, note that not all the isotopes visible in the identification pattern in Fig. 3.7 and 3.9 of the previous chapter may be found in Fig. 4.3. In case of the lightest residues this is a consequence of their broad velocity distributions, which were not fully measured for all the detected isotopes and thus the cross section could not be properly determined. Similarly some isotopes are missing in the isotopic distributions close to the projectile. This is a consequence of the presence of slits in some of the settings in the vicinity of the beam, which introduce a severe cut in the velocity distributions of some isotopes and thus the corresponding production cross sections cannot be determined. This was in particularly the case of the one-neutron removal channel in case of ^{124}Xe projectile, which therefore had to be removed from the analysis. In some cases the cross sections could have been extracted, but still the influence of the presence of slits may be observed in both experiments in the slight deviations of the affected isotopes from the smooth shape of the isotopic distributions, especially on their neutron rich side in the vicinity of the projectile. Moreover, as discussed in section 3.2.4, due to the improper function of the constant-fraction discriminator processing the signals from the left hand side of the S2 scintillation detector in the ^{124}Xe+Pb experiment, the isotopes of Z=18-22 elements were reconstructed both from light- and heavy- fragment settings and the corresponding results are shown in figure by squares and crosses, respectively. A slightly lower values in case of some isotopes reconstructed from heavy-fragment settings may be observed (pink crosses), which may be related to the geometrical cut of the FRS of these isotopes, which could not be corrected fully. Therefore only the isotopes reconstructed from light-fragment settings will be used for the estimation of the cross sections. In case of Z=19 we decided to consider the isotopes reconstructed from heavy-fragment settings, however, with corresponding error bars.

The main aim of both experiments was to provide full isotopic distributions over a broad range of elements, so that the production cross sections over several orders of magnitude had to be measured. Fig. 4.3 shows that the production cross sections measured in both experiments extend over a broad range of ~10^{-3} mb to 10^{3} mb (the highest cross sections corresponds to one- and two-neutron removal channels of ^{136}Xe), and the production cross sections measured for a single element extend in most cases over three orders of magnitude. Thanks to this broad range of production cross sections measured in both experiments, the full isotopic distributions are available for all except the lightest elements, and their main features may be investigated in greater detail.

Indeed, several interesting observations may be made by comparing the shapes of the isotopic distributions produced in the reactions of the two projectiles largely differing in the initial N/Z (^{124}Xe with N/Z=1.30 and ^{136}Xe with N/Z=1.52). A slightly enhanced production of more neutron-rich isotopes is observed in the isotopic distributions of the lightest elements (Z~5-9) measured in fragmentation of the more n-rich ^{136}Xe projectile. This enhancement of n-rich isotopic production cross sections is replaced by a shift of the isotopic distributions towards more n-rich isotopes for elements with charge above Z~10. A clear difference between the positions of maxima of the isotopic distributions from fragmentation of ^{124}Xe and ^{136}Xe projectiles may be observed, which increases with increasing nuclear charge. The largest difference corresponds to the elements in the vicinity of the projectile, since here a pronounced memory on the initial isotopic composition is preserved due to rather low excitation energies acquired in the collision. With decreasing nuclear charge this memory is considerably reduced due to higher excitation energies introduced in the collision and thus a longer deexcitation process. Nevertheless, already from this comparison it is obvious that the memory on the initial N/Z is preserved in the whole nuclear-charge range despite the influence of the evaporation process. This observation is investigated in more detail in section 4.5, where the first moments of the isotopic distributions in terms of the mean N-over-Z ratio ($\langle N \rangle/Z$) are discussed.

Apart of the observation that a more n-rich projectile results in more n-rich final residues, the isotopic distributions from the ^{136}Xe projectile appear to be slightly broader, which is especially pronounced for elements in the vicinity of the projectile. In the initial collision certain isotopic distribution of the primary projectile-like fragments is formed. These initial fragments, each having a certain distribution of excitation energies will deexcite by emission of neutrons, protons and eventually more complex clusters. During this process, the initial isotopic distribution will be transformed into the distribution of the final residues. Due to the higher neutron excess in case of the ^{136}Xe projectile, the excited primary fragments (prefragments) formed in the initial collision reduce their excitation energy predominantly by neutron evaporation. The evaporation thus may be viewed as progressing close to a horizontal line of constant Z in the chart of nuclides. A rather broad range of isotopes of the same element may be populated in this process. On the contrary, in case of the less n-rich projectile ^{124}Xe, due to its lower neutron excess, the emission of neutrons is not so favorable anymore, and the competition between neutron and proton evaporation (eventually emission of other charged particles in case of higher excitation energies) occurs, which depopulates a given isotopic chain in favor of producing isotopes of lower elements. As a consequence, only a rather narrow range of isotopes of the same element is populated in the evaporation in case of this less n-rich projectile. The broader isotopic distributions in the vicinity of the projectile may thus be expected for ^{136}Xe. The isotopic distributions from ^{124}Xe in the nuclear-charge range (Z>~30) are narrower, but at the same time the cross sections of the most produced isotopes are considerably higher than the cross sections of the most produced isotopes in case of ^{136}Xe. To investigate the difference between the production cross sections from these two projectiles more closely the charge and mass distributions are studied in section 4.4.

It is especially interesting to see that slightly broader isotopic distributions from fragmentation of ^{136}Xe may be seen also in case of the lightest residues. The increased production of the n-rich isotopes in case of the ^{136}Xe beam signals that even the lightest residues preserve some memory on the neutron excess of the projectile nucleus at the end of the evaporation process. This may be an indication that a complete N/Z equilibration is not attained in the evaporation process in a sense that the residue corridor is not reached [Char98].

Apart of the trends of the mean values and widths, another interesting feature may be observed in the final isotopic distributions from both experiments. In the nuclear-charge range Z~5-15 a slight staggering in the production cross sections of the neighboring isotopes may be seen. This staggering is a manifestation of an even-odd effect, which is a consequence of the pairing interaction between the like-nucleons in the nucleus. The pairing interaction in case of nuclei having even number of protons and/or neutrons or vice versa (even-even/even-odd, odd-even nuclei) provides an additional contribution to the binding energy making these nuclei more stable. Clearly the most stable configuration is the one, where all the nucleons are paired (even-even nucleus) and the least stable is the configuration with one unpaired neutron and proton (odd-odd nuclei). As a consequence, in case of even-Z elements an enhanced production of even-even isotopes with respect to even-odd ones may be expected. Similarly in case of odd-Z elements the production cross sections of odd-even isotopes should be enhanced with respect to odd-odd ones. This effect may be very nicely seen in the isotopic distributions measured in both experiments. The even-odd staggering disappears around Z~15 due to the increasing competition of the γ-emission as a consequence of increasing level density below the particle emission threshold. In [Ric04] a quantitative discussion of the even-odd staggering in the production cross sections may be found. It is remarkable in the present data that also for the heavy isotopes in the vicinity of the projectile an even-odd staggering of the production cross sections is observed (Z=53). Such a trend was not observed in the previously studied heavier projectiles (Pb+Cu, Pb+^{1,2}H, Au+^{1}H) [deJon98,Enq01,Enq02,Rej01].

In both experiments also the charge-pickup reactions were measured (isotopes of elements Z=55,56). While in case of the less neutron-rich projectile only single charge-pickup channels are observed (Z=55), in case of ^{136}Xe also the double charge-pickup residues were detected (Z=56). The charge-pickup reactions proceed [Gaar91] either through a quasi-elastic collision between a proton and a neutron of target and projectile nuclei, respectively, where the proton replaces the neutron inside the projectile-like fragment (charge-exchange), or through the excitation of a projectile (or target) nucleon into the Δ(1232)-resonance state and its subsequent decay. Due to the excitation and subsequent decay of the Δ-resonance, the produced primary fragment may get considerably excited. In case of the more n-rich projectile the primary projectile-like fragment after charge-pickup reaction is still considerably n-rich so that the neutron emission dominates in the evaporation process. As a consequence, the isotopes of the same nuclear charge as the excited projectile-like fragment are predominantly produced. On the contrary, the competition between the neutron and proton emission in case of the primary projectile-like fragment from the less n-rich projectile may lead to the depopulation of a given isotopic chain and contribution to the production of isotopes of lower elements. This may be the reason, why the double charge-pickup residues (isotopes of *Z*=56 element) are observed in case of the ^{136}Xe projectile, but do not survive the deexcitation process in case of the less n-rich ^{124}Xe projectile.

Fig. 4.3: Secondary reactions corrected isotopic distributions measured in ^{136}Xe+Pb (blue points, *Z*=3-56) and ^{124}Xe+Pb (pink squares, *Z*=5-55, pink crosses *Z*=18-22). The dashed lines serve to guide the eye. Statistical error bars are smaller than the size of the symbols.

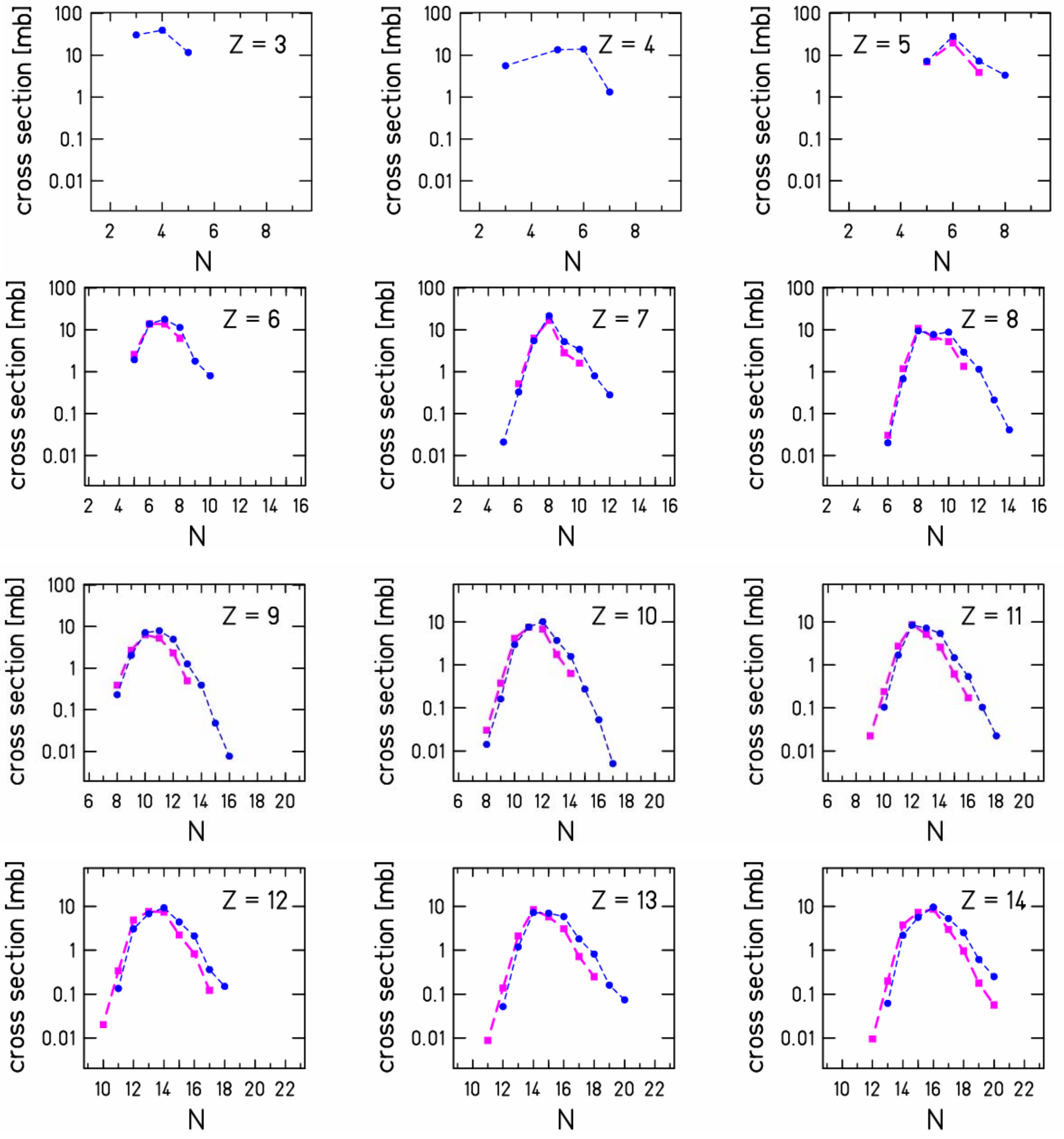

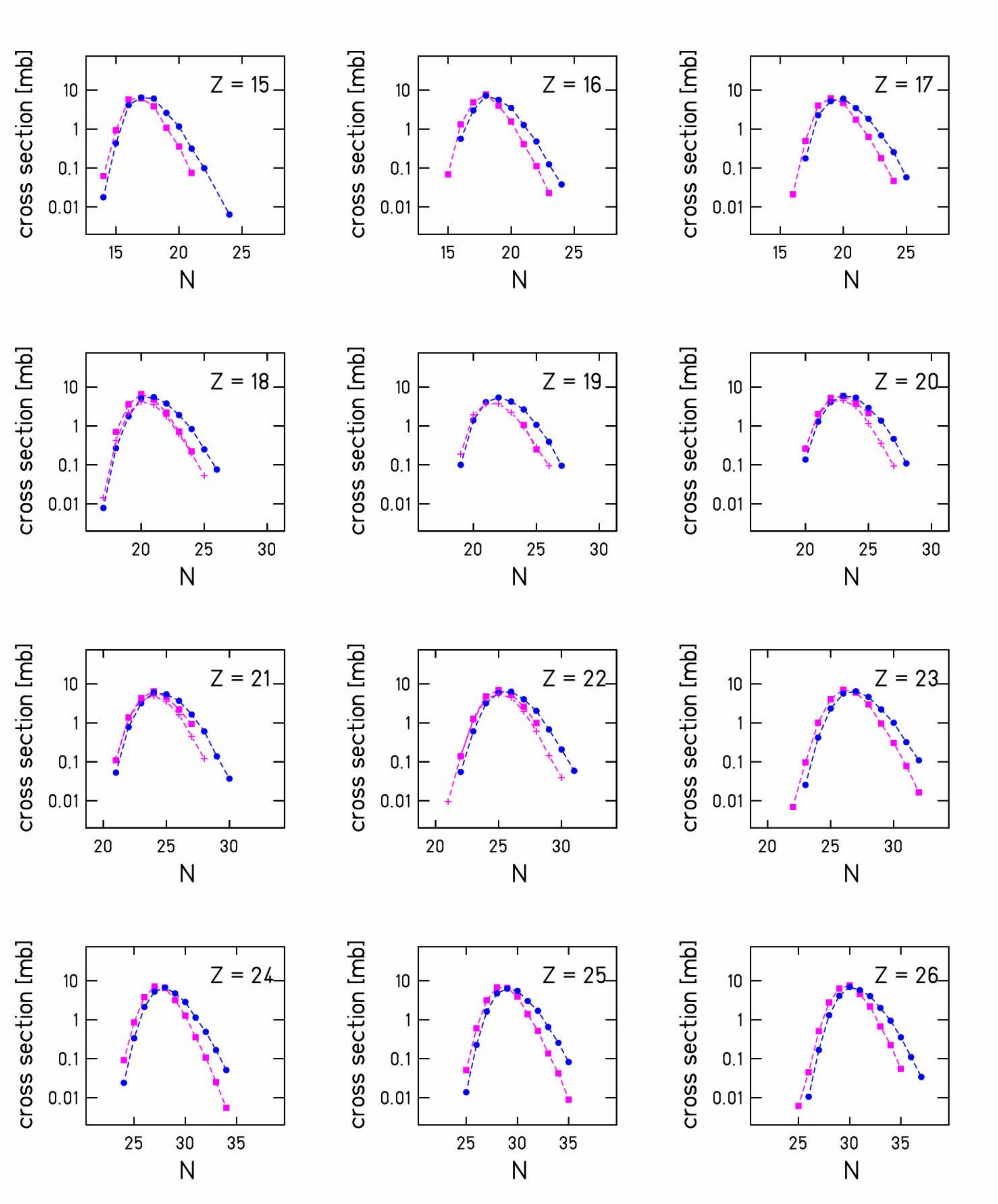
Z = 15
Z = 16
Z = 17
Z = 18
Z = 19
Z = 20
Z = 21
Z = 22
Z = 23
Z = 24
Z = 25
Z = 26
cross section [mb]
10
1
0.1
0.01
N
15
20
25
30
35

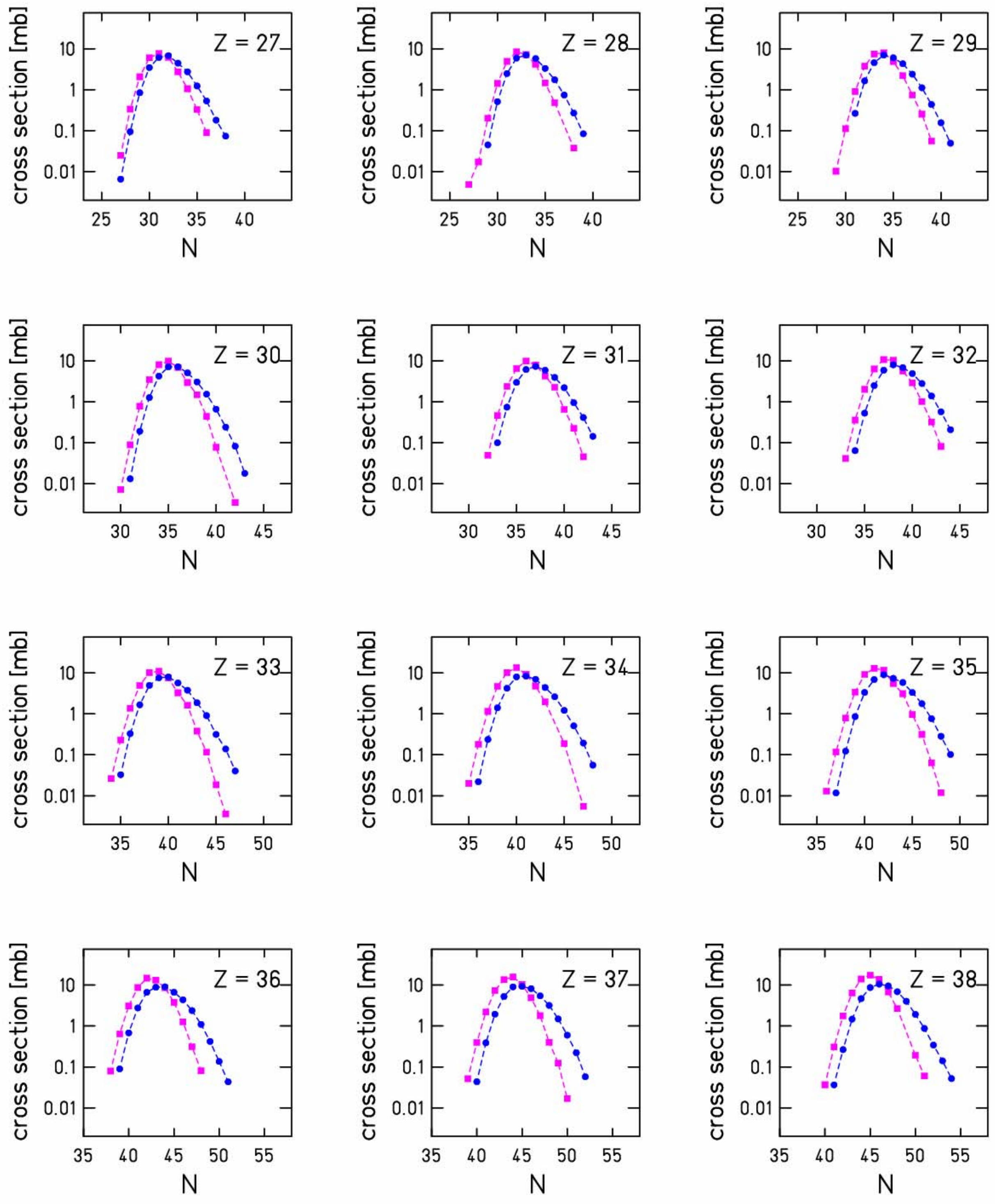
Z = 27
Z = 28
Z = 29
Z = 30
Z = 31
Z = 32
Z = 33
Z = 34
Z = 35
Z = 36
Z = 37
Z = 38
cross section [mb]
10
1
0.1
0.01
N
25
30
35
40
45
50
55

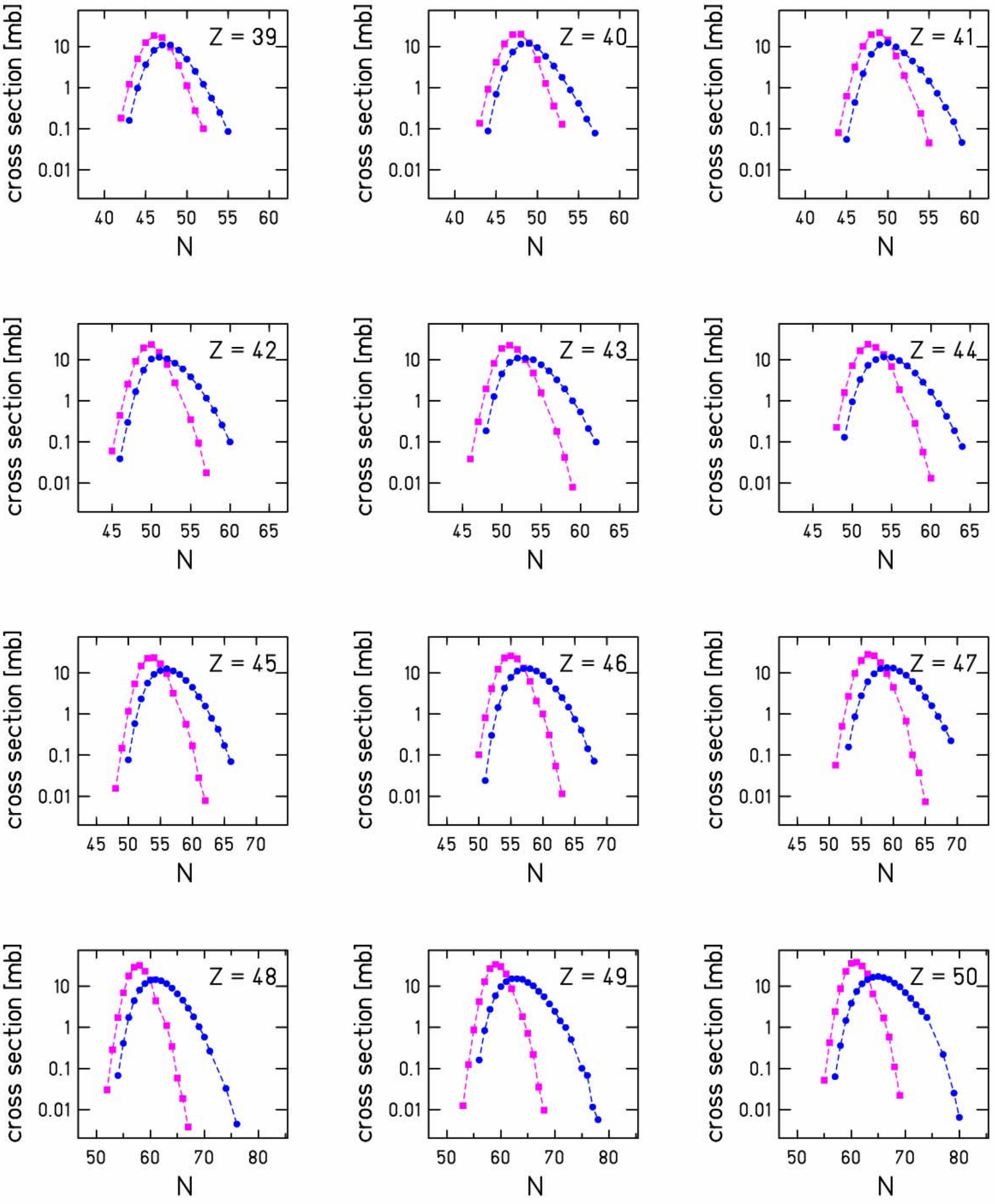
Z = 39
Z = 40
Z = 41
Z = 42
Z = 43
Z = 44
Z = 45
Z = 46
Z = 47
Z = 48
Z = 49
Z = 50
cross section [mb]
10
1
0.1
0.01
N
40 45 50 55 60
45 50 55 60 65
45 50 55 60 65 70
50 60 70 80

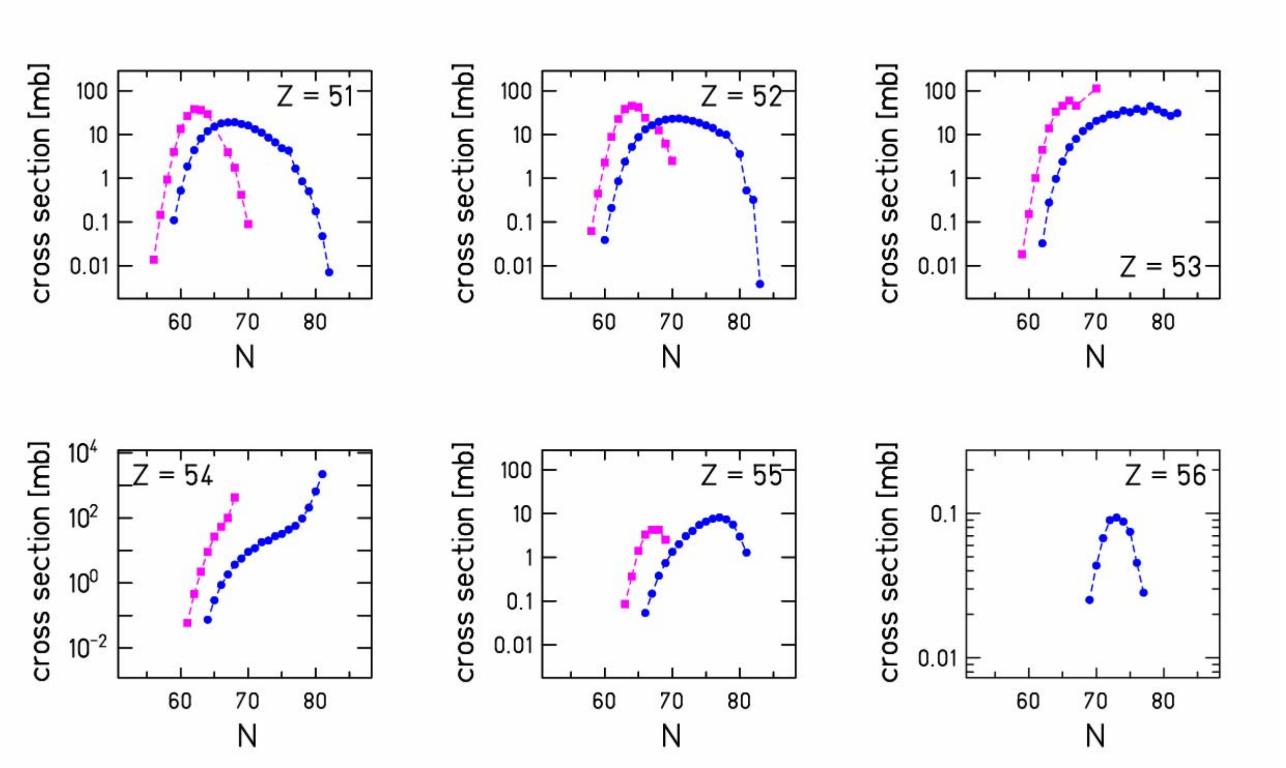

4.3. Transmission-corrected isotopic distributions

As discussed in section 2.3.1, the limited angular acceptance of the FRS affects the measurements of the production cross sections of lighter residues produced with broad angular distributions. To obtain the total production cross sections, the correction of the limited transmission of single isotopes through the FRS must be applied. In Fig. 4.4 and Fig. 4.5 the transmission and secondary reactions corrected isotopic distributions (open symbols) measured in the ^{136}Xe+Pb and ^{124}Xe+Pb reactions, respectively are compared with the angular acceptance integrated (i.e. transmission-uncorrected) isotopic distributions (full symbols), which were presented in the previous section. In case of *Z*=19 results from both, light- and heavy-fragment settings are shown.

The principles of the transmission correction introduced in section 3.3.3 are valid for the processes characterized by the Gaussian-type distribution in the 3-dimensional velocity space (i.e. fragmentation reactions). In other cases (fission, break-up with strong Coulomb repulsion) a different treatment of the transmission correction must be considered [Benll02]. As was shown in section 4.1, the velocity distributions for the lightest elements (below *Z*~9) reveal a slightly double-humped structure, which makes the determination of the transmission correction for these isotopes rather complicated, due to the overlap of the forward component of the double-peak (from processes other than fragmentation) and of the fragmentation peak. Therefore, the following investigation will be restricted to the properties of the final residues in the nuclear-charge range above *Z*~10, where the transmission correction valid for fragmentation events is applicable and which still allows to study the global trends of the measured isotopic distributions over a broad range of elements, which is the main aim of this work. The numerical values of the transmission- and secondary reactions corrected production cross sections for both experiments are listed in table A.1 in appendix A.

As mentioned in section 3.3.3, the transmission through the FRS varies between 25% for Z~10 and reaches 100% for Z~40 for both experiments. From Fig. 4.4 and Fig. 4.5 the influence of the transmission correction on the shapes of the isotopic distributions in case of the ^{136}Xe and ^{124}Xe beams, respectively may be investigated. Only the most strongly affected elements are shown as an illustration of the overall effect of the correction. As expected, the transmission correction increases the production cross sections of the lighter isotopes and its influence decreases with increasing nuclear charge, since the heavier residues are produced with narrower angular distributions and thus are better transmitted through the FRS. It may be seen in case of both experiments that the transmission correction generally introduces an increase of the production cross sections, but almost does not affect the shape of the isotopic distributions. The influence of the transmission correction on the first moments of the isotopic distributions is shown in more detail in section 4.5.

To complete this section, the transmission corrected production cross sections of all the isotopes in the nuclear-charge range Z=10-55(56) in case of ^{124}Xe+Pb and ^{136}Xe+Pb experiments, respectively, may be found in table A.1 in Appendix A.

Fig. 4.4: Comparison of transmission-corrected (open points) and transmission-uncorrected (full points) isotopic distributions measured in the reaction ^{136}Xe+Pb in the nuclear charge range Z=10-27. The dashed lines serve to guide the eye. Statistical error bars are smaller than the size of the symbols.

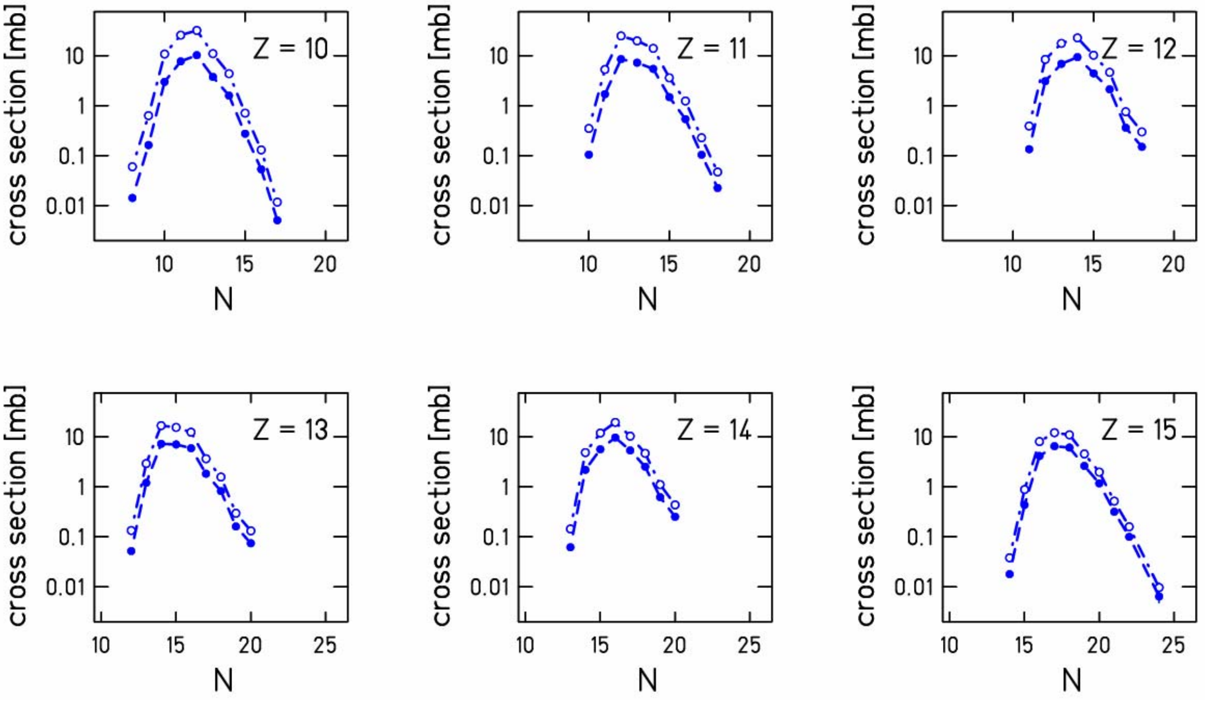

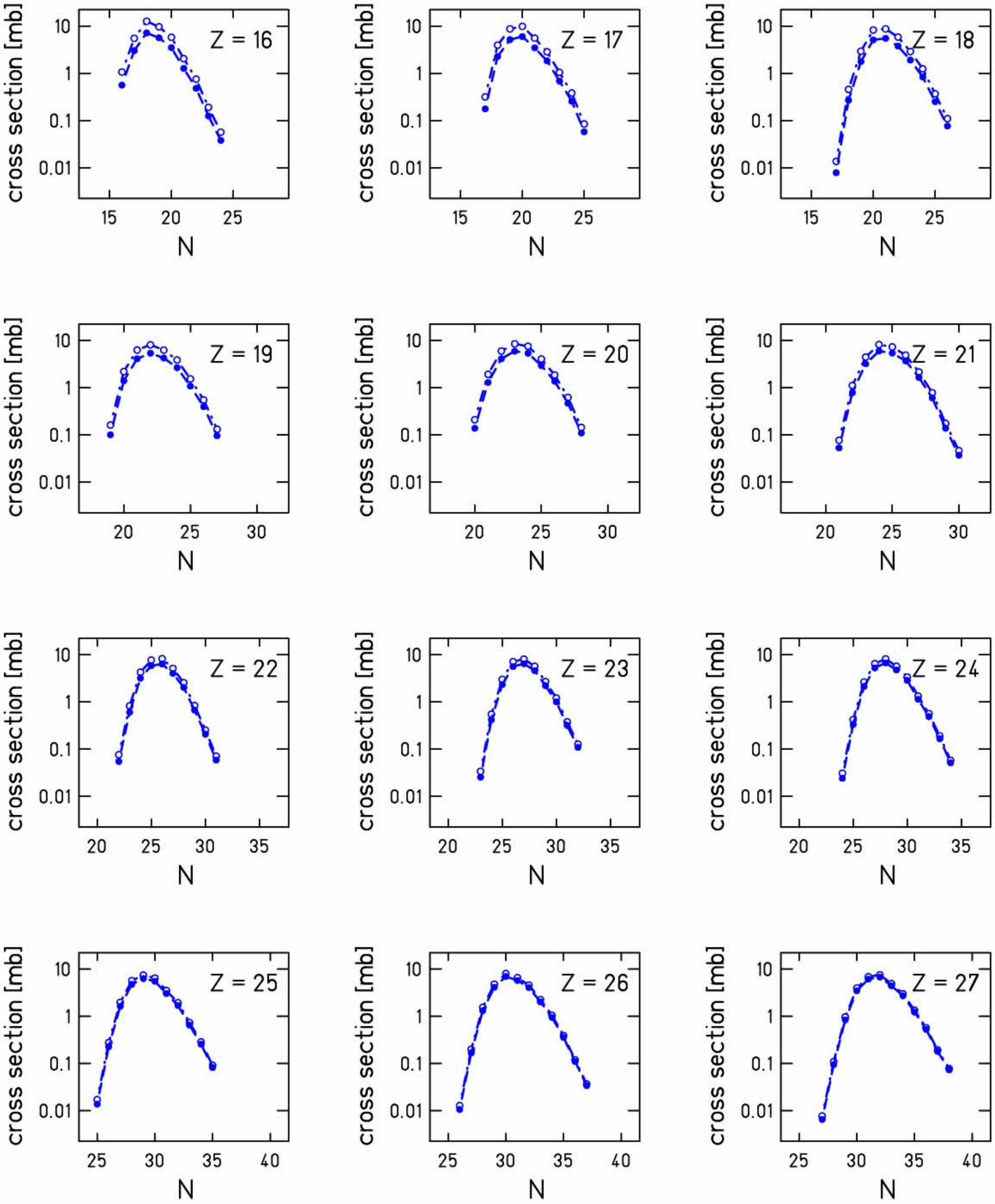
cross section [mb]
10
1
0.1
0.01
N
Z = 16
15
20
25
Z = 17
Z = 18
Z = 19
30
Z = 20
Z = 21
Z = 22
35
Z = 23
Z = 24
Z = 25
40
Z = 26
Z = 27

Fig. 4.5: Comparison of transmission-corrected (open squares, *Z*=19 open triangles) and transmission-uncorrected (full squares, *Z*=19 crosses) isotopic distributions measured in the reaction ^{124}Xe+Pb in the nuclear charge range *Z*=10-27. The dashed lines serve to guide the eye. Statistical error bars are smaller than the size of the symbols.

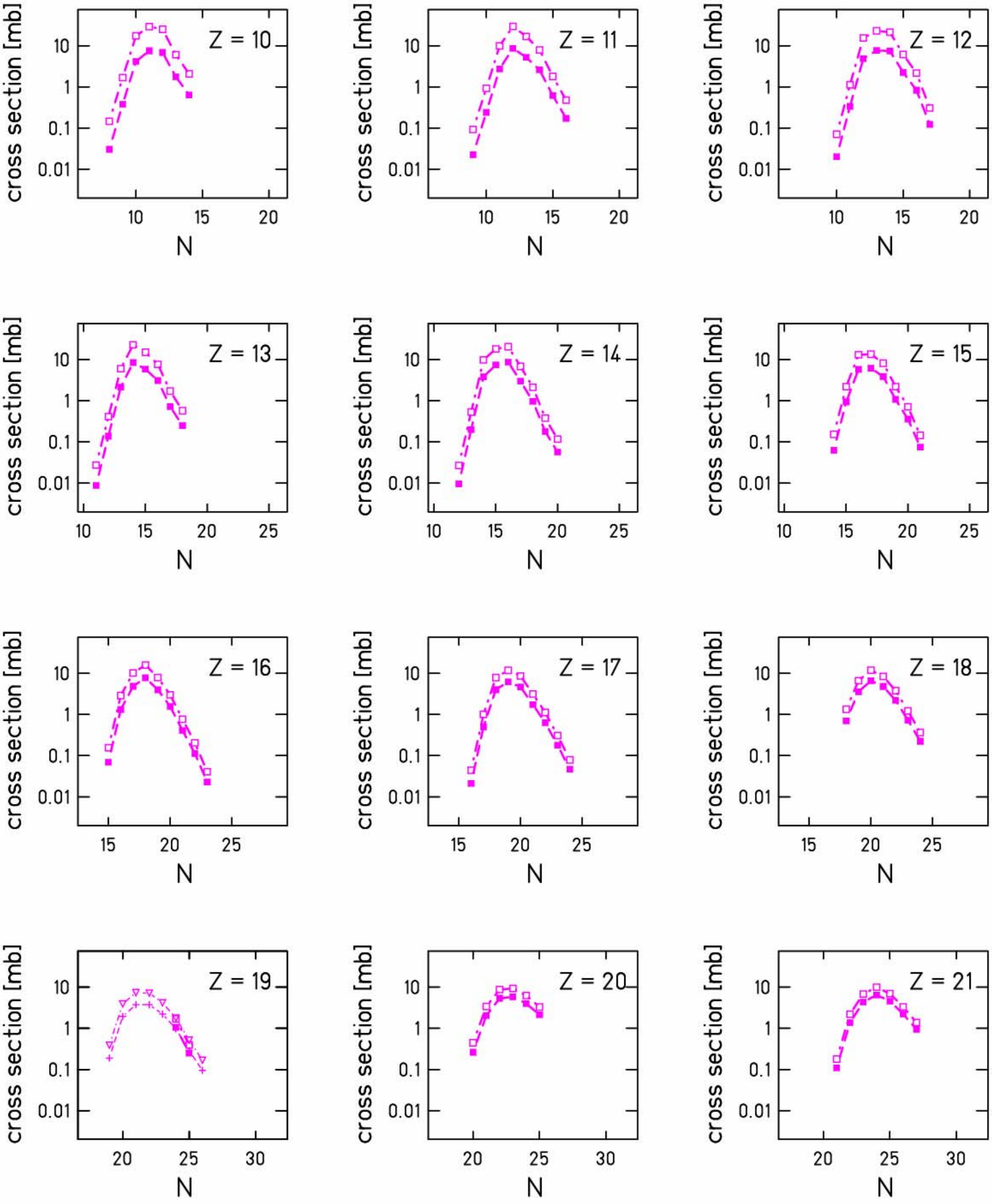

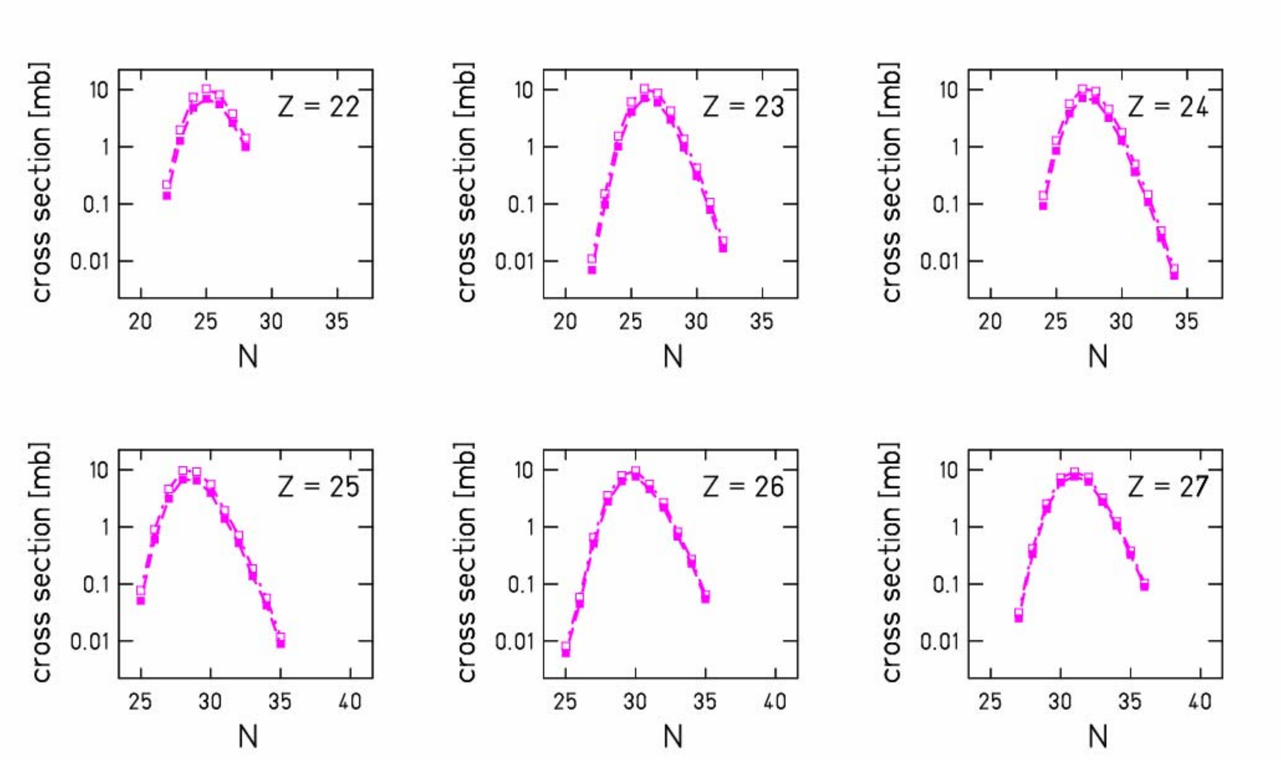

4.4. Mass and charge distributions

The mass and nuclear-charge distributions determined from the production cross sections measured in both Xe experiments, corrected for secondary reactions and the FRS transmission are presented in Fig. 4.6. Please note a slight depletion observed in the mass distribution in the mass range *A*~40, which is presumably a consequence of the fact that the isotopes of the element *Z*=19 were reconstructed from the heavy-fragment settings and may still suffer from the cut due to the limited FRS dimensions, since these isotopes passed FRS rather close to its borders. Similarly a slightly lower value of the total elemental cross section of this element may be observed in the charge distribution. Overall, rather similar trends in case of both projectiles may be observed, characterized by steeply decreasing cross sections of the heavy residues with decreasing mass (charge), followed by a plateau of rather constant cross sections below *A*~65 (*Z*~30) and an exponential increase of the cross sections of the light fragments. In the earlier investigations of the mass and nuclear-charge distributions, the evolution of the shape of the charge (mass) distributions was observed from two distinct regions corresponding to large residues close to the projectile (or target) and to light fragments produced in evaporation, towards the typical U-shape charge (mass) distributions. The former case is typical for the sequential evaporation from moderately excited nuclear source, while the latter one is observed in case of collisions where considerably higher excitation energies were introduced, leading eventually to the break-up of the highly excited nuclear source. Exploring the mass (charge) distributions measured in our experiments it may be observed, that the cross sections of residues in the plateau regions are only approximately a factor of 2-3 lower than the cross sections of the lightest fragments observed. This moderate change of the cross section as a function of mass (charge) is more similar to trends of the mass (charge) distributions measured in reactions with considerably high excitation energies introduced in the collision, which may proceed through the break-up stage. The signatures of the nuclear break-up process in case of our reactions will be investigated in more detail in chapter 6.

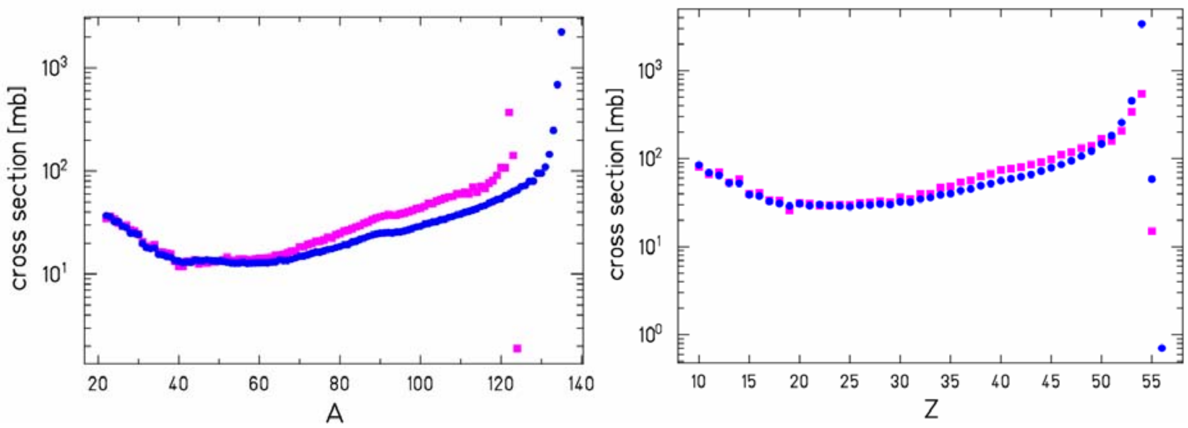

Fig. 4.6: Mass (left) and nuclear-charge (right) distributions measured in the ^{136}Xe+Pb (blue points) and ^{124}Xe+Pb (pink squares) experiments.

Let us now discuss the features observed in the mass and charge distributions in more detail. A steep decrease of the production cross sections in the vicinity of the projectile in case of both systems is observed in the mass as well as in the nuclear-charge distributions. This may be understood as a consequence of the diffuseness of the nuclear-matter distributions. Since the density of the matter in the nucleus does not correspond to a sharp-cutoff distribution, rather it has a diffuse tail, only this diffuse tail will be accessed in the very peripheral collisions. As a consequence, for a rather broad range of the large impact parameters only a few nucleons will be removed in the initial collision. On the contrary, in the less peripheral collisions, where the greater part of the matter of the two nuclei will overlap, the small change of the impact parameter will result in the removal of different number of nucleons and production of prefragments of different masses. Therefore, high production cross sections of nuclei in the direct vicinity of the projectile may be expected, followed by a rapid decrease with decreasing mass (charge).

The shift between the two mass distributions observed in the vicinity of the projectile is related to the different sizes of the two studied systems. This shift gradually decreases with decreasing mass of the final residues until the lightest residues appear to be rather insensitive to the size of the original system. The difference between the two mass distributions may be viewed more closely by exploring the ratio of the total isobaric cross sections of residues from ^{124}Xe versus ^{136}Xe projectiles, shown in Fig. 4.7 left. Also in this figure the staggering of the ratio in the region of A~40 is a consequence of the slightly lower evaluated cross-section values of isotopes of element Z=19. From this figure a rather monotonous decrease of the ratio in the full mass range may be observed. Close to the projectile, the total isobaric cross sections for ^{124}Xe are considerably higher than in case of ^{136}Xe, since lower mass loss is needed to produce the final fragments of a given mass from the ^{124}Xe projectile. This trend decreases with decreasing mass of the final residues, until the ratio of the total isobaric cross sections from the two systems approaches 1 in the region of masses below A~40. Within the estimated experimental errors within this mass range (see section 3.4 and table A.1) the total isobaric cross sections appear to be rather independent of the size of the initial system. This observation indicates that the sensitivity to the small initial mass difference gets gradually lost with the larger mass removals in the abrasion process.

Additional information may be gained by exploring the nuclear-charge distributions, where the dependence on the initial size of the system is removed; nevertheless the comparison of the elemental production cross sections between the two projectiles reflects the importance of the relative neutron and proton emission during the deexcitation process. Overall, the trends observed in the charge distributions measured in the two experiments closely resemble the features already discussed while investigating the shapes of the isotopic distributions, but here the interplay between the widths and maxima of the isotopic distributions may be viewed simultaneously. To explore the trends of the nuclear-charge distributions measured in the two experiments in more detail, the ratio of the elemental cross sections is investigated in Fig. 4.7 right.

The value of the ratio in the vicinity of the projectile remains below 1 and rather steeply increases with decreasing nuclear charge. Please note, that the significantly low value of the ratio in case of Z=54 is partially a consequence of the presence of the slits in the beam line, as discussed in section 4.2, which affected the strong one-neutron removal channel in case of ^{124}Xe projectile. The values below 1 in this nuclear-charge range may be related to the different neutron excess of the two projectiles and thus different evaporation paths as discussed already in section 4.2. Indeed, the dominant neutron emission from primary fragments formed from the ^{136}Xe projectile results in broad isotopic distributions and thus high elemental cross sections, while the competition between the neutron and proton emission in case of the less neutron-rich projectile produces rather narrow isotopic distributions with correspondingly lower elemental cross sections. As may be seen by comparing the full isotopic distributions in this nuclear-charge range, the width of the isotopic distributions from ^{136}Xe projectile is sufficient to compensate the higher maximum of the isotopic cross sections seen in case of ^{124}Xe. The values of the ratio of the elemental cross sections increase and exceed 1 around Z~50, which is related to the decreasing width of the isotopic distributions from the ^{136}Xe projectile and contribution from the competing neutron and proton evaporation in case of the less n-rich projectile, which tends to depopulate the isotopes of heavy elements in favor of isotopes of lower elements. As a consequence, higher total elemental cross sections in case of the ^{124}Xe projectile may be observed in this nuclear-charge range (below Z~50), with the ratio of the elemental cross sections from the two systems being rather constant in the nuclear-charge range app. $35 \geq Z \geq 50$. Below Z~35 a slight decrease of the ratio may be observed, which approaches 1 for the lightest residues (below Z~25). Therefore it seems that within the experimental uncertainties (see section 3.4 and table A.1), similarly as in case of the mass distribution, the elemental yields in this nuclear charge range appear to be rather independent of the initial system, which is also reflected in a close similarity of the widths and maxima of the isotopic distributions in this charge range. However, the above investigation concerns only the integrals of the isotopic distributions and does not reflect the relative abundances of the single isotopes produced from the two projectiles. Indeed, as mentioned in section 4.2, the higher production of the more n-rich isotopes in case of the more n-rich system was observed together with the overall shift of the mean values of the isotopic distributions in the full range of the nuclear charge. Therefore, the mean values of the isotopic distributions in terms of the mean N-over-Z are in the focus of the investigation in the following chapter.

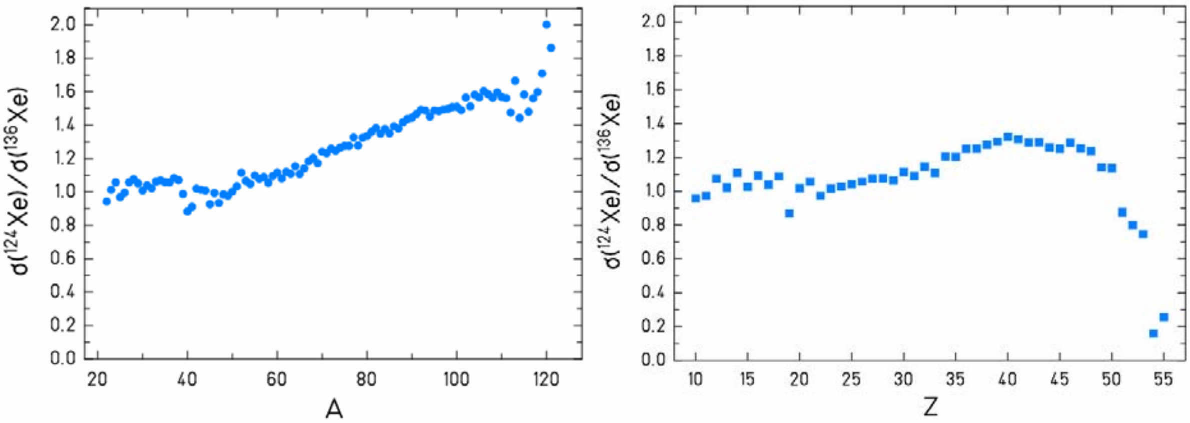

Fig. 4.7: Ratio of total isobaric (left) and elemental (right) cross sections measured in fragmentation of ^{124}Xe versus ^{136}Xe projectiles.

4.5. Mean N-over-Z of the final residues

Already from the comparison of the measured isotopic distributions, the enhanced production of more neutron-rich isotopes in the ^{136}Xe+Pb reaction could be observed together with a shift of the isotopic distributions produced from ^{136}Xe towards more n-rich isotopes above Z~10. This trend suggests a dependence of the final isotopic composition on the N/Z of the projectile and may be studied in more detail if the mean values of the isotopic distributions from both experiments are compared. For this purpose, the mean N-over-Z ratio ($<N>/Z$) is determined from each isotopic distribution, which allows a direct comparison with the N/Z of the two projectiles. Fig. 4.8 shows the $<N>/Z$ of the final residues measured in both experiments as a function of the nuclear charge. Both, the angular-acceptance integrated (transmission-uncorrected) and transmission-corrected isotopic distributions were used to determine the final $<N>/Z$ in order to study the influence of the transmission correction on this observable more closely. For $Z<10$ only the transmission-uncorrected values are shown, since for these elements the transmission correction of section 3.3.3 could not be applied, as explained in section 4.3. It may be seen that the transmission correction has almost no influence on the first moments of the isotopic distributions. Only the lightest residues (below Z~15) are slightly less n-rich on average after applying the transmission correction. This may be understood due to the smaller mass of the less n-rich residues in a given isotopic chain, which are thus produced with slightly broader angular distributions than more n-rich residues, and as a consequence their transmission through the FRS is slightly reduced. After applying the transmission correction, their relative importance in the isotopic distribution increases lowering thus the corresponding $<N>/Z$ ratio.

From Fig. 4.8, the main features of the first moments of the isotopic distributions may be investigated. The data are compared with the stability line [Marm69]. Three different regions may be identified in the data. (i) For the nuclei in the vicinity of the projectile (below Z=54) a rather steep decrease of the $<N>/Z$ is observed with decreasing nuclear charge. (ii) This trend changes around Z~50, where a rather moderate dependence on the nuclear charge establishes. (iii) Finally, the lightest residues (below Z~20 for ^{136}Xe and Z~12 for ^{124}Xe) appear to be even more neutron rich than the stable nuclei and their <*N*>/*Z* strongly staggers. In the following, these trends are discussed in more detail.

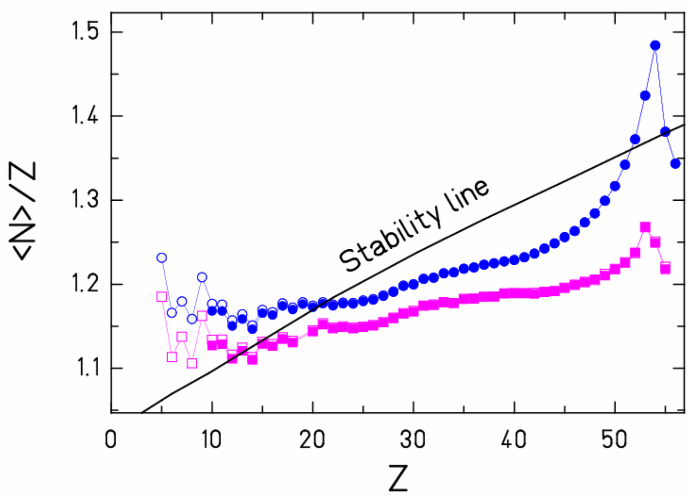

Fig. 4.8: Comparison of the <*N*>/*Z* of final residues determined from the transmission-corrected (full symbols) and transmission-uncorrected (open symbols) isotopic distributions from the reactions ^{136}Xe(*N/Z*=1.52)+Pb (blue points) and ^{124}Xe(*N/Z*=1.30)+Pb (pink squares) at 1 *A* GeV. The full line represents the <*N*>/*Z* of the stable isotopes [Marm69].

(i) A rather steep decrease of the <*N*>/*Z* of the final residues close to the ^{136}Xe projectile may be observed, which appears to be slightly less steep in case of the ^{124}Xe projectile. These observations may be understood as a consequence of very peripheral collisions producing the final residues in the vicinity of the projectile, where rather low excitation energies are introduced. As was already discussed before, in this nuclear-charge range the neutron emission dominates the evaporation process in case of ^{136}Xe primary fragments, since the excitation energies acquired in the collision are too low for protons to overcome the Coulomb barrier. This prevalent neutron emission strongly affects the *N/Z* of the residues, which results in the steep trend observed in the figure. On the contrary, in case of the less n-rich projectile ^{124}Xe the emission of neutrons and protons may compete in the evaporation process already at rather low initial excitation energies, which makes the change of the *N/Z* of residues close to the projectile less steep than in case of ^{136}Xe.

(ii) In the region of *Z* below ~ 50 the transition to a smoother dependence of the <*N*>/*Z* on the nuclear charge may be observed. This is a consequence of higher excitation energies introduced in the collision and thus the competing emission of neutrons, protons and eventually more complex clusters during the evaporation. Once the emission channels of protons and light charged particles become accessible, the *N/Z* ratio of fragments does not decrease so strongly anymore. Nevertheless, as may be seen in the figure, despite the decreasing nuclear charge (increasing excitation energy acquired in the collision), the final residues from the ^{136}Xe projectile remain to be more neutron-rich on average than the residues from ^{124}Xe in the whole nuclear-charge range. This was observed already in the relative shift of the isotopic distributions from the two projectiles in section 4.2. This observation is particularly interesting, since as discussed in [Duf82,Char98], the isotopic composition of the final residues after the long evaporation process is expected to gradually approach the region of equilibrium neutron and proton emission probabilities, known as the evaporation-attractor line (EAL) or the residue corridor. The isotopic composition of the final residues far from the projectile should thus no longer depend on the *N/Z* of the initial system. The extent to which the corridor appears to be 'attractive' to the final residues, however, depends on the neutron or proton excess of the initial system, which may due to the emission of more complex clusters in the evaporation even prevent the final residues from reaching the residue corridor at all [Char98]. At the same time, as mentioned in chapter 1, the highly excited nuclear source may undergo a break-up process, which may affect the isotopic composition as well as the excitation energy of the produced fragments entering the evaporation process and thus the isotopic composition of the final residues. The broad range of isotopes investigated in our experiments allows to explore a broad range of initial excitation energies introduced in the collision for the two projectiles largely differing in their *N/Z*. It is especially interesting to investigate the memory on the initial *N/Z* revealed in the final $<N>/Z$ of our data in order to explore the contribution of different reaction mechanisms (evaporation and nuclear break-up) to the isotopic composition of the final residues and to study the sensitivity of the measured $<N>/Z$ to the conditions at the beginning of the evaporation process. These investigations are introduced in chapter 6.

(iii) Finally let us discuss the $<N>/Z$ of the lightest residues (below Z~20 for ^{136}Xe and Z~12 for ^{124}Xe). Although these residues may be expected to be predominantly produced in the most violent collisions, where considerably high excitation energies are introduced [Schü96], they appear to be clearly more neutron-rich than the isotopes on the stability line. This may suggest that the excitation energy acquired in the collision is exhausted before the most stable configuration is reached, which might be a signature of break-up of a highly excited nuclear source reducing partially the excitation energy available for the evaporation process. On the other hand, also the emission of rather cold more n-rich clusters during evaporation from the excited nuclei with initial neutron excess may contribute to the enhanced production of light n-rich residues. This observation may serve as an additional motivation for closer investigation of the influence of these two processes on the final isotopic composition.

The staggering of the $<N>/Z$ values observed in the nuclear-charge range below Z~15 may be explained by exploring the full isotopic distributions introduced in section 4.2. The region of nuclear charge below Z~15 coincides with the charge range, where the even-odd effect is particularly pronounced in the isotopic distributions. The even-odd effect results from the pairing interaction between the nucleons of the same type, which increases the binding energy of the nuclei with even number of neutrons and/or protons. As a consequence, the even-even and even-odd nuclei are more stable than odd-odd nuclei and thus are more often produced. It is especially the enhancement of the production of the even-even stable isotopes (mostly $N=Z$) for even nuclear charge, which is responsible for the shift of the mean values of the even-*Z* isotopic distributions towards the less neutron-rich isotopes. This shift is reflected in the lower values of the $<N>/Z$ of the final residues with even nuclear charge.

Chapter 5

Comparison of the experimental data with the EPAX parameterization

It is one of the main interests of the present research to extend the experimental investigations towards the rarely produced isotopes with extreme isospin in order to investigate their structure properties or to study the dependence of the nuclear equation of state on the isotopic composition of the system. To produce these exotic nuclei experimentally a reliable description of the production cross sections is necessary in order to predict the expected production rates. It is especially useful for such a purpose to formulate the description of the production cross sections analytically rather than using time consuming Monte-Carlo based calculations. For this purpose, analytical descriptions for the production cross sections were developed [Rud66,Silb73,Süm00] of which the most recent and most often used one is the EPAX parameterization developed in [Süm00].

Presently, there are several projects around the world for building of new experimental facilities for the production of exotic beams [EURISOL, RIA, FAIR (SUPER-FRS), RIBF]. Especially in case of the EURISOL project a special interest comprises the production cross sections of neutron-rich isotopes in the nuclear charge range $40 \leq Z \leq 46$, which cannot be extracted directly from the ISOL source [Rav87], but are considered to be produced by the fragmentation of the secondary neutron-rich beam [Hel03]. A reliable prediction of the production cross sections in this region of isotopes is thus especially needed. The isotopically resolved residues measured within this thesis over the broad range of the nuclear charge in the two experiments with extremely N/Z-different Xe projectiles form an extremely useful data base for testing the predictive power of the cross-section parameterizations especially from the point of view of the isospin dependence. In the following, a comparison of the isotopic distributions and the mean N-over-Z ratios from these two experiments with the predictions of the EPAX parameterization is presented.

5.1. Empirical parameterization of the fragmentation cross sections EPAX

EPAX is an empirical parameterization of the fragmentation cross sections based on experimental data. The original EPAX [Süm90] is based on the previous parameterizations

[Rud66,Silb73], and it was derived using the proton-induced spallation cross sections measured in the GeV energy range. Later, when more experimental data from relativistic heavy-ion induced fragmentation reactions became available, the parameterization was refined to include new features not observed in the proton induced reactions [Süm00]. EPAX was developed predominantly based on the production cross sections measured in the first experiments with the Fragment Separator at GSI, where several projectiles were investigated with different isotopic composition, and the production cross sections of residues not too far from the projectile were measured.

The EPAX parameterization is valid only in the limiting-fragmentation regime, where the fragmentation yields do no longer depend on the projectile energy. This regime corresponds to energies well above the Fermi energy (~40 *A* MeV), where the assumption of the limiting fragmentation is valid, and is thus well satisfied in the relativistic energy regime investigated in our experiments. The EPAX parameterization is developed based on the fragmentation reactions of medium- to heavy-mass projectiles. The description of fission reactions or of the multifragment break-up is not included. According to EPAX, the final residues in the vicinity of the projectile keep a memory on its isotopic composition, i.e. the isotopic distributions of fragments produced in the fragmentation of a more neutron- (proton-) rich projectile are shifted towards more n- (p-) rich isotopes. This memory is considered to gradually decrease as the fragments more far away from the projectile are produced. This description corresponds to the idea of the residue corridor also known as the evaporation attractor line (EAL) [Char98], according to which the isotopic composition of the final residues after the long sequential evaporation gradually approaches the region of equilibrium probabilities of proton and neutron emission.

EPAX is based on the an analytical function, which is used to parameterize the isotopic distributions and the parameters of which depend smoothly on the fragment mass:

$$\sigma(A,Z) = Y_A \sigma(Z_{\max} - Z) = Y_A n \exp(-R|Z_{\max} - Z|^{U_{n(p)}}) \tag{5.1}$$

where Y_A represents the mass yield (sum of the isobaric cross sections) and the term $\sigma(Z_{\max} - Z)$ describes the charge dispersion around $Z_{\max}$. The parameters *R* and $U_{n(p)}$ determine the shape of the charge dispersion, where *R* controls the width and $U_{n(p)}$ account for different slopes of the isobaric distributions on the neutron- (proton-) rich side of the valley of stability, respectively, n represents the normalization factor. The mass yield is considered to depend exponentially on the difference between the projectile (A_p) and the fragment (*A*) masses:

$$Y_A = SP \exp[-P(A_p - A)] \tag{5.2}$$

with two parameters *P* and *S* depending on the projectile mass and the circumference of the interacting nuclei, respectively. In order to obtain a better agreement with the experimental data in the vicinity to the projectile, the mass yield is additionally corrected if $A/A_p \geq a_2$:

$$Y_A = Y_A[1 + a_1(A/A_p - a_2)^2] \tag{5.3}$$

with the constants a_1=200 and a_2=0.90 [Süm00].

The parameter *R*, describing the width of the charge dispersion is assumed to depend on the mass of the fragment only for fragments far from the projectile. In the vicinity of the projectile the width of the charge dispersion is additionally reduced to obtain a close agreement with the experimental data. Apart of U_n, which is assumed to be constant, the parameter U_p is considered to depend on fragment mass.

The maximum of the charge dispersion is assumed to be shifted from the valley of stability by a parameter Δ towards a neutron deficient side. The parameter Δ depends solely on the fragment mass, and is gradually reduced to zero for fragments in the vicinity of the projectile located on the stability line. In case of projectiles outside the stability line, the final residues not too far from the projectile are considered to keep a memory on the initial isotopic composition through a parameter Δ_m, so that the maximum of the charge dispersion is shifted by $\Delta+\Delta_m$ with respect to the stability line:

$$Z_{\max} = Z_{\beta} + \Delta + \Delta_m \qquad (5.4)$$

The parameter Δ_m is considered to be proportional to the difference of projectile charge and the charge of the stable isotope with the same mass $(Z_p - Z_{\beta p})$. The memory parameter Δ_m gradually approaches zero with increasing mass loss.

5.2. Comparison of EPAX with the isotopic distributions

To obtain a complete overview on the predictive power of EPAX the predicted isotopic distributions are compared with the measured ones in the full nuclear-charge range investigated in the two Xe experiments (Z=10-54). The corresponding comparison is presented in Fig. B.1 and B.2 of Appendix B, for the ^{124}Xe+Pb and ^{136}Xe+Pb experiments, respectively. It may be observed that the production cross sections of the lighter elements are strongly underestimated by EPAX in case of both experiments and this trend is preserved in a reduced form also in case of heavy residues. In case of the less neutron-rich projectile ^{124}Xe a slight shift of the isotopic distributions predicted by EPAX towards less neutron-rich isotopes may be seen (below Z~36). Nevertheless, in case of this projectile the width and the mean values of the isotopic distributions seem to be rather well reproduced for heavy elements. The isotopic distributions predicted for the more neutron-rich projectile appear to be shifted towards the less neutron-rich isotopes in the nuclear-charge range below Z~35 and the production cross sections on the neutron-deficient side of the isotopic distributions for elements above Z~43 appear to be slightly underestimated by the EPAX. The more detailed investigation of the EPAX prediction of the mean isotopic composition of the final residues is presented in the next section in terms of the mean N-over-Z ratio.

Generally relatively worse agreement of the experimental isotopic distributions with the EPAX prediction may be observed in case of ^{136}Xe projectile especially for the residues in the vicinity of the projectile. This may be understood by exploring the data base used to establish the EPAX parameterization. For this purpose the data measured in the fragmentation of ^{124}Xe, ^{129}Xe and ^{136}Xe projectiles at energies ranging from 0.8 – 1.1 *A* GeV were used [Schn96,Rei98,Fri92]. Fig. 5.1 shows the Sn isotopes measured in these experiments, which were available for the parameterization of the production cross sections. According to [Fri92], in the ^{136}Xe fragmentation experiment only the cross sections of neutron-rich isotopes of ^{136}I, ^{135}Te, ^{134}Te, ^{132}Sb, ^{133}Sb, ^{129}Sn, ^{130}Sn, ^{127}In, ^{124}Cd, ^{122}Ag, ^{119}Pd, ^{116}Rh were measured. While in case of the less neutron-rich xenon projectiles a broader range of heavy isotopes in the nuclear charge range *Z*~40-55 was available to establish the EPAX parameterization, the experimental data in case of the ^{136}Xe projectile are much scarcer and concentrated only on the neutron-rich side of the isotopic distribution. This absence of the experimental data on the isotopic production cross sections from the more neutron-rich Xe projectile may explain the failure of the EPAX prediction on the neutron-deficient side of the isotopic distributions.

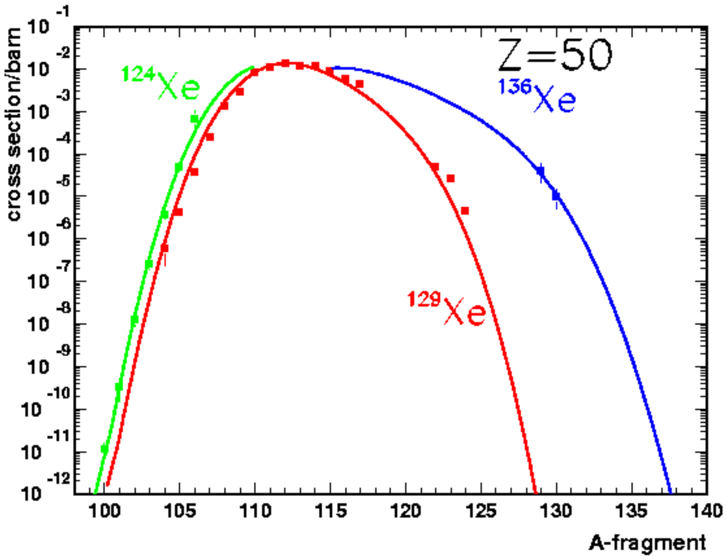

Fig. 5.1: The experimental data of tin isotopes from fragmentation of ^{124}Xe, ^{129}Xe and ^{136}Xe projectiles at 0.8 to 1.1 *A* GeV (Refs.[Schn96,Rei98,Fri92]), which were used to establish the EPAX parameterization.

As may be found in [Süm00] only isotopes in the vicinity of the projectile were available for the formulation of the EPAX parameterization. This is the case also for the production cross sections of the lighter residues used to establish the EPAX parameterization, since these were measured in the reactions of nuclei of lower masses, e.g. ^{40}Ar, ^{43}Ar, ^{86}Kr, ^{48}Ca, ^{58}Ni, ^{24}Mg, ^{28}Mg [Webb90,Shu99,Web94, Wes79, Bla94, Webb90,Shu99]. The residues in the vicinity of the projectile are generally produced in rather peripheral collisions where low to moderate excitation energies are introduced. On the contrary, the lighter residues far away from the projectile, which were also measured in our experiments, are predominantly produced in the more violent collisions, where considerably higher excitation energies may be expected. As already discussed, under the influence of the high excitation energies the nucleus may not survive in one piece rather it may break-up into fragments of various sizes. This process was observed to contribute to an enhanced production of the intermediate-mass fragments (IMF, $3 \leq Z \leq 20$) [Schü96]. This might provide an explanation of the significant underestimation of the production cross sections predicted by EPAX in this nuclear-charge range, observed for both projectiles. A closer investigation of the influence of the nuclear break-up on the isotopic composition of the final residues measured in our experiments is presented in chapter 6.

5.3. Comparison of EPAX with the mean N-over-Z

According to previous section, in a certain range of the nuclear charge the EPAX parameterization does not correctly reproduce the mean values of the isotopic distributions. This observation is investigated in more detail in this chapter, using the mean N-over-Z ($<N>/Z$) ratio determined from every isotopic distribution as a function of nuclear charge. In Fig. 5.2 the mean N-over-Z ratio determined from the first moments of the measured isotopic distributions is compared with the prediction of the EPAX parameterization.

As observed already by comparing the full isotopic distributions, a generally worse overall agreement between the experimental data and EPAX may be observed in case of the more neutron-rich projectile. While the average isotopic composition of the heavy residues (above $Z\sim40$) from the ^{124}Xe projectile is rather well reproduced, the $<N>/Z$ in case of the ^{136}Xe projectile is considerably overestimated in this nuclear-charge range. This observation may be understood as a consequence of underestimated production cross sections of the neutron-deficient residues in the isotopic distributions in this nuclear-charge range discussed in the previous section.

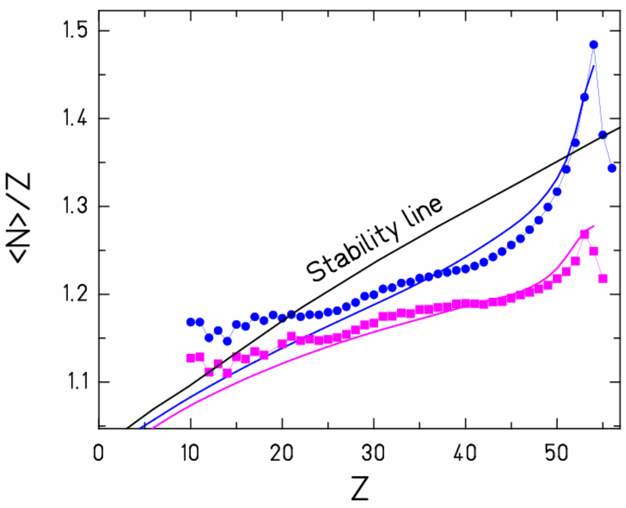

Fig. 5.2: Comparison of the $<N>/Z$ measured in reactions ^{136}Xe+Pb (blue points) and ^{124}Xe+Pb (pink squares) with the prediction of the EPAX parameterization for both systems (blue and pink lines).

As mentioned in section 5.1, the final residues in the vicinity of the projectile, which is not located on the stability line, keep a memory on the initial isotopic composition introduced through the parameter Δ_m. This memory is assumed to be gradually removed for residues more far away from the projectile. This may be clearly seen in Fig. 5.2 in the decrease of the difference between the $<N>/Z$ of the final residues from the two projectiles, predicted by EPAX, with decreasing nuclear charge. This strong reduction of the memory on the initial N/Z is nevertheless not observed in the $<N>/Z$ of the experimental data, which preserve almost a constant difference over the broad nuclear-charge range. At the time the EPAX parameterization was formulated, no experimental data were available in such a broad nuclear-charge range as is the case in our experiments. The data used for the EPAX parameterization originate mostly from the specific production cross sections measurements (such as investigations of the production of ^{100}Sn or study of proton-removal channels), where the interest was focused only on the limited range of isotopes and no systematic investigations beyond this region were performed. At the same time, to obtain high production rates the experiments mostly concentrated on the isotopes in the vicinity of the projectile. From this point of view the present data are a unique source of complete experimental information concerning the isotopic composition of the final residues.

As argued in the previous section, the residues far away from the projectile are predominantly produced in more violent collisions introducing high excitation energies. The less strong loss of memory on the initial isotopic composition in case of the experimental data then predicted by EPAX suggests that despite the high excitation energy is acquired in the collision it is more efficiently consumed in the evaporation process than predicted by EPAX. The reduction of the memory in the EPAX basically corresponds to an assumption of a kind of a 'residue corridor', the location of which is defined by the parameter Δ (see section 5.1) and which depends solely on the mass of the source. The idea of the residue corridor was introduced in [Char98] and physically it corresponds to a region, where the final isotopic distributions for larger mass loss are largely universal. However, as discussed in [Char98], the residue corridor appears to be 'attractive' only in the last steps of the evaporation process. In case the high excitation energies are acquired in the collision, the emission of more complex clusters may become a rather common process, which is not the case for residues in the vicinity of the projectile used to establish the EPAX parameterization. By emitting more complex clusters the nucleus may decrease its excitation energy, while preserving to a large extent its *N/Z* ratio. Finally as the nucleus cools down and the neutron emission starts to play a significant role, there may not be enough evaporation steps for the nucleus to be 'attracted' by the residue corridor. This process may result in an enhanced memory on the initial *N/Z* compared to EPAX and may lead to the production of more neutron-rich final residues as observed in the experimental data.

At the same time, as mentioned also in the previous section, under the influence of the high excitation energies the nucleus may undergo a break-up process. It may be expected that during this process some portion of the excitation energy will be consumed for the formation of fragments, which may thus reduce the excitation energy available for the evaporation process. As well, as mentioned in chapter 1, the process of isospin fractionation should affect the isotopic composition of the fragments produced in break-up. Both of these effects may influence the final isotopic composition and may favor the production of more n-rich residues far away from the projectile than predicted by EPAX.

Although from this comparison with EPAX it is not clear, which process has dominating influence on the final isotopic composition observed in our experiments, it is obvious that the isotopic composition of the final residues not too close to the projectile cannot be explained by the parameterization as suggested by EPAX. It is predominantly the unavailability of the experimental data in the broad nuclear-charge and isospin range, which is responsible for deficiencies of the EPAX parameterization in predicting the production cross sections in the extremes of the isotopic distributions and far away from the projectile. Nevertheless, the presented comparison with the new experimental data clearly suggests that the EPAX parameterization should be considered with caution and may not be well suited for the predictions of the production cross sections of very exotic isotopes. The data from the presented experiments will certainly allow to formulate an improved empirical parameterization for projectiles around mass 100, in particular for lighter fragments.

Chapter 6

Mean N-over-Z of the final residues

In chapter 4 the overall features of the isotopic distributions from ^{136}Xe+Pb and ^{124}Xe+Pb reactions were discussed and it was observed that the final residues preserve the memory on the N/Z ratio of the initial system over the broad nuclear-charge range. The comparison with EPAX in the previous chapter showed that the final residues not too close to the projectile, which are predominantly produced in the more violent collisions, remain to be more n-rich than the EPAX prediction, which suggests that the available excitation energy is consumed before the residues appear to be attracted by the residue corridor. These observations were interpreted as a possible contribution of the emission of more complex clusters during the evaporation process or of the nuclear break-up of the highly excited nucleus formed in the collision. In the following sections, the sensitivity of the $\langle N\rangle/Z$ of the final residues to these two processes will be investigated in detail with the use of the ABRABLA code, introduced in section 6.1. Special emphasis is put on the exploration of the sensitivity of the final isotopic composition to the length and modeling of the evaporation process. The information gained by this investigation is used for back tracking of the thermal properties of an excited nuclear source.

6.1. ABRABLA code

To investigate the final isotopic composition over the broad range of nuclear charge, the ABRABLA code [Gaim91] is used. ABRABLA is an abrasion-ablation code developed for the modelling of the fragmentation process in the relativistic-energy regime. It is based on the geometrical abrasion and Weisskopf evaporation models. To account for the possible break-up of a highly excited nuclear source, an intermediate break-up stage was optionally implemented. In the following, the treatment of the different stages of the reaction process as implemented in ABRABLA is described.

6.1.1. Abrasion

Geometrical abrasion is a description generally used in the high (relativistic) energy domain for the modelling of the first, fast stage of the collision process. The abrasion picture is based on the clean cut of the target nucleons by the interacting projectile (and vice versa). Because in the relativistic energy regime, the relative velocity of the interacting nuclei exceeds the Fermi velocity of the constituent nucleons, the nucleon-nucleon interactions occur only within the overlapping zone of the interacting projectile and target. The rest of the projectile and target (spectators) remain almost unaffected by the collision and continue to move with nearly the same velocities as before the collision. The number of nucleons, which are removed during the abrasion, depends only on the collision impact parameter. It is clear that this picture is valid only in case of peripheral to mid-peripheral collisions. From the number and 'type' of nucleons removed the excitation energy and the isotopic composition of the primary fragment may be determined. These are the important points, since both the excitation energy as well as the *N/Z* ratio of the primary fragment must be determined as realistically as possible to be able to obtain a correct 'initial condition' for the following stage (evaporation or break-up) and a realistic description of the final isotopic composition.

The amount of excitation energy introduced in the abrasion stage is determined according to the statistical hole-energy model [Gaim91]. Within this approach the excitation energy is determined as the sum of the energies of holes created due to the removal of nucleons from various single-particle levels during the abrasion. Using the Wood-Saxon potential (E_p=-47.4 MeV) and assuming that the probability for creating a hole is the same for all the single-particle levels, the average excitation energy of 13.3 MeV per hole (i.e. per abraded nucleon) was deduced. Additional investigation [Schm93] nevertheless showed that this value is not sufficient to reproduce the isotopic distributions of the final residues produced in the fragmentation of gold. Only the increase of this value by a factor of 2 allowed to reproduce the experimental data for this energy and size of the projectile. The relevance of this increase for fragmentation of heavy projectiles at relativistic energies was subsequently verified with ^{208}Pb and ^{238}U beams. This additional increase of excitation energy may be understood as a consequence of the interactions of nucleons back scattered to the projectile (or target) from the overlapping zone of the two interacting nuclei. The excitation energy introduced in the abrasion stage is thus determined as $\Delta A \cdot 27$ MeV, where ΔA represents the mass lost in the abrasion stage.

The formulation of the abrasion process as a clean cut of nucleons in the overlapping region of projectile and target nuclei determines only the number of nucleons abraded, but does not specify the isotopic composition of the produced primary fragment. The ratio of abraded neutrons and protons may be determined based on several different considerations, depending on the extent to which the correlations between the removed neutrons and protons are considered. The first extreme corresponds to the situation, when full correlation between the removal of neutrons and protons is assumed, which means that the primary fragment keeps exactly the same *N/Z* as the projectile nucleus. The opposite extreme may be obtained if no correlation between the removal of neutrons and protons is assumed at all and every nucleon may be with a certain probability a neutron or a proton. This probability is determined by the *N/Z* of the projectile nucleus. This approach results in the broadest charge distributions and is represented by a hypergeometrical distribution. The latter approach was observed to result in a better agreement with the experimental data [Gaim91] and is used in the ABRABLA code.

6.1.2. Break-up

To investigate the influence of the break-up process on the isotopic composition of the final residues, a break-up process was included in the ABRABLA code. Since with the Fragment Separator peripheral to mid-peripheral collisions are predominantly investigated, where the largest residue survives the reaction process, the main concern of this implementation was to follow the influence of the break-up process on the mass and excitation-energy loss of the largest fragment formed in the reaction.

In ABRABLA there are two possibilities for the reaction to proceed depending on the excitation energy introduced in the abrasion stage: break-up or a direct evaporation. To determine whether the process of break-up occurs, the temperature of the primary fragment corresponding to the excitation energy that it acquired in the abrasion stage is compared with the temperature corresponding to the freeze-out of the break-up process, where the excitation energy and temperature are related as follows:

$$E^{*}(T) = aT^{2} \tag{6.1}$$

with *a* being the level density parameter, calculated according to description of [Ign75].

The freeze-out corresponds to the situation, when the fragments formed in the nuclear break-up do not interact anymore via the nuclear interactions. System of fragments and nucleons at freeze-out is often assumed to be in a thermal equilibrium characterized by a temperature $T_{freeze-out}$ [Bon95]. This assumption is adopted in the ABRABLA so that in case the temperature of the primary fragment exceeds the value of the freeze-out temperature ($T_{init} > T_{freeze-out}$) a break-up process occurs. In the opposite case the direct evaporation follows. In case the primary fragment undergoes a break-up, its mass and excitation energy are reduced to correspond to the conditions at the freeze-out of the break-up process. Based on equation (6.1) the excitation energy corresponding to the freeze-out temperature $E^{*}(T_{freeze-out})$ is calculated. The initial excitation energy is then reduced in form of mass loss under the assumption that 10 MeV of energy is carried away by removed nucleon:

$$\Delta A = (E^{*}_{init.} - E^{*}(T_{freeze-out}))/10 \tag{6.2}$$

The value of 10 MeV was deduced form a comparison with the experimental mass distributions in ^{238}U+Ti. This way the fragment of mass $A_{init} - \Delta A$ is created. Its excitation energy at freeze-out is again determined from equation (6.1), using the new value of mass in the level density parameter. The produced fragment enters the evaporation process, detailed in the following section. Only the largest fragment is followed, since the fragments carrying the removed mass ΔA are not specified explicitly.

A critical point in this description is the determination of the isotopic composition of the produced fragment of mass $A_{init} - \Delta A$. According to the statistical treatment of the nuclear break-up [Bot01], a rather moderate change of *N*/*Z* of heavy fragments during the break-up process is predicted. Therefore, in ABRABLA an approximation is adopted that the *N*/*Z* of the produced fragment is on average that of the primary fragment entering the break-up. This assumption is rather simplifying, since as mentioned in chapter 1, according to some descriptions of the nuclear break-up (e.g. [Müll95, Bar02]), the process of isospin fractionation should result in the different isotopic compositions in case of heavy and light fragments (i.e. liquid and gas phase). In the isospin fractionation process the neutrons are driven away from the dense (liquid) regions towards more dilute regions (gas) with lower chemical potential [Bar02]. As a consequence the heavy fragments after the break-up may appear to be slightly less neutron-rich than the original system (and vice versa for the light fragments).

Nevertheless, despite this simplifying assumption, it may be expected that the evaporation process will still keep the dominant influence on the evolution of the *N/Z* of the largest fragment produced in the break-up and thus the uncertainty introduced by assuming the conservation of the *N/Z* in the break-up process should not be too high and should not significantly affect the qualitative results.

6.1.3. Evaporation

While neglecting the isospin fractionation process will likely introduce only a small uncertainty, the description of the evaporation process must be carefully investigated to assure that it is as realistic as possible in order to obtain a relevant prediction of the final isotopic composition. The original version of the evaporation model implemented in the ABRABLA includes the emission of neutrons, protons and alpha particles only and was described in [Gaim91, Jun98]. To investigate the influence of the emission of the more complex clusters on the isotopic composition of the final residues, the evaporation model in ABRABLA was extended to consider also the emission of ^{2}H, ^{3}H, ^{3}He and isotopes with Z>2. The following sections summarize the main ideas behind the original model as well as the new developments.

Original model

The description of the evaporation process in the ABRABLA is based on the Weisskopf statistical model [Wei37]. According to this model the particle emission from a highly excited nucleus may be considered to be independent on the first stage of the reaction process, since the information on the initial conditions is lost due to the large density of nuclear levels at high excitation energies and thus large number of different decay channels contributing to the formation of a given final nucleus. The emission of particles is then determined by the phase space available for a given emission channel, i.e. by the corresponding level densities and by the corresponding transmission coefficients. The emission probability W_ν of particle ν from the nucleus having the excitation energy E_i may be determined as follows:

$$W_\nu(E_i) = \frac{\Gamma_\nu(E_i)}{\sum_k \Gamma_k(E_i)} \tag{6.3}$$

where Γ is the emission width of particle ν and the sum in the denominator runs over all the possible decay channels. The emission width is related to the level density in the mother and daughter nuclei and to the corresponding transmission coefficient. Utilizing the principle of detailed balance, the transmission coefficients for particle emission may be replaced by the transmission coefficients of the inverse process, the particle capture, and the emission width may thus be expressed through the capture cross section:

$$\Gamma_\nu(E_i) = \frac{2\cdot s_\nu + 1}{2\cdot \pi \cdot \rho(E_i)} \cdot \frac{2\cdot m_\nu}{\pi \cdot \hbar^2} \cdot \int_0^{E_i - S_\nu} \sigma_c(\varepsilon_\nu)\cdot \rho(E_f)\cdot(\varepsilon_\nu - B_\nu)\mathrm{d}E_f \tag{6.4}$$

where the integration over all possible final excitation energies is performed. In this expression $\varepsilon_\nu = E_i - S_\nu - E_f$ is the kinetic energy of the evaporated particle, S_ν is its binding energy and E_f

is the energy of the final nucleus; $\rho(E_i)$, $\rho(E_f)$ are the level densities of the initial and final nuclei, respectively; m_ν is the particle mass and B_ν the barrier for particle emission. The determination of the barrier for the emission of charged particles is based on the assumption that the emission barrier equals to the fusion barrier and is calculated using the fusion nuclear potential of Bass [Bas79, Jon98] and the Coulomb potential of [Jon98]. To obtain the agreement with the abundant p and α emission observed experimentally, the barriers for p and α are reduced by increasing the nuclear radius constant entering the Bass potential according to [Kil95].

It should be noted that in the original version of the evaporation model as described in [Gaim91, Jun98] a geometrical parameterization of the capture cross section was considered. In the present version of the code, the capture cross section includes the wave nature of the emitted (or captured) particles as well as the influence of the Coulomb barrier, which may decrease the capture cross section at low particle energies ε_ν:

$$\sigma_c(\varepsilon_\nu) = \pi \cdot R^2 \cdot \left(1 - \frac{B_\nu}{\varepsilon_\nu}\right), \quad R = R_{geom} + R_\lambda \tag{6.5}$$

where

$$R_{geom} = 1.16 \cdot \left(A_f^{1/3} + A_\nu^{1/3}\right), \quad \text{and} \quad R_\lambda = \sqrt{\frac{\hbar^2}{2 \cdot \mu \cdot E_{cm}}} \tag{6.6}$$

where μ is the reduced mass ($\mu = M_f M_\nu/(M_f+M_\nu)$), $E_{cm} = \varepsilon_\nu(A_f - A_\nu)/A_f$ and R_λ is the deBroglie wave length; M_f, M_ν and A_f, A_ν represent the masses and mass numbers of the daughter nucleus and the emitted particle, respectively. The increase of the capture cross section due to the tunnelling through the potential barrier B_ν is considered as well according to the description introduced in [Avi78].

Finally the particle to be emitted is selected via a random sampling of the emission probabilities W_ν corresponding to all the deexcitation channels and the corresponding change of mass, excitation energy and neutron excess is determined in each evaporation step. The evaporation is followed until the excitation energy decreases below the lowest particle emission threshold. For the excitation energies close to the particle threshold the deexcitation through γ emission is considered as a competition. The γ deexcitation is described using the formula for the γ decay width introduced in [Ign00].

Implementation of light clusters and intermediate-mass fragments (IMF) emission

The crucial quantity in the investigation of the influence of the evaporation process on the isotopic composition of the final fragments is the change of the N/Z in each evaporation step. This change is directly determined by the neutron and proton number of the particle, which was evaporated. Let us assume that more complex stable clusters contribute to the evaporation process. In such a case it may be expected that the N/Z ratio of the emitting system does not change strongly in one evaporation step and as a consequence the production of final residues with higher N/Z ratio might be expected with the same amount of the excitation energy available. Therefore, it is of particular importance to investigate the influence of the emission of more complex clusters on the course of the evaporation process and on the final isotopic distributions. In the following, the implementation of the emission of light clusters (^{2}H,^{3}H,^{3}He) and the intermediate mass fragments in the nuclear-charge range $Z \geq 3$ in the original evaporation model will be described.

Treatment of the ^{2}H, ^{3}H, ^{3}He and the IMF emission

The emission of hydrogen and ^{3}He isotopes is included in the same way as the emission of n, p and α described in the previous section. Also in case of these clusters the emission probabilities are calculated for each isotope separately from the level densities of the daughter nuclei and the corresponding change of mass, excitation energy and neutron excess are determined in each evaporation step. Since the first excitation levels of these nuclei correspond to rather high energies, these fragments are considered to be produced in their ground states.

The implementation of the IMF emission in the above described evaporation formalism needs a bit more care. In this respect, a special considerations should be made concerning the transition between the very asymmetric fission and evaporation of IMFs. As discussed in [Mor75], the evaporation and fission should be considered as two manifestations of the same type of the binary process and in some codes such as GEMINI [Char88] the evaporation process is described in a similar way as a very asymmetric fission. Nevertheless, in [Ricc05] it was shown that the lighter (IMF) fragments measured in the reaction of ^{238}U+^{1}H at 1 A GeV may be assumed to be formed in an asymmetric binary decay from relatively undeformed nuclei on the contrary to typical fission products of heavier mass, which originate from a gradually increasing deformation of the nucleus. The emission of IMFs is thus in ABRABLA treated as an evaporation process. However, slight differences occur with respect to the description introduced above and used for lighter clusters.

In the first step the emission of different IMFs is not considered individually, rather as one class characterized by the total emission width Γ_{imf}. To calculate the total emission width it is sufficient to calculate explicitly only the contribution of isotopes of the most abundant elements, which makes the calculation considerably faster. The total IMF emission width competes with the emission widths of lighter clusters in the Monte-Carlo code. Only in case the IMF emission should occur, the competition between the different IMFs is considered explicitly. To calculate the barriers for emission of given IMF again the fusion nuclear potential of Bass [Bas79, Jon98] and the Coulomb potential of [Jon98] are used, the same as in case of emission of the lighter clusters.

On the contrary to lighter clusters, IMFs may be emitted in an excited state and thus the level density $\rho(E_f)$ in expression (6.4) includes not only the level density of the daughter nucleus but also the level density of the IMF ($\rho(E_f)= \rho(E_{imf}) \cdot \rho(E_{daughter})$). The evaporation from IMFs is also included explicitly.

6.2. Investigation of the influence of cluster emission and break-up process on the final <N>/Z

As mentioned earlier, the following chapters are dedicated to the extensive investigation of the influence of complex cluster emission in the evaporation process and of the process of nuclear break-up on the final isotopic distributions. In section 6.2.1 the influence of the emission of more complex clusters in the evaporation, introduced in the code as described in section 6.1.3, is investigated. In section 6.2.2 the sensitivity of the first moments of the isotopic distributions to the thermal conditions defining the properties of the nucleus entering the evaporation process after the break-up is studied. Finally, the comparison of the measured isotopic distributions with the calculations with and without the nuclear break-up is presented in appendix C.

6.2.1. Influence of cluster emission

As was discussed in previous chapters, the $<N>/Z$ of the final residues far away from the projectile still preserves the memory on the initial N/Z in contradiction to the idea of the residue corridor, where this memory gets gradually lost. On the other hand, it was proposed in [Char98, Duf82] that the final residues from the very neutron-rich projectile may never reach the residue corridor. In case of primary fragments with high excitation energy the relative energy cost of the emission of nucleons and clusters becomes less important and evaporation of clusters starts to be more common. The emission of clusters results in a considerable loss of mass, while the neutron-to-proton ratio remains rather unaffected. As a consequence, in the first steps of the evaporation process the evaporation preserves a memory on the initial N/Z and may be viewed as proceeding along the constant N/Z in the chart of nuclides. As the fragment cools down during the course of evaporation, the energy cost for the emission of more complex clusters and eventually protons starts to be important again and the dominating neutron evaporation sets in. It is just during these last steps of the evaporation process that the fragment is 'attracted' by the residue corridor. However, the number of these steps is limited before the excitation energy is exhausted, which limits also the approaching to the residue corridor. Therefore, the final residues from primary fragments with large neutron or proton excess may never reach the corridor [Char98].

In this section the influence of the emission of more complex clusters on the final isotopic composition is investigated with the use of the ABRABLA code. Fig. 6.1 shows the comparison of the $<N>/Z$ of the final residues measured in both Xe experiments with the abrasion-evaporation calculation performed with the ABRABLA code. In the left figure the emission of neutrons, protons and alpha particles only was included. In this case the calculated final $<N>/Z$ is considerably reduced and the evaporation results in the loss of memory on the initial N/Z for the lightest residues (below Z~20) in accordance with the idea of the residue corridor. In case only emission of n, p and α is included, the excitation energy at the last steps of the evaporation is still sufficient to emit a considerable number of neutrons, which shifts the final isotopic composition towards the residue corridor.

To investigate the expectation that the competing emission of more complex clusters prevents the final residues from reaching the residue corridor, the emission of more complex clusters was incorporated in ABRABLA as described in section 6.1.3. The results of this calculation are compared with the experimental data in Fig. 6.1 right. Indeed, an important influence on the final isotopic composition may be observed and the final residues after the evaporation process preserve memory on the initial neutron excess over the full nuclear-charge range. In case the emission of clusters is included in the evaporation process, only a reduced number of evaporation steps may be available to approach the residue corridor before the full excitation energy is consumed. This is observed to have a considerable influence on the final isotopic composition of the residues from the more n-rich projectile, which are more neutron rich than in calculation, where only emission of neutrons, protons and α particles was considered, and do not loose the memory on the initial N/Z. On the other hand, the calculation in case of the less n-rich projectile seems to be less affected by the emission of more complex clusters. Apart of the slight decrease of the <*N*>/*Z* in the region close to the projectile, only moderate increase may be observed for the lighter residues if the emission of more complex clusters is considered. This may be understood as a consequence of the lower neutron excess of this projectile, which is located closer to the residue corridor. Thus despite the reduction of the number of steps, where the residue corridor appears to be attractive, the fragments may loose considerable portion of the initial neutron excess even with the cluster emission included.

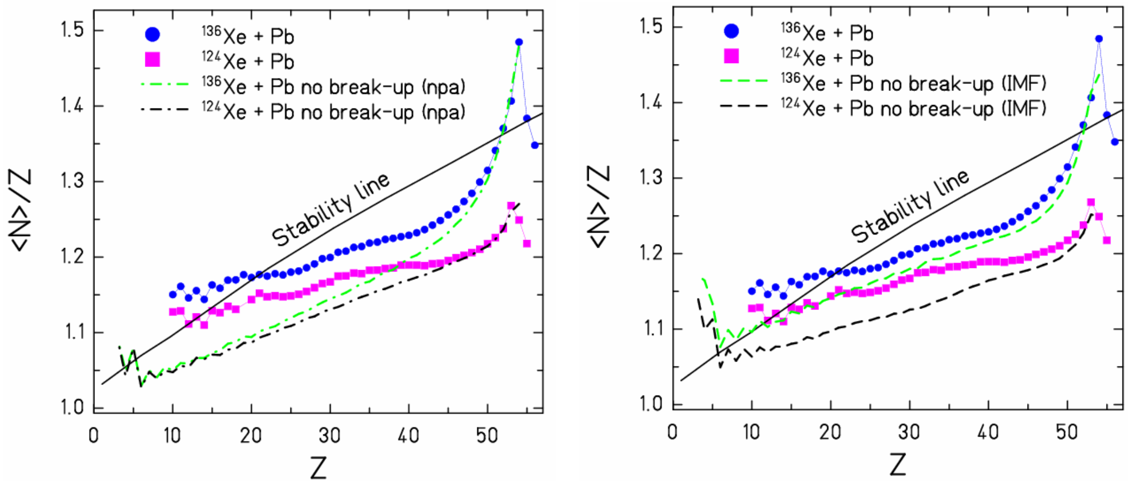

Fig. 6.1: Mean N-over-Z measured in the reactions ^{124}Xe+Pb and ^{136}Xe+Pb compared with the abrasion-evaporation calculation performed with ABRABLA; (left) only emission of neutrons, protons and alpha clusters included in evaporation (dash-dotted lines), (right) evaporation description extended towards emission of more complex clusters (dashed lines).

From the above comparison it may be seen that emission of more complex clusters indeed significantly influences the process of the evaporation cascade. Nevertheless, as may be observed from Fig. 6.1 right, even upon including the cluster emission in the evaporation process the experimental data still appear to be more neutron-rich than the calculation and in case of the lightest residues even than the stability line. This suggests that the purely evaporation process is not sufficient to reproduce the isotopic composition of the experimental data far away from the projectile. In chapter 5 it was suggested that an additional process could occur in the heavy-ion collisions investigated in our experiments, which could be responsible for the preserved memory on the initial *N/Z* observed in the experimental data and for the increase of production cross sections in the IMF range – the break-up of a highly excited nuclear source. The influence of this process, specifically of the thermal conditions at the freeze-out of this process, on the final isotopic composition is investigated in the following section.

6.2.2. Influence of the thermal conditions at the freeze-out of the break-up stage

In the following we would like to investigate if the signature of the break-up process may be found in our data by studying in more detail the influence of the break-up process on the final isotopic composition. For this purpose, the break-up stage was optionally included in the ABRABLA code as introduced in section 6.1.2.

At first the excitation energy introduced in the collision is investigated for both Xe projectiles in Fig. 6.2. The excitation energy (in MeV) introduced in the abrasion stage of the reaction is calculated with the ABRABLA code as a function of mass of the primary fragment (prefragment). It may be seen that in case of both projectiles the initial excitation energies extend over a broad range. As discussed in chapter 1, the break-up of a highly excited nuclear source occurs for excitation energies exceeding app. 3 MeV per nucleon. This value is indicated in Fig. 6.2 by the black line. According to [Hub91,Schm02], in the relativistic energy regime, the excitation energies above this value are acquired already in rather peripheral collisions corresponding to a rather low mass loss, which are predominantly investigated in our experiments. This is confirmed in the calculation shown below, where it may be seen that already for a mass loss of the order of 10% the excitation energies above 3 MeV per nucleon are acquired. Although the large fraction of the primary fragments acquires excitation energies lower than this value, there is still a considerable portion of nuclei with excitation energies above 3 MeV per nucleon. The occurrence of the break-up process in the reactions investigated in this work may thus be expected.

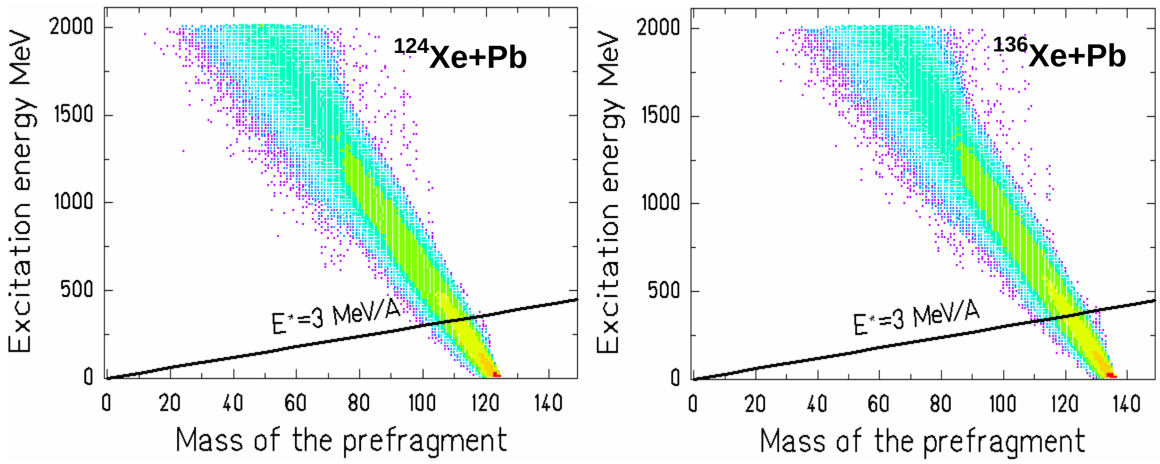

Fig. 6.2: Excitation energy introduced in the abrasion stage of the reaction of ^{124}Xe+Pb (left) and ^{136}Xe+Pb (right) as calculated with the ABRABLA code.

In the following the influence of the break-up stage on the isotopic composition of the final residues is investigated, and the sensitivity of the final isotopic composition to the thermal conditions at the freeze-out of this process are explored. During the break-up stage the initial nucleus disintegrates into fragments of different sizes, which cool down by the subsequent evaporation process. Assuming that the thermal equilibrium is established at the freeze-out of the break-up stage, where all the nuclear interactions cease, the excitation energy of the produced fragments may be determined by the thermal conditions of this configuration according to relation $E^*_{freeze-out} = aT^2_{freeze-out}$. The subsequent evaporation will modify the isotopic composition of the fragments and ‘drive’ them towards the residue corridor. The extent to which the presence of the break-up stage in the reaction process modifies the influence of the evaporation on the isotopic composition is investigated in Fig. 6.3 for the ^{136}Xe+Pb reaction.

As described in section 6.1.2, the break-up process occurs only if the temperature corresponding to the excitation energy acquired in the collision exceeds the temperature corresponding to the freeze-out of the break-up process. In the opposite case, the direct evaporation follows immediately after the initial collision. In such a case, the final isotopic composition is determined directly by the length of the evaporation process corresponding to the excitation energy the primary fragment acquired in the collision. On the contrary in case the break-up process occurs, the initial excitation energy is reduced due to the energy cost of the fragment formation. As a consequence, lower excitation energy is available for the subsequent evaporation process, which affects the length of the evaporation cascade. The excitation energy at the beginning of the evaporation cascade following the nuclear break-up is determined by the thermal conditions at the freeze-out of the break-up stage. Calculations were performed assuming different values of the freeze-out temperature, ranging from 3 to 8 MeV.

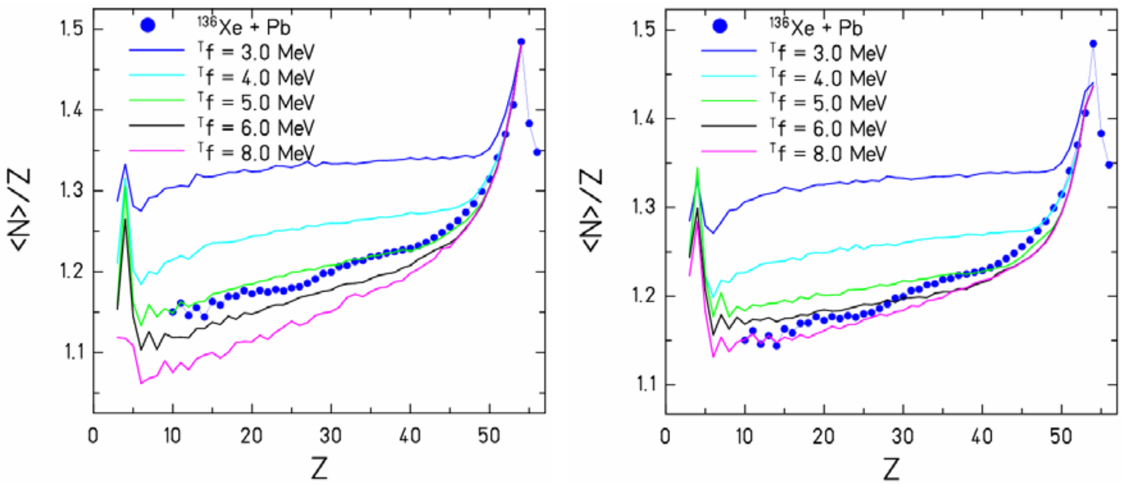

Fig. 6.3: Sensitivity of the <*N*>/*Z* of fragments measured in the reaction of ^{136}Xe+Pb (blue points) to the thermal conditions at the freeze-out of the break-up stage. Lines of different colors represent different values of the freeze-out temperatures assumed in the ABRABLA calculations; (left) emission of n, p and α only was assumed in the evaporation, (right) calculations including the evaporation of complex clusters.

From the above figure the sensitivity of the <*N*>/*Z* to the length of the evaporation process may be observed, which is determined solely by the thermal conditions at the freeze-out of the break-up stage. With increasing freeze-out temperature (increasing excitation energy available for evaporation), the final <*N*>/*Z* shifts towards lower values due to the increasing length of the evaporation process. Fig. 6.3 left and right compares the calculations performed including only emission of n, p and α during the evaporation process with calculations where also the emission of more complex clusters is included, respectively. Similarly as in the previous section an important influence of the cluster emission on the final isotopic composition may be seen, but still the thermal conditions at the freeze-out process significantly influence the results. Indeed, it is observed that the break-up stage included in the reaction process results in the modification of the final isotopic composition and leads to an improved agreement with the experimental data for a certain range of the freeze-out temperatures. While in the case of ‘simple’ evaporation (n, p, α) the experimental data are best reproduced assuming a universal value of temperature of 5 MeV at the freeze-out of the break-up process, the temperatures ranging from 5 to 8 MeV are observed to reproduce the different ranges of elements in case the emission of more complex clusters is included in the calculation.

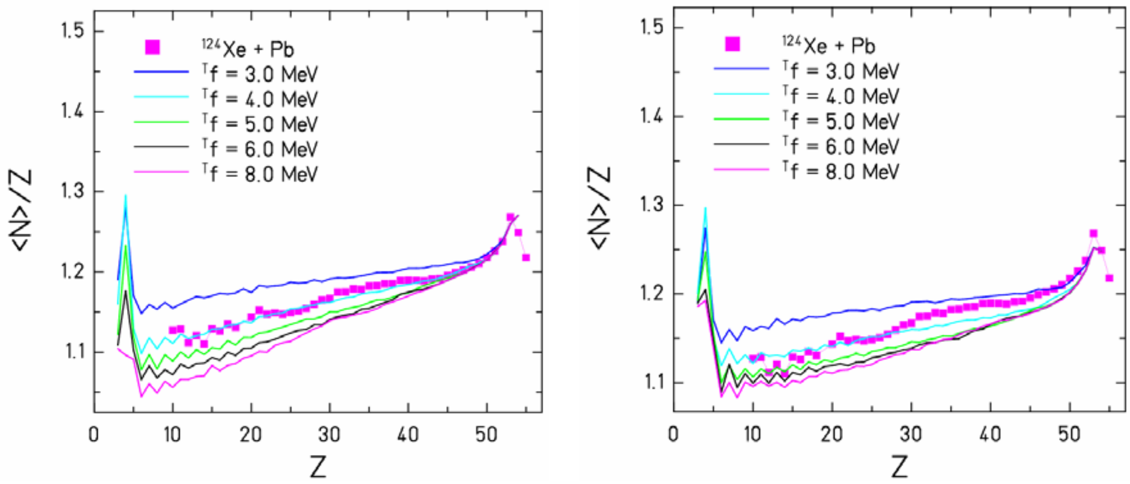

Fig. 6.4: The same as in Fig. 6.3 for the case of data from ^{124}Xe+Pb reaction (pink squares).

Fig. 6.4 shows the same comparison for the reaction of ^{124}Xe+Pb. Also in this case the sensitivity of the final $<N>/Z$ to the thermal conditions at the freeze-out of the break-up stage may be observed. On the contrary to the more n-rich projectile, in this case the data are rater well reproduced assuming 4 MeV freeze-out temperatures in a broad nuclear-charge range in both calculations. This reflects the observation from the previous section that in case of this less n-rich projectile the emission of more complex clusters does not affect the final isotopic composition so significantly. Moreover, in case of this projectile the difference among the final $<N>/Z$ corresponding to different thermal conditions assumed in the calculation is much less pronounced. This indicates essentially a lower sensitivity of the final residues to the length of the evaporation process in case of this less n-rich projectile. To illustrate the possible explanation of this observation, let us consider a highly excited nuclear source, which is less neutron-rich. The break-up of this source partially reduces its initial excitation energy so that somewhat lower excitation energy may be available for the following evaporation process. Nevertheless, in case of a less neutron-rich source, the reduction of the excitation energy in the break-up may still not be sufficient to prevent the final residues from approaching the residue corridor more closely. From the 'definition' of the residue corridor it follows that upon reaching this region any memory on the initial conditions of the evaporation process is lost. Since the final residues from the less neutron-rich sources may be very close to the residue corridor, their sensitivity to the conditions at the beginning of evaporation may be considerably reduced, which is observed in our data.

It may be observed in case of both systems that in the vicinity of the projectiles the calculations with different freeze-out temperatures start to merge. This may be easily understood, since the residues close to the projectile are produced in very peripheral collisions, where rather low excitation energies are introduced. These excitation energies are presumably not sufficient for the break-up of the nucleus to occur and lead to a direct evaporation of the excited primary fragment. In such a case the different values of the freeze-out temperatures assumed in the calculation do not influence the results. On the contrary, the isotopic composition of these heavy residues is determined directly by the excitation energy of the primary fragment formed in the collision. This aspect is investigated in more detail in the following chapter by comparing the isotopic composition of the final residues close to the projectile, produced in the reactions of the ^{136}Xe projectile with targets of extremely different sizes.

To explore the influence of the break-up process on the isotopic composition of the final residues more closely the comparison of the full isotopic distributions measured in both experiments with the calculations with and without the nuclear break-up is presented in appendix C, Fig. C.1 and C.2 for ^{136}Xe and ^{124}Xe projectiles, respectively. Both calculations, with as well as without the nuclear break-up include the emission of complex clusters. In case of calculations including the nuclear break-up, the results corresponding to values of the freeze-out temperatures that lead to the best reproduction of the $\langle N \rangle / Z$ in Fig. 6.3 and Fig. 6.4 are shown. It may be observed that the lightest residues are considerably underpredicted by the calculations including the nuclear break-up in case of both systems. This may be related to the fact that in the description of the nuclear break-up within the ABRABLA the further evolution of the largest residue only is followed. As a consequence lower production cross sections predicted by the ABRABLA in the intermediate mass range (IMF, $3 \leq Z \leq 20$) may be expected, since these fragments are often produced in the configurations of more fragments of rather similar size [Schü96] and the products of such a process are not followed explicitly in the code. Nevertheless, overall an improved agreement with the experimental data may be observed in case the nuclear break-up is included in the calculation. However, slightly broader isotopic distributions are predicted by the calculation with break-up in the nuclear-charge range below $Z \sim 40$ and 45 for the ^{136}Xe and ^{124}Xe projectiles, respectively and an enhanced production of less n-rich fragments may be observed in the region close to the projectile ($Z>52$). This suggests that despite the improvement in the overall features of the experimental data, additional work is still needed in order to model the whole process more reliably.

The above investigations indicate that the break-up process significantly affects the isotopic composition of the final residues and may considerably reduce the length of the evaporation process producing thus more neutron-rich residues than observed in case of the direct sequential evaporation investigated in section 6.2.1. In particularly it seems that the thermal conditions at the freeze-out of the break-up stage are important in determining the isotopic composition of the final residues. Similar observation led in [Schm02] to the formulation of the isospin-thermometer method, which attempts to trace back the thermal conditions at the beginning of the evaporation process from the final isotopic distributions and a rather universal value of the freeze-out temperature of 5 MeV for the fragmentation of the ^{238}U projectile was extracted. In [Schm02], however, the original version of the evaporation process, including only emission of n, p and α in the ABRABLA code was used. Despite the improvements of the overall agreement between the experimental data and the calculations for certain values of the assumed freeze-out temperatures, observed in the present investigation, it should be considered that the emission of more complex clusters in the evaporation process notably affects the final isotopic composition especially in case of the more n-rich ^{136}Xe projectile. Based on the present analysis of this projectile no single universal value of the freeze-out temperature may be extracted anymore. Rather a range of values depending on the nuclear charge of the residue (T=5-8 MeV for $Z \sim 40$-10) is observed to reproduce the $\langle N \rangle / Z$ of the experimental data. The value of temperature reproducing the lightest residues (below $Z \sim 16$), however, seems to be too high than expected from other experimental investigations of the multifragment break-up of nuclear systems of the similar sizes as formed in the collisions of this Xe projectile [Hau00, Nat02, Ort04].

The above analysis and the investigations of the thermal conditions at the freeze-out of the break-up stage are based on the description of the reaction process as included in the ABRABLA code. Indeed, there are many aspects in the complex process of the nuclear reaction, which may certainly influence such an analysis and their importance should be further investigated (in particular the process of isospin fractionation). Nevertheless, the investigation of the average isotopic composition of the final residues presented in the previous chapters suggests that it should be considered as an important experimental observable, which, being carefully analyzed, may provide an access to the thermal conditions at the beginning of the evaporation process.

6.3. Dependence of the final isotopic composition on the target material

In this section the mean N-over-Z of the final residues produced in the interaction of the ^{136}Xe projectile with the heavy Pb (N/Z~1.54), Ti (N/Z~1.18) and light ^{1}H targets is investigated. This allows to investigate the influence of the isotopic composition and size of the target on the $\langle N\rangle/Z$ of the final residues. The experimental data measured in reactions ^{136}Xe+Ti and ^{1}H were taken over from [Nap04b].

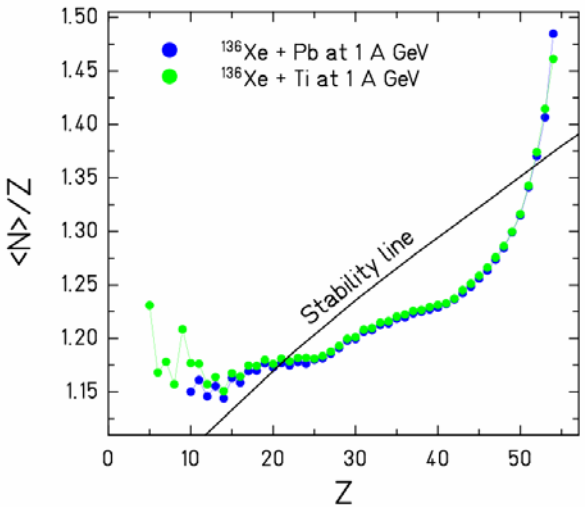

Fig. 6.5: Comparison of the $\langle N\rangle/Z$ measured in the reactions ^{136}Xe+Pb and ^{136}Xe+Ti.

In Fig. 6.5, the final $\langle N\rangle/Z$ measured in the reaction of ^{136}Xe+Pb and ^{136}Xe+Ti is displayed. A very good agreement of the $\langle N\rangle/Z$ in the broad nuclear charge range may be observed. This indicates a low sensitivity of the isotopic composition of final residues to the N/Z of the target material, which is consistent with the expectation that almost no N/Z mixing occurs between the interacting projectile and target nuclei in the relativistic energy regime. Despite the different mass (size) of the two targets, no difference is observed in the final $\langle N\rangle/Z$. This may be understood with the help of the abrasion model, according to which the excitation energy introduced is directly proportional to the mass loss. In order to observe the final residue of a given mass, the two reactions (^{136}Xe+Pb and ^{136}Xe+Ti) proceed through collisions with different impact parameters, which assures the same mass loss and thus the same initial excitation energy in both cases. As a consequence, the isotopic composition of the final residues does not depend on the target mass.

The slightly lower values of the $\langle N\rangle/Z$ in case of interaction of ^{136}Xe with a lead target in the nuclear charge range below Z~25 might be attributed to the different treatment of the transmission correction in the two data sets.

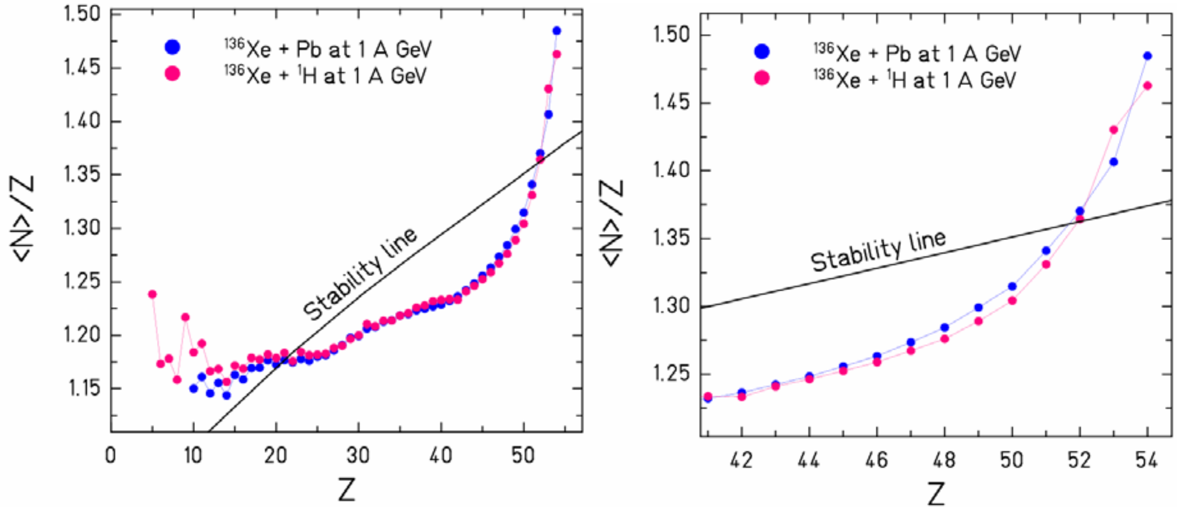

Fig. 6.6: (left) comparison of the <*N*>/*Z* measured in the reactions of ^{136}Xe+Pb and ^{136}Xe+^{1}H; (right) detail of the <*N*>/*Z* of residues close to projectile

In Fig. 6.6 left the <*N*>/*Z* of the final residues measured in the ^{136}Xe+Pb and ^{136}Xe+^{1}H reactions is compared. Apart of the difference in the region of low nuclear charges observed also in the case of the titanium target, a clear difference in the final <*N*>/*Z* may be observed also for the residues in the vicinity of the projectile. On the contrary to the region of light charges, the residues in the vicinity of the projectile are fully transmitted through the FRS so that the limited transmission does not affect these data. To explore the different <*N*>/*Z* in this region more closely it is shown in Fig. 6.6 right in detail. As may be seen from this figure, the final residues from ^{136}Xe fragmentation on hydrogen are less neutron rich at the end of the evaporation process. This reflects a different amount of excitation energy acquired in the two reactions. Indeed, from the observation of lower final <*N*>/*Z* in the reaction with hydrogen target it may be deduced that the proton is more efficient in distributing the excitation energy in the colliding nucleus. The higher excitation energy acquired in the collision with the hydrogen target results in a longer evaporation process, producing thus less neutron-rich final residues.

On the contrary to the previous comparison of ^{136}Xe+Pb and ^{136}Xe+Ti reactions, where no influence of the target size on the final isotopic composition was observed, here a different signature is found. This might be related to the observation that in the individual collisions of proton inside the nucleus majority of the nucleons participating in the collision process remain inside the nucleus (apart from few nucleons knock out in the collision) and share the acquired energy among the remaining nucleons. On the contrary, in case of the abrasion process, only the nucleons in the overlapping region directly participate in the collisions and may thus contribute to the excitation of the nucleus.

The observation of Fig. 6.6 is a clear indication of the sensitivity of the final <*N*>/*Z* to the length of the evaporation process investigated in the previous section. Despite the emission of more complex clusters was observed to significantly influence the interpretation of results in the previous section, here (Fig. 6.6) a direct experimental signature of the sensitivity of the final <*N*>/*Z* to the length of the evaporation process is seen. On the contrary to the previous section, where the influence of the thermal conditions at the freeze-out of the break-up stage was explored, the residues in the vicinity of the projectile are produced solely by an evaporation process and their isotopic composition is affected directly by the different excitation energies introduced in the initial collision. An application of the idea of the isospin-thermometer method to these data would allow to reconstruct and directly compare the amount of excitation energy of fragments entering the evaporation cascade in the two reactions. The data from Fig. 6.6 provide an additional support for the observation that the isotopic composition of the final residues indeed contains information on the conditions specifying the length of the evaporation process, which may be explored to extract some of the hot system properties.

Chapter 7

Symmetry energy of hot fragments

In the investigations performed in the previous chapter, the contribution of the process of nuclear break-up was identified in the final isotopic distributions measured in this work. As pointed out in chapter 1, the formation of the fragments in the multifragment break-up of the highly excited nuclear system may influence the value of the symmetry-energy coefficient in their binding energy. The method based on the experimental isoscaling was introduced in order to deduce the information on the coefficient of the symmetry-energy from the experimental data. In the following sections the isoscaling behavior exhibited by the data measured in our two reaction systems (^{136}Xe+Pb and ^{124}Xe+Pb) will be investigated and a method introduced in chapter 1 will be applied to extract the corresponding experimental symmetry-energy coefficient.

7.1. Isoscaling and its statistical interpretation

In this section the isoscaling and its statistical interpretation, introduced already in more detail in chapter 1, are briefly summarized. The isoscaling is an observation that the yield ratios R_{21} of fragments of the same type produced in reactions with different isospin asymmetry exhibit an exponential dependence on N and Z:

$$R_{21}(N,Z) = Y_2(N,Z)/Y_1(N,Z) = C\exp(\alpha N + \beta Z) \tag{7.1}$$

with three parameters C, α and β, where $\alpha = \Delta\mu_n / T$ and $\beta = \Delta\mu_p / T$ and the notation that $Y_2(N,Z)$ and $Y_1(N,Z)$ stand for the yield of isotope (N,Z) in the more neutron-rich and more neutron-deficient reaction system respectively.

Naturally the ratio of isotopic distributions includes information from both their first as well as second moments. The magnitude of the isoscaling parameter α directly reflects the width and relative position of the final isotopic distributions (e.g. broader and/or more overlapping isotopic distributions result in lower values of α). The advantage of the use of isoscaling over the full isotopic distributions for extracting the isospin properties averaged over all fragments is the observation that the ratio of yields allows for eliminating fluctuations caused by the structure effects [Ric04].

Within the framework of the SMM code (Statistical Multifragmentation Model) [Bon95] the simple relationship between the isoscaling parameter α and the symmetry-energy coefficient was derived:

$$\alpha = \frac{\Delta\mu_n}{T} = -\frac{4\gamma}{T}\left(\frac{Z_1^2}{A_1^2} - \frac{Z_2^2}{A_2^2}\right) \tag{7.2}$$

where $\Delta\mu_n$ is the difference between the neutron chemical potentials of the two systems; γ stands for the symmetry-term coefficient and Z_1,A_1 and Z_2,A_2 are the charges and masses of the two source systems. Upon determining the temperature and the isotopic composition of the two source systems, the above relation may be used to extract the apparent coefficient of the symmetry-energy term (γ_{app}) utilizing the isoscaling parameter α, deduced from the measured cold fragments. As mentioned in chapter 1, equation (7.2) refers to fragments formed at the temperature T and the evaporation process may influence the value of parameter α, which is experimentally extracted from the cold residues and thus may be different from the value corresponding to high temperature. Indeed, the evaporation shifts the final isotopic distributions closer to the residue corridor, reducing thus the difference between the maxima of the two distributions and affecting their widths. As a consequence, a modification of the isoscaling parameter α may be expected. As well it is possible that the mentioned effects of the evaporation process would compensate each other, making the parameter α rather insensitive to the evaporation process as observed in [Tsa01b]. Indeed, it is necessary to investigate the influence of the evaporation process for every reaction individually, which is performed for the case of our data in section 7.3.1 with the use of the SMM code.

7.2. Application to the experimental data

7.2.1. Isoscaling phenomenon

The isoscaling phenomenon was observed in a large variety of reaction mechanisms including the evaporation process and multifragment break-up of highly excited nuclear systems, provided that the temperature of the two reaction systems was nearly the same [Tsa01c]. These investigations focused predominantly on the light (Z<~8) isotopically resolved residues. The isotopic identification performed in the full nuclear charge range for the two reaction systems ^{136}Xe(N/Z=1.52)+Pb and ^{124}Xe(N/Z=1.30)+Pb analyzed within this work provide an excellent opportunity to investigate the isoscaling phenomenon over almost complete nuclear-charge range. To perform this investigation, the ratio R_{21} of isotopic distributions measured in both reactions was calculated keeping the more neutron-rich system in the numerator. Fig. 7.1 shows this ratio for isotopes in the nuclear-charge range Z=5-53 as a function of neutron number. Please note that the angular-acceptance integrated cross sections were used in the ratio in order to avoid possible systematic uncertainties related to the different treatment of the transmission correction in case of the light-fragment settings from ^{124}Xe+Pb experiment.

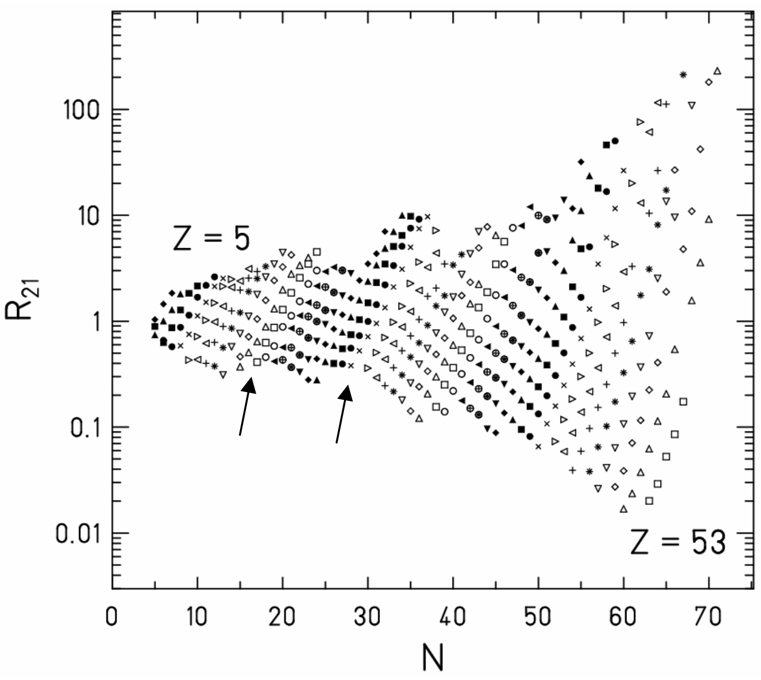

Fig. 7.1: The isoscaling exhibited by fragments with Z=5-53 produced in the reactions of ^{136}Xe(N/Z=1.52)+Pb and ^{124}Xe(N/Z=1.30)+Pb at 1 A GeV analyzed in this work.

It may be seen that the isoscaling behavior (equation (7.1)) is very well respected in almost complete nuclear-charge range. A slight deviation from the strictly linear trend (in a logarithmic scale) may be observed for the heaviest elements around Z~49. The oscillations of the ratio in the vicinity of the projectile observed in case of the most n-rich isotopes is most probably related to the presence of the slits in the beam line in some of the magnetic field settings, which as discussed in section 4.2 affected the production cross sections determined for some n-rich isotopes. A rather constant distance between the isotones of given N may be observed in the broad range of neutron numbers. For more n-rich isotones this pattern starts to deteriorate close to N~38, which again may be related to the influence of the slits. The constant distance between the isotones suggests that also the exponential dependence on the proton number is rather well respected. Some irregular patterns may be observed in the data, namely the change of slope of the dependence of lines with N=Z+k, with k=1,2…, as a function of neutron number may be seen between the chains of Z~17-23 and around Z~28 (both are indicated by arrows in the figure). The former range corresponds to the range of isotopes, which were at most affected by the improper function of the CFD unit of the scintillator detector at S2 as explained in chapter 3.2.4 in the ^{124}Xe+Pb experiment. As described in chapter 3.2.4, the yields of these isotopes had to be identified by a different method than all other isotopes, which inevitably introduces a systematic error, which affects the extracted cross sections and is reflected in an irregular pattern in the constructed isotopic ratio. The second change of the pattern of the displayed isoscaling correspond to the region, where the transition is made between the light and heavy settings. This may be related to different secondary reaction corrections considered in the light- and heavy-fragment settings, introduced due to degrader, which was inserted in the beam line only in case of the light-fragment settings.

In [Tsa01c] it was shown that the isoscaling behavior arises if the temperatures of systems formed in the two reactions are very similar, which leads to cancellation of the binding energy terms in equation (1.14). Recalling the discussion at the end of chapter 6, the observation that the isoscaling is very well respected in our data supports the smaller difference between the freeze-out temperatures than obtained by the analysis with the present version of the ABRABLA code.

The slight deviation of the data points from the regular pattern in the vicinity of the projectile may be observed. This may be understood by recalling the shapes of the isotopic distributions shown in Fig. 4.3. The isotopic distributions of elements in the region close to the projectile measured in the two Xe-experiments have rather different width and shapes and in the direct vicinity to the projectile they even deviate from the Gaussian-shape. This may be the reason for failure of the exponential dependence of the yield ratio in this nuclear-charge range.

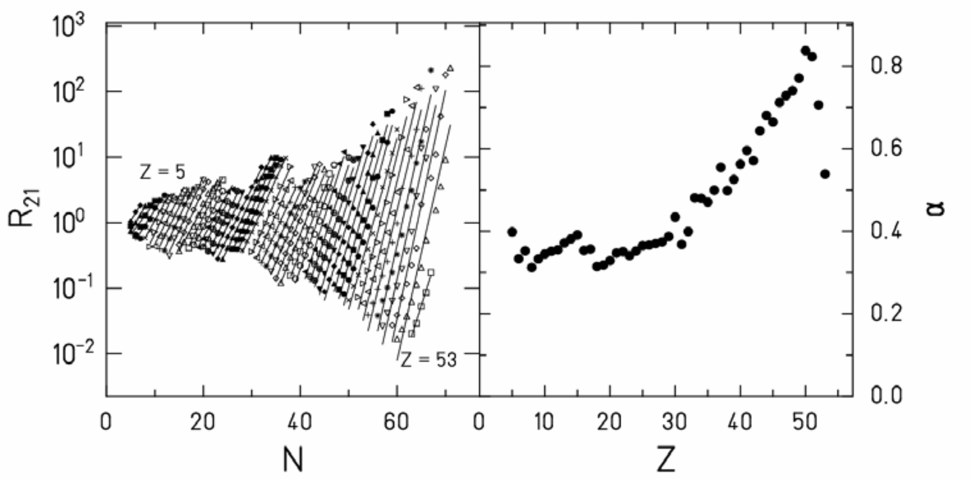

Fig. 7.2: (left) The exponential fit of the isoscaling exhibited by fragments with *Z*=5-53 from Fig. 7.1; (right) The corresponding extracted isoscaling parameter.

Fig. 7.2 (left) shows an exponential fit to the experimental data depicted by the full lines with the corresponding isoscaling parameters *α* extracted for each element (Fig. 7.2 (right)), displayed as a function of the nuclear charge. A systematic, rather steep decrease of the parameter *α* with decreasing charge may be observed in this nuclear-charge range. The corresponding values of *α* ranging from 0.5 to 0.8 are consistent with the values extracted from the yield ratio of isotopes produced in purely evaporation process [Tsa01a,Bot02]. Indeed, the steep decrease of *α* reflects a rapid change of the relative position and widths of the final isotopic distributions, which may be understood as a consequence of the dominant neutron evaporation of the low excited primary fragment produced in the very peripheral collision. For lower *Z* the decrease of *α* is smoother with much lower values, between 0.3 and 0.4. These values are in similar range as values extracted from isoscaling analysis of multifragmentation reactions [e.g. Bot02,LeFev05].

7.2.2. Apparent symmetry-energy coefficient

Knowing the isoscaling parameter α it is now possible to employ equation (7.2) in order to deduce the symmetry-energy coefficient of the hot fragments. To address the symmetry energy under the conditions of low densities and high temperatures it is desirable to focus on the fragments produced solely in the multifragmentation process. In order to investigate the symmetry energy in such a configuration we focus in the following on the residues in the nuclear charge range Z=10-13. According to the information from the large acceptance experimental devices such as ALADIN spectrometer [ALADIN], the final residues in this charge range are predominantly produced in multifragmentation events, composed of many fragments of similar size [Schü96]. The isoscaling parameter corresponding to this nuclear-charge range was determined to be $\alpha = 0.36 \pm 0.01$.

In order to determine the value of the symmetry-energy coefficient from equation (7.2) it is needed to determine the temperature of both multifragmenting systems and their isotopic composition. Recalling the discussion in section 6.2.2 and triggered by the observation of very good isoscaling phenomenon revealed by our data, the similar temperatures may be expected in the two reactions at least in the considered nuclear-charge range. Indeed, according to [Hau00,Ort04,Nat02], the freeze-out temperature of the system of the similar size as produced in our reactions ranges between T~4-6 MeV, which is used as an estimate of the freeze-out temperature also for our data.

To determine the factor $\Delta(Z^2/A^2) = (Z_1/A_1)^2 - (Z_2/A_2)^2$ the isotopic composition of the multifragmenting sources needs to be known. This information is unfortunately not available in our experiments, nevertheless since both experiments were performed in the relativistic energy regime it is possible to approximate this isotopic compositions by the isotopic compositions of the fragmenting projectiles. Indeed, in the relativistic-energy regime a geometrical abrasion picture is a good description of the first stage of the peripheral collision. In the abrasion process only nucleons in the geometrical overlap of the colliding nuclei are removed with the probability to remove neutrons or protons corresponding to their abundance in the nuclei. Moreover, in this energy regime the exchange of nucleons between the interacting nuclei may be neglected. In [LeFev05] the change of the factor $\Delta(Z^2/A^2)$ due to the possible emission of nucleons before the equilibration was studied using the Liège-cascade-percolation [Vol04] and relativistic mean-field models [Gai04], and difference of less than 6% was observed. The isotopic composition of the ^{136}Xe and ^{124}Xe projectiles is therefore a good approximation to determine the factor $\Delta(Z^2/A^2)$, which then corresponds to 0.032.

Inserting the values of temperature and $\Delta(Z^2/A^2)$ into the equation (7.2) and using the experimentally determined value of the isoscaling parameter α, an 'apparent' symmetry energy coefficient $\gamma_{ap} \approx 14 \pm 3$ MeV is obtained, which is considerably lower than the values typically obtained from the binding energies of cold nuclei, which usually range from 20-25 MeV. As already discussed, the term apparent reflects the fact that to determine the symmetry energy of hot fragments, the isoscaling parameter extracted from the final cold residues was used. The influence of the evaporation process on the isoscaling parameter and on the extracted value of the symmetry-energy coefficient is studied in the next section.

7.3. Comparison of the experimental results with the SMM-code calculations

For the comparison of the experimentally determined apparent symmetry-energy coefficient γ_{ap} with the theoretical prediction, the Statistical Multifragmentation Model (SMM) [Bon95] is used. Below it is applied to investigate the influence of the evaporation process on the ratio of isotopic yields and to extract the symmetry-energy coefficient needed to reproduce the final $<N>/Z$ of the experimental data.

SMM is one of the most extensively used statistical models developed for the description of the multifragmentation process. It determines the probability of multifragment break-up of an excited nuclear system into a particular set of nucleons and fragments according to the phase space available for this process. It considers all possible channels composed of nucleons and excited fragments taking into account the conservation of energy, electric charge and baryon number. Different channels are generated by Monte Carlo sampling according to their statistical weights. The input parameters specifying mass, nuclear charge and excitation energy of the multifragmenting system must be defined. The model assumes statistical equilibrium at a low-density freeze-out stage, typically at one-third of the normal nuclear density. After the break-up, the Coulomb repulsion and the secondary deexcitation of primary hot fragments are taken into account.

The crucial question in applying a statistical model to the description of the nuclear reaction process is to which extent the formation of an equilibrated system may be assumed. According to several experimental observations (e.g. [D'Ago96,Bot95,Ent01,Scha01]), the formation of an equilibrated source in the multifragmentation reactions may be expected. These observations are supported by the general success of the statistical models to describe many various features of the experimental data.

7.3.1. Influence of the secondary deexcitation

The formula (7.2) may be used to calculate the symmetry energy coefficient γ of hot fragments produced in the system of temperature T. The experimentally determined isoscaling parameter α was, however, obtained from the cold final residues after the evaporation process. In order to establish the connection between γ of hot fragments and γ_{app} extracted from the isoscaling parameter α of observed cold fragments, the process of the secondary deexcitation should be taken into account.

The influence of the evaporation process on the isoscaling parameter α was investigated with the use of the SMM code. The symmetry energy of hot fragments with mass number A and nuclear charge Z is in SMM parameterized as follows:

$$E_{AZ}^{sym} = \gamma (A-2Z)^2 / A \tag{7.3}$$

where γ is the symmetry-energy coefficient. The value of the symmetry-energy coefficient is usually determined from the fit to the binding energies of cold nuclei in their ground state. In the SMM version, utilized for this investigation, the symmetry-energy coefficient of γ = 25 MeV is considered [Bot87]. However, the experimentally determined γ_{app} is considerably lower than the value extracted from the ground states of cold nuclei. To take this 'apparent' lowering of the symmetry-energy coefficient of the hot fragments into account, the value of the symmetry-energy coefficient in equation (7.3) was varied in the code in the range from 4 to 25 MeV. The hot fragments formed in the multifragmentation with the lower symmetry-energy coefficient cool down in the evaporation process, which leads to the restoration of their ground state masses, characterized by $\gamma = 25$ MeV. The value of the symmetry-energy coefficient thus should evolve during the evaporation process. Unfortunately, it is not exactly known at what stage of the secondary deexcitation the nuclei restore the ground state masses with the standard symmetry energy. It may happen at later times during the Coulomb propagation of the fragments from the freeze-out volume, when the fragments cool down sufficiently. Nevertheless, according to [Ign78] it should take place for isolated nuclei at $T \leq 1$ MeV.

To take into account the evolution of the symmetry energy during the evaporation process, leading to the restoration of the ground state masses, the following parameterization of the nuclear masses $m_{A,Z}$ is used [Hen05,Buy05]:

$$m_{A,Z} = m_{\mathrm{ld}}(\gamma) \cdot \xi + m_{\exp} \cdot (1 - \xi) \tag{7.4}$$

where m_{ld} represents the mass of the nucleus according to the liquid-drop model, $m_{\exp}$ stands for the experimental masses taken from nuclear tables, and $\xi = \beta \cdot E^*/A$, with [β = 1 MeV^{-1}]. At the beginning of the evaporation process, when the internal excitation energy of the fragment (A,Z) is large enough ($\xi > 1$), its mass is determined according to the liquid-drop model prescription ($m_{A,Z} = m_{\mathrm{ld}}(\gamma)$) with γ in the range of 4 - 25 MeV. As the fragment cools down, after its excitation energy decreases to $\xi \leq 1$, a smooth transition to the experimental masses with shell effects ($m_{\exp}$) is adopted according to equation (7.4).

With the above prescription describing the evolution of the symmetry-energy coefficient during the deexcitation, the influence of the evaporation process on the isoscaling parameter α may be investigated. These calculations were performed with the microcanonical Markov-chain version of the SMM [Bot01] for ^{136}Xe and ^{124}Xe projectile sources at excitation energies of E^*=4-6 A MeV, which are expected in multifragmentation. In order to check the source-size effect on the results, similar calculations for sources with 60% of the projectile masses and with the same Z/A ratios were performed, where no significant change of the isospin characteristics under study was found. Thus, in the following only the results from calculations with ^{136}Xe and ^{124}Xe projectile sources are discussed.

To estimate how the symmetry energy changes the isospin properties of the final fragments after evaporation, the calculations were performed with several values of the symmetry-energy coefficient γ of the hot fragments in the range from 4 to 25 MeV. The isoscaling parameter α was extracted from the best exponential fit to the ratio of the calculated isotopic yields of hot and cold fragments, respectively, in the nuclear charge range Z=10-13. Fig. 7.3 shows the calculated isoscaling parameter α as a function of different values of symmetry-energy coefficient γ for two values of the excitation energy of the source. It may be observed that the α-parameter deduced from the isotopic distributions of hot fragments exhibits a linear dependence on γ in agreement with equation (7.2). The evaporation process affects the isoscaling parameter α differently for different values of γ. Assuming $\gamma = 25$ MeV for hot fragments, the evaporation process causes a slight broadening of the final isotopic distributions resulting in lower value of the corresponding α. For smaller values of symmetry-energy coefficient γ of hot fragments the dominant effect of the evaporation process is the decay of the wings of the wider initial isotopic distributions. As a consequence the cold distributions are narrower and the corresponding α larger then before the evaporation. Fig. 7.3 also demonstrates the difference between the two kinds of the evaporation calculations, one according to the old evaporation code [Bot87], and the other one according to the new version taking into account the symmetry energy (mass) evolution during evaporation. The new evaporation description predicts final values of α much closer to the initial ones at smaller values of the symmetry-energy coefficient. The difference between the two versions of the calculation serves as a qualitative measure of the uncertainty expected in the secondary deexcitation description.

Overall, the evaporation process spoils the initial linear dependence of the isoscaling parameter α on the symmetry-energy coefficient of hot fragments as predicted by equation (7.2). Nevertheless, a nontrivial dependence on the symmetry-energy coefficient is still preserved. It may be observed that the experimentally determined value of α is best reproduced if the symmetry-energy coefficient of hot fragments is well below γ=25 MeV extracted from the ground states of cold nuclei. Indeed, the isoscaling parameter α is best reproduced assuming $\gamma \approx$ 11-12 MeV and 5-8 MeV with the new and old evaporation calculation, respectively, for the investigated excitation energies.

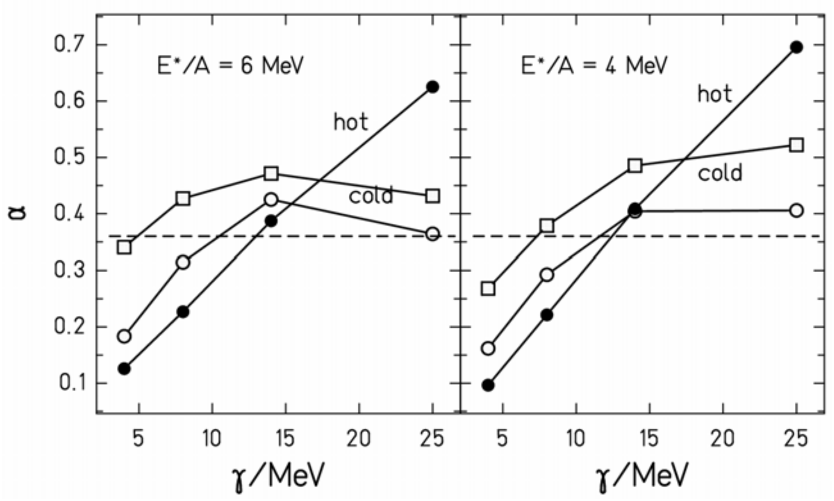

Fig. 7.3: The isoscaling parameter α versus the symmetry-energy coefficients γ obtained from fragments with Z=10-13 in SMM calculations for ^{136}Xe and ^{124}Xe sources having excitation energies 6 A MeV (left panel) and 4 A MeV (right panel). Solid symbols represent the results for primary hot fragments, empty symbols for final cold fragments; the new evaporation description is shown by open circles, the old evaporation by open squares. The dashed line shows α extracted from the experimental data.

7.3.2. Extraction of the symmetry-energy coefficient from <*N*/*Z*>

In the previous section, the dependence of the isoscaling parameter of cold nuclei on the symmetry-energy coefficient was investigated. Although it is not linear anymore it still allows to extract the symmetry-energy coefficient needed to reproduce the value of the experimentally determined isoscaling parameter α. Similarly as in the previous section, the symmetry-energy coefficient needed to reproduce the experimental <N>/Z of the final residues may be investigated.

For this purpose, the SMM calculations of the previous section were used. Again we focus on the nuclear-charge range *Z*=10-13. From the calculated isotopic distributions of hot and cold fragments the corresponding <*N/Z*> is obtained, averaged over *Z*=10-13. Fig. 7.4 shows the <*N/Z*> ratio calculated with different values of the symmetry-energy coefficient γ and two values of the source excitation energy. The dashed line indicates the <*N/Z*> ratio extracted from the experimental data measured in each reaction system.

It may be seen that in case of the old evaporation calculation without the evolution of the symmetry-energy coefficient the primary neutron-rich fragments loose a lot of neutrons during the secondary deexcitation, which results in a considerable decrease of their <*N/Z*>. At the same time, the final <*N/Z*> values appear to be almost independent on the value of the symmetry-energy coefficient. These observations may be understood as a consequence of the observation that although the hot fragments are assumed to be formed with the lower value of the symmetry-energy coefficient, the experimental masses are used at all steps of the evaporation process in the old evaporation model. This leads to the suppression of the emission of charged particles by both the binding energy and the Coulomb barrier and the final residues are considerably less neutron rich. On the other hand, if the symmetry-energy evolution is included in the evaporation process, the final <*N/Z*> increases with decreasing symmetry-energy coefficient, and for the lowest values of γ the final fragments appear to be more neutron-rich than before the evaporation. This effect may be understood as follows. While in the case of small γ at the beginning of the evaporation the binding energy essentially favors the emission of charged particles, when the fragment sufficiently cools down and the transition to the experimental masses is performed, the remaining excitation energy is rather low (i.e. below 1 *A* MeV) to allow for evaporation of many neutrons.

From the comparison of the calculated <*N/Z*> averaged over *Z*=10-13 it may be observed that the symmetry-energy coefficient γ ≈ 14-15 MeV of hot fragments is needed in the new evaporation version to describe the experimental <*N/Z*> for both projectiles. Thus, also this additional analysis, utilizing directly the first moments of the isotopic distributions, suggests the lowering of the symmetry-energy coefficient for hot fragments formed in the break-up of the highly excited nuclear source.

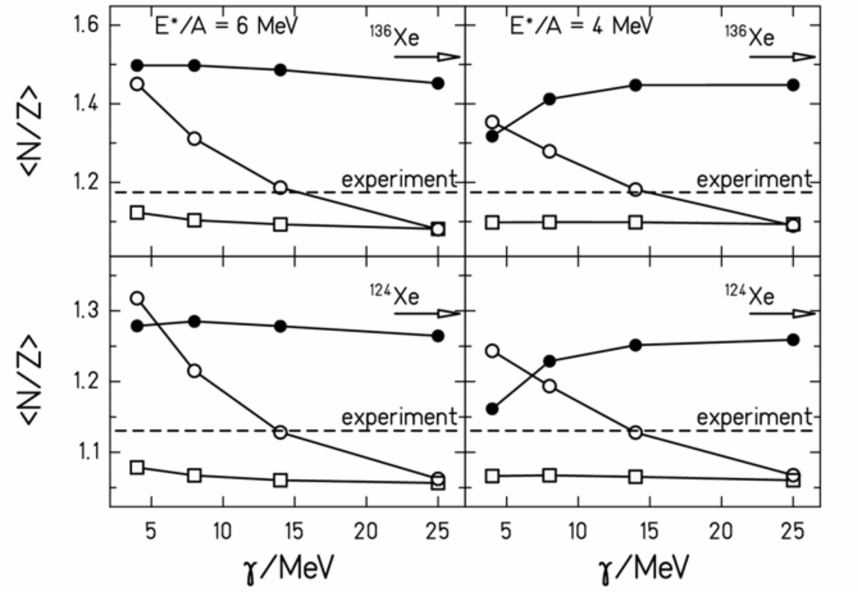

Fig. 7.4: The <*N/Z*> ratio versus the symmetry-energy coefficients γ for fragments with *Z*=10-13 obtained from SMM calculations for ^{136}Xe (top panel) and ^{124}Xe (bottom panel) sources, and with excitation energies 6 *A* MeV (left panel) and 4 *A* MeV (right panel). The notation is the same as in Fig. 7.3, arrows indicate the *N/Z* values of both projectiles.

7.4. Discussion

For the purpose of the study of the symmetry-energy coefficient the SMM code was used. The symmetry energy of hot fragments with mass number A and nuclear charge Z is in SMM parameterized as $E_{AZ}^{sym} = \gamma(A-2Z)^2/A$, where in order to fit the binding energies of isolated cold nuclei in the ground state γ is taken to be 25 MeV [Bot87]. This type of parameterization exhibits a volume character, since it changes as A when N and Z are scaled by one factor. Such a parameterization suggests that the interior contribution to the nuclear binding decreases with increasing asymmetry. Less binding energy is then needed to be compensated for when developing the surface suggesting that the surface tension should also decrease with increasing asymmetry [Dan03]. Indeed, it was discussed on many occasions that not only the volume but the surface as well should contribute to the symmetry energy in the nuclear binding (e.g. [Dan03,Latt93]). Let us consider two different parameterizations of the symmetry energy including both the volume and the surface contributions based on the liquid-drop [Latt93] and the liquid-droplet [Dan03] models, respectively:

$$E_{sym} = (a_v - a_s A^{-1/3})\frac{(A-2Z)^2}{A} \tag{7.5}$$

and

$$E_{sym} = \frac{a_v}{1+\frac{a_s}{a_v}A^{-1/3}}\frac{(A-2Z)^2}{A} \tag{7.6}$$

where a_v and a_s are the volume and surface parameters, respectively. From the above equations it may be seen that the extent to which the surface term contributes to the symmetry energy depends on the size of the fragment. It is less important for the heavy nuclei and affect more strongly lighter nuclei.

Assuming the fragments in the nuclear charge range investigated in the previous sections (Z = 10-13), these parameterizations lead to the symmetry-energy coefficient in the range of 16-20 MeV, the value which is also considerably lower than the value of 25 MeV. Thus it might seem unclear whether the reason for lowering of the symmetry energy coefficient observed for hot light fragment is a consequence of their formation in the hot and dilute environment or of the surface contribution to the symmetry energy, which generally decreases the symmetry-energy coefficient of cold light nuclei. However, hot fragments formed in the nuclear break-up may interact with each other in the freeze-out volume, for instance by exchanging neutrons. This effect of the surroundings can also lead to the change of the properties of hot fragments.

As shown in Fig. 1.5, it was observed in [LeFev05] that the apparent symmetry-energy coefficient for hot light fragments ($Z \leq 5$) formed in the reactions of ^{12}C + ^{112,124}Sn at E/A = 300 MeV and 600 MeV decreases with decreasing impact parameter (i.e. increasing introduced excitation energy) from the value of 25 MeV for very peripheral collisions to the value around 15 MeV or lower for more central collisions. Investigations of the influence of the evaporation process on this result suggest that this dependence for the ‘real’ γ of hot fragments should be even steeper [LeFev05]. This dependence of the symmetry-energy coefficient on the centrality of the collision suggests the lowering of the magnitude of the symmetry energy in the processes, where high excitation energies are involved. Therefore, the experimental investigations of the characteristics of fragments formed in the break-up of the highly excited source, including the symmetry energy, remain indispensable to constrain the properties of hot nuclei.

The present analysis showed that with the use of the equation (7.2) the apparent symmetry-energy coefficient $\gamma_{app} \sim 14$ MeV may be extracted. Investigation of the influence of the evaporation process with the use of the SMM code showed that the experimental isoscaling parameter may be reproduced only with $\gamma \approx 11$-12 MeV using the new evaporation description. On the other hand, by analyzing the $<N/Z>$ it was shown that the same new evaporation calculation predicts values which are consistent with the experimental $<N/Z>$ only if $\gamma \approx 14$-15 MeV. Thus taking into account the uncertainty of the model, it may be concluded that the essential decrease of the symmetry energy of hot light fragments down to $\gamma \approx 11$-15 MeV is observed. In this respect, the experimental γ_{ap} may be even larger than the real γ of the fragments in the freeze-out. The observed decrease of the symmetry coefficient is consistent with the previous investigations of the symmetry energy of hot light nuclei formed in multifragmentation processes [LeFev05,She05]. Indeed, the size and excitation energy of the source formed in the central collision of ^{12}C + ^{112,124}Sn ([LeFev05]) may be expected to be close to the excited sources formed in the peripheral collision of ^{124,136}Xe+Pb and thus the quantitative agreement of both investigations gives additional support to the result extracted in this work. The coincidence of both approaches used in this work to extract the symmetry-energy coefficient, namely the isoscaling and $<N>/Z$ ratio, provides more confidence on the lowering of the symmetry energy of hot light fragments. As demonstrated in [Bot04], this observation may have important consequences for processes in the supernovae, where densities and temperatures close to the conditions corresponding to the nuclear multifragmentation can be reached.

According to the above analysis, the fragments formed in the multifragment break-up of the highly excited nuclear source seem to be produced with a reduced value of the symmetry-energy coefficient with respect to the cold nuclei. The calculations presented in chapter 6.2.2 using the three-stage version of the ABRABLA code (i.e. including the break-up process) were performed with the binding energy calculated according to FRLDM (finite range liquid drop model) [Sie86] with the symmetry-energy coefficient of cold nuclei. As found in Fig. 6.3 right, the calculations with temperatures assumed in the above analysis (T=4-6 MeV) do not correctly reproduce the $<N>/Z$ of the data in the lowest nuclear charge range considered in the above investigation. However, it should be emphasized that the ABRABLA code is not well suited for the description of the multifragmentation events composed of several fragments of similar sizes in the sense that, as stated in section 6.1.2, only the largest residue formed in the collision is followed after the break-up process. This consideration is motivated by the experimental conditions at the FRS, however, it may lead to the incomplete description of the lighter residues (in the intermediate mass range), which may be produced in the break-up and are not fully taken into account in the calculation. This limitation of the ABRABLA code was already mentioned in section 6.2.2. in relation to the observed underestimation of the experimental isotopic distributions of the lighter residues, presented in Fig. C1 and C2 in appendix C. Despite this limitation, however, the results concerning the heavier residues presented in chapter 6 remain valid, since it may be expected that in the configurations, where one large fragment survives the break-up process surrounded by few smaller clusters and a nucleon gas, lower influence of the surroundings could favor the symmetry-energy coefficient of cold nuclei.

Conclusions

Within this work the residues produced in the interactions of two projectiles with largely different isotopic composition on lead nuclei (^{124}Xe(N/Z=1.30) + Pb and ^{136}Xe(N/Z=1.52) + Pb, both at 1 A GeV), were measured and investigated. Both experiments were performed with the high-resolution magnetic spectrometer, the Fragment Separator at GSI, which provides a high mass resolution, allowing thus for the identification of the reaction residues in the complete mass and nuclear-charge range. This experimental information was used to measure the isotopic distributions over a broad range of the nuclear charge in both experiments. More than 1100 isotopes were measured in both experiments, which cover the isotopes of Z=3-56 elements in case of the ^{136}Xe+Pb reaction and Z=5-55 elements in case of the ^{124}Xe+Pb system. The angular-acceptance integrated cross sections were determined for isotopes in the complete nuclear-charge range, and the transmission-corrected production cross sections, which correspond to the real production rate of single isotopes, were determined for isotopes in the nuclear-charge range Z=10-55(56) for the ^{124}Xe and ^{136}Xe projectile, respectively. The production cross sections measured in each experiment range over several orders of magnitude from 1μb to 3b with the relative uncertainty corresponding to 8-15% in most cases.

There are two important aspect of such extensive experimental information. Firstly, the isotopic distributions measured over a broad nuclear-charge range from reactions of projectiles, which largely differ in their isotopic composition, may be analyzed in order to access some of the specific properties of the highly excited nuclear system formed in the collision. Moreover, the availability of the broad range of production cross sections serves as an important data base for testing the validity of codes and parameterizations of the production cross sections, which is especially useful for the planning and design of the facilities for the rare ion beams production.

One of the original motivations of this work was to investigate to what extent the process of break-up of a highly excited nuclear system may manifest in the isotopic composition of the final residues, produced in the relativistic heavy-ion collisions and identified in a broad range of the nuclear charge, and eventually by exploring this observable to extract some properties of the hot fragments formed in this process. Particularly two aspects were investigated with the available experimental data – the sensitivity of the final isotopic composition to the thermal conditions at the freeze-out of the break-up stage and the possibility to extract information on the symmetry-energy coefficient of fragments formed in the process of multifragment break-up.

As observed in [Schm02, Sté91,Morr80] the mean isotopic composition of the final residues reveals a sensitivity to the excitation energy of the system entering the evaporation process. In [Schm02] a specific approach to investigate this sensitivity to the thermal conditions determining the excitation energy of the nucleus entering the evaporation process following the nuclear break-up was proposed. This method was named the isospin-thermometer method and was based on the observation that the final residues do not reach the residue corridor, characterized by the equilibrium proton and neutron emission probabilities. Nevertheless, already in [Char98] it was suggested that the final residues from the very n- (p-) rich projectiles may never reach this corridor as a consequence of the emission of more complex clusters during evaporation, which may become rather common for a highly excited nuclear system. It was one of the aims of this work to explore the influence and competition of these two processes (nuclear break-up and evaporation of complex clusters) on the isotopic composition of the final residues in the complete nuclear-charge range, profiting from the measurement with two projectiles largely differing in their N/Z. For the purpose of this investigation the mean N-over-Z ratio ($\langle N\rangle/Z$) of the final residues was used, which allows a direct comparison with the N/Z of the two projectiles. By exploring this observable, a clear memory on the isotopic composition of the projectile, preserved over the whole range of the nuclear charge investigated was seen, which in case of the lightest isotopes even prevent them from reaching the stability line. A dedicated investigation of the relative importance of the two processes and their influence on the experimental data was performed with the ABRABLA code [Gaim91]. It was found that indeed, the emission of complex cluster results in an enhanced production of more n-rich final residues with respect to the calculation considering solely the n, p and α emission and its influence was observed to be more pronounced in case of the more n-rich projectile. However, in case of both projectiles it was observed that the emission of complex clusters is not sufficient to reproduce the 'magnitude' of the memory on the initial N/Z, which suggested a contribution of additional process, possibly the nuclear break-up. Indeed, the calculation including the break-up process resulted in an improved description not only for the $\langle N\rangle/Z$, but also for the overall shape of the isotopic distributions for a certain range of the assumed freeze-out temperatures. This observation suggests that the influence of the process of nuclear break-up is reflected in the final isotopic composition, which appears to be sensitive in particularly to the thermal conditions ruling the properties of the nucleus entering the evaporation process. This result basically confirms the findings of [Schm02]. Nevertheless, it was observed in the present analysis that the emission of more complex clusters indeed considerably influences the course of the evaporation process and as a consequence calculations assuming different temperatures of T=5-8 MeV were observed to reproduced different regions of the experimental data in case of the more n-rich projectile. In light of other experimental results and the observation of very good isoscaling in the experimental data [Tsa01c], the quantitative values of the nuclear temperature extracted by this analysis appear to be too high especially in the nuclear-charge range below Z~15, and a lower difference between the two systems may be expected. This suggests that additional considerations are still needed to improve the description of the process of the nuclear break-up and following evaporation in ABRABLA in order to be able to draw more quantitative conclusions. Nevertheless, the present investigation showed that the mean N-over-Z of the final residues may indeed serve as a relevant experimental observable to extract the thermal properties of the hot system entering the evaporation process. In particular, a direct experimental indication of the sensitivity of the final $\langle N\rangle/Z$ to the excitation energy acquired in the collision for the nuclei close to projectile could be observed in the comparison of the reactions of ^{136}Xe with ^{1}H and Pb targets.

It was discussed in [Tsa01c] that the phenomenon of isoscaling, i.e. an exponential dependence of the yield ratio of products from two systems differing in their isotopic composition, on N or Z, was observed in many different reaction mechanisms. The investigations of isoscaling were predominantly performed in a rather narrow nuclear-charge range, corresponding mostly to Z=1-8 [LeFev05,She05,Tsa01c] and over a broader range in the Fermi energy regime [Sou03,Sou04]. It was one of the interests of this work to investigate to what extent the isoscaling is respected in the broad nuclear-charge range explored in our data and to apply the method introduced in [Bot02] to investigate the symmetry-energy coefficient of fragments formed in the multifragment configurations. It was observed that the isoscaling phenomenon is very well respected in an almost complete nuclear-charge range, which is the first observation of the isoscaling phenomenon in such a broad range of elements in the relativistic energy regime. A slight deviation was observed only in the direct vicinity of the projectile, which may be attributed to increasingly different widths of the isotopic distributions in this range of nuclear charge, which in case of $Z \geq 52$ even deviate from a Gaussian shape. From the observed isoscaling, the corresponding exponent α for nuclei in the complete nuclear charge range was extracted, which reveals a steep decrease with decreasing charge, a trend consistent with similar investigations of isoscaling in evaporation and multifragmentation reactions, respectively. For the purpose of the symmetry energy investigation the coefficient of isoscaling in the nuclear-charge range Z=10-13 was considered, which corresponds to a multifragment break-up into fragments of similar size [Schü96]. In order to estimate the symmetry-energy coefficient, a method introduced in [Bot02] was used, according to which the isoscaling parameter and the symmetry-energy coefficient may be related through the temperature and isotopic composition of the multifragmenting systems. For the purpose of temperature estimation we had to rely on the knowledge delivered by other experimental investigations of systems of similar size as studied in our experiments, since as discussed earlier the quantitative analysis of the thermal conditions at the freeze-out of the break-up stage, performed with the ABRABLA code cannot yet be used for this purpose. By assuming the nuclear temperature of the order of T=4-6 MeV [Hau00,Ort04,Nat02] and neglecting the change of the isotopic composition of source systems after the initial collision, the symmetry-energy coefficient of 14±3MeV was extracted. This result is considerably lower than values generally obtained from the properties of cold nuclei. Similar indications of lowering of the symmetry-energy coefficient in the multifragment break-up processes were found in [LeFev05,She05]. This observation indicates a change of properties of hot fragments formed in the multifragment break-up of a highly excited source and as discussed in [Bot04] it may have important consequences for the processes in supernovae

Finally, the experimental data measured in the two reaction systems studied within this work serve as an important data base for comparison with the present codes and parameterizations of the production cross sections. For this purpose, the data were compared with the EPAX parameterization of the fragmentation cross sections, presently extensively considered for predictions of the production cross sections for the purpose of the rare ion beam facilities. This comparison revealed some deficiencies of the EPAX parameterization especially in the prediction of the production cross sections of lighter residues, which may be accounted for by the fact that only fragments in the vicinity of the projectile were available for establishing this parameterization [Webb90,Shu99,Web94,Wes79,Bla94, Webb90,Shu99]. Moreover, it was observed that the production cross sections of the n-deficient isotopes are underestimated in the vicinity of the more n-rich ^{136}Xe projectile. This may be related to the fact that only the end-products from the less n-rich Xe-isotopes were available when the parameterization was formulated. This comparison between the present experimental data and the EPAX parameterization seems to be of particular importance especially in use of EPAX for the prediction of the production cross sections of n-rich isotopes, which are of special interest in ISOL-based facilities for the production of rare ion beams by fragmentation of secondary n-rich beam. The present data provide an extensive data base and may be used to contribute to an improved formulation of the EPAX parameterization, especially considering the production of fragments in the vicinity to the projectile in case of the more n-rich system as well as of the lighter residues.

The production cross sections measured within this work were analyzed with respect to the information on the properties of highly excited nuclear systems, which was one of the initial motivations of this work. Indeed, the influence of the nuclear break-up reflected in the isotopic composition of the final residues was found, in particular the analysis showed that the thermal properties of hot system are reflected in the final mean N-over-Z ratio, which being carefully analyzed may indeed serve as a relevant experimental observable to extract this information. The production cross sections of a broad range of isotopes available for the two Xe-projectiles will allow to improve the description of the reaction process in the ABRABLA code and may contribute to the improved parameterization of the production cross sections of exotic nuclei.

Appendix A

Compilation of the cross sections measured in ^{136}Xe+Pb and ^{124}Xe+Pb reactions

In this section the production cross sections measured in the two experiments analyzed within this work are summarized. The angular acceptance-integrated production cross sections were determined for all isotopes measured in the two experiments, which correspond to isotopes of elements Z=5-55 and Z=3-56 in case of ^{124}Xe+Pb and ^{136}Xe+Pb experiments, respectively. An overview of the complete data is shown in Fig. A.1 below. As discussed in section 4.3, the correction for the limited transmission through the FRS could be performed only for isotopes of elements above Z=10 in both experiments. The transmission corrected production cross sections represent the real formation cross sections in the target and are listed in table A.1. The corresponding absolute errors (values include both, statistical and systematical errors) are indicated.

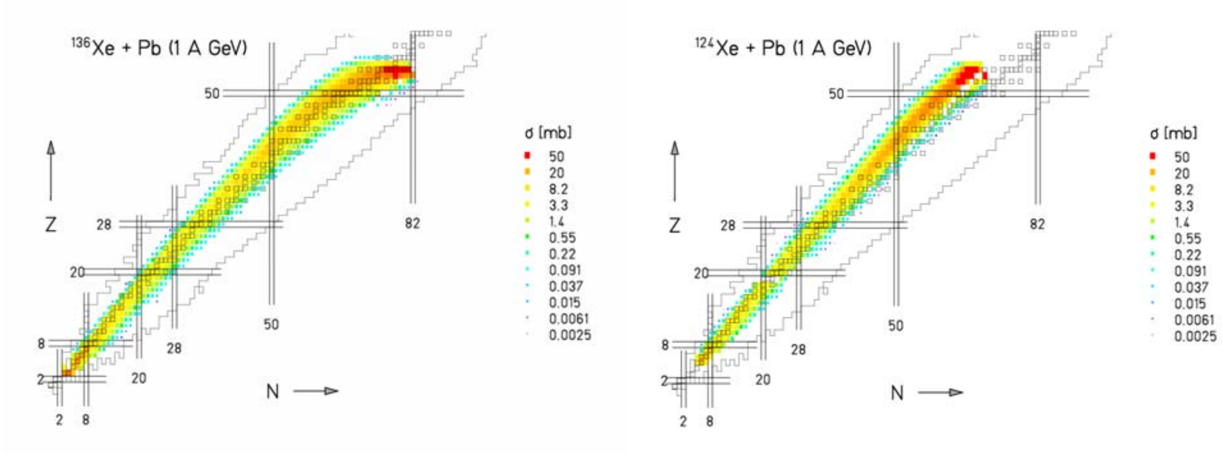

Fig. A.1: The angular-acceptance integrated production cross sections for isotopes of Z=5-55 and Z=3-56 elements measured in ^{124}Xe+Pb and ^{136}Xe+Pb experiments, respectively, presented in the chart of nuclides.

Table A.1: The full list of the transmission corrected production cross sections of isotopes of *Z*=10-55(56) elements measured in the ^{136}Xe+Pb (left column) and ^{124}Xe+Pb (right column) experiments. The production cross sections of isotopes of element *Z*=19 both from heavy- and light-fragment settings are presented. The absolute errors include statistical and systematical uncertainties.

^{136}Xe+Pb 1 A GeV				^{124}Xe+Pb 1 A GeV			
Z	**N**	**σ [mb]**	**Δσ[mb]**	**Z**	**N**	**σ [mb]**	**Δσ[mb]**
10	8	0.0598	0.0082	10	8	0.146	0.015
10	9	0.630	0.073	10	9	1.68	0.17
10	10	10.7	1.2	10	10	17.3	1.7
10	11	25.6	2.9	10	11	29.1	2.9
10	12	31.7	3.6	10	12	25.0	2.5
10	13	10.9	1.2	10	13	6.04	0.60
10	14	4.33	0.49	10	14	2.07	0.21
10	15	0.706	0.083				
10	16	0.130	0.016	11	9	0.0922	0.0103
10	17	0.0118	0.0021	11	10	0.921	0.092
				11	11	9.87	0.98
11	10	0.349	0.040	11	12	29.3	2.9
11	11	5.27	0.59	11	13	16.7	1.7
11	12	24.7	2.8	11	14	7.90	0.79
11	13	19.7	2.2	11	15	1.79	0.18
11	14	13.9	1.6	11	16	0.477	0.048
11	15	3.59	0.40				
11	16	1.24	0.14	12	10	0.0709	0.0076
11	17	0.227	0.027	12	11	1.122	0.112
11	18	0.0469	0.0071	12	12	15.4	1.5
				12	13	23.0	2.2
12	11	0.390	0.044	12	14	21.3	2.1
12	12	8.38	0.93	12	15	6.12	0.61
12	13	17.5	1.9	12	16	2.17	0.22
12	14	22.6	2.5	12	17	0.307	0.031
12	15	10.2	1.1				
12	16	4.61	0.51	13	11	0.0273	0.0031
12	17	0.752	0.085	13	12	0.407	0.041
12	18	0.298	0.035	13	13	5.98	0.59
				13	14	22.6	2.3
13	12	0.133	0.016	13	15	15.0	1.5
13	13	2.90	0.31	13	16	7.63	0.76
13	14	16.6	1.8	13	17	1.71	0.17
13	15	15.3	1.6	13	18	0.569	0.057
13	16	12.3	1.3				
13	17	3.62	0.39	14	12	0.0267	0.0030
13	18	1.56	0.17	14	13	0.529	0.053
13	19	0.294	0.035	14	14	9.73	0.97
13	20	0.131	0.018	14	15	18.1	1.8
				14	16	20.4	2.0
14	13	0.143	0.016	14	17	6.77	0.67
14	14	4.81	0.50	14	18	2.11	0.21
14	15	11.8	1.2	14	19	0.377	0.038
14	16	19.3	2.0	14	20	0.116	0.012
14	17	10.2	1.1				

^{136}Xe+Pb 1 A GeV ^{124}Xe+Pb 1 A GeV

Z	N	σ [mb]	Δσ[mb]	Z	N	σ [mb]	Δσ[mb]
14	18	4.64	0.49	15	14	0.152	0.016
14	19	1.10	0.12	15	15	2.19	0.22
14	20	0.432	0.048	15	16	13.0	1.3
				15	17	13.4	1.3
15	14	0.0378	0.0051	15	18	8.12	0.81
15	15	0.875	0.089	15	19	2.19	0.22
15	16	7.97	0.81	15	20	0.710	0.071
15	17	12.0	1.2	15	21	0.144	0.015
15	18	10.9	1.1				
15	19	4.51	0.46	16	15	0.156	0.016
15	20	1.96	0.20	16	16	2.87	0.29
15	21	0.513	0.054	16	17	10.2	1.0
15	22	0.158	0.018	16	18	15.8	1.6
				16	19	7.88	0.78
16	16	1.06	0.16	16	20	3.00	0.30
16	17	5.50	0.81	16	21	0.765	0.076
16	18	12.7	1.9	16	22	0.205	0.021
16	19	9.62	1.43	16	23	0.0406	0.0043
16	20	5.78	0.86				
16	21	2.04	0.30	17	16	0.0443	0.005
16	22	0.753	0.113	17	17	1.00	0.10
16	23	0.190	0.029	17	18	7.84	0.78
16	24	0.0568	0.0098	17	19	11.8	1.2
				17	20	8.62	0.86
17	17	0.317	0.052	17	21	3.15	0.31
17	18	3.94	0.64	17	22	1.12	0.11
17	19	8.71	1.41	17	23	0.309	0.031
17	20	9.85	1.60	17	24	0.0790	0.0081
17	21	5.54	0.90				
17	22	2.85	0.46	18	18	1.33	0.15
17	23	1.04	0.17	18	19	6.60	0.74
17	24	0.381	0.063	18	20	11.8	1.3
17	25	0.0844	0.0151	18	21	8.39	0.93
				18	22	3.78	0.42
18	17	0.0136	0.0021	18	23	1.22	0.13
18	18	0.456	0.057	18	24	0.366	0.041
18	19	2.93	0.37				
18	20	8.27	1.03	19	19	0.388	0.055
18	21	8.71	1.09	19	20	3.88	0.55
18	22	5.85	0.73	19	21	7.32	1.03
18	23	2.89	0.36	19	22	7.12	1.01
18	24	1.24	0.16	19	23	4.14	0.58
18	25	0.366	0.047	19	24	1.77	0.25
18	26	0.109	0.018	19	25	0.512	0.072
				19	26	0.167	0.024

^{136}Xe+Pb 1 A GeV

Z	N	σ [mb]	Δσ[mb]
19	19	0.161	0.019
19	20	2.19	0.25
19	21	6.26	0.72
19	22	8.07	0.93
19	23	6.25	0.72
19	24	3.84	0.44
19	25	1.52	0.17
19	26	0.549	0.064
19	27	0.131	0.018
20	20	0.209	0.019
20	21	1.92	0.17
20	22	5.97	0.54
20	23	8.46	0.77
20	24	7.51	0.68
20	25	4.03	0.37
20	26	1.86	0.17
20	27	0.620	0.057
20	28	0.144	0.014
21	21	0.0767	0.0072
21	22	1.11	0.09
21	23	4.44	0.39
21	24	8.16	0.73
21	25	7.27	0.65
21	26	4.87	0.43
21	27	2.14	0.19
21	28	0.777	0.069
21	29	0.174	0.017
21	30	0.0461	0.0063
22	22	0.0761	0.0070
22	23	0.825	0.073
22	24	4.27	0.37
22	25	7.72	0.67
22	26	8.23	0.72
22	27	5.14	0.45
22	28	2.55	0.22
22	29	0.835	0.074
22	30	0.254	0.023
22	31	0.0710	0.0104
23	23	0.0340	0.0033
23	24	0.549	0.048
23	25	3.00	0.26

^{124}Xe+Pb 1 A GeV

Z	N	σ [mb]	Δσ[mb]
19[#]	24	1.69	0.19
19[#]	25	0.393	0.044
20	20	0.444	0.050
20	21	3.39	0.38
20	22	8.68	0.97
20	23	9.26	1.03
20	24	6.24	0.69
20	25	3.27	0.37
21	21	0.179	0.021
21	22	2.20	0.25
21	23	6.80	0.76
21	24	9.93	1.11
21	25	6.91	0.77
21	26	3.30	0.37
21	27	1.38	0.15
22	22	0.22	0.02
22	23	1.98	0.22
22	24	7.36	0.82
22	25	10.4	1.15
22	26	8.15	0.91
22	27	3.79	0.42
22	28	1.42	0.16
23	22	0.0110	0.0014
23	23	0.150	0.015
23	24	1.53	0.15
23	25	6.08	0.61
23	26	10.4	1.0
23	27	8.63	0.86
23	28	4.25	0.42
23	29	1.36	0.14
23	30	0.426	0.043
23	31	0.107	0.011
23	32	0.0224	0.0024
24	24	0.140	0.014
24	25	1.28	0.13
24	26	5.65	0.56
24	27	10.4	1.0
24	28	9.40	0.94
24	29	4.52	0.45
24	30	1.78	0.18

[#] isotopes from light-fragment settings

^{136}Xe+Pb 1 A GeV

Z	N	σ [mb]	Δσ[mb]
23	26	7.16	0.61
23	27	8.09	0.69
23	28	5.70	0.49
23	29	2.69	0.23
23	30	1.21	0.10
23	31	0.379	0.033
23	32	0.128	0.012
24	24	0.0309	0.0030
24	25	0.423	0.036
24	26	2.64	0.22
24	27	6.46	0.54
24	28	8.17	0.69
24	29	5.70	0.48
24	30	3.37	0.29
24	31	1.33	0.11
24	32	0.565	0.048
24	33	0.190	0.017
24	34	0.0580	0.0075
25	25	0.0172	0.0019
25	26	0.278	0.024
25	27	1.97	0.16
25	28	5.67	0.47
25	29	7.45	0.62
25	30	6.44	0.53
25	31	3.50	0.29
25	32	1.93	0.16
25	33	0.735	0.062
25	34	0.287	0.024
25	35	0.0911	0.0089
26	26	0.0128	0.0022
26	27	0.199	0.017
26	28	1.55	0.13
26	29	4.80	0.39
26	30	8.01	0.65
26	31	6.57	0.53
26	32	4.56	0.37
26	33	2.26	0.18
26	34	1.05	0.09
26	35	0.390	0.032
26	36	0.119	0.011
26	37	0.0368	0.0043

^{124}Xe+Pb 1 A GeV

Z	N	σ [mb]	Δσ[mb]
24	31	0.493	0.049
24	32	0.145	0.015
24	33	0.0340	0.0035
24	34	0.0073	0.0009
25	25	0.0772	0.0079
25	26	0.895	0.089
25	27	4.59	0.46
25	28	9.73	0.97
25	29	9.24	0.92
25	30	5.51	0.55
25	31	1.93	0.19
25	32	0.711	0.071
25	33	0.185	0.019
25	34	0.0565	0.0058
25	35	0.0118	0.0013
25	36	0.0021	0.0003
26	25	0.0081	0.0016
26	26	0.0588	0.0093
26	27	0.661	0.103
26	28	3.55	0.55
26	29	7.99	1.25
26	30	9.53	1.49
26	31	5.61	0.88
26	32	2.67	0.42
26	33	0.813	0.127
26	34	0.269	0.042
26	35	0.0643	0.0101
27	27	0.0314	0.0047
27	28	0.417	0.060
27	29	2.53	0.37
27	30	7.31	1.05
27	31	9.15	1.32
27	32	7.38	1.07
27	33	3.22	0.47
27	34	1.23	0.18
27	35	0.378	0.055
27	36	0.103	0.015
28	27	0.0059	0.0012
28	28	0.0209	0.0029
28	29	0.240	0.032
28	30	1.69	0.22

^{136}Xe+Pb 1 A GeV

Z	N	σ [mb]	Δσ[mb]
27	27	0.0077	0.0011
27	28	0.110	0.009
27	29	0.97	0.08
27	30	3.95	0.31
27	31	6.88	0.55
27	32	7.56	0.60
27	33	4.92	0.39
27	34	2.99	0.24
27	35	1.34	0.11
27	36	0.572	0.046
27	37	0.194	0.016
27	38	0.0781	0.0091
28	29	0.0512	0.0045
28	30	0.577	0.046
28	31	2.76	0.22
28	32	6.54	0.51
28	33	7.69	0.60
28	34	6.25	0.49
28	35	3.58	0.28
28	36	1.87	0.15
28	37	0.786	0.062
28	38	0.284	0.023
28	39	0.0883	0.0077
29	31	0.291	0.023
29	32	1.79	0.14
29	33	4.96	0.39
29	34	7.54	0.59
29	35	6.44	0.50
29	36	4.56	0.36
29	37	2.52	0.20
29	38	1.17	0.09
29	39	0.455	0.036
29	40	0.162	0.013
29	41	0.0511	0.0052
30	31	0.0144	0.0016
30	32	0.207	0.017
30	33	1.36	0.11
30	34	4.54	0.35
30	35	7.55	0.59
30	36	7.56	0.59
30	37	5.34	0.42
30	38	3.19	0.25

^{124}Xe+Pb 1 A GeV

Z	N	σ [mb]	Δσ[mb]
28	31	5.75	0.76
28	32	9.83	1.31
28	33	8.27	1.10
28	34	4.75	0.63
28	35	1.66	0.22
28	36	0.544	0.072
28	37	---	---
28	38	0.0416	0.0056
29	29	0.0121	0.0015
29	30	0.130	0.015
29	31	1.04	0.12
29	32	4.31	0.51
29	33	8.44	0.98
29	34	8.94	1.04
29	35	5.45	0.63
29	36	2.44	0.28
29	37	0.819	0.096
29	38	0.279	0.033
29	39	0.0612	0.0072
30	31	0.0982	0.0108
30	32	0.836	0.091
30	33	3.80	0.41
30	34	8.73	0.95
30	35	10.5	1.1
30	36	7.26	0.79
30	37	3.60	0.39
30	38	1.54	0.17
30	39	---	---
30	40	0.104	0.012
30	41	0.0202	0.0024
30	42	0.0034	0.0005
31	32	0.0551	0.0056
31	33	0.489	0.048
31	34	2.55	0.25
31	35	6.95	0.68
31	36	10.3	1.0
31	37	8.33	0.82
31	38	4.32	0.42
31	39	2.29	0.23
31	40	0.861	0.088
31	41	0.272	0.028
31	42	0.0406	0.0042

^{136}Xe+Pb 1 A GeV

Z	N	σ [mb]	$\Delta\sigma_{stat}$ %
30	39	1.59	0.12
30	40	0.681	0.054
30	41	0.248	0.020
30	42	0.0842	0.0076
30	43	0.0183	0.0027
31	33	0.107	0.008
31	34	0.782	0.058
31	35	3.14	0.23
31	36	6.43	0.47
31	37	7.61	0.56
31	38	6.13	0.45
31	39	4.06	0.30
31	40	2.27	0.17
31	41	0.974	0.072
31	42	0.422	0.031
31	43	0.146	0.012
32	34	0.0676	0.0055
32	35	0.552	0.041
32	36	2.60	0.19
32	37	6.12	0.44
32	38	8.26	0.60
32	39	7.04	0.51
32	40	5.02	0.36
32	41	2.85	0.21
32	42	1.41	0.10
32	43	0.58	0.04
32	44	0.211	0.016
33	35	0.0341	0.0030
33	36	0.342	0.025
33	37	1.72	0.12
33	38	5.10	0.37
33	39	7.79	0.56
33	40	8.15	0.59
33	41	5.79	0.42
33	42	3.83	0.28
33	43	1.89	0.14
33	44	0.914	0.066
33	45	0.318	0.023
33	46	0.140	0.016
33	47	0.0406	0.0042

^{124}Xe+Pb 1 A GeV

Z	N	σ [mb]	$\Delta\sigma_{stat}$ %
32	33	0.0440	0.0044
32	34	0.371	0.036
32	35	2.12	0.20
32	36	6.61	0.63
32	37	11.1	1.1
32	38	10.7	1.0
32	39	5.86	0.56
32	40	2.99	0.29
32	41	1.06	0.10
32	42	0.331	0.034
32	43	0.0839	0.0083
33	34	0.0347	0.0028
33	35	0.240	0.017
33	36	1.41	0.10
33	37	5.08	0.36
33	38	10.4	0.7
33	39	11.1	0.8
33	40	7.54	0.54
33	41	3.49	0.25
33	42	1.54	0.11
33	43	0.389	0.031
33	44	0.159	0.013
33	45	0.0180	0.0016
33	46	0.0035	0.0004
34	35	0.0216	0.0018
34	36	0.184	0.013
34	37	1.18	0.08
34	38	4.81	0.34
34	39	10.3	0.7
34	40	13.6	0.9
34	41	9.33	0.66
34	42	5.04	0.36
34	43	1.98	0.15
34	44	---	---
34	45	0.231	0.019
34	46	---	---
34	47	0.0056	0.0005
35	36	0.0129	0.0012
35	37	0.119	0.009
35	38	0.798	0.057
35	39	3.46	0.25
35	40	9.27	0.66

^{136}Xe+Pb 1 A GeV				^{124}Xe+Pb 1 A GeV			
Z	**N**	**σ [mb]**	**Δσ[mb]**	**Z**	**N**	**σ [mb]**	**Δσ[mb]**
34	36	0.0228	0.0021	35	41	13.0	0.9
34	37	0.244	0.018	35	42	11.6	0.8
34	38	1.44	0.10	35	43	5.53	0.39
34	39	4.32	0.31	35	44	2.97	0.21
34	40	8.16	0.58	35	45	0.973	0.071
34	41	8.45	0.60	35	46	0.274	0.022
34	42	7.08	0.50	35	47	0.133	0.013
34	43	4.44	0.32	35	48	0.0092	0.0008
34	44	2.63	0.19				
34	45	1.22	0.09	36	38	0.0786	0.0058
34	46	0.513	0.037	36	39	0.639	0.045
34	47	0.195	0.015	36	40	3.09	0.22
34	48	0.0562	0.0049	36	41	8.73	0.62
				36	42	14.6	1.0
35	37	0.0120	0.0013	36	43	13.2	0.9
35	38	0.126	0.009	36	44	8.53	0.60
35	39	0.873	0.063	36	45	3.72	0.27
35	40	3.39	0.24	36	46	1.24	0.09
35	41	6.97	0.49	36	47	0.329	0.025
35	42	9.10	0.65	36	48	0.0797	0.0059
35	43	7.46	0.53				
35	44	5.88	0.42	37	39	0.0465	0.0035
35	45	3.33	0.24	37	40	0.393	0.028
35	46	1.78	0.13	37	41	2.18	0.15
35	47	0.766	0.055	37	42	7.33	0.52
35	48	0.285	0.021	37	43	13.4	0.9
35	49	0.102	0.009	37	44	15.5	1.1
				37	45	10.2	0.7
36	39	0.0908	0.0072	37	46	5.06	0.36
36	40	0.686	0.049	37	47	1.72	0.12
36	41	2.79	0.20	37	48	0.380	0.030
36	42	6.69	0.47	37	49	0.126	0.009
36	43	8.89	0.63	37	50	0.0171	0.0015
36	44	9.09	0.64				
36	45	6.68	0.47	38	40	0.0343	0.0027
36	46	4.36	0.31	38	41	0.296	0.021
36	47	2.38	0.17	38	42	1.74	0.12
36	48	1.09	0.08	38	43	6.37	0.45
36	49	0.419	0.030	38	44	13.9	0.9
36	50	0.136	0.010	38	45	17.2	1.2
36	51	0.0432	0.0068	38	46	13.7	1.0
				38	47	6.69	0.47
37	40	0.0439	0.0048	38	48	2.70	0.19
37	41	0.391	0.028	38	49	---	---
37	42	1.95	0.14	38	50	0.194	0.014

^{136}Xe+Pb 1 A GeV

Z	N	σ [mb]	Δσ[mb]
37	43	5.29	0.38
37	44	9.05	0.64
37	45	9.28	0.66
37	46	8.17	0.58
37	47	5.43	0.38
37	48	3.18	0.23
37	49	1.48	0.11
37	50	0.595	0.043
37	51	0.222	0.016
37	52	0.0574	0.0051
38	41	0.0367	0.0038
38	42	0.266	0.019
38	43	1.47	0.11
38	44	4.67	0.33
38	45	8.69	0.62
38	46	10.4	0.7
38	47	9.51	0.67
38	48	6.86	0.49
38	49	4.00	0.28
38	50	1.92	0.14
38	51	0.867	0.062
38	52	0.340	0.025
38	53	0.140	0.011
38	54	0.0518	0.0056
39	43	0.159	0.012
39	44	0.973	0.069
39	45	3.62	0.26
39	46	8.04	0.57
39	47	10.9	0.8
39	48	10.9	0.8
39	49	8.09	0.57
39	50	4.89	0.35
39	51	2.50	0.18
39	52	1.21	0.09
39	53	0.551	0.039
39	54	0.245	0.018
39	55	0.0852	0.0071
40	44	0.0881	0.0070
40	45	0.690	0.049
40	46	2.93	0.21
40	47	7.31	0.52
40	48	11.4	0.8

^{124}Xe+Pb 1 A GeV

Z	N	σ [mb]	Δσ[mb]
38	51	0.0602	0.0069
39	42	0.178	0.013
39	43	1.20	0.09
39	44	4.93	0.35
39	45	12.3	0.9
39	46	18.2	1.3
39	47	16.2	1.1
39	48	9.47	0.67
39	49	3.52	0.25
39	50	1.13	0.08
39	51	0.246	0.019
39	52	0.0642	0.0048
40	43	0.132	0.009
40	44	0.899	0.064
40	45	4.13	0.29
40	46	11.5	0.8
40	47	19.4	1.4
40	48	19.6	1.4
40	49	12.0	0.9
40	50	4.75	0.34
40	51	1.27	0.09
40	52	0.385	0.033
40	53	0.127	0.009
41	44	0.0776	0.0057
41	45	0.615	0.044
41	46	3.16	0.22
41	47	10.0	0.7
41	48	19.3	1.4
41	49	21.5	1.5
41	50	14.2	1.0
41	51	5.78	0.41
41	52	1.99	0.14
41	53	---	---
41	54	0.217	0.016
41	55	0.0450	0.0035
42	45	0.0550	0.0041
42	46	0.438	0.031
42	47	2.53	0.18
42	48	9.13	0.65
42	49	19.3	1.4
42	50	23.2	1.6

^{136}Xe+Pb 1 A GeV

^{124}Xe+Pb 1 A GeV

Z	N	σ [mb]	Δσ[mb]	Z	N	σ [mb]	Δσ[mb]
40	49	11.9	0.8	42	51	14.9	1.1
40	50	9.39	0.66	42	52	7.61	0.54
40	51	5.72	0.41	42	53	2.71	0.19
40	52	3.34	0.24	42	54	---	---
40	53	1.78	0.13	42	55	0.346	0.026
40	54	0.874	0.062	42	56	0.0931	0.0069
40	55	0.411	0.030	42	57	0.0165	0.0014
40	56	0.172	0.013				
40	57	0.0779	0.0071	43	46	0.0347	0.0027
				43	47	0.308	0.022
41	45	0.0548	0.0052	43	48	1.94	0.14
41	46	0.433	0.032	43	49	8.05	0.57
41	47	2.18	0.16	43	50	18.7	1.3
41	48	6.47	0.46	43	51	22.3	1.6
41	49	11.0	0.8	43	52	17.6	1.2
41	50	12.2	0.9	43	53	9.78	0.69
41	51	9.69	0.69	43	54	4.60	0.33
41	52	6.96	0.49	43	55	1.39	0.10
41	53	4.44	0.31	43	57	0.186	0.014
41	54	2.71	0.19	43	58	0.0415	0.0032
41	55	1.44	0.10	43	59	0.0077	0.0008
41	56	0.724	0.052				
41	57	0.329	0.024	44	48	0.221	0.016
41	58	0.148	0.012	44	49	1.56	0.11
41	59	0.0461	0.0055	44	50	7.06	0.50
				44	51	16.5	1.2
42	46	0.0389	0.0051	44	52	23.6	1.7
42	47	0.298	0.022	44	53	19.8	1.4
42	48	1.66	0.12	44	54	13.3	0.9
42	49	5.54	0.39	44	55	6.58	0.5
42	50	10.4	0.7	44	56	1.67	0.13
42	51	11.4	0.8	44	57	---	---
42	52	10.6	0.8	44	58	0.340	0.025
42	53	8.24	0.58	44	59	0.0871	0.0071
42	54	5.97	0.42	44	60	0.0131	0.0011
42	55	3.82	0.27				
42	56	2.22	0.16	45	48	0.0154	0.0013
42	57	1.16	0.08	45	49	0.142	0.010
42	58	0.585	0.042	45	50	1.16	0.08
42	59	0.257	0.019	45	51	5.42	0.38
42	60	0.0998	0.0086	45	52	14.7	1.0
				45	53	22.6	1.6
43	48	0.186	0.014	45	54	23.4	1.7
43	49	1.27	0.09	45	55	16.3	1.2
43	50	4.51	0.32	45	56	9.60	0.68

^{136}Xe+Pb 1 A GeV				^{124}Xe+Pb 1 A GeV			
Z	**N**	**σ [mb]**	**Δσ[mb]**	**Z**	**N**	**σ [mb]**	**Δσ[mb]**
43	51	8.64	0.61	45	57	4.62	0.34
43	52	10.9	0.8	45	58	---	---
43	53	10.8	0.77	45	59	0.582	0.042
43	54	9.99	0.71	45	60	0.169	0.012
43	55	7.57	0.54	45	61	0.0275	0.0022
43	56	5.32	0.38	45	62	0.0077	0.0007
43	57	3.24	0.23				
43	58	1.94	0.14	46	50	0.102	0.007
43	59	0.999	0.071	46	51	0.804	0.057
43	60	0.538	0.039	46	52	4.11	0.29
43	61	0.211	0.016	46	53	12.2	0.9
43	62	0.0994	0.0102	46	54	23.1	1.6
				46	55	25.8	1.8
44	49	0.129	0.010	46	56	21.6	1.5
44	50	0.946	0.068	46	57	13.1	0.9
44	51	3.26	0.23	46	58	6.20	0.44
44	52	7.29	0.52	46	59	1.97	0.14
44	53	10.0	0.7	46	60	0.805	0.087
44	54	11.7	0.8	46	61	0.315	0.023
44	55	11.4	0.8	46	62	0.0857	0.0068
44	56	9.46	0.67	46	63	0.0109	0.0010
44	57	7.05	0.50				
44	58	4.72	0.33	47	51	0.0550	0.0041
44	59	2.82	0.20	47	52	0.499	0.036
44	60	1.63	0.12	47	53	2.69	0.19
44	61	0.852	0.061	47	54	9.70	0.69
44	62	0.418	0.031	47	55	20.1	1.4
44	63	0.187	0.015	47	56	28.2	2.0
44	64	0.0771	0.0081	47	57	25.7	1.8
				47	58	17.8	1.3
45	50	0.0769	0.0063	47	59	9.20	0.65
45	51	0.584	0.042	47	60	3.92	0.28
45	52	2.33	0.17	47	61	---	---
45	53	5.65	0.40	47	62	0.566	0.040
45	54	9.24	0.65	47	63	0.169	0.013
45	55	11.4	0.8	47	64	0.0364	0.0028
45	56	12.6	0.9	47	65	0.0072	0.0006
45	57	11.2	0.8				
45	58	9.17	0.65	48	52	0.0284	0.0022
45	59	6.57	0.47	48	53	0.278	0.020
45	60	4.47	0.32	48	54	1.71	0.12
45	61	2.63	0.19	48	55	6.88	0.49
45	62	1.56	0.11	48	56	17.7	1.3
45	63	0.789	0.057	48	57	28.7	2.0
45	64	0.425	0.031	48	58	31.5	2.2

^{136}Xe+Pb 1 A GeV				^{124}Xe+Pb 1 A GeV			
Z	**N**	**σ [mb]**	**Δσ[mb]**	**Z**	**N**	**σ [mb]**	**Δσ[mb]**
45	65	0.171	0.014	48	59	22.9	1.63
45	66	0.0698	0.008	48	60	14.1	1.0
				48	61	6.34	0.45
46	51	0.0241	0.0025	48	62	---	---
46	52	0.303	0.022	48	63	1.09	0.08
46	53	1.45	0.10	48	64	0.274	0.020
46	54	4.27	0.30	48	65	0.0577	0.0043
46	55	7.78	0.55	48	66	0.0181	0.0015
46	56	11.1	0.8	48	67	0.0032	0.0005
46	57	12.9	0.9				
46	58	12.7	0.9	49	53	0.0124	0.0011
46	59	11.1	0.8	49	54	0.124	0.009
46	60	8.73	0.62	49	55	0.861	0.061
46	61	6.20	0.44	49	56	4.20	0.30
46	62	4.11	0.29	49	57	12.8	0.9
46	63	2.51	0.18	49	58	26.5	1.9
46	64	1.46	0.10	49	59	33.5	2.4
46	65	0.742	0.054	49	60	29.4	2.1
46	66	0.402	0.030	49	61	19.7	1.4
46	67	0.144	0.013	49	62	9.55	0.68
46	68	0.0715	0.0080	49	63	---	---
				49	64	1.54	0.11
47	53	0.159	0.012	49	65	0.729	0.052
47	54	0.859	0.062	49	66	0.218	0.016
47	55	2.79	0.20	49	67	0.0326	0.0025
47	56	6.11	0.43	49	68	0.0094	0.0008
47	57	9.49	0.67				
47	58	12.6	0.9	50	55	0.0484	0.0036
47	59	13.4	0.9	50	56	0.420	0.030
47	60	13.1	0.9	50	57	2.38	0.17
47	61	11.0	0.8	50	58	8.64	0.61
47	62	8.81	0.62	50	59	22.6	1.6
47	63	6.17	0.44	50	60	35.9	2.5
47	64	4.28	0.30	50	61	37.7	2.7
47	65	2.58	0.18	50	62	31.0	2.2
47	66	1.59	0.11	50	63	22.4	1.6
47	67	0.872	0.063	50	64	6.51	0.46
47	68	0.458	0.034	50	65	---	---
47	69	0.224	0.018	50	66	1.66	0.12
				50	67	0.581	0.042
48	54	0.0673	0.0058	50	68	0.108	0.008
48	55	0.408	0.030	50	69	0.0219	0.0017
48	56	1.73	0.12				
48	57	4.43	0.31	51	56	0.0137	0.0012
48	58	8.09	0.57	51	57	0.144	0.010

^{136}Xe+Pb 1 A GeV

Z	N	σ [mb]	Δσ[mb]
48	59	11.6	0.8
48	60	13.9	1.0
48	61	14.5	1.0
48	62	13.5	1.0
48	63	11.5	0.9
48	64	8.99	0.64
48	65	6.51	0.46
48	66	4.58	0.32
48	67	2.90	0.21
48	68	1.79	0.13
48	69	1.03	0.07
48	70	0.576	0.043
48	71	0.263	0.022
48	72	---	---
48	73	---	---
48	74	0.0325	0.0037
48	75	---	---
48	76	0.0044	0.0004
48	77	0.0013	0.0002
49	56	0.161	0.012
49	57	0.834	0.060
49	58	2.73	0.19
49	59	5.87	0.42
49	60	9.75	0.69
49	61	12.9	0.9
49	62	15.1	1.1
49	63	15.2	1.1
49	64	14.7	1.0
49	65	12.3	0.9
49	66	10.2	0.7
49	67	7.50	0.53
49	68	5.57	0.39
49	69	3.70	0.26
49	70	2.44	0.17
49	71	1.43	0.10
49	72	0.993	0.080
49	73	0.505	0.051
49	74	---	---
49	75	0.101	0.017
49	76	0.0676	0.0064
49	77	0.0115	0.0010
49	78	0.0057	0.0005

^{124}Xe+Pb 1 A GeV

Z	N	σ [mb]	Δσ[mb]
51	58	0.927	0.066
51	59	3.95	0.28
51	60	13.3	0.9
51	61	26.7	1.9
51	62	36.9	2.6
51	63	36.1	2.6
51	64	28.6	2.0
51	65	---	---
51	66	---	---
51	67	3.88	0.27
51	68	1.73	0.12
51	69	0.417	0.030
51	70	0.0872	0.0064
52	58	0.0594	0.0045
52	59	0.438	0.032
52	60	2.26	0.16
52	61	8.74	0.62
52	62	22.5	1.6
52	63	36.7	2.6
52	64	45.2	3.2
52	65	41.6	2.9
52	66	24.2	1.7
52	67	---	---
52	68	12.4	0.9
52	69	6.08	0.43
52	70	2.23	0.16
53	59	0.0175	0.0017
53	60	0.145	0.011
53	61	0.973	0.070
53	62	4.41	0.31
53	63	13.8	1.0
53	64	31.0	2.2
53	65	45.3	3.2
53	66	59.0	4.2
53	67	40.7	2.9
53	68	---	---
53	69	---	---
53	70	112	8
54	61	0.0568	0.0087
54	62	0.444	0.067
54	63	2.21	0.33
54	64	8.89	1.34

^{136}Xe+Pb 1 A GeV

Z	N	σ [mb]	Δσ[mb]
50	57	0.0630	0.0070
50	58	0.359	0.033
50	59	1.46	0.13
50	60	3.84	0.35
50	61	7.44	0.68
50	62	11.5	1.0
50	63	14.5	1.3
50	64	16.5	1.5
50	65	17.2	1.6
50	66	16.2	1.5
50	67	14.6	1.3
50	68	11.9	1.1
50	69	9.58	0.87
50	70	6.96	0.63
50	71	5.07	0.46
50	72	3.54	0.32
50	73	2.43	0.22
50	74	1.73	0.16
50	75	---	---
50	76	---	---
50	77	0.218	0.021
50	78	---	---
50	79	0.0251	0.0024
50	80	0.0064	0.0006
51	59	0.109	0.011
51	60	0.516	0.048
51	61	1.87	0.17
51	62	4.37	0.40
51	63	8.10	0.73
51	64	11.9	1.1
51	65	15.1	1.4
51	66	17.9	1.6
51	67	18.8	1.7
51	68	19.1	1.7
51	69	17.4	1.6
51	70	16.0	1.5
51	71	13.2	1.2
51	72	11.0	1.0
51	73	8.46	0.77
51	74	6.62	0.60
51	75	4.84	0.44
51	76	4.28	0.41
51	77	1.66	0.17
51	78	0.844	0.078

^{124}Xe+Pb 1 A GeV

Z	N	σ [mb]	Δσ[mb]
54	65	24.6	3.7
54	66	53.5	8.0
54	67	96.7	14.5
54	68	333	50
54	69	24.9	3.7
55	63	0.0764	0.013
55	64	0.360	0.062
55	65	1.34	0.23
55	66	3.52	0.60
55	67	4.22	0.72
55	68	3.75	0.64
55	69	1.70	0.29
*****	*****	*****	*****
*****	*****	*****	*****

^{136}Xe+Pb 1 A GeV

Z	N	σ [mb]	Δσ[mb]
51	79	0.502	0.049
51	80	0.174	0.018
51	81	0.0469	0.0043
51	82	0.0070	0.0007
52	60	0.0386	0.0059
52	61	0.208	0.024
52	62	0.849	0.095
52	63	2.38	0.26
52	64	5.18	0.57
52	65	8.66	0.96
52	66	13.1	1.5
52	67	16.3	1.8
52	68	19.5	2.2
52	69	21.9	2.4
52	70	22.9	2.5
52	71	23.2	2.6
52	72	22.0	2.4
52	73	20.5	2.3
52	74	18.5	2.0
52	75	16.1	1.8
52	76	14.1	1.6
52	77	10.9	1.2
52	78	9.86	1.11
52	79	----	---
52	80	3.56	0.39
52	81	0.525	0.059
52	82	0.319	0.035
52	83	0.0038	0.0005
53	62	0.0323	0.0047
53	63	0.277	0.037
53	64	0.966	0.127
53	65	2.39	0.31
53	66	5.07	0.66
53	67	7.92	1.03
53	68	11.9	1.6
53	69	15.6	2.0
53	70	20.5	2.7
53	71	23.1	3.0
53	72	28.7	3.7
53	73	28.5	3.7
53	74	35.2	4.6
53	75	32.2	4.2
53	76	38.3	5.0

^{136}Xe+Pb 1 A GeV

Z	N	σ [mb]	Δσ[mb]
53	77	33.9	4.4
53	78	44.5	5.8
53	79	37.4	4.9
53	80	31.7	4.3
53	81	26.6	3.5
53	82	30.6	3.9
54	64	0.0746	0.0121
54	65	0.294	0.045
54	66	0.864	0.130
54	67	1.83	0.28
54	68	3.66	0.55
54	69	5.63	0.85
54	70	9.07	1.36
54	71	11.7	1.8
54	72	18.0	2.7
54	73	20.1	3.0
54	74	27.5	4.1
54	75	32.5	4.9
54	76	44.0	6.6
54	77	57.0	8.6
54	78	95.8	14.4
54	79	207	31
54	80	656	98
54	81	2201	331
55	66	0.0533	0.0099
55	67	0.147	0.026
55	68	0.377	0.065
55	69	0.738	0.126
55	70	1.32	0.23
55	71	2.00	0.34
55	72	3.04	0.52
55	73	4.01	0.68
55	74	5.45	0.93
55	75	6.56	1.12
55	76	7.60	1.29
55	77	8.17	1.39
55	78	7.39	1.26
55	79	5.59	0.95
55	80	2.98	0.51
55	81	1.28	0.22
56	69	0.0252	0.0048
56	70	0.0435	0.0078

^{136}Xe+Pb 1 A GeV (continuation)

Z	N	σ [mb]	$\Delta\sigma_{stat}$ %
56	71	0.0673	0.0118
56	72	0.0897	0.0156
56	73	0.0934	0.0162
56	74	0.0876	0.0152
56	75	0.0745	0.0130
56	76	0.0455	0.0080
56	77	0.0283	0.0051

Appendix B

Comparison of the measured isotopic distributions with EPAX

In the following figures is presented the comparison of the full isotopic distributions measured in ^{136}Xe+Pb and ^{124}Xe+Pb experiments with the prediction of the EPAX parameterization for both reaction systems.

Fig. B.1: The isotopic distributions measured in ^{136}Xe+Pb experiment for elements *Z*=10-54, compared with the prediction of the EPAX parameterization (full line). Statistical errors are smaller than the size of the points.

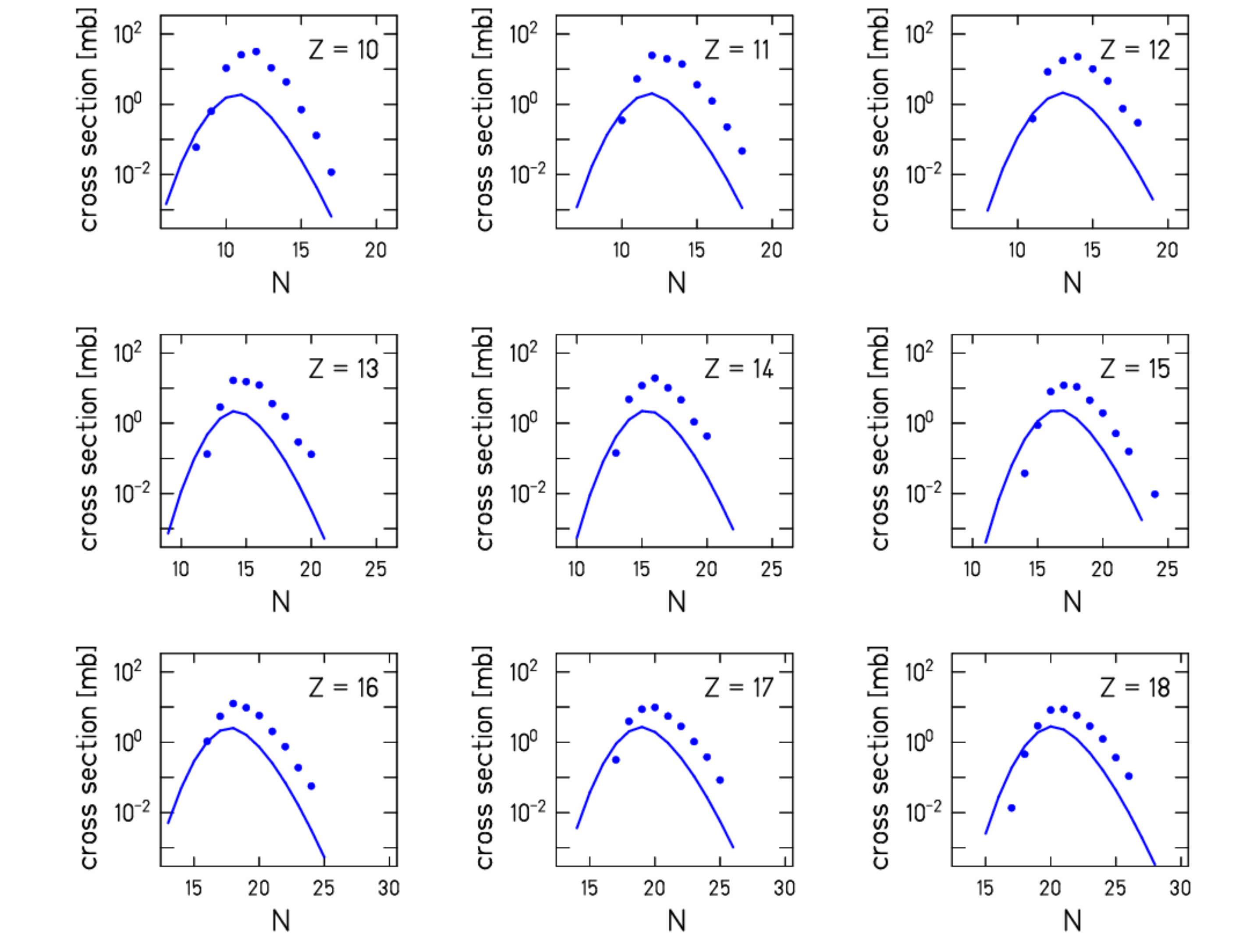

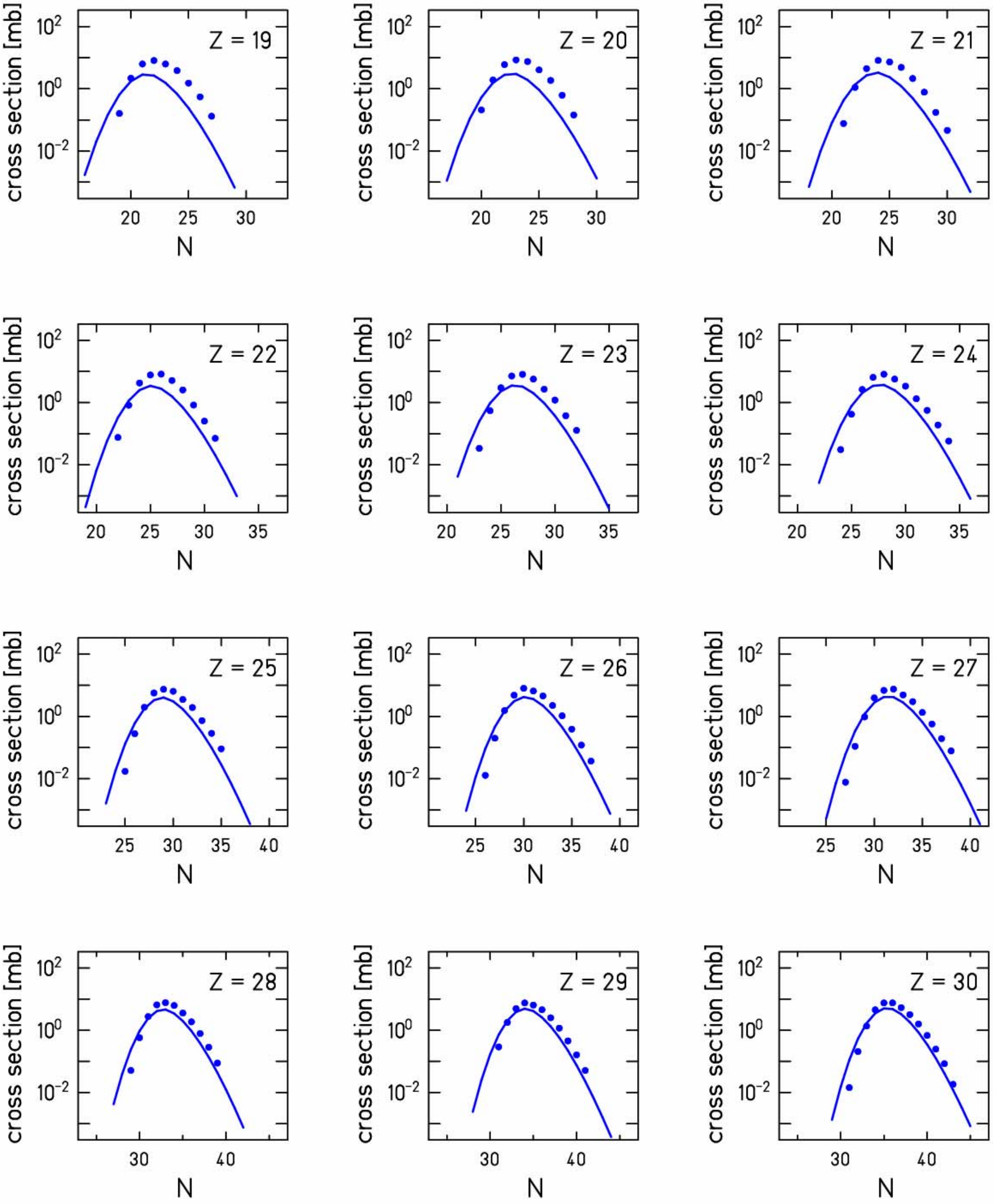
cross section [mb]
10^2
10^0
10^-2
N
Z = 19
Z = 20
Z = 21
Z = 22
Z = 23
Z = 24
Z = 25
Z = 26
Z = 27
Z = 28
Z = 29
Z = 30
20
25
30
35
40

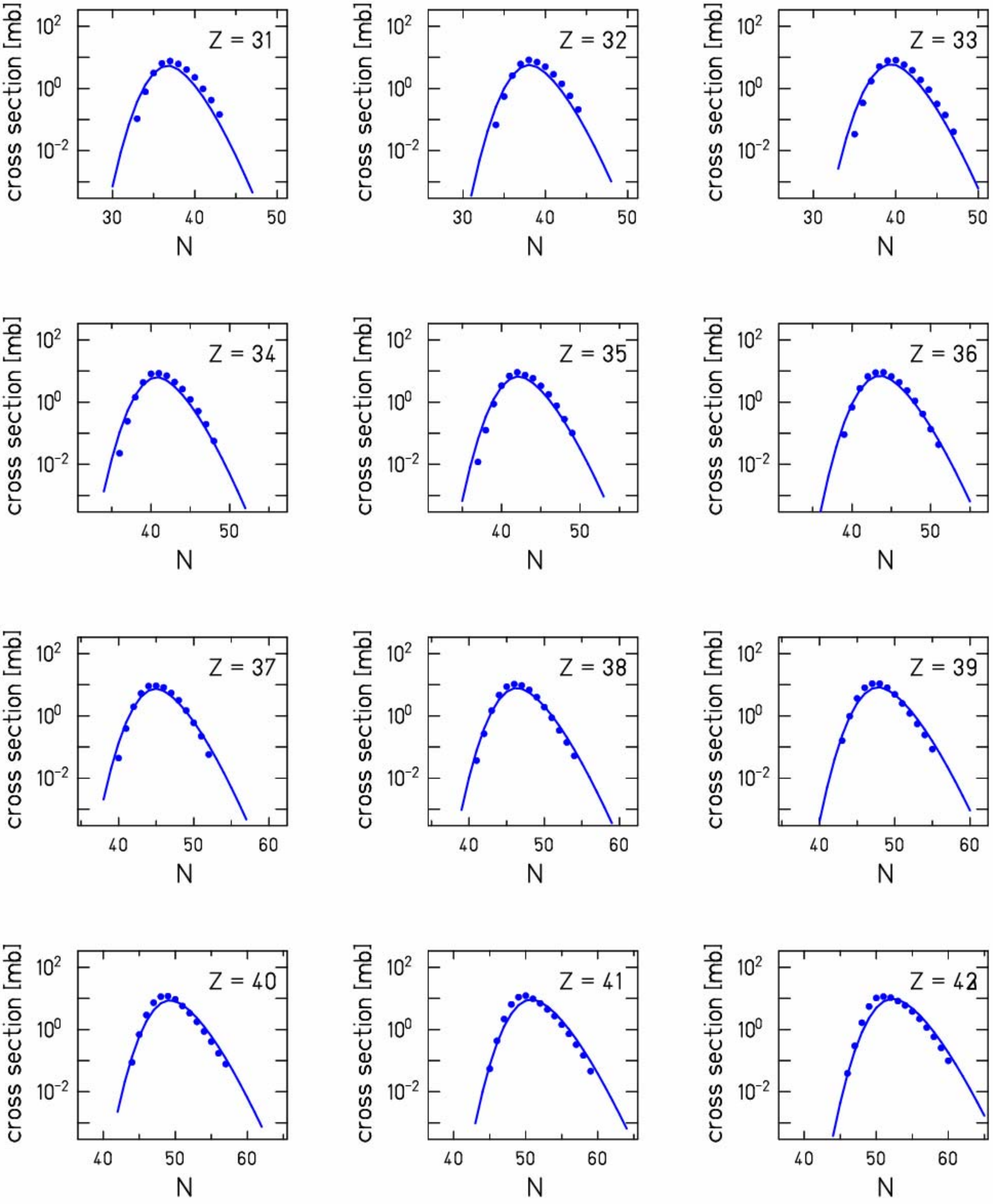
Z = 31
Z = 32
Z = 33
Z = 34
Z = 35
Z = 36
Z = 37
Z = 38
Z = 39
Z = 40
Z = 41
Z = 42
cross section [mb]
10^2
10^0
10^{-2}
N
30
40
50
60

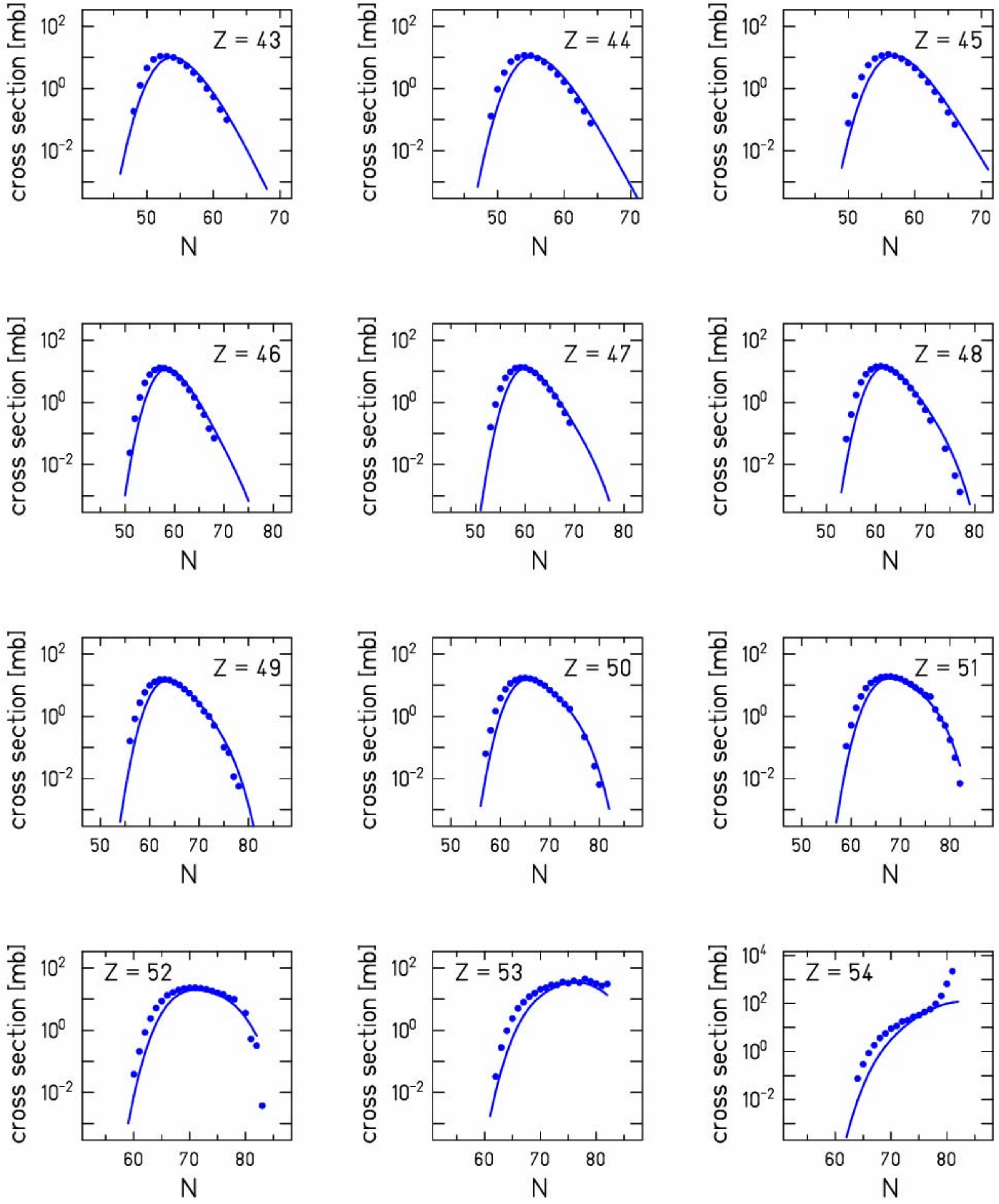
Z = 43
Z = 44
Z = 45
Z = 46
Z = 47
Z = 48
Z = 49
Z = 50
Z = 51
Z = 52
Z = 53
Z = 54
cross section [mb]
10^2
10^0
10^{-2}
10^4
N
50
60
70
80

Fig. B.2: The isotopic distributions measured in ^{124}Xe+Pb experiment for elements *Z*=10-54, compared with the prediction of the EPAX parameterization (full line). Crosses in case of element *Z*=19 indicate the isotopes reconstructed from the heavy-fragment settings. Statistical errors are smaller than the size of the points.

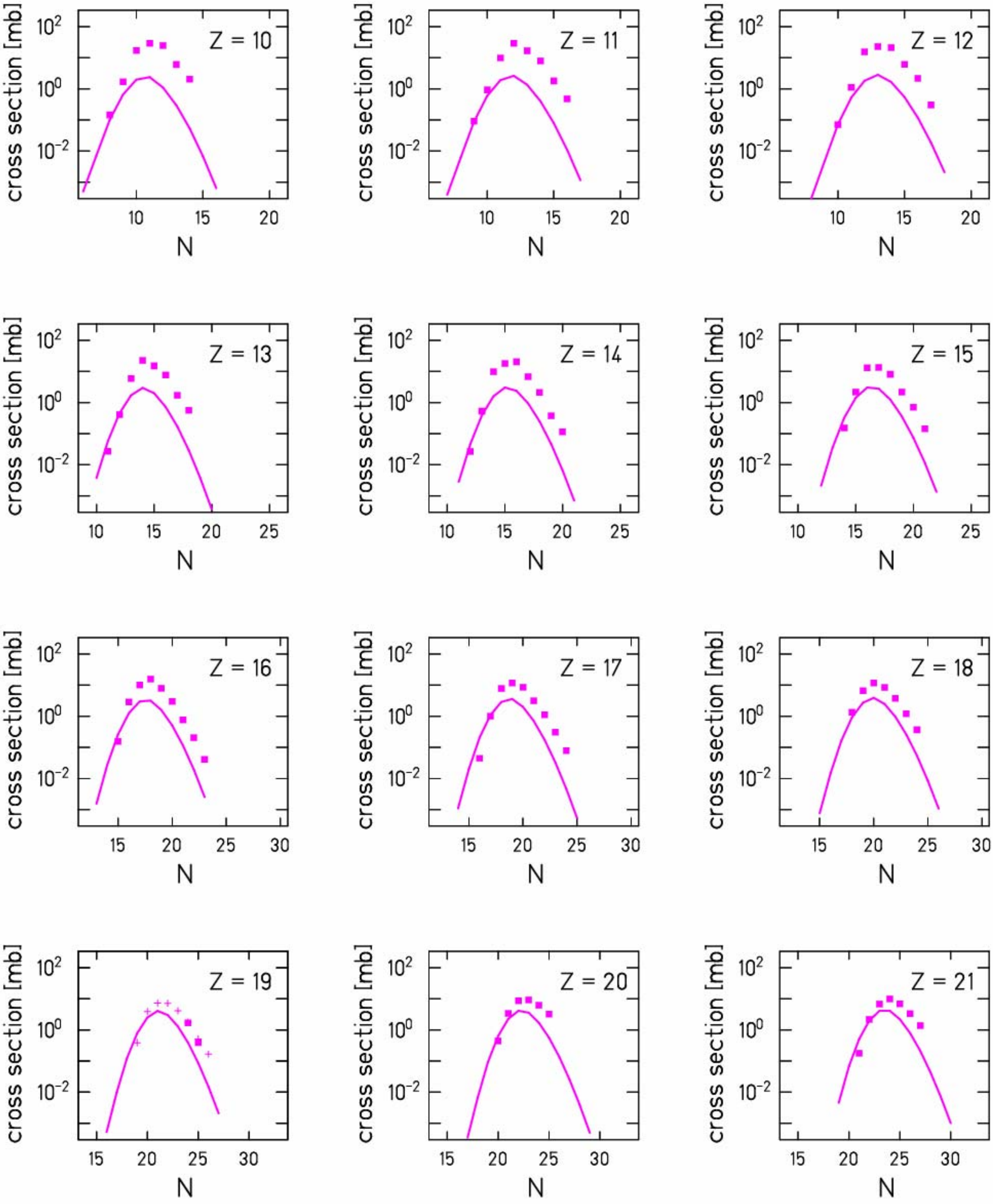

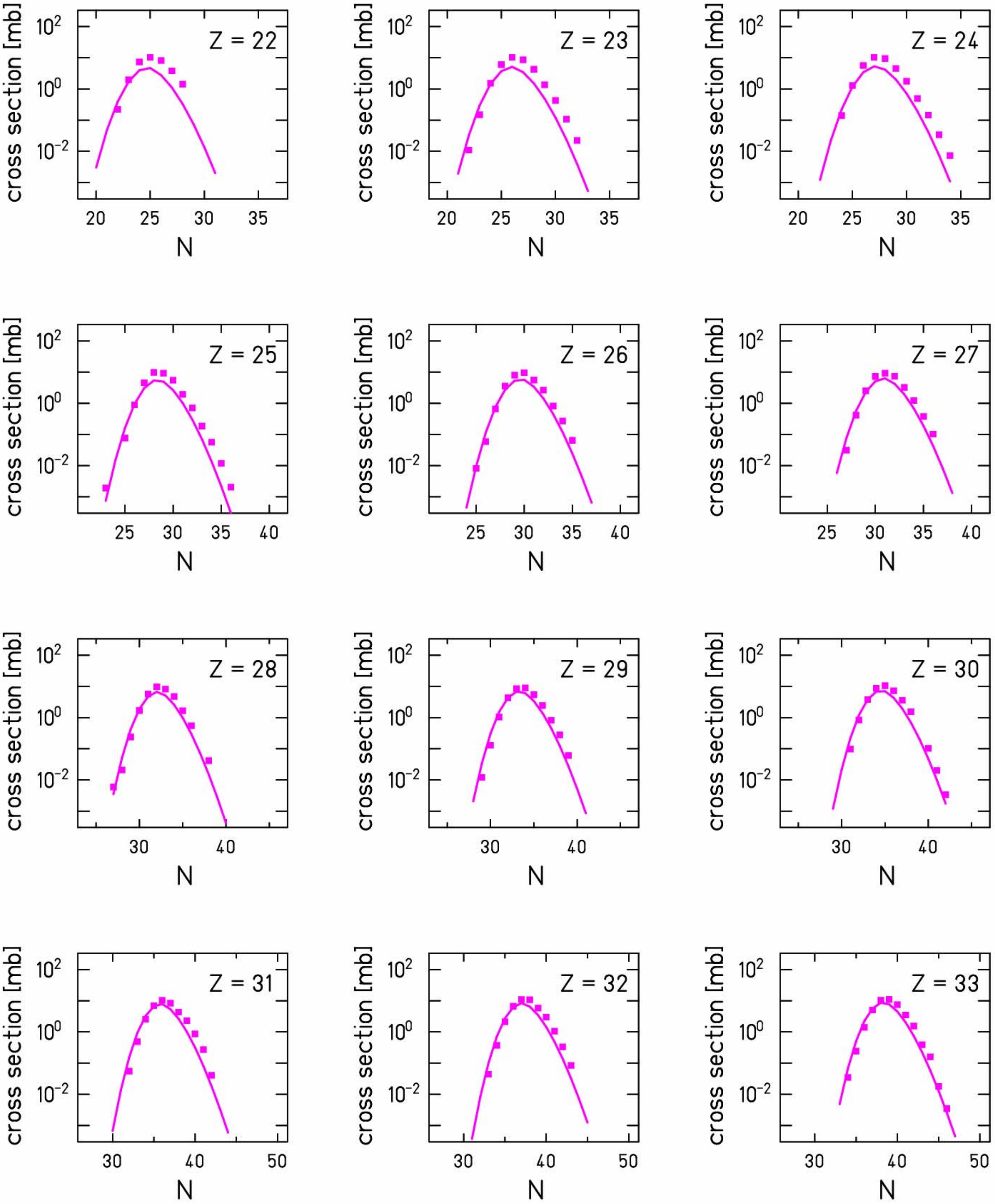
Z = 22
Z = 23
Z = 24
Z = 25
Z = 26
Z = 27
Z = 28
Z = 29
Z = 30
Z = 31
Z = 32
Z = 33
cross section [mb]
10^2
10^0
10^{-2}
N
20
25
30
35
40
50

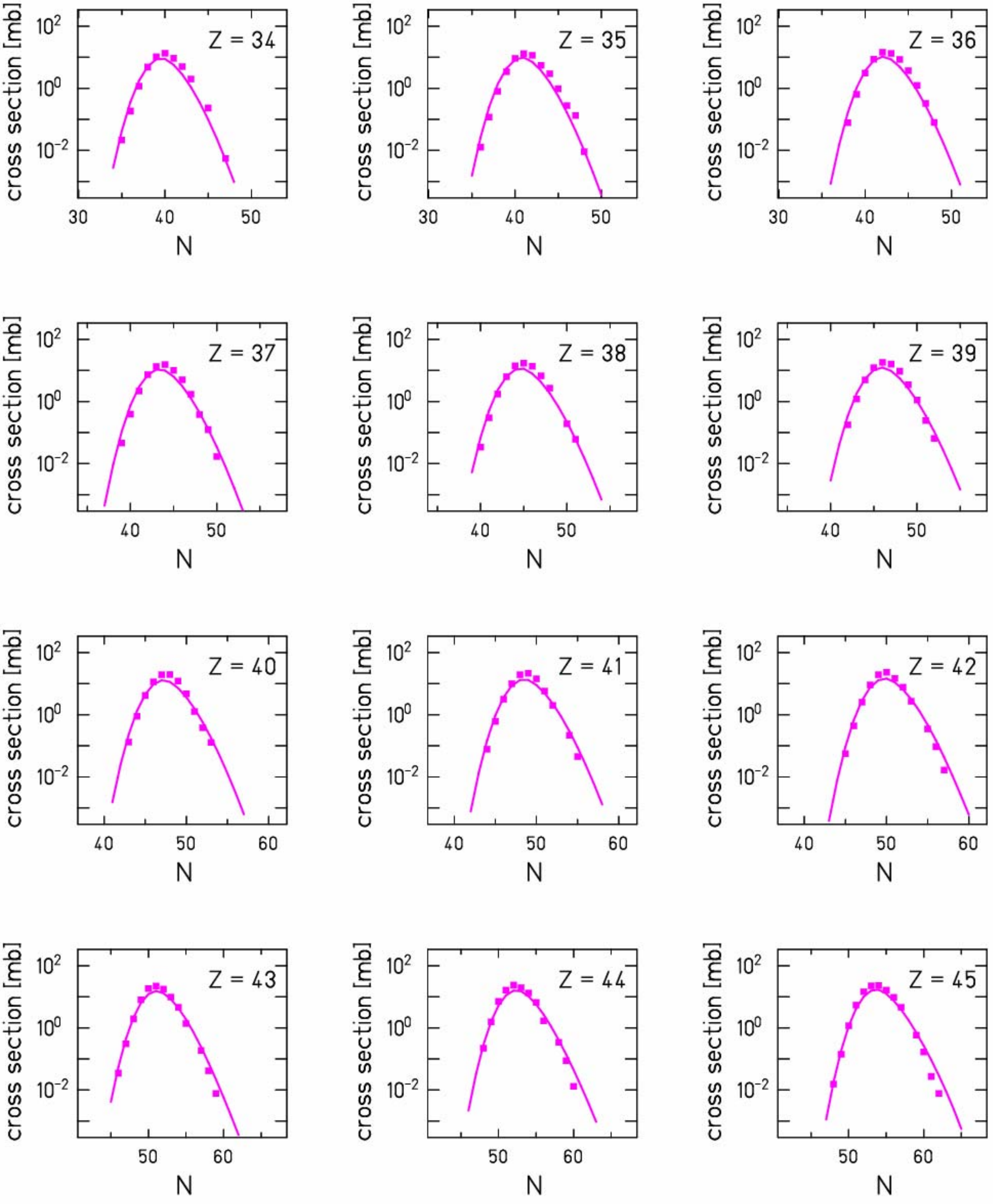
cross section [mb]
10^2
10^0
10^{-2}
N
Z = 34
Z = 35
Z = 36
Z = 37
Z = 38
Z = 39
Z = 40
Z = 41
Z = 42
Z = 43
Z = 44
Z = 45
30
40
50
60

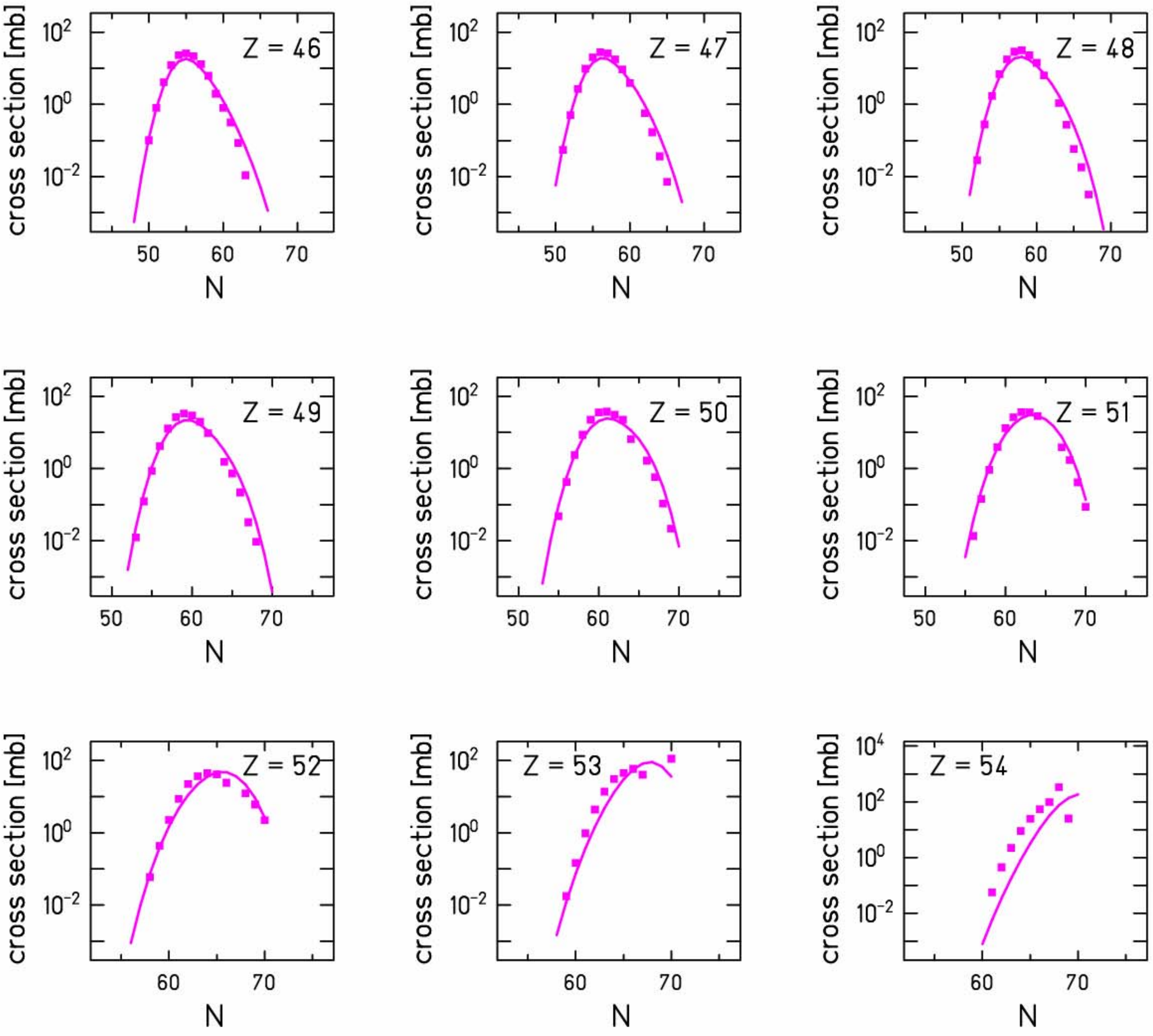
Z = 46
Z = 47
Z = 48
Z = 49
Z = 50
Z = 51
Z = 52
Z = 53
Z = 54
cross section [mb]
10^4
10^2
10^0
10^{-2}
50
60
70
N

Appendix C

Comparison of the measured isotopic distributions with ABRABLA calculations

The following figures summarize the comparison between the full isotopic distributions measured in ^{136}Xe+Pb and ^{124}Xe+Pb reactions and the ABRABLA code calculations, performed with and without the nuclear break-up, as discussed in chapter 6.

Fig. C.1: The isotopic distributions measured in ^{136}Xe+Pb experiment for elements Z=10-54, compared with the ABRABLA calculations; dashed line – calculation without break-up, full line – calculation including break-up, assuming freeze-out temperatures listed in the figures. In both calculations the cluster emission during the evaporation process was considered. Statistical errors are smaller than the size of the points.

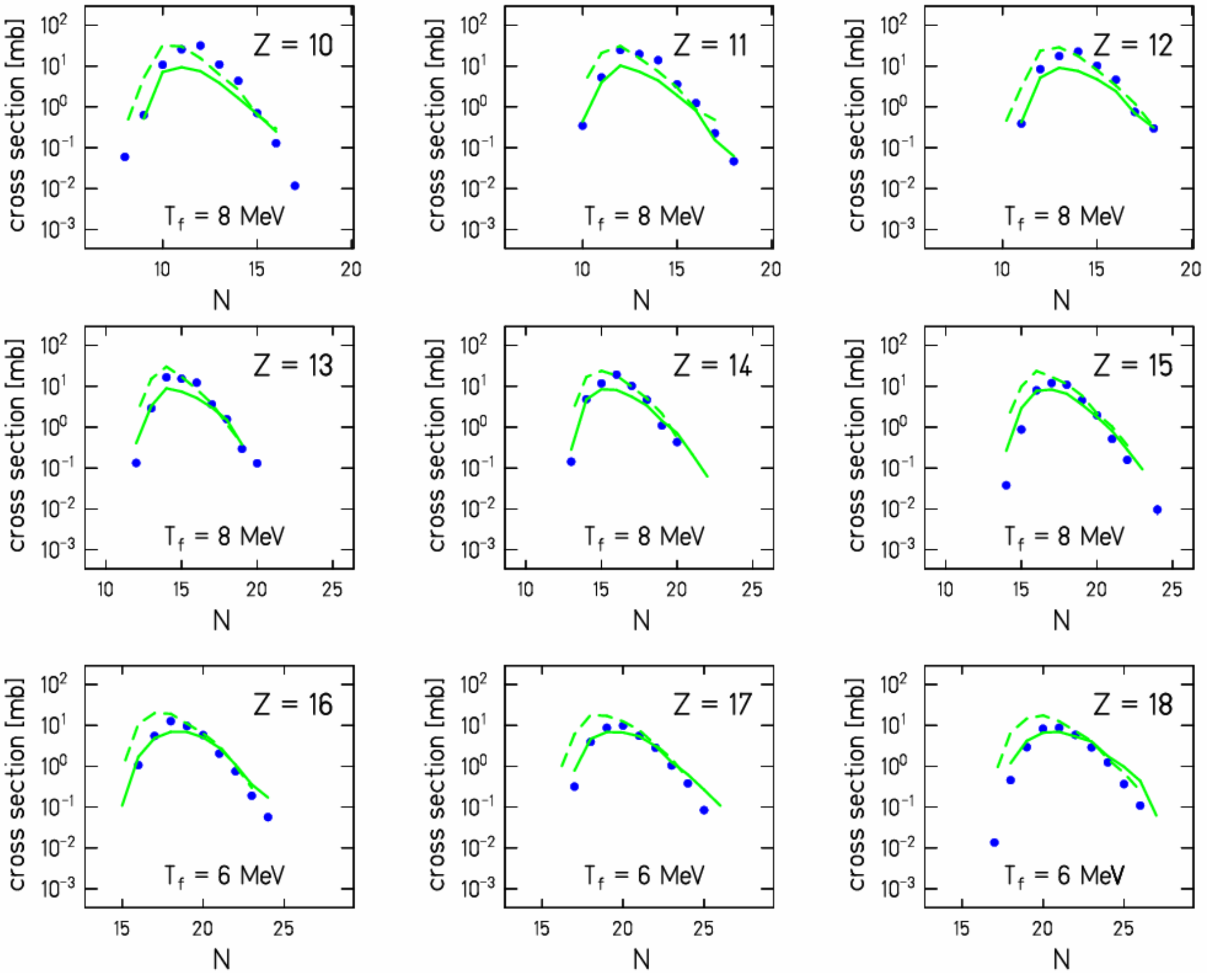

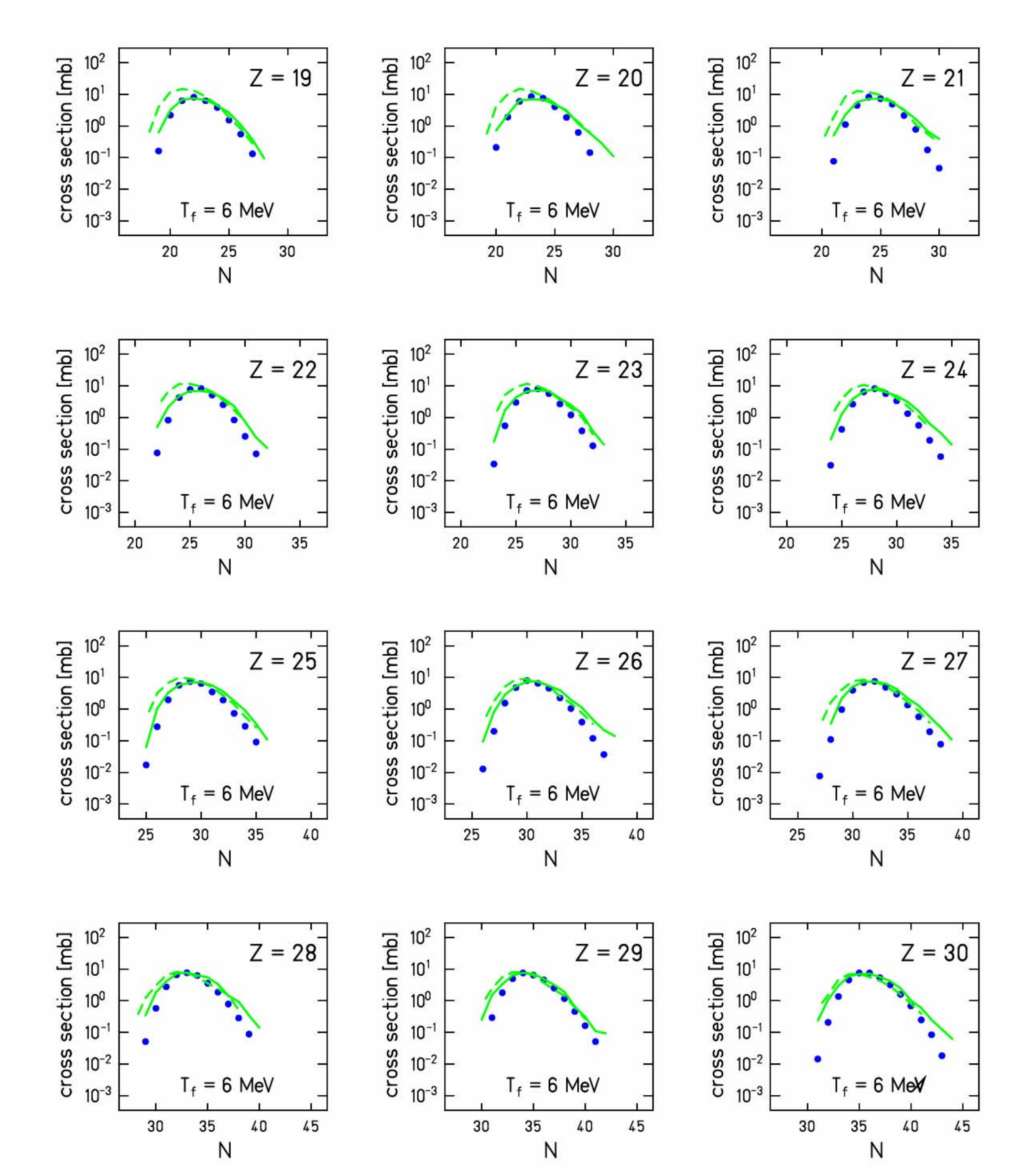
cross section [mb]
10^{2}
10^{1}
10^{0}
10^{-1}
10^{-2}
10^{-3}
N
Z = 19
T_f = 6 MeV
20
25
30
Z = 20
T_f = 6 MeV
20
25
30
Z = 21
T_f = 6 MeV
20
25
30
Z = 22
T_f = 6 MeV
20
25
30
35
Z = 23
T_f = 6 MeV
20
25
30
35
Z = 24
T_f = 6 MeV
20
25
30
35
Z = 25
T_f = 6 MeV
25
30
35
40
Z = 26
T_f = 6 MeV
25
30
35
40
Z = 27
T_f = 6 MeV
25
30
35
40
Z = 28
T_f = 6 MeV
30
35
40
45
Z = 29
T_f = 6 MeV
30
35
40
45
Z = 30
T_f = 6 MeV
30
35
40
45

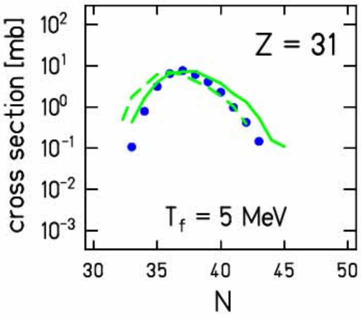
cross section [mb]
10^{2}
10^{1}
10^{0}
10^{-1}
10^{-2}
10^{-3}
Z = 31
T_f = 5 MeV
30
35
40
45
50
N

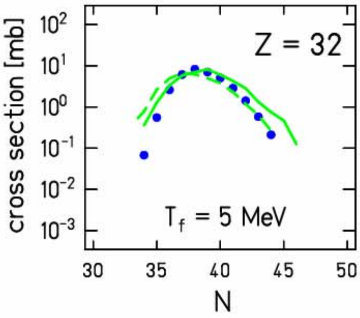
cross section [mb]
10^{2}
10^{1}
10^{0}
10^{-1}
10^{-2}
10^{-3}
Z = 32
T_f = 5 MeV
30
35
40
45
50
N

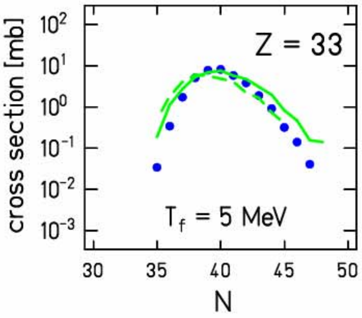
cross section [mb]
10^{2}
10^{1}
10^{0}
10^{-1}
10^{-2}
10^{-3}
Z = 33
T_f = 5 MeV
30
35
40
45
50
N

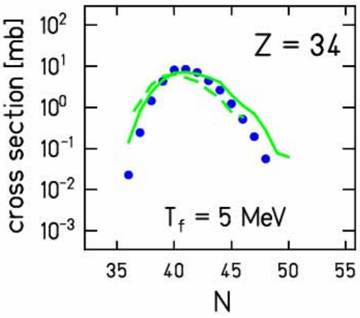
cross section [mb]
10^{2}
10^{1}
10^{0}
10^{-1}
10^{-2}
10^{-3}
Z = 34
T_f = 5 MeV
35
40
45
50
55
N

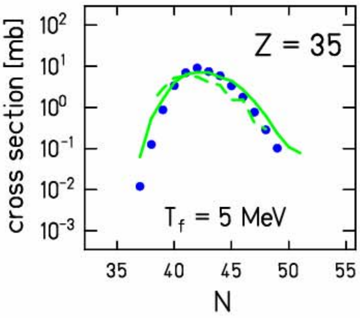
cross section [mb]
10^{2}
10^{1}
10^{0}
10^{-1}
10^{-2}
10^{-3}
Z = 35
T_f = 5 MeV
35
40
45
50
55
N

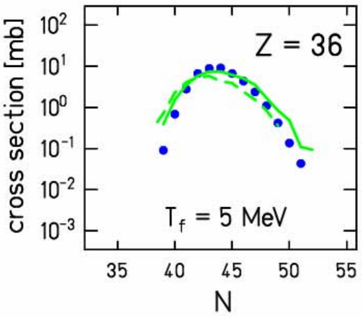
cross section [mb]
10^{2}
10^{1}
10^{0}
10^{-1}
10^{-2}
10^{-3}
Z = 36
T_f = 5 MeV
35
40
45
50
55
N

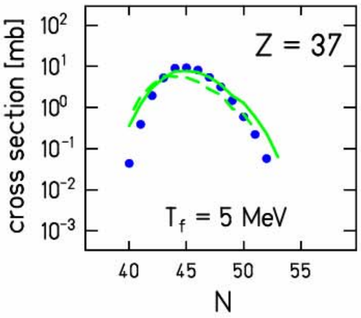
cross section [mb]
10^{2}
10^{1}
10^{0}
10^{-1}
10^{-2}
10^{-3}
Z = 37
T_f = 5 MeV
40
45
50
55
N

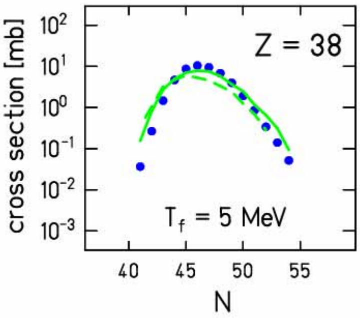
cross section [mb]
10^{2}
10^{1}
10^{0}
10^{-1}
10^{-2}
10^{-3}
Z = 38
T_f = 5 MeV
40
45
50
55
N

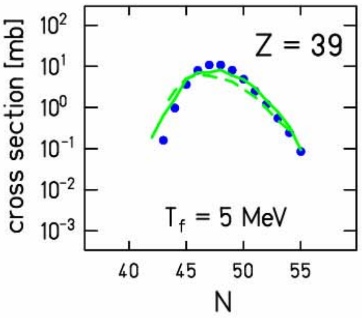
cross section [mb]
10^{2}
10^{1}
10^{0}
10^{-1}
10^{-2}
10^{-3}
Z = 39
T_f = 5 MeV
40
45
50
55
N

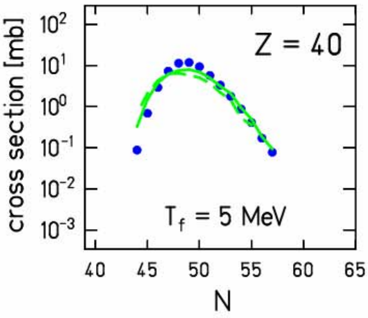
cross section [mb]
10^{2}
10^{1}
10^{0}
10^{-1}
10^{-2}
10^{-3}
Z = 40
T_f = 5 MeV
40
45
50
55
60
65
N

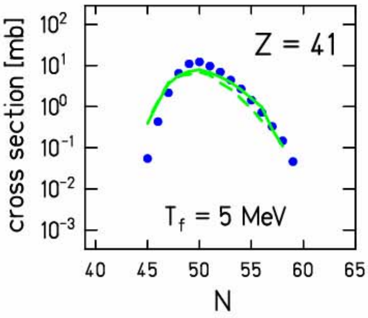
cross section [mb]
10^{2}
10^{1}
10^{0}
10^{-1}
10^{-2}
10^{-3}
Z = 41
T_f = 5 MeV
40
45
50
55
60
65
N

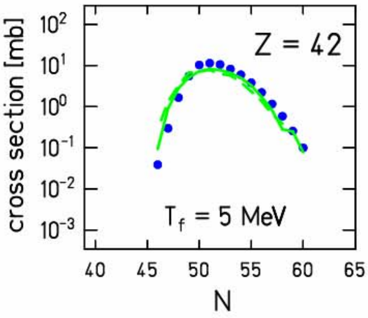
cross section [mb]
10^{2}
10^{1}
10^{0}
10^{-1}
10^{-2}
10^{-3}
Z = 42
T_f = 5 MeV
40
45
50
55
60
65
N

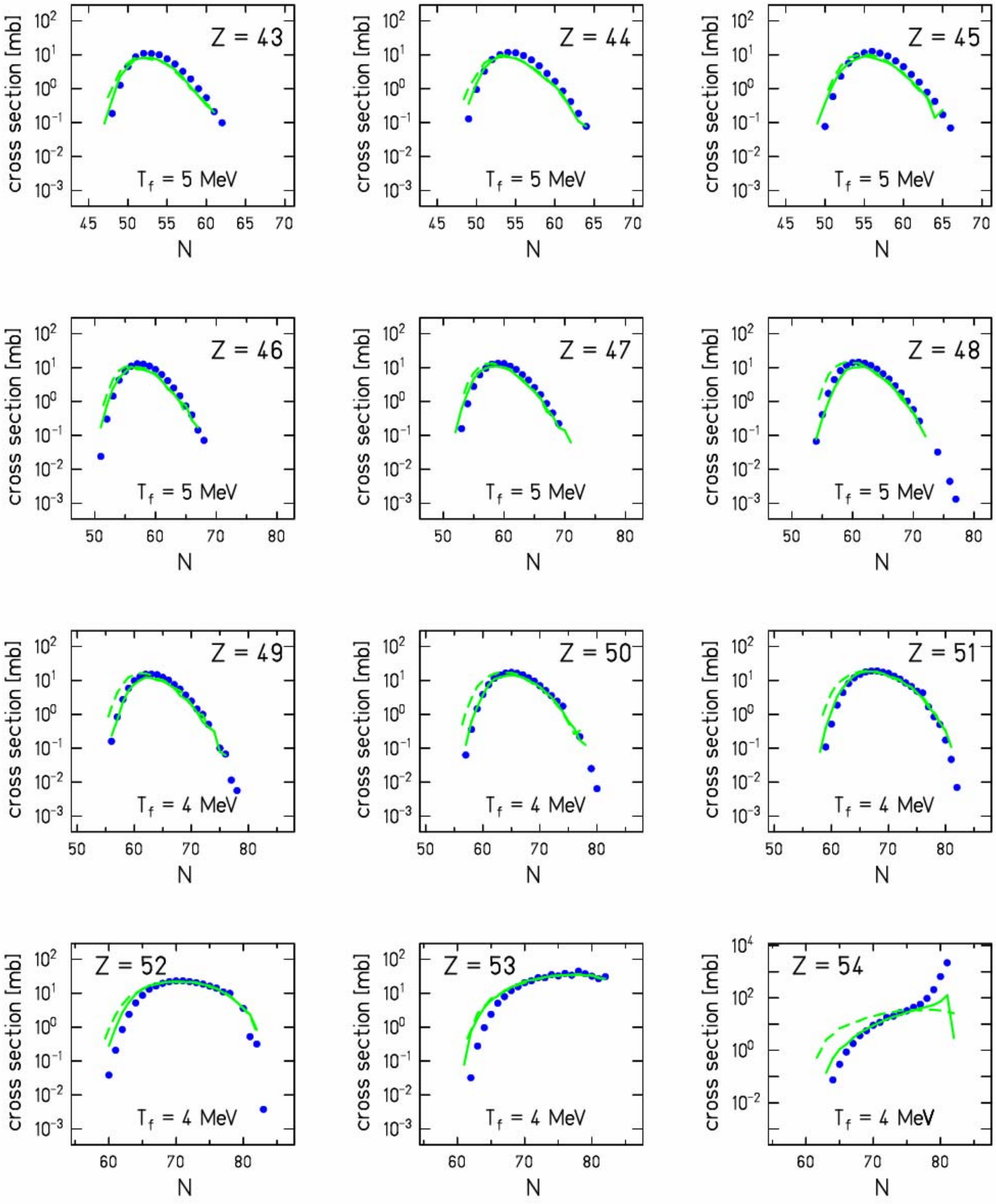
Z = 43
Z = 44
Z = 45
Z = 46
Z = 47
Z = 48
Z = 49
Z = 50
Z = 51
Z = 52
Z = 53
Z = 54
T_f = 5 MeV
T_f = 4 MeV
cross section [mb]
N
10^{-3}
10^{-2}
10^{-1}
10^{0}
10^{1}
10^{2}
10^{4}
45
50
55
60
65
70
80

Fig. C.2: The isotopic distributions measured in ^{124}Xe+Pb experiment for elements *Z*=10-54 (crosses in case of *Z*=19 correspond to isotopes reconstructed from heavy-fragment settings), compared with the ABRABLA calculations; dashed line – calculation without break-up, full line – calculation including break-up, assuming freeze-out temperatures listed in the figures. In both calculations the cluster emission during the evaporation process was considered. Statistical errors are smaller than the size of the points.

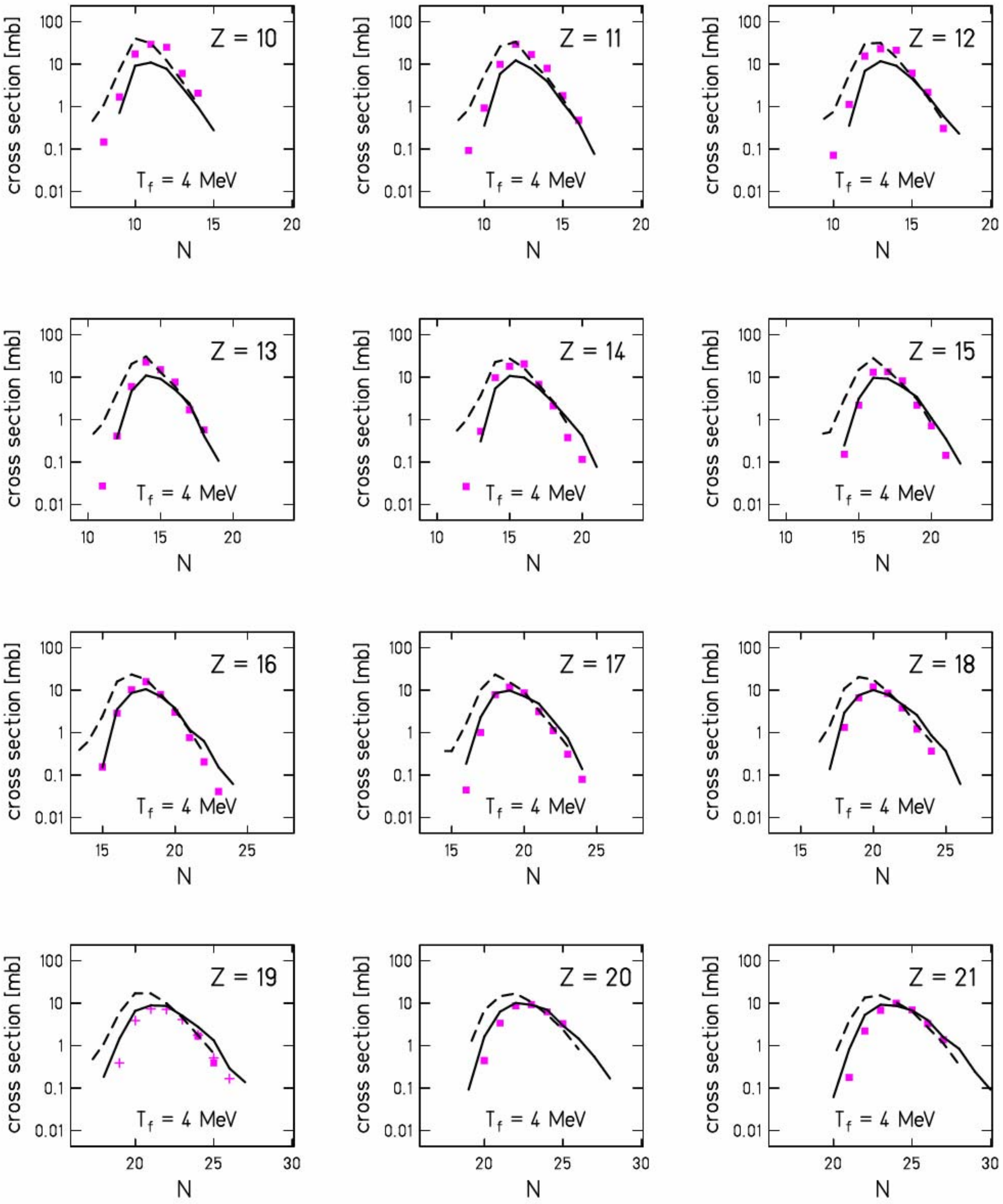

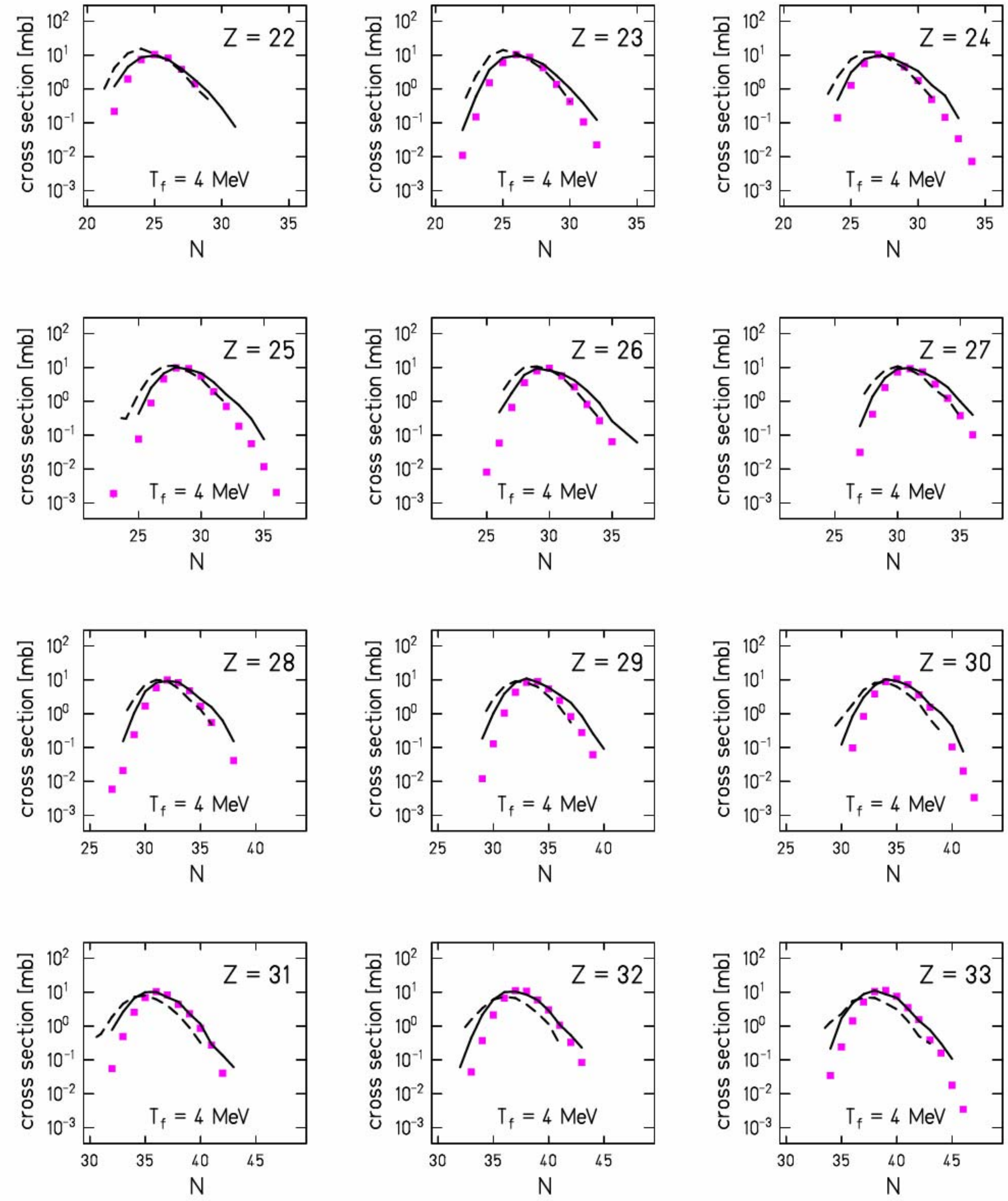
Z = 22
Z = 23
Z = 24
Z = 25
Z = 26
Z = 27
Z = 28
Z = 29
Z = 30
Z = 31
Z = 32
Z = 33
T_f = 4 MeV
cross section [mb]
N
10^2
10^1
10^0
10^{-1}
10^{-2}
10^{-3}
20
25
30
35
40
45

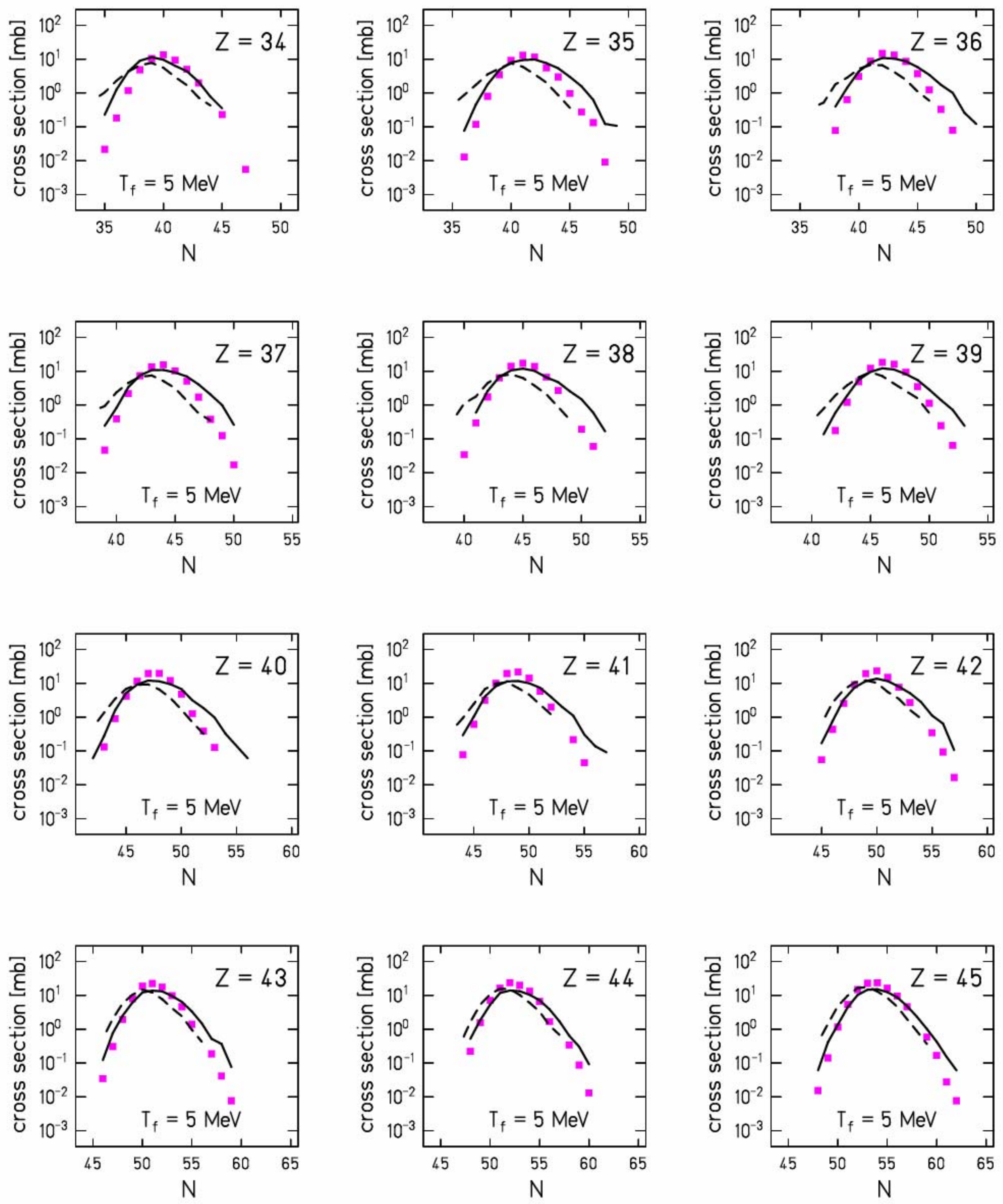
Z = 34
Z = 35
Z = 36
Z = 37
Z = 38
Z = 39
Z = 40
Z = 41
Z = 42
Z = 43
Z = 44
Z = 45
T$_f$ = 5 MeV
cross section [mb]
N
10^2
10^1
10^0
10^{-1}
10^{-2}
10^{-3}
35
40
45
50
55
60
65

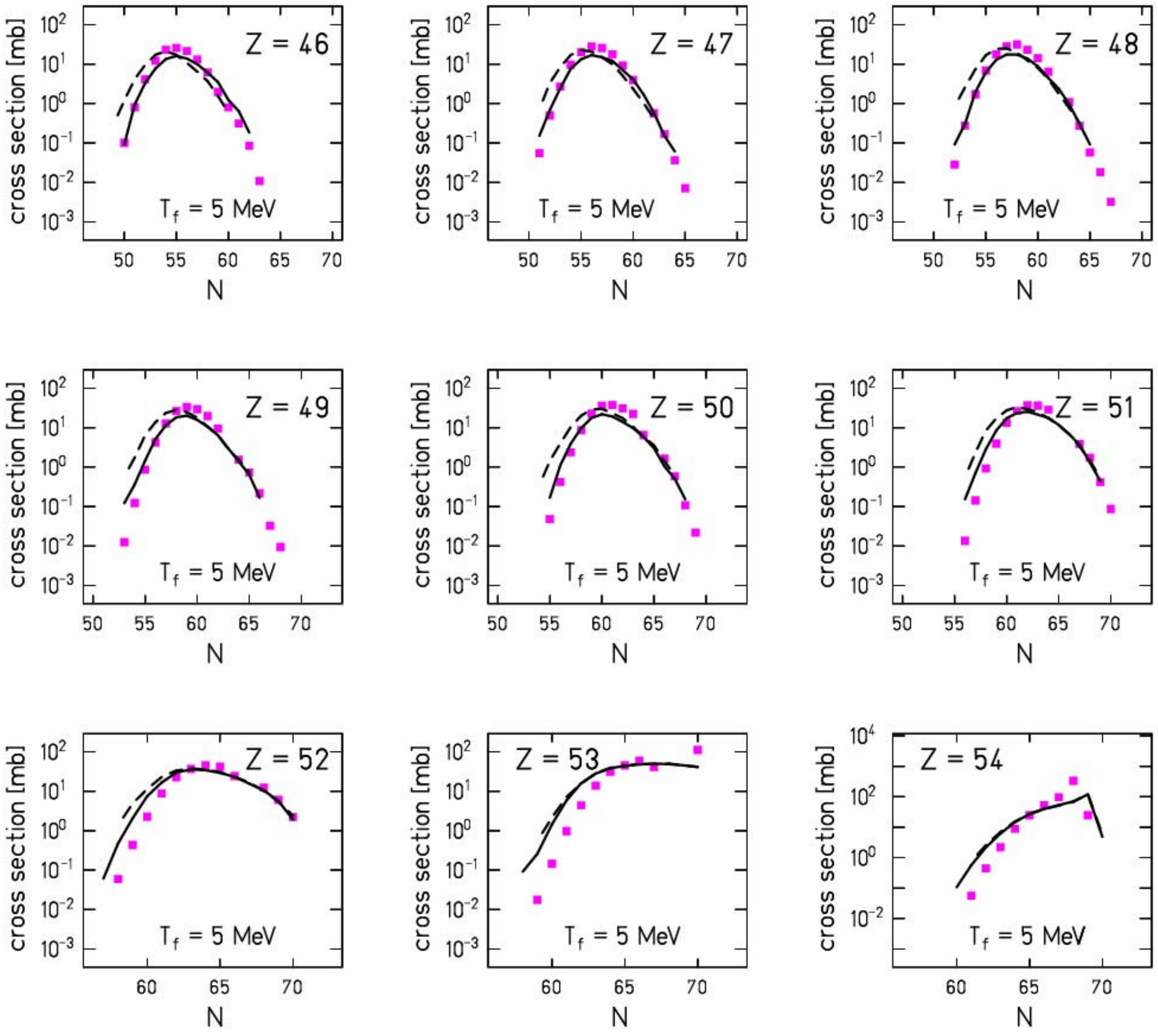
Z = 46
Z = 47
Z = 48
Z = 49
Z = 50
Z = 51
Z = 52
Z = 53
Z = 54
T_f = 5 MeV
cross section [mb]
N
10^{-3}
10^{-2}
10^{-1}
10^{0}
10^{1}
10^{2}
10^{4}
50
55
60
65
70

Bibliography

[Ahl80] S. P. Ahlen, Rev. Mod. Phys. 52 (1980) 121
[ALADIN] http://www-kp3.gsi.de/www/kp3/aladinhome.html, see also [Lin93]
[Alb85] S. Albergo et al., Nuovo Cimento 89 A (1985) 1
[AMA] K.-H. Schmidt et al., Nucl. Instr. Meth. A 260 (1987) 287; also http://www-w2k.gsi.de/charms/amadeus.htm
[Avi78] Y. Avishai, Z. Physik A 286 (1978) 285
[Bad93] A. Badalà et al.,Phys. Rev. C 48 (1993) 633
[Bar98] V. Baran et al., Nucl. Phys. A 632 (1998) 287
[Bar02] V. Baran et al., Nucl. Phys. A 703 (2002) 603
[Bar05] V. Baran et al., Phys. Rep. 410 (2005) 335
[Bas79] R. Bass, Proc. Of the Symposium on Deep-Inelastic and Fusion Reactions with Heavy Ions, Berlin 1979, Springer Verlag, Berlin
[Bene98] C. J. Benesh, B. C. Cook, J. P. Vary, Phys. Rev. C 40 (1989) 1198
[Benll01] J.Benlliure, http://www-w2k.gsi.de/charms/Preprints/EnergyLoss/paper.pdf
[Benll02] J. Benlliure, J. Pereira- Conca, K.-H. Schmidt, Nucl. Instrum. Methods A 478 (2002) 493
[Bla94] B. Blank et al., Phys. Rev. C 50 (1994) 2398
[Boh39] N. Bohr, J.A. Wheeler, Phys. Rev. 56 (1939) 426
[Bon95] J.P. Bondorf et al., Phys. Rep. 257 (1995) 133
[Bor01] B. Borderie, nucl-ex/0102016 (2001) to be published by World Scientific
[Bote00] R. Botet and M. Ploszajczak, phys. Rev. E 62 (2000) 1825
[Bot87] A.S. Botvina *et al.*, Nucl. Phys. A 475 (1987) 663
[Bot95] A.S. Botvina *et al.*, Nucl. Phys. A 584 (1995) 737
[Bot01] A.S.Botvina, I.N.Mishustin, Phys. Rev. C 63 (2001) 061601
[Bot02] A.S. Botvina, O.V. Lozhkin and W. Trautmann, Phys. Rev. C 65 (2002) 044610
[Bot04] A.S. Botvina and I.N. Mishustin, Phys. Lett. B 584 (2004) 233
[Buy05] N.Buyukcizmeci, et al., Eur. Phys. J., A25 (2005) 57
[Char88] R. J. Charity et al., Nucl. Phys. A 483 (1988) 371
[Char98] R.J.Charity, Phys. Rev. C 58 (1998) 1073
[CHIMERA] http://www.lns.infn.it/research/chimera/
[Chom99] Ph. Chomaz and F. Gulminelli, Nucl. Phys. A 647 (1999) 153
[Chom04] P. Chomaz, nucl-ex/0410024 (2004) and references therein
[Col02] M. Colonna et al., Phys. Rev. Lett. 88 (2002) 122701
[D'Ago96] M. D'Agostino *et al.*, Phys. Lett. B 371 (1996) 175
[d'Ent02] D.G. d'Enterria et al., Phys. Lett. B 538 (2002) 27
[DasGu00] S. Das Gupta et al., arXiv:nucl-th/0009033 (2000)
[deJon98] M. de Jong et al., Nucl. Phys. A 628 (1998) 479
[Dan02] P. Danielewicz, W.G. Lynch, R. Lacey, Science 298 (2002) 1592
[Dan03] P. Danielewicz, Nucl. Phys. A 727 (2003) 233

[Don94] P. Donati et al., Phys. Rev. Lett. 72 (1994) 2835
[Duf82] J.-P. Dufour et al., Nucl. Phys. A 387 (1982) 157c
[Enq01] T. Enqvist et al., Nucl. Phys. A 686 (2001) 481
[Enq02] T. Enqvist et al., Nucl. Phys. A 703 (2002) 435
[Ent01] D.G. d'Enterria *et al.*, Phys. Rev. Lett. 87 (2001) 022701
[EURISOL] http://www.ganil.fr/eurisol/Final_Report.html
[FAIR] W.F. Henning, Nucl. Instrum. Meth. A 214 (2004) 211; also http://www.gsi.de/fair/index_e.html
[Fish67] M.E. Fisher, Physics 3 (1967) 255
[Fri92] J. Friese et al., Nucl. Phys. A 553 (1993) 753c
[Frie88] W.A. Friedman, Phys. Rev. Lett. 60 (1988) 2125
[Gaar91] C. Gaarde et al., Ann. Rev. Nucl. Part. Sci. 41 (1991) 187
[Gaim91] J.-J Gaimard, K.-H. Schmidt, Nucl. Phys. A 531 (1991) 709
[Gai04] T. Gaitanos *et al.*, Nucl. Phys. A732 (2004) 24
[Gold74] A.S. Goldhaber, Phys. Lett. B 53 (1974) 306
[Hau00] J.A. Hauger et al., Phys. Rev. C 62 (2000) 024616
[Hel03] K. Helariutta et al., Eur. Phys. J. A 17 (2003) 181
[Hen05] D. Henzlova *et al.*, nucl-ex/0507003 (2005)
[Hub91] J.Hubele et al., Z. Phys. A 340 (1991) 263
[Ign75] A.V. Ignatyuk et al., Sov. J. Nucl. Phys. 21 (1975) 612
[Ign78] A.V. Ignatiuk *et al.*, Phys. Lett. B 76 (1978) 543
[Ign00] A.V. Ignatyuk, in: G.C. Bonsignori, M. Bruno, A. Ventura, D. Vretenar (Eds.), Proceedings on of the Conference Bologna 2000: Structure of the Nucleus at the Dawn of the Century, Bologna, Italy 29 May–3 June 2000, World Scientific, Singapore, 2001.
[Jan00] H.-Th. Janka and M. Rampp, Astrophys. J. Lett. 539 (2000) L33
[Jon98] M. de Jong, „Experimentalle Untersuchungen und Modellrechnungen zur Projektilfragmentation schwerer Kerne am Beispiel von ^{208}Pb", TU Darmstadt, 1998
[Jun98] A.R. Junghans et al., Nucl. Phys. A 629 (1998) 635
[Jur02] B. Jurado, K.-H. Schmidt, K.-H. Behr, Nucl. Instr. Meth. A 483 (2002) 603
[Kil95] M. Kildir et al., Phys. Rev. C 51 (1995) 1873 and references therein
[Kol97] A. Kolomiets et al., Phys. Rev. C 55 (1997) 1376
[Lar99] A.B. Larionov et al., Nucl. Phys. A 658 (1999) 375
[LASSA] http://groups.nscl.msu.edu/hira/lassa/lassa.html
[Latt93] J.M. Lattimer and F.D. Swesty, „Dense Matter and the Supernova Mechanism" in *Origin and Evolution of the Elements*, eds. N. Prantzos, E. Vangioni-Flam, and M. Casse (Cambridge, Cambridge) (1993) 331
[Latt04] J.M. Lattimer, M. Prakash, Science 304 (2004) 536
[LeFev05] A. Le Fevre *et al.*, Phys. Rev. Lett. 94 (2005) 162701
[Lin93] V. Lindenstruth, "Dynamik der Multifragmentation", PhD Thesis, Univ. Frankfurt, 1993, Report GSI-93-18
[Ma97] Y.G. Ma et al., Phys. Lett B 390 (1997) 41
[Ma04] Y.G. Ma et al., arXiv:nucl-ex/0410018
[Marg03] J. Margueron and P. Chomaz, Phys. Rev. C 67 (2003) 041602
[Marm69]P. Marmier, E. Sheldon, Physics of Nuclei and Particles, Academic Press (1969) 36
[Mezz01] A. Mezzacappa, Nucl. Phys. A688 (2001) 158c
[Mil98] P.M. Milazzo et al., Phys. Rev. C 58 (1998) 953
[Mor75] L. G. Moretto, Nucl. Phys. A 247 (1975) 211
[Mor93] L.G. Moretto, G.J. Wozniak, Ann. Rev. Nucl. Part. Sci. 43 (1993) 379 and references therein
[Morr80] D.J. Morrissey et al., Phys. Rev. C 21 (1980) 1783

[Morr94] D.J. Morrissey et al., Ann. Rev. Nucl. Part. Sci. 44 (1994) 27

[Müll95] H. Müller and B.D. Serot, Phys. Rev. C 52 (1995) 2072

[Nap04a] P. Napolitani et al., Phys. Rev. C 70 (2004) 054607

[Nap04b] P. Napolitani, PhD thesis: "New findings on the onset of thermal disassembly in spallation reactions", Université Paris XI, France, September 2004

[Nör00] W. Nörenberg et al., Eur. Phys. J. A 9 (2000) 327; Eur. Phys. J. A 14 (2002) 43

[Nat02] J. Natowitz et al., Phys. Rev. C 65 (2002) 034618

[Ode00] T. Odeh et al., Phys. Rev. Lett. 84 (2000) 4557

[Ono03] A. Ono et al., Phys. Rev. C 68 (2003) (051601)R

[Ort04] R. Ortega et al., Nucl. Phys. A 734 (2004) 541

[Pag04] A. Pagano et al., Nucl. Phys. A 734 (2004) 504

[Poch87] J. Pochodzalla et al., Phys. Rev. C 35 (1987) 1695

[Poch97] J. Pochodzalla, Prog. Part. Nucl. Phys. 39 (1997) 443 and references therein

[Poch95] J. Pochodzalla et al., Phys. Rev. Lett. 75 (1995) 1040

[Poch01] J. Pochodzalla and W. Trautmann, „Chemical Equlibrium and Isotope Temperatures" in Isospin Physics in Heavy-Ion Collisions at Intermediate Energies, ed. by B.-A. Li and W.U. Schröder (Nova Science Publishers, New York) p. 451 (2001)

[Rad00] Al. H. Raduta and Ad. R. Raduta, Phys. Rev. C 59 (1999) R1855; Nucl. Phys. A 671 (2000) 609

[Ran81] J. Randrup and S.E. Koonin, Nucl. Phys. A 356 (1981) 223

[Rav87] H. L. Ravn, Nucl. Instrum. Methods B 26 (1987) 72

[Rei98] J. Reinhold et al., Phys. Rev. C 58 (1998) 247

[Rej01] F. Rejmund et al., Nucl. Phys. A 683 (2001) 540

[RIA] J.A. Nolen et al., Nucl. Instr. Meth. B 204 (2003) 293

[RIBF] http://www.rarf.riken.go.jp/

[Ric05a] M.V. Ricciardi, PhD thesis: "High-resolution measurements of light nuclides produced in 1 *A* GeV ^{238}U-induced reactions in hydrogen and in titanium", Universidad de Santiago de Compostela, Santiago de Compostela, Spain (2005)

[Ric05b] M.V. Ricciardi et al., nucl_ex/0508027

[Ric04] M.V. Ricciardi et al., Nucl. Phys. A 733 (2004) 299

[Rich01] J. Richert, P. Wagner, Phys. Rep. 350 (2001) 1 and references therein

[Rud66] G. Rudstam, Z. Naturforsch. A 21 (1966) 1027

[SEE] http://www-w2k.gsi.de/charms/seetraminfo/news.htm

[Scha01] R.P. Scharenberg *et al.*, Phys. Rev. C 64 (2001) 054602

[She05] D.V. Shetty *et al.*, Phys. Rev. C 71 (2005) 024602

[Schm93] K.-H. Schmidt et al., Phys. Lett. B 300 (1993) 313

[Schm02] K.H. Schmidt et al., Nucl. Phys. A 710 (2002) 157

[Schn96] R. Schneider, PhD thesis, TU München (1996); Zeit. für Phys. A 348 (1994) 241

[Schü96] A. Schüttauf et al., Nucl. Phys. A 607 (1996) 457

[Shu99] Shuying Wan, Ph.D. thesis, University of Heidelberg (1999)

[Sie86] A. J. Sierk, Phys. Rev. C 33 (1986) 2039

[Silb73] R. Silberberg and C.H. Tsao, Astrophys. J., Suppl. 25 (1973) 335

[Sou03] G.A. Souliotis et al., arXiv:nucl-ex/0305027

[Sou04] G.A. Souliotis et al., Phys. Lett. B 588 (2004) 35

[Sri02] B. K. Srivastava et al., Phys. Rev. C 65 (2002) 054617

[Sté91] C. Stéphan et al., Phys. Lett. B 262 (1991) 6

[Ste92] M. Steiner et al., Nucl. Instr. Meth. A 312 (1992) 420

[Süm90] K. Sümmerer et al., Phys. Rev. C 42 (1990) 2546

[Süm00] K. Sümmerer, B. Blank, Phys. Rev. C 61 (2000) 034607

[Tsa97a] M.B. Tsang et al., Phys. Rev. Lett. 78 (1997) 3836

[Tsa97b] M.B. Tsang et al., Phys. Rev. C 55 (1997) R557
[Tsa01a] M.B. Tsang *et al.*, Phys. Rev. Lett. 86 (2001) 5023
[Tsa01b] M.B. Tsang *et al.*, Phys. Rev. C 64 (2001) 054615
[Tsa01c] M.B. Tsang *et al.*, Phys. Rev. C 64 (2001) 041603
[Ves01] M. Veselsky et al., Phys. Lett. B 497 (2001) 1
[Ves04] M. Veselsky, nucl-ex/0407002
[Vol04] C. Volant *et al.*, Nucl Phys. A734 (2004) 545
[Webb90] W.R. Webber, J.C. Kish, and D.A. Schrier, Phys. Rev. C 41 (1990) 547
[Web94] M. Weber et al., Nucl. Phys. A578 (1994) 659
[Wei37] V. Weisskopf, Phys. Rev. 52 (1937) 295
[Wes79] G.D. Westfall et al., Phys. Rev. Lett. 43 (1979) 1859
[Xi97] H. Xi et al., Z.Phys. A359 (1997) 397; erratum in: Eur.Phys.J. A1 (1998) 235
[Xu00] H.S. Xu et al., Phys. Rev. Lett. 85 (2000) 716
[Zie92] C. Ziegler, Diploma Thesis, Institut für Kernphysik, TH Darmstadt (1992)

Acknowledgements

Last but not least, I would like to devote the following lines to express my warm thanks and gratitude to all those, who have accompanied me during my PhD years at GSI and without whom this work would not be possible.

First of all I would like to express my deepest thanks to Dr. Karl-Heinz Schmidt, my scientific supervisor, who was always present and ready anytime the discussion or advice were needed. It was for the first time that I experienced the inspiring collaboration, where I could ask any question I might have had and always obtained a very dedicated and clarifying explanation. Those were the common discussions, which brought me the true insight into the nuclear physics and which showed me its amazing world in pictures and imaginations without the need of the complicated equations. But not only was the understanding of the peculiar features of the experimental data brought to me in a very extensive form, but as well I could gain an essential experience with the experimental electronics and detector equipment, which I appreciate very much. Therefore, it certainly deserves to be expressed that thanks to you, Karl-Heinz, I experienced what it truly means to be a *scientist*. And I hope we still find some time to finally play the Fantasia from Schubert together!

As well I would like to frankly thank to Dr. Vladimír Wagner, my main supervisor, who provided an important connection to the Czech Technical University, where this thesis was submitted. I am very thankful for his useful comments after reading the first manuscript of this thesis and especially for his engagement and help with all the duties at the University, which would be otherwise almost impassable over such a long distance.

I am as well very grateful to Dr. Alexander Botvina for many interesting discussions at the beginning of my PhD as well as for introducing me the SMM code. I would like to express my thanks for his SMM calculations and scientific contribution to the part of the thesis dedicated to the investigation of the symmetry energy coefficient.

As well I would like to express my gratitude to Dr. Francesca Gulminelli for her very useful and clarifying remarks and suggestions upon reading the draft of this thesis.

At the beginning of my PhD it was especially Andreas Heinz, who helped me with his very inspiring suggestions and useful comments to learn and improve the way of presenting my work on seminars and conferences, which is an indispensable skill of a future scientist. As well I am very thankful for his enthusiastic and very efficient contribution to the first experiment performed within this thesis. For the strong support and engagements during both experiments I would like to express my gratitude as well to Fanny Rejmund, Timo Enqvist, Arnd Junghans, and to the technicians of the Fragment Separator as well as to Nikolas Kurz for his very useful advices in preparing the data acquisition for the second beam time. My thanks go as well to Jorge Pereira-Conca for providing the FRS transmission calculations for both of my experiments.

For a continuous support and great motivation during my whole PhD period I would like to thank to my colleagues and friends, Aleksandra Kelić and M.Valentina Ricciardi. I would like to express my gratitude to Aleksandra for her numerous and very useful advices anytime I needed help and for unceasing moral support as well as for her comments and suggestions during the reading of the first draft of the thesis. To Vale I would like to express my thanks especially for her great interest and curiosity in my work, which in fact is a continuation of her very rich PhD thesis. As well I would like to thank you, Vale, to provide me a lot of advices and great help during my beginning with the FRS data analysis (I appreciate very much especially your very useful notes – indeed from you, Vale, I learned how are the good notes important!). I would like to thank to both of you, Ale and Vale, for your enthusiastic interest and efficient help any time I entered your office!

My special thank belongs to Paolo Napolitani for his strong support and friendship, in him I could find the true physicist, who really appreciates any single detail of the experimental data with very inspiring excitement (or better said "excitation" ? ;-)). As well I would like to thank to all my 'new CHARMS' friends Lydie Giot, Radek Pleskač, Pavel Nadtochy, Strahinja Lukić and Antoine Bacquias who entered our group just recently, for making our group full of life and new experiences! I hope our group will always remain as CHARMing as it nowadays is!

Finally, I would like to express my sincerest thanks to my dear friend Adriana Banu, who filled my GSI life with many great moments and a lot of fun! I am really happy to have met you, Adi, and I am looking forward that our adventures will continue even between Texas A&M and MSU! I hope that we can make all our wishes become truth!

Last but not least my deepest thanks are dedicated to my beloved husband, Vladimir, he is the one who kept me going when I thought I cannot anymore, who supported and accompanied me in all the sad and happy times and gave me the biggest inspiration and motivation I could ever imagine. Although it may seem impossible to many, it is the greatest experience and the most beautiful choice to follow the common path in the everyday life and to be able to share the support and understanding with someone who can encounter the very same obstacles as well as successes. My dearest love, there are not enough words to express my gratitude and love! Without you this work would be impossible.

The same deepest thank is devoted to my beloved mum and my dearest family for their overwhelming support and sincere interest and motivation to my work. I am very thankful to my mum for giving me the possibility to study, for being always ready to provide any help and support I might need and especially for being always there during my entire life. *Moje nejdražší maminko, děkuji ti za všechnu tvou péči, lásku a starostlivost!*